# Precision measurement of the weak charge of the proton and parity violation in the N $\rightarrow \Delta$ transition

Anna R. Lee

Dissertation submitted to the Faculty of the

Virginia Polytechnic Institute and State University

in partial fulfillment of the requirements for the degree of

Doctor of Philosophy

in

Physics

Mark L. Pitt, Chair

Patrick Huber

Jonathan Link

Nahum Arav

September 13, 2019

Blacksburg, Virginia

Keywords: nuclear physics, electromagnetic, electroweak, parity violation, symmetry, proton, weak charge

# Precision measurement of the weak charge of the proton and parity violation in the N $\rightarrow \Delta$ transition

Anna R. Lee

## ABSTRACT

The $Q_{weak}$ Experiment ran for two and a half years at the Thomas Jefferson National Accelerator Facility in pursuit of $Q_w^p$, the neutral weak analog to the electric charge of the proton. $Q_{weak}$ measured the parity-violating asymmetry in elastic electron-proton scattering at an extreme forward angle ($Q^2 = 0.0249\,(\mathrm{GeV/c})^2$). From the data gathered via the 1.16 GeV 180 $\mu$A longitudinally polarized electron beam scattering off the unpolarized photons in the liquid hydrogen target, a value of $Q_w^p\,(\mathrm{PVES}) = 0.0719 \pm 0.0045$ was determined. The Standard Model has a definite prediction of $Q_w^p\,(\mathrm{SM}) = 0.0708 \pm 0.0003$, consistent with the value determined by $Q_{weak}$ which sets a limit on possible new physics up to 7.5 TeV.

The theory behind the main measurement of the $Q_{weak}$ Experiment is described in this document, along with the apparatus that made the measurement possible. Understanding the kinematics of the apparatus was a vital component to $Q_{weak}$'s final measurement. An in-depth explanation of the tracking system responsible for benchmarking the momentum transfer and scattering angle simulations is included. The unblinded analysis of $Q_{weak}$'s final result is outlined, as are additional physics results related to the N$\rightarrow \Delta$ transition.

During April 2012, an opportunity was seized to take ancillary data on the inelastic N$\rightarrow \Delta$ transition at a different beam energy(877 MeV) than the nominal $Q_{weak}$ data. This data, combined with the inelastic data taken at nominal beam energy and a previous measurement, determined a constraint on $d_\Delta$, a low energy constant related to hadronic parity violation, of $(3.8 \pm 14.7) g_\pi$. It also resulted in a measurement of the beam-normal single-spin asymmetry of the N$\rightarrow \Delta$ transition of $149 \pm 3$ (stat) $\pm 72$ (syst) ppm. This document includes both the longitudinal and transverse analysis of the 877 MeV data.

# Precision measurement of the weak charge of the proton and parity violation in the N $\rightarrow \Delta$ transition

Anna R. Lee

## GENERAL AUDIENCE ABSTRACT

The $Q_{weak}$ Experiment, run at the Thomas Jefferson National Accelerator Facility, measured the weak charge, the weak force analog of the electric charge of the electromagnetic force, of the proton. Unlike the well-know Large Hadron Collider, which operates on the energy-frontier and directly searches for new particles, $Q_{weak}$ operates by precisely measuring the results of scattering electrons off of protons. This approach is referred to as the precision-frontier and is used to test the Standard Model, which has a well-defined prediction for the weak charge of the proton. Deviations from the Standard Model would suggest that there was new physics beyond the Standard Model affecting the results. However, the $Q_{weak}$ measured weak charge of the proton, $Q_w^p$ (PVES) $= 0.0719 \pm 0.0045$, is in good agreement with the Standard Model predicted value. This provides a new limit, 7.5 TeV, on possible new physics beyond the Standard Model.

The theoretical background and apparatus of the $Q_{weak}$ experiment will be explained in this document. A vital component of the final result was understanding the path and energy of the electron as it passed through the apparatus. This was done via simulation but benchmarked by the tracking system. The tracking system will be explained in detail. The final analysis of the $Q_{weak}$ measurement of the weak charge will also be explained.

A secondary result discussed here focuses on data taken using the $Q_{weak}$ apparatus but at a different beam energy than the nominal $Q_{weak}$ data. For this data, the electron scatter inelastically off the proton. The lost kinetic energy of the electron causes the proton to be excited into the first resonance state, the $\Delta$, which quickly decays away. This transition grants access to a low energy constant, $d_\Delta$, and a measurement linked to the spins of the electrons being polarized perpendicular to the direction of the beam, $B_n$. The extraction of these values is covered in detail.

# Acknowledgments

There are many people who have helped me along the way to finishing this dissertation. I owe them all many thanks.

The first one I will mention is my advisor, Mark Pitt. He has been in my corner for the entirety of my graduate student career and has always been helpful and understanding. He introduced me to the $Q_{weak}$ Experiment when I came to Virginia Tech on a graduate school visit and I joined the collaboration prior to even starting at Virginia Tech. John Leacock and Juliette Mammei, Mark's previous graduate students, were fonts of advice and help on many subjects.

Speaking of the collaboration, many people have been exceedingly helpful over the years. David Armstrong, Siyuan Yang, and Valerie Gray were instrumental in my work on the tracking system of $Q_{weak}$. David and Val also both assisted with the analysis of the 877 MeV data, as did Steve Woods, Hend Nuhait, and Thamraa Alshayeb. Other $Q_{weak}$ collaborators were always willing to chime in with advice, programming help, and other assistance: Greg Smith, Paul King, Mark Dalton. Overall, the entire $Q_{weak}$ Collaboration has been extremely

welcoming and helpful, thank you to you all!

Another collaborator I need to thank is Wade Duvall. He has been programming guru, editor, and a great friend. Thank you for always answering when I have questions.

I would also like to thank my committee: Nahum Arav, Patrick Huber, and Jonathon Link. Thank you for helping me in finishing my PhD and being willing to read this tome!

The final people I need to thank are my family: my parents who have always been on my side and at my back, my sister who is always willing to listen to me vent, and my brothers who are always cheering me on. Thank you so much for always being there for me!

# Contents

# List of Figures

# List of Tables

# Chapter 1

# Introduction

This dissertation will discuss the $Q_{weak}$ Experiment's measurement of the weak charge of the proton as well as one of the ancillary measurements, the N$\rightarrow \Delta$ transition at 877 MeV. Both measurements were taken via the $Q_{weak}$ apparatus installed in Hall C of the Thomas Jefferson National Accelerator Facility, commonly referred to as Jefferson Lab, in Newport News, Virginia. Jefferson Lab provided a highly polarized 180 $\mu$A electron beam, which was necessary to obtain the statistics required for $Q_{weak}$, as well as an established Møller polarimeter. The $Q_{weak}$ Collaboration designed and installed a Compton polarimeter, a high-power liquid hydrogen target, a toroidal magnet spectrometer, three collimators and various shielding structures, and various detectors. These are explained in detail in Chapter 3. A subset of the detectors, the tracking system, was involved in measuring the kinematics and various backgrounds and is described in detail in Chapter 4.

The $Q_{weak}$ Collaboration, which spread across 23 different institutions, was over 100 people strong. The focus of the collaboration was to develop an experiment that would measure the weak charge of the proton, $Q_w^p$, to a very high precision. The purpose of this measurement was to act as a precision frontier test of the Standard Model(SM). This is possible due to the fact that $Q_w^p$ is very well predicted by the SM. By elastically scattering a forward angle polarized electron beam off unpolarized protons in a liquid hydrogen target, an asymmetry was determined. This asymmetry, $A_{ep}$, was combined with the world's parity-violating electron-scattering(PVES) data to extract $Q_w^p$. The theoretical structure of the SM, $Q_w^p$, and $A_{ep}$ are described in Chapter 2.

A detailed analysis of $Q_{weak}$'s extraction of the $Q_w^p$ is described in Chapter 5. There are three stages to obtaining a final value. The first step was to get the raw asymmetry as observed by the detectors (Section 5.1). The second step involves removing false asymmetries from the raw asymmetry to determine the measured asymmetry (Section 5.2). The final step had multiple corrections applied (Section 5.3). These corrections include correcting the polarization, removing background asymmetries from the measured asymmetry, and several multiplicative corrections. The result is the physics $A_{ep}$, which was then combined with the world's PVES data to extract $Q_w^p$ (Section 5.4) and other SM predictions.

The second measurement discussed in this dissertation was taken using the $Q_{weak}$ apparatus during April 2012, when there was a period of time that the beam provided by Jefferson Lab was incompatible with the measurement of $Q_w^p$. Part of this time was used to gather inelastic data at a beam energy of 877 MeV in order to obtain a measurement of the

N$\rightarrow \Delta$ transition. There was another measurement of this transition taken at the nominal $Q_{weak}$ kinematics, used to extract the inelastic background, that has been previously analyzed by John Leacock [4]. The 877 MeV data was taken with a large transverse component due to beam conditions at the time. This has resulted in the analysis of this data, detailed in Chapter 6, being split into the longitudinal analysis and transverse analysis.

The theoretical background for the longitudinal N$\rightarrow \Delta$ transition can be found in Section 2.4. The resulting asymmetry has an unusual component, the Siegert term, that is nonzero when $Q^2 = 0$. This component is parametrized by a low energy constant $d_\Delta$, which is connected to a puzzle in Weak Hyperon Decay that suggests values for $d_\Delta$ up to 100 times the natural scale of the value, $g_\pi$. By combining the two values of $d_\Delta$ determined with the $Q_{weak}$ apparatus with a previously measured value by the G0 collaboration [20], a limit on possible values for $d_\Delta$ can be obtained.

The transverse N$\rightarrow \Delta$ results in the measurement of a beam-normal single-spin asymmetry(BNSSA). The theoretical framework for this BNSSA can be found in Section 6.7. In the elastic interaction, the electromagnetic form-factors related to the BNSSA are well understood by theorists but in the inelastic N$\rightarrow \Delta$ transition there are two unknown electromagnetic form-factors. While the 877 MeV BNSSA will not be enough to extract either of these values, it is a start in building a data set. With more theoretical work on these form-factors and future measurements adding to the data set, these form-factors will hopefully be determined.

# Chapter 2

# Theory

## 2.1 The Standard Model

The Standard Model(SM) is currently the best predictor of electromagnetic, weak, and strong interactions. These interactions occur between elementary particles, quarks and leptons, and are mediated by the exchange of gauge bosons. Figure 2.1 presents these particles in an organized manner.

The SM correctly predicts three out of four of the fundamental forces of the universe. The weakest of the four forces, gravity, is not within the current scope of the SM. The strong force is carried by gluons which will only couple to quarks or other gluons. The weak force is carried by the $W^+$, $W^-$, and Z bosons which only couple with fermions. The electromagnetic force is carried by the photon. The electromagnetic and weak force are unified as a single

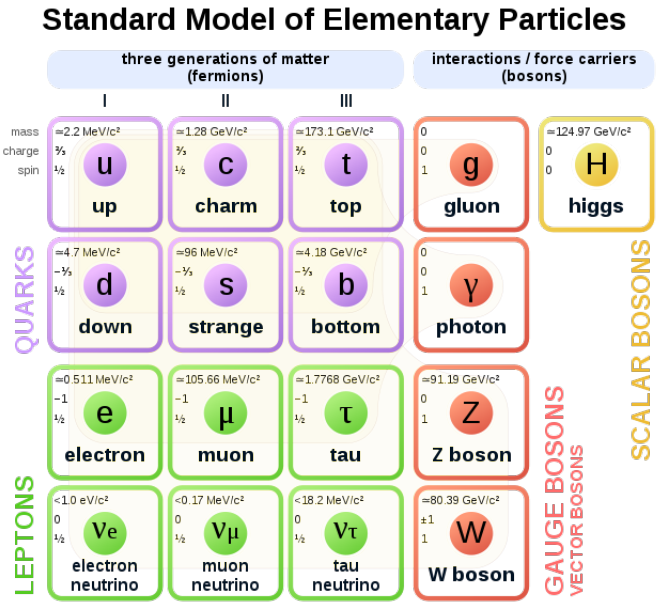


**Figure 2.1:** *The elementary particles of the Standard Model. Leptons and quarks have three generations and Gauge bosons are also shown. As of 2013, the Higgs boson has been observed by two experiments, ATLAS and CMS, at the LHC. Image from [1].*

electroweak force whose predictions form the basis of the $Q_{weak}$ Experiment.

## 2.2 Electroweak Force

The SM equations of motion can be determined by writing down a Lagrangian $\mathcal{L}$ with an action S. The formalism from field theory is

$$S \equiv \int \mathcal{L}\left(q : q_1, ..., q_n\right) d^n q. \tag{2.1}$$

By minimizing the action, $\delta S = 0$, we can extract the equations that define that system. When this formalism is applied to the Weak Interaction, the result is the Lagrangian for the

mass terms of the four gauge fields $W_\mu^\alpha$ and $B_\mu$ [22], as seen in

$$\mathcal{L}_{EW}^{MT} = -\frac{1}{8}g'^2v^2\left|W_\mu^1 - iW_\mu^2\right|^2 - \frac{1}{8}v^2\left(g'^2B_\mu - g^2W_\mu^3\right)^2. \tag{2.2}$$

This also requires the use of field coupling constants, $g$ and $g'$, and the vacuum expectation value $v$.

It is clear that $W_\mu^1$ and $W_\mu^2$ are mixed, as are $W_\mu^3$ and $B_\mu$, but the two sets of gauge fields are independent of each other. This allows $W_\mu^1$ and $W_\mu^2$ to be treated separately from $W_\mu^3$ and $B_\mu$.

The quadratic terms $\left(W_\mu^1 W_{1\mu}\text{and}W_\mu^2 W^{2\mu}\right)$ of Equation (2.2) can be written out as

$$\mathcal{L}_{W_\mu^1} = -\frac{1}{8}g'^2v^2W_\mu^1W_{1\mu} \quad \text{and} \quad \mathcal{L}_{W_\mu^2} = -\frac{1}{8}g'^2v^2W_\mu^2W^{2\mu}. \tag{2.3}$$

These mass terms can be related to the kinetic term of an arbitrary Lagrangian,

$$\mathcal{L}_{\text{kinetic term}} \equiv -\frac{1}{2}M^2K^\mu K_\mu, \tag{2.4}$$

where $M$ is the mass of the "particle."

By relating the mass terms of $W_\mu^1$ and $W_\mu^2$ to equation (2.4), the mass of the gauge fields can be determined as

$$-\frac{1}{2}M^2 = -\frac{1}{8}g'^2v^2 \quad \Rightarrow \quad M^2 = \frac{1}{4}g'^2v^2. \tag{2.5}$$

These masses can be written as eigenstates of, and therefore invariant under, the electromagnetic charge $Q$. The two eigenstates,

$$W_\mu^+ \equiv \frac{1}{\sqrt{2}}\left(W_\mu^1 - iW_\mu^2\right) \quad \text{and} \quad W_\mu^- \equiv \frac{1}{\sqrt{2}}\left(W_\mu^1 + iW_\mu^2\right), \tag{2.6}$$

are bosons [23] that have opposite charges. These two eigenstates, which are the $W$ bosons found in figure 2.1, have equal mass

$$M_{W_\mu^\pm} = \frac{1}{2}g'v. \tag{2.7}$$

This method can be repeated with the $W_\mu^3$ and $B_\mu$ gauge fields. To define these mass eigenstates, the weak mixing angle $\theta_W$ (also known as the Weinberg angle) needs to be defined from the field coupling constants $g$ and $g'$ via trigonometric functions

$$\sin\theta_W = \frac{g}{\sqrt{g^2+g'^2}} \quad \text{and} \quad \cos\theta_W = \frac{g'}{\sqrt{g^2+g'^2}}. \tag{2.8}$$

The weak mixing angle is then used to build the mass eigenstates

$$\begin{gathered} Z_\mu = -B_\mu \sin\theta_W + W_\mu^3 \cos\theta_W \\ \text{and} \\ A_\mu = B_\mu \cos\theta_W + W_\mu^3 \sin\theta_W. \end{gathered} \tag{2.9}$$

These eigenstates can be written as a matrix

$$\begin{pmatrix} A_\mu \\ \\ Z_\mu \end{pmatrix} = \begin{pmatrix} \cos\theta_W & \sin\theta_W \\ \\ -\sin\theta_W & \cos\theta_W \end{pmatrix} \begin{pmatrix} B_\mu \\ \\ W^3_\mu \end{pmatrix}. \tag{2.10}$$

where the weak mixing angle mediates the mixing between the two neutral currents. This matrix can then be transformed in such a way as to allow access to the mass terms of $W^3_\mu$ and $B_\mu$:

$$\begin{pmatrix} B_\mu \\ \\ W^3_\mu \end{pmatrix} = \begin{pmatrix} \cos\theta_W & -\sin\theta_W \\ \\ \sin\theta_W & \cos\theta_W \end{pmatrix} \begin{pmatrix} A_\mu \\ \\ Z_\mu \end{pmatrix}. \tag{2.11}$$

Applying the new definitions of $W^3_\mu$ and $B_\mu$ to the second term in equation (2.2), the Lagrangian for these gauge fields can be written in terms of $A_\mu$ and $Z_\mu$,

$$\mathcal{L}_{A_\mu, Z_\mu} = -\frac{1}{8} v^2 \left[ -Z_\mu \left( g' \cos\theta_W + g \sin\theta_W \right) + A_\mu \left( -g' \sin\theta_W + g \cos\theta_W \right) \right]^2. \tag{2.12}$$

This allows access to the mass terms

$$\begin{gathered} M_{Z_\mu} = \frac{1}{2} v \left( g' \cos\theta_W + g \sin\theta_W \right) \\ \text{and} \\ M_{A_\mu} = \frac{1}{2} v \left( -g' \sin\theta_W + g \cos\theta_W \right) \end{gathered} \tag{2.13}$$

for the $Z_\mu$ and $A_\mu$ gauge fields.

Using the definitions of $\cos\theta_W$ and $\sin\theta_W$ (Equation (2.8)), the mass terms can be simplified farther to

$$M_{Z_\mu} = \frac{1}{2} v \sqrt{g^2 + g'^2}$$
$$\text{and} \tag{2.14}$$
$$M_{A_\mu} = 0.$$

The $Z_\mu$ field represents a massive and chargeless particle, the $Z^0$ boson, which is a mediator of the weak force. The $A_\mu$ field on the other hand has zero mass and is also chargeless , and therefore clearly represents the photon $\gamma$, the mediator of the electromagnetic force. Now it is clear that the weak and electromagnetic forces are unified.

## 2.3 Parity-Violating Asymmetry

### 2.3.1 Parity and the Weak Force

To understand the Parity-Violating Asymmetry, we first need to understand what is meant by parity. The parity operator **P** flips the signs of the spatial coordinates of a given object

$$\mathbf{P}\,(x, y, z) = (-x, -y, -z)\,. \tag{2.15}$$

This can be visualized as taking a mirror-image of a given object. When an object remains unchanged under the parity operator, it is referred to as parity-conserving. An example of this would be a circle around the origin of a plane. When an object changes under a parity operation, it is referred to as parity-violating(PV). An example of this would be a hand print. When reversed by a mirror, the thumb of the handprint would change sides therefore violating parity. These examples are illustrated in Figure 2.2.

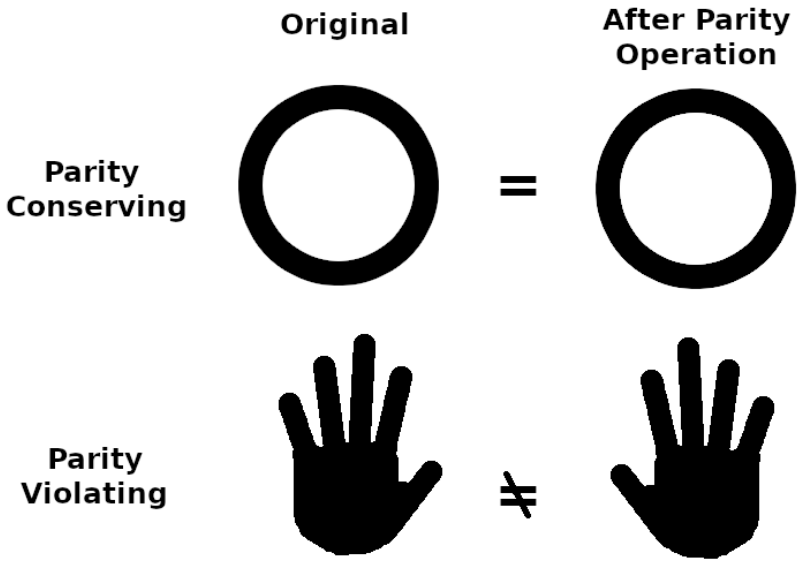


**Figure 2.2:** *Examples of parity-conserving(circle) and parity-violating(handprint) objects. The figures on the left show the original shape while the figures on the right show the shapes after the parity operation is applied. The circle is the same before and after(parity-conserving), but the handprint is not(parity-violating).*

Parity violation in the SM was first proposed in 1956 by Lee and Yang [24], and was quickly confirmed by Madame Wu in 1957 [25]. A strong magnetic field was used to polarize a $^{60}$Co nucleus and the angular distribution of the beta decay was observed. The magnetic field was then used to reverse the polarization of the $^{60}$Co and the observation was repeated.

If parity was conserved in beta decay, the two observations would have been the same. However the detected beta particles were different for the two polarizations, therefore beta decay violates parity. As beta decay is a result of the weak force, it is actually the weak force that violates parity.

### 2.3.2 Cross Sections and Form Factors

The tree level electron-proton interaction consists of two possible particle exchanges, either a photon ($\gamma$) or a massive boson ($Z^0$). Figure 2.3 displays these exchanges as Feynman diagrams. These represent the electromagnetic ($\gamma$) and weak ($Z^0$) interactions.

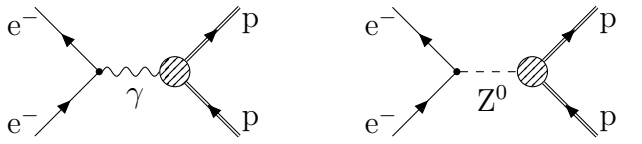


**(a)** *Electron scattering via photon*

**(b)** *Electron scattering via $Z^0$ boson*

**Figure 2.3:** *Feynmann diagrams representing the tree level electron-proton interactions. The electromagnetic interaction is mediated by a photon($\gamma$) and is shown in diagram a. The weak interaction is mediated by the Z boson($Z^0$) and is shown in diagram b. Figures from the dissertation of Wade Duvall [2], generated via TikZ from Juan-Carlos Cornejo.*

When the electron-proton interaction involves unpolarized electrons scattering from a nucleon, the cross section is given by

$$\frac{d\sigma}{d\Omega} = \left(\frac{d\sigma}{d\Omega}\right)_{\text{Mott}} \left|F\left(Q^2\right)\right|^2 \tag{2.16}$$

with the Mott cross section defined as

$$\left(\frac{d\sigma}{d\Omega}\right)_{\text{Mott}} = \frac{\alpha^2\hbar^2c^2\cos^2\theta/2}{4E^2\sin^2\theta/2} \tag{2.17}$$

and $F\left(Q^2\right)$ being the form factor containing the internal structure of the proton.

The $F\left(Q^2\right)$ for the tree level electromagnetic interactions is defined as

$$\begin{aligned} \left|F\left(Q^2\right)\right|^2 &= \frac{E'}{E}\left[\frac{G_E^2+\tau G_M^2}{1+\tau} + 2\tau G_M^2\tan^2\theta/2\right] \\ \text{where} \quad \tau &= \frac{Q^2}{4M_p^2} \quad \text{and} \quad \frac{E'}{E} = \frac{1}{1+\frac{2E}{M_p}\sin^2\frac{\theta}{2}} \ . \end{aligned} \tag{2.18}$$

These values are dependent on laboratory variables: the beam energy $E$, the electron scattering angle $\theta$, and the four momentum transfer of the interactions $Q^2$ which is defined as

$$-Q^2 \equiv q^\mu q_\mu = \left(E-E'\right)^2 - \left(\mathbf{p}-\mathbf{p'}\right)^2 \tag{2.19}$$

where in the relativistic limit $E \approx p$ and $E' \approx p'$.

Figure 2.3 has four vertices that are of interest. In this context, a vertex is where two particles meet and each vertex has an associated current that is dependent on the particles involved, both the interacting fermion and the carrier boson. The electron currents, $J^\mu_{e,\gamma}$

(electromagnetic) and $J^{\mu}_{e,Z}$(neutral weak), are defined as

$$\begin{gathered} J^{\mu}_{e,\gamma} = -e\bar{u}_e\gamma^{\mu}u_e \\ \text{and} \\ J^{\mu}_{e,Z} = \bar{u}_e\gamma^{\mu}\left(g^e_V - g^e_A\gamma^5\right)u_e \end{gathered} \tag{2.20}$$

where $\gamma^{\mu}$ and $\gamma^5$ are Dirac matrices and $g^e_V$ and $g^e_A$ are the vector and axial-vector couplings of the electron. Parity violation requires the vector-axial vector combination(V-A) found in the neutral weak current.

The proton currents, $J^{\mu}_{p,\gamma}$(electromagnetic) and $J^{\mu}_{p,Z}$ (weak), are more complicated than the electron currents due to the internal structure of the proton necessitating the use of structure functions $F_i$. They are defined as

$$\begin{gathered} \langle N|J^{\mu}_{p,\gamma}|N\rangle = \bar{\psi}_N\left[F^{\gamma}_1\left(Q^2\right)\gamma^{\mu} + F^{\gamma}_2\left(Q^2\right)\frac{i\sigma^{\mu\nu}q_{\nu}}{2M_N}\right]\psi_N \\ \text{and} \\ \langle N|J^{\mu}_{p,Z}|N\rangle = \bar{\psi}_N\left[F^{Z}_1\left(Q^2\right)\gamma^{\mu} + F^{Z}_2\left(Q^2\right)\frac{i\sigma^{\mu\nu}q_{\nu}}{2M_N} + G^{Z}_A\left(Q^2\right)\gamma^{\mu}\gamma^5\right]\psi_N. \end{gathered} \tag{2.21}$$

The Sach's form factors can be written as functions of the structure functions,

$$\begin{gathered} G_E\left(Q^2\right) = F_1\left(Q^2\right) - \tau F_2\left(Q^2\right) \\ \text{and} \\ G_M\left(Q^2\right) = F_1\left(Q^2\right) + F_2\left(Q^2\right). \end{gathered} \tag{2.22}$$

Unpolarized electron scattering has been used to study the electromagnetic form factors of the proton, $G_E^{p,\gamma}(Q^2)$ and $G_M^{p,\gamma}(Q^2)$. The electric form factor describes the distribution of the electric charge through the proton. In the forward angle limit, $G_E^{p,\gamma}(Q^2 \to 0)$ is equivalent to the proton's electric charge and $G_M^{p,\gamma}(Q^2 \to 0)$ is equivalent to the proton's magnetic moment, removing any sensitivity to the proton's internal structure. When the Z boson is exchanged, there are analogous neutral weak form factors $G_E^{p,Z}(Q^2)$ and $G_M^{p,Z}(Q^2)$. Via isospin symmetry and using the three lightest quarks, the proton's form factors can be written as

$$\begin{aligned} G_{E,M}^{p,\gamma} &= \frac{2}{3}G_{E,M}^{u} - \frac{1}{3}\left(G_{E,M}^{d} + G_{E,M}^{s}\right), \\ G_{E,M}^{p,Z} &= \frac{2}{3}\left(1 - \frac{8}{3}\sin^2\theta_W\right)G_{E,M}^{u} + \frac{1}{3}\left(-1 + \frac{4}{3}\sin^2\theta_W\right)\left(G_{E,M}^{d} + G_{E,M}^{w}\right), \end{aligned} \tag{2.23}$$

and

$$G_A^Z = -G_A^u + G_A^d + G_A^s.$$

Due to the extremely forward angle of the $Q_{weak}$ Experiment, the axial form factor is suppressed. Analogous to the electric charge, the $G_E^{p,Z}(Q^2 \to 0)$ limit is equivalent to the weak charge of the proton $Q_W^p$.

Various parity-violating electron-scattering experiments have provided measurements that support the contribution of the strange form factor, $G_{E,M}^s$, being small. They are all a part of the rich history of the strange quark content of the quark sea. [26]

### 2.3.3 Elastic PV Asymmetry and Weak Charge of the Proton

Using the tree level matrix elements, $\mathcal{M}_\gamma$(electromagnetic) and $\mathcal{M}_Z$ (neutral current weak), a total matrix element, $\mathcal{M}_{\text{tot}}$, can be used to determine the $\text{Q}_{\text{weak}}$ cross section,

$$\sigma_{R,L} = |\mathcal{M}_{tot}|^2 = |\mathcal{M}_\gamma + \mathcal{M}_Z|^2 = \mathcal{M}_\gamma^2 + \mathcal{M}_Z^2 + 2\text{Re}\left(\mathcal{M}_\gamma^* \mathcal{M}_Z\right). \tag{2.24}$$

This cross section will be different for the two helicity states of the incident electron, spin being parallel to the electron's momentum(right-handed(R) helicity) and spin being anti-parallel to the electron's momentum(left-handed(L) helicity).

The interference term, $2\text{Re}\left(\mathcal{M}_\gamma^* \mathcal{M}_Z\right)$, has the same sign as the helicity of the electron. Due to the two cross sections being different, an asymmetry can be built from the two helicities,

$$A = \frac{\sigma_R - \sigma_L}{\sigma_R + \sigma_L}. \tag{2.25}$$

At the $Q^2 \to 0$ limit the electromagnetic term is much larger than the neutral weak current term. That allows Equation (2.25) to simplify to

$$A \sim \frac{2\mathcal{M}_\gamma \mathcal{M}_Z}{\mathcal{M}_\gamma^2} \sim \frac{2\mathcal{M}_Z}{\mathcal{M}_\gamma}. \tag{2.26}$$

The scale of this asymmetry can be determined by relating the matrix elements to the mass of the Z boson [27], $M_Z = (91.1876 \pm 0.0021)\,\frac{GeV}{c^2}$, and the four momentum transfer

for $Q_{weak}$, $Q^2 \sim 0.025 \frac{GeV}{c^2}$. This leads to the order of magnitude estimation

$$\frac{\mathcal{M}_Z}{\mathcal{M}_\gamma} \sim \frac{Q^2}{(M_Z)^2} \sim 10^{-6}. \tag{2.27}$$

For simplicity's sake, the asymmetries will be quoted in either parts per million (ppm $\equiv 10^{-6}$) or parts per billion (ppb $\equiv 10^{-9}$).

The asymmetry can now be written using the form factors from Equation (2.23) as

$$A = -\frac{G_F Q^2}{4\pi\alpha\sqrt{2}} \left[ \frac{\epsilon G_E^\gamma G_E^Z + \tau G_M^\gamma G_M^Z - \left(1 - 4\sin^2\theta_W\right) \epsilon' G_M^\gamma G_A^e}{\epsilon \left(G_E^\gamma\right)^2 + \tau \left(G_M^\gamma\right)^2} \right]$$

where

$$\tau = \frac{Q^2}{4M_p^2}, \quad \epsilon = \left[1 + 2\left(1+\tau\right)\tan^2\frac{\theta}{2}\right]^{-1}, \text{ and } \epsilon' = \sqrt{\tau\left(1+\tau\right)\left(1-\epsilon^2\right)} \tag{2.28}$$

Due to the forward angle nature of the $Q_{weak}$ experiment, the $Q^2 \to 0$ limit can be applied to Equation (2.28), which causes $\tau \sim 0$ and $\epsilon \sim 1$. This results in a simpler equation for the asymmetry,

$$A = -\frac{G_F Q^2}{4\pi\alpha\sqrt{2}} \left(Q_W^p + Q^2 B\left(Q^2\right)\right). \tag{2.29}$$

The weak charge of the proton($Q_W^p$), in analogy to the electromagnetic charge of the proton, is clearly defined in Equation (2.29) and isolated from the form factors which are contained within $B\left(Q^2\right)$. The weak charge of the proton can be further isolated by reducing the asymmetry to

$$\frac{A}{A_0} = Q_W^p + Q^2 B\left(Q^2\right) \quad \text{with} \quad A_0 = -\frac{G_F Q^2}{4\pi\alpha\sqrt{2}}. \tag{2.30}$$

This reduced version of the asymmetry has the weak charge of the proton as the intercept of the axis when the world's parity violating electron scattering(PVES) data is plotted. The high statistics and forward angle nature of $Q_{weak}$ causes it to strongly affect the fit of the PVES data at the intercept. As the weak charge of the proton is predicted by the Standard Model, measuring it acts as a test for new physics. Some TeV scale new physics that $Q_{weak}$ would be sensitive to are leptoquarks, super-symmetry, and generic Z'. $Q_{weak}$ would also be sensitive to very weakly coupled MeV-GeV mediators such as dark photons [28].

### 2.3.4 Other Expected Physical Quantites measured by $Q_{weak}$

The weak charge of the neutron($Q_w^n$) is related to the weak charge of the proton($Q_w^p$) via the neutral weak quark coupling constants($C_{1u}$ and $C_{1d}$). The neutral weak coupling constants are combined to get the weak charges of the proton and neutron as

$$\begin{gathered} Q_w^p = -2\left(2C_{1u} + C_{1d}\right) \\ \text{and} \\ Q_w^n = -2\left(C_{1u} + 2C_{1u}\right). \end{gathered} \tag{2.31}$$

$Q_{weak}$ will extract a value for the weak charge of the proton, establishing limits on $C_{1u}$ and $C_{1d}$. By combining the data from $Q_{weak}$ and other parity-violating electron scattering(PVES) experiments with the constraints determined from atomic parity violating(APV) experiments, which are nearly orthogonal to the PVES limits, values for $C_{1u}$ and $C_{1d}$ can be

determined. From these values, the weak charge of the neutron can be extracted.

The weak charge of the proton also grants access to the weak mixing angle($\sin^2\theta$) via

$$Q_W^p = (\rho + \Delta_e)\left(1 - 4\sin^2\theta_W + \Delta_e'\right) + \Box_{WW} + \Box_{ZZ} + \Box_{\gamma Z}(0). \tag{2.32}$$

This relation depends on the WW and ZZ radiative corrections($\Box_{WW}$ and $\Box_{ZZ}$), the low-energy renormalization($\rho$) of the weak neutral-current($Z^0$) to charged current($W^\pm$) interactions, the electron vertex correction($\Delta_e$), the electron anapole moment($\Delta_e'$), and the energy-independent part of the electroweak radiative correction ($\Box_{\gamma Z}$) [17].

The weak mixing angle's dependence on the masses($M_W$ and $M_Z$) of the W and Z bosons is a key prediction of the Standard Model [29] [30]. The predicted dependence is

$$\sin^2\theta_W = 1 - \left(\frac{M_W}{M_Z}\right)^2 \approx \frac{1}{4}. \tag{2.33}$$

The Standard Model suppression of $Q_W^p$ comes from combining the leading order version of Equation (2.32),

$$Q_W^p \approx 1 - 4\sin^2\theta_W, \tag{2.34}$$

and Equation (2.33).

The final value of interest that will be improved with the $Q_{weak}$ measurement is the mass reach. Mass reach refers to the limit on the mass scale of any "new physics" represented by $\Lambda$ with coupling $g$. This is a standard method of introducing a "new physics term" ($g^2/\Lambda^2$)

to the Standard Model Lagrangian [31]. The Standard Model Lagrangian is

$$\mathcal{L}^{\mathrm{PV}}_{\mathrm{SM}} = -\frac{G_F^2}{\sqrt{2}}\bar{e}\gamma_\mu\gamma_5 e\sum_q C_1\bar{q}\gamma^\mu q. \tag{2.35}$$

Adding the "new physics term" to this Lagrangian leads to the Beyond Standard Model(BSM) Lagrangian,

$$\mathcal{L}^{\mathrm{PV}}_{\mathrm{BSM}} = -\frac{g^2}{\Lambda^2}\bar{e}\gamma_\mu\gamma_5 e\sum_q h_v^q\bar{q}\gamma^\mu q. \tag{2.36}$$

Both of the Lagrangians depicted in Equations (2.35) and (2.36) are summed over the up and down quarks($q$), and the BSM Lagrangian includes projections $h_v^u$ and $h_v^d$ which depend on the quark-flavour mixing angle($\theta_h$). These projections are defined as

$$h_v^u = \cos\theta_h \quad \text{and} \quad h_v^d = \sin\theta_h. \tag{2.37}$$

Combining the $\mathrm{Q_{weak}}$ data with other PVES experiments will result in a phase-space($\Lambda/g$ vs. $\theta_h$) curve of the mass reach. The APV data will provide another curve in the same space, and the combination of the two curves will provide the final mass reach values.

## 2.4 N$\rightarrow\Delta$ Transition

An important ancillary result of the $\mathrm{Q_{weak}}$ Experiment was the opportunity to measure inelastic parity-violating asymmetry in the N$\rightarrow\Delta$ transition. The original impetus to measure

the inelastic parity-violating asymmetry was due to the fact that there were inelastic events present in the beam in nominal running mode. The expected rate of these events is very low in comparison to the elastic events, however the elastic asymmetry is only a tenth as large as the expected inelastic asymmetry. Therefore, the contribution of inelastic events to the beam signal, also referred to as the inelastic dilution factor, needs to be determined as well as measuring the inelastic asymmetry. These values are required to determine the inelastic correction to the elastic asymmetry.

Due to a week of beam time that was ineligible to contribute to the main measurement, the elastic parity-violating asymmetry, there was an opportunity to obtain a second measurement of the inelastic parity-violating asymmetry at a different set of kinematics. This data set, taken at a lower beam energy, will be discussed in greater detail in chapter 6.

### 2.4.1 The $\Delta$ Resonance

When an electron scatters off a nucleon inelastically, the lost energy can be transferred to the internal structure of the nucleon. The resulting particle is a resonance of the nucleon. The resonances of the proton are represented by the peaks in Figure 2.4 seen after the sharply defined elastic spike. The first resonance of a nucleon, located $\sim$1.2 GeV, is the $\Delta$ and has a width of 118 MeV. Using the delta lifetime

$$\Gamma = \frac{\hbar}{\tau}, \tag{2.38}$$

**Table 2.1:** *Associated properties of nucleons and* $\Delta$ *resonances.*

| Particle | Charge | Quarks | Spin | Isospin | $I_3$ |
|---|---|---|---|---|---|
| proton | +1 | uud | $\uparrow\uparrow\downarrow$ | $\frac{1}{2}$ | $+\frac{1}{2}$ |
| neutron | 0 | udd | $\uparrow\downarrow\downarrow$ | $\frac{1}{2}$ | $-\frac{1}{2}$ |
| $\Delta^{++}$ | +2 | uuu | $\uparrow\uparrow\uparrow$ | $\frac{3}{2}$ | $+\frac{3}{2}$ |
| $\Delta^{+}$ | +1 | uud | $\uparrow\uparrow\uparrow$ | $\frac{3}{2}$ | $+\frac{1}{2}$ |
| $\Delta^{0}$ | 0 | udd | $\uparrow\uparrow\uparrow$ | $\frac{3}{2}$ | $-\frac{1}{2}$ |
| $\Delta^{-}$ | -1 | ddd | $\uparrow\uparrow\uparrow$ | $\frac{3}{2}$ | $-\frac{3}{2}$ |

the width of the resonance ($\Gamma$) can be related to the mean lifetime ($\tau$). Therefore the average lifetime of the $\Delta$ is $5.58 \times 10^{-24}$ seconds with the dominant decay mode being a strong interaction resulting in a nucleon and pion.

The possible states of the $\Delta$ resonance are shown in Table 2.1 with the nucleons. Nucleons, the proton and the neutron, are composed of either two up and one down quarks (proton) or one up and two down quarks (neutron). In a simple quark model picture, both have two quark spins that are aligned and one that is antiparallel to the other two, which leads to a total spin $J = \frac{1}{2}$. The $\Delta$ resonances have a mass of 1232 MeV and are composed of any combination of three up and down quarks with parallel spins. This leads to a total spin of $J = \frac{3}{2}$.

The simplest interaction that creates a $\Delta$ consists of either a $\gamma$ or a $Z$ boson interacting with a nucleon and flipping the antiparallel quark spin to match the other two. Depending on the original nucleon, this results in either a $\Delta^{+}$(proton) or a $\Delta^{0}$(neutron). The other two versions of $\Delta$, $\Delta^{++}$ and $\Delta^{-}$, require both a spin flip and a quark flavor change(u $\rightarrow$ d or d

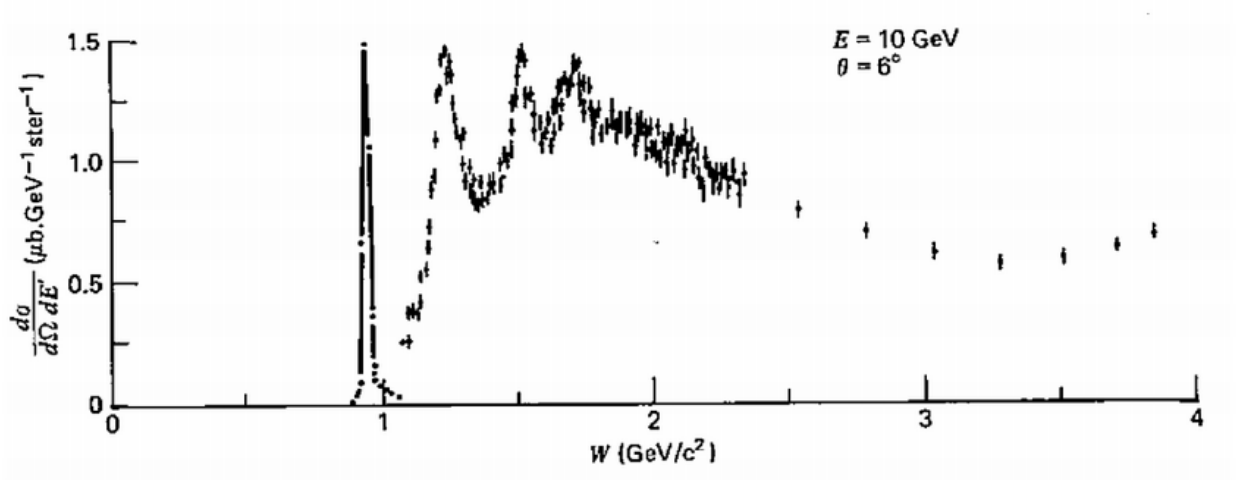


**Figure 2.4:** *Elastic peak and $\Delta$ resonances of the proton as function of invariant mass. Image is from Halzen and Martin's Quarks and Leptons [3].*

$\rightarrow$ u). This can be caused by interacting with a charged current weakly interacting particle. As $Q_{weak}$ uses electron-proton scattering, the $\Delta^+$ is the only resonance that will be discussed further. This interaction also gives access to information on the distribution of quark spin, which is contained in the axial transtion form factor $G^A_{N\rightarrow\Delta}$.

### 2.4.2 Inelastic Parity-Violating Asymmetry

The dominant interaction of the inelastic contribution is the N$\rightarrow$ $\Delta$ transition, illustrated in Figure 2.5. As discussed in the previous section, this involves the $Z$ boson triggering a spin flip in the proton's single antiparallel spin and resulting in a $\Delta^+$ with three parallel quark spins. The $\vec{e} + p \rightarrow e + \Delta^+$ interaction has a change in isospin of one,

$$\Delta I = I_{\Delta^+} - I_p = \frac{3}{2} - \frac{1}{2} = 1. \tag{2.39}$$

This results in an isovector only transition.

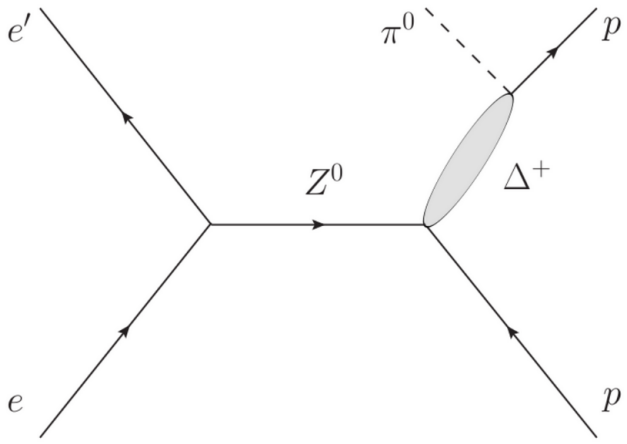


**Figure 2.5:** *Fenynam diagram of N→ Δ transition and subsequent decay. The incident electron(e) exchanges a $Z^0$ with the proton(p). The electron loses energy during the exchange(e') exciting the proton to a $\Delta^+$, which then decays into a pion($\pi^0$) and proton(p). Image from the dissertation of John Leacock [4].*

This transition has the neutral weak current of

$$J_\mu^Z = \frac{e}{2\sin\theta_W \cos\theta_W}\left[\left(1-2\sin^2\theta_W\right)V_\mu^3 + A_\mu^3\right], \tag{2.40}$$

composed of the vector($V_\mu$) and axial-vector($A_\mu$) currents. The form factors for the neutral weak current have not been well studied, but the conserved vector current hypothesis (CVC) suggests that the well known electromagnetic vector current form factos can be used to obtain the neutral current form factors. Measurements of charged weak interactions($W$ boson exchange) provide values for the axial-vector charged current form factors which can then be used to obtain the axial-vector neutral current form factors.

There are many different contributions to the inelastic asymmetry, but they can grouped

into three categories to simplfy the model [32],

$$A_{\text{inel}} = -\frac{G_F Q^2}{4\pi\alpha\sqrt{2}} \left[\Delta^{\pi}_{(1)} + \Delta^{\pi}_{(2)} + \Delta^{\pi}_{(3)}\right]. \tag{2.41}$$

The resonant terms are grouped into $\Delta^{\pi}_{(1)}$. The resonant terms are isovector, have no dependence on the hadronic structure, and are determined by Standard Model coupling

$$\Delta^{\pi}_{(1)} = 2\left(1 - \sin^2\theta_W\right). \tag{2.42}$$

The nonresonant terms are grouped into $\Delta^{\pi}_{(2)}$ which only has a very small contribution to the asymmetry at $\text{Q}_{\text{weak}}$ kinematics. The final term, $\Delta^{\pi}_{(3)}$, contains all axial-vector reactions involving the hadron vertex, including both resonant and nonresonant contributions. Hammer and Drechsel [33] found that the asymmetry contribution of the inteference between the resonant and nonresonant terms of $\Delta^{\pi}_{(3)}$ was of similar magnitude and opposite sign to the contribution of the nonresonant terms, making the resonant terms of $\Delta^{\pi}_{(3)}$,

$$\Delta^{\pi}_{(3)} \approx 2\left(1 - 4\sin^2\theta_W\right) F\left(Q^2\right), \tag{2.43}$$

to be the dominant asymmetry.

The electromagnetic $(H^{\gamma}(Q^2))$ and axial $\left(G^{A}_{N\to\Delta}(Q^2)\right)$ form factors are contained in $F(Q^2)$ as

$$F\left(Q^2\right) = \frac{E + E'}{M} H^{\gamma}\left(Q^2\right) G^{A}_{N\to\Delta}\left(Q^2\right). \tag{2.44}$$

Carrisa Capuano's thesis [34] has derivations of these form factors. The final version of the axial transition form factor is

$$G^A_{N\to\Delta} = g_3 C^A_3 + g_4 C^A_4 + g_5 C^A_5. \tag{2.45}$$

The $g_i$ [35] used in this form factor are defined as

$$\begin{aligned} g_3 &= \frac{M}{2M'}\left[(M+M')(M-M') - 2(M-M')^2 - Q^2\right], \\ g_4 &= \frac{1}{2}\left[(M+M')(M-M') + Q^2\right], \\ &\quad \text{and} \\ g_5 &= -M^2. \end{aligned} \tag{2.46}$$

Equation (2.44) now consists of known electromagnetic form factors being multiplied by $C^A_i$ form factors. One method of expressing these $C^A_i$ involves using dipole form factors $G^A_D$,

$$G^A_D\left(Q^2\right) = \left[1 + \frac{Q^2}{M_A^2}\right]^{-2}, \tag{2.47}$$

where $M_A$ is the axial dipole mass with a current world value of $1.03 \pm 0.02$ GeV [36], and Adler form factors $\xi^A$,

$$\xi^A\left(Q^2\right) = 1 + \frac{a'Q^2}{b' + Q^2}, \tag{2.48}$$

where $a' = -1.2$ and $b' = 2\,(GeV/c)^2$ for $Q^2 < 0.5$ GeV. The $a'$ and $b'$ values are fit parameters determined by Schreiner and von Hippel [37]. The axial term is given more $Q^2$ dependence

via Equation (2.48). This notation is called the Adler parameterization [38, 39],

$$C_i^A\left(Q^2\right) = C_i^A\left(0\right) G_D^A\left(Q^2\right) \xi^A\left(Q^2\right)$$
$$\text{which results in} \tag{2.49}$$
$$C_3^A\left(0\right) = 0, \quad C_4^A\left(0\right) = -0.35, \quad \text{and} \quad C_5^A\left(0\right) = 1.20.$$

To this point, the discussed asymmetry has been limited to tree level interactions. Zhu et al discovered that introducing radiative corrections to the asymmetry had an interesting result, $A\left(Q^2 = 0\right) \neq 0$ [40, 5]. This nonzero asymmetry is linked to the mass difference between the initial and final states of the nucleon. In the elastic interaction, the nucleon does not change mass therefore this effect is not present. Zhu et al determined a final expression for $\Delta_{(3)}^{\pi}$,

$$\Delta_{(3)}^{\pi}\left(\text{total}\right) = \Delta_{(3)}^{\pi}\left(\text{SM}\right) + \Delta_{(3)}^{\pi}\left(\text{Siegert}\right) + \Delta_{(3)}^{\pi}\left(\text{anapole}\right) + \Delta_{(3)}^{\pi}\left(\text{d-wave}\right). \tag{2.50}$$

The Standard Model term $\Delta_{(3)}^{\pi}\left(\text{SM}\right)$ is equivalent to Equation (2.43) which has already been discussed. The $\Delta_{(3)}^{\pi}\left(\text{d-wave}\right)$ term is due to a PV d-wave $\pi N\Delta$ contribution. The remaining two terms, $\Delta_{(3)}^{\pi}\left(\text{anapole}\right)$ and $\Delta_{(3)}^{\pi}\left(\text{Siegert}\right)$, are both due to the PV $\gamma N\Delta$ coupling. The Siegert term gets its name due to being derived from Siegert's theorem on electric multipole transitions [41, 42]. The Siegert term carries the non-zero asymmetry

$$A\left(Q^2 = 0\right) \approx -\frac{2d_{\Delta}}{C_3^{\gamma}}\frac{M}{\Lambda_{\chi}} + ..., \tag{2.51}$$

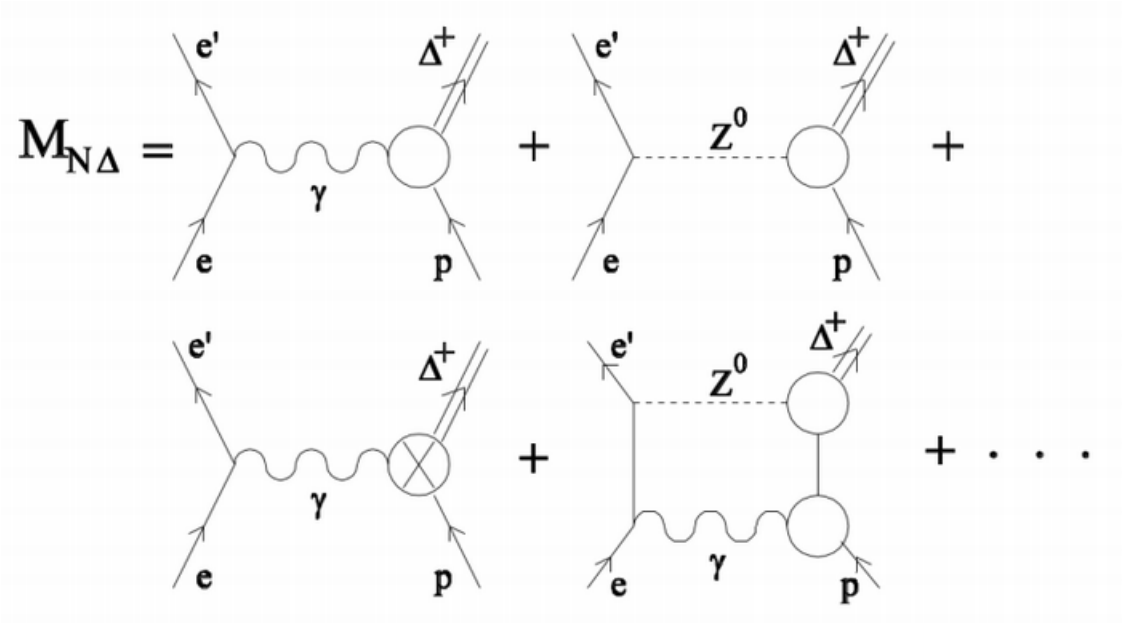


**Figure 2.6:** *Feynman diagram of dominant $\Delta$ producing interactions. Image from the dissertation of John Leacock [4].*

hence why it is separated from the anapole term. Figure 2.6 shows the $\Delta$ producing interactions. The tree-level (EM and neutral weak) interactions are represented by the top two diagrams, while the third diagram represents the $\gamma N\Delta$ coupling (anapole and Siegert terms). The final diagram represents the $\gamma Z$ box contribution.

Due to the forward angle nature of the $Q_{weak}$ Experiment, the Siegert term is a major component of the PV inelastic asymmetry. $C_3^\gamma$ is another of the Adler form factors(Equation (2.49)) with a value of 1.85 [35]. $\Lambda_\chi \sim 1$ GeV represents the mass scale of chiral symmetry breaking. Higher order effects and $\frac{1}{M}$ terms are indicated by the ellipse. Figure 2.7 indicates the PV vertex in the Feynman diagram of the Siegert term. The $d_\Delta$ is a low energy constant associated with hadron decay which parametrizes the Siegert term. While the natural scale of $d_\Delta$ is $g_\pi = 3\times10^{-8}$, the hadronic coupling constant for PV charged current interactions, there

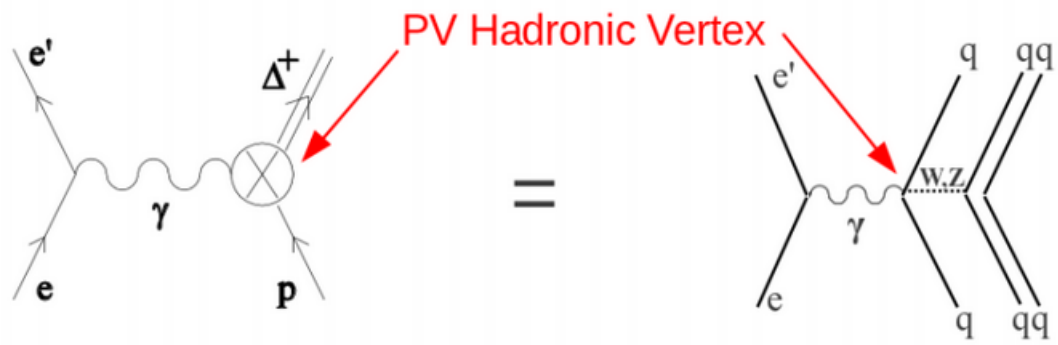


**Figure 2.7:** *The Siegert interaction term with the parity-violating vertex indicated by the red arrows. The Feynman diagram on the left shows the bosons(initial proton, final Δ), while the diagram on the right shows the boson broken down into quarks, where the γ is coupled to a quark-quark weak interaction. Image from the dissertation of John Leacock [4].*

is a puzzle in Weak Hyperon Decay that suggests values of $d_\Delta$ up 100 $g_\pi$ [43]. Experimental values of the asymmetry parameter in the decay of $\Sigma^+$ to a proton were significantly larger and the opposite sign of the theoretical values, but a dynamical solution that couples heavy $\frac{1}{2}^-$ resonances to the hyperon and daughter nucleon brings the theoretical solution into better agreement with the experimental value [43].

Equation (2.50), $\Delta^\pi_{(3)}\,(\text{total})$, can be written such that the radiative corrections are grouped together as

$$\Delta^\pi_{(3)}\,(\text{total}) = 2\left(1 - 4\sin^2\theta_W\right)\left(1 + R_A^\Delta\right)F\left(Q^2\right). \tag{2.52}$$

The contributions of the anapole, Siegert, and d-wave terms have been combined with the one-quark electroweak interaction, the sum of which is represented by $R_A^\Delta$. For tree-level terms, $R_A^\Delta = 0$ and Equation (2.52) reduces to Equation (2.43).

Figure 2.8 shows the three components of the $A_{\text{inel}}$ at low $Q^2$. There are multiple possible

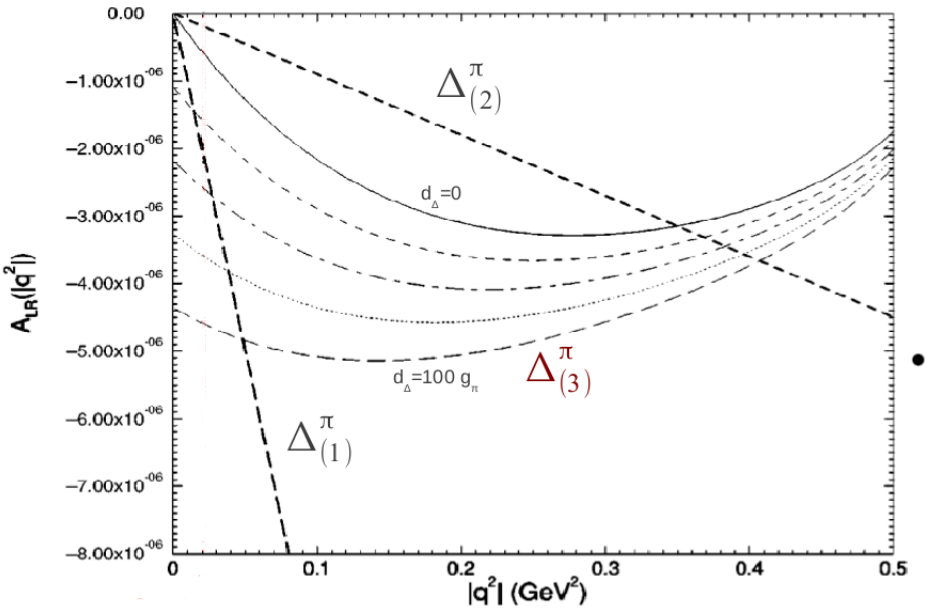


**Figure 2.8:** *The $\Delta^{\pi}_{(1)}$, $\Delta^{\pi}_{(2)}$, $\Delta^{\pi}_{(3)}$ components of $A_{inel}$ plotted for $Q^2$. $\Delta^{\pi}_{(3)}$ is shown for varying values of $d_\Delta$ starting at 0 and increasing to 100 $g_\pi$ via increments of 25 $g_\pi$. Image from the dissertation of John Leacock [4] in which it was adapted from Zhu et al [5].*

values shown for $\Delta^{\pi}_{(3)}$, depending on the chosen value of $d_\Delta$. The main $Q_{weak}$ kinematics will be made at roughly $Q^2 \sim 0.02$ GeV$^2$ and the extra lower energy measurement will be made at roughly $Q^2 \sim 0.01$ GeV$^2$. These measurements are at low enough $Q^2$ with high enough precision that they should be able to place a limit on the possible range of $d_\Delta$.

## 2.5 Beam-Normal Single-Spin Asymmetry for N$\rightarrow \Delta$

For the elastic longitudinal electron-proton parity-violating asymmetry at 1165 MeV(the main measurement of $Q_{weak}$), the beam normal single spin asymmetry(BNSSA) was a false background asymmetry. Dedicated measurements were taken to quantify the effect of the parity-conserving asymmetry. The elastic BNSSA for 1165 MeV has been well documented

in the thesis of D. Buddhini P. Waidyawansa [44].

The electron beam during the 877 MeV $N \rightarrow \Delta$ measurement had a large transverse component($\sim 43\%$). This provides a measurement of the $B_n$ in the $\vec{e}+p \rightarrow e+\Delta$ transition.

### 2.5.1 Beam-normal Single-spin Asymmetry

When a transversely polarized beam of electrons has a scattering plane off an unpolarized target that is normal to the polarization, a beam-normal single-spin asymmetry($B_n$), defined as

$$B_n = \frac{\sigma_\uparrow - \sigma_\downarrow}{\sigma_\uparrow + \sigma_\downarrow} = \frac{2\mathrm{Im}\left(T_{2\gamma} \cdot T_{1\gamma}^*\right)}{|T_{1\gamma}|^2}, \tag{2.53}$$

is observed. $\sigma_\uparrow$ and $\sigma_\downarrow$ represent the cross sections for electrons that are either parallel or anti-parallel to the scattering plane normal. The scattering plane normal is defined as

$$\vec{\xi} = \frac{\vec{k} \times \vec{k'}}{|\vec{k} \times \vec{k'}|}, \tag{2.54}$$

with $\vec{k}$ the incoming momentum of the electron and $\vec{k'}$ the outgoing momentum of the electron [21].

This asymmetry does not contribute to the Born term(the single-photon exchange approximation) due to time-reversal invariance forcing the time-reversal odd $B_n$ to disappear. As shown in Equation 2.53, the leading order term for $B_n$ comes from interference between the single-photon exchange and the two-photon exchange. In Equation 2.53, the two-photon

exchange amplitude is represented by $T_{2\gamma}$ and the single-photon exchange amplitude is represented by $T_{1\gamma}$. [6]

### 2.5.2 $\vec{e} + p \rightarrow e + \Delta$ via two-photon exchange

Single-photon exchanges do not carry a nonzero $B_n$. When limited to looking at an initial and final electron, that requires the exchange of more than one photon. [21]

The lowest order processes that can produce $B_n$ in the electro-production of $\Delta$ are shown in Figure 2.9. These are the same processes that contribute to the 877 MeV data-taking. The $\Delta$ electro-production is caused by a proton being excited into a $\Delta$ via energy transfer with a lepton, as shown in the Feynman diagrams of Figure 2.9. In the context of $Q_{weak}$, the lepton would be an electron.

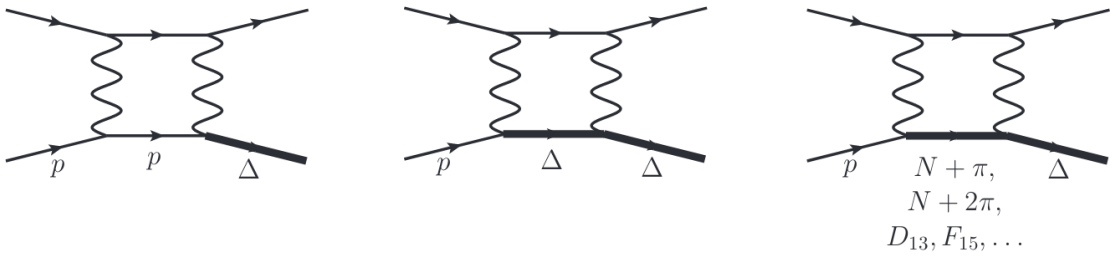


**(a)** *Hadronic part of loop is a proton*

**(b)** *Hadronic part of loop is a* $\Delta$

**(c)** *Hadronic part of loop is an excited state other than* $\Delta$

**Figure 2.9:** *The Feynman diagrams shown above represent the lowest order process for which* $B_n$ *may not equal zero. The two-photon exchanges shown above represent* $\Delta$ *electro-production. The diagrams were taken from Mark Dalton's proceedings for the 2015 Intersections conference [6].*

The three diagrams show different options for the hadronic part of the loop. The amplitudes for each diagram require the form-factors for the respective vertices. The first di-

agram(Figure 2.9a) has the proton contributing to the loop, and depends on the $\gamma^* pp$ and $\gamma^* p\Delta$ form-factors. The second diagram(Figure 2.9b) shows the $\Delta$ contributing to the loop, and depends on the $\gamma^* p\Delta$ and $\gamma^* \Delta\Delta$ form-factors. The third diagram(Figure 2.9c) represents any higher-order excited state of the proton contributing to the loop and depends on $\gamma^* pX$ and $\gamma^* X\Delta$, form-factors associated with a higher-order excited state X. The total $B_n$ value for the two-photon electro-production of the $\Delta$ requires calculations for all of the form-factors mentioned. [6]

The majority of the form-factors have already been measured. These include the proton elastic form-factor($\gamma^* pp$) and the transition form factors($\gamma^* p\Delta$ and $\gamma^* pX$). Two of the electromagnetic form-factors are less established. Measuring the N$\rightarrow \Delta$ transition may provide access to the $\Delta$ elastic form-factor($\gamma^* \Delta\Delta$). The final form-factor($\gamma^* X\Delta$) is currently an unknown and while theorists are starting to look into it, it currently blocks the extraction of the $\Delta$ elastic form-factor from the N$\rightarrow \Delta$ transition measurement of $B_n$. [6]

The prospect of measuring the electromagnetic form factors of the $\Delta$ is one of the main motivations for making measurements of the transverse asymmetry in the N$\rightarrow \Delta$ transition, since it is one of the few observables that makes this possible [21]. While the 877 MeV measurement of the $\Delta$ electro-production $B_n$ is not enough to extract information on electromagnetic form factors of the $\Delta$ by itself, combining it with $Q_{weak}$'s 1165 MeV measurement of the same starts building a data set. With the addition of future measurements and more theoretical work, the electromagnetic form factors of the $\Delta$ may be revealed.

# Chapter 3

# $Q_{weak}$ Apparatus

## 3.1 $Q_{weak}$ Goals and Specifications

The goal of $Q_{weak}$ was to precisely measure the asymmetry between two helicity states of elastically scattered electrons off a proton target at an extreme forward angle. The Standard Model predicts this value to be -230 parts per billion ($-2.3 \times 10^{-7}$). To reach the required precision on this measurement, $Q_{weak}$ could not track individual electrons all the time. Instead it integrated the light generated in the main detectors while the electron beam ran at 180 $\mu$A. This was referred to as current, or integration, mode. To reach the necessary precision, $Q_{weak}$ required 125 days of integration mode running. The parameters for integration mode running can be found in Table 3.1.

While integration mode was the primary data-taking mode, it was still necessary to peri-

**Table 3.1:** *Integration mode parameters.*

| Parameter | Value |
|---|---|
| Incident beam energy | 1.16 GeV |
| Beam current | 180 $\mu$A |
| Beam polarization | 89% |
| $LH_2$ target power | 2.5 kW |
| Central scattering angle | $9 \pm 2^{\circ}$ |
| Phi acceptance | 50 % of $2\pi$ |
| Average $Q^2$ | 0.025 GeV$^2$ |
| Acceptance averaged asymmetry | -230 ppb |
| Integrated rate per detector | 730 MHz |
| Total integrated rate | 5.8 GHz |

odically track individual electrons through the apparatus. This allowed access to kinematic information that could be used to benchmark simulation. This mode was referred to as tracking mode and required currents of $\leq$ 50 nA.

## 3.2 Beamline

The $Q_{\text{weak}}$ Experiment ran at the Thomas Jefferson National Accelerator Facility, commonly referred to as Jefferson Lab, in Newport News, Virginia. It was housed in Hall C, one of the three operational experimental halls at the time. A fourth hall(D) was added on in 2014, two years after $Q_{\text{weak}}$ finished running. The experimental halls receive a polarized electron beam produced by the Continuous Electron Beam Accelerator Facility(CEBAF)

which consists of a pair of linear accelerators(linacs) and steering magnets to allow the beam to be sent through the linacs multiple times, bring the maximum beam energy up to 6 GeV at the time $Q_{weak}$ was running. It has since been upgraded bringing the maximum energy up to 12 GeV. There is also a separator magnet which allows CEBAF to provide simultaneous beam to the three original experimental halls [45], as shown in Figure 3.1.

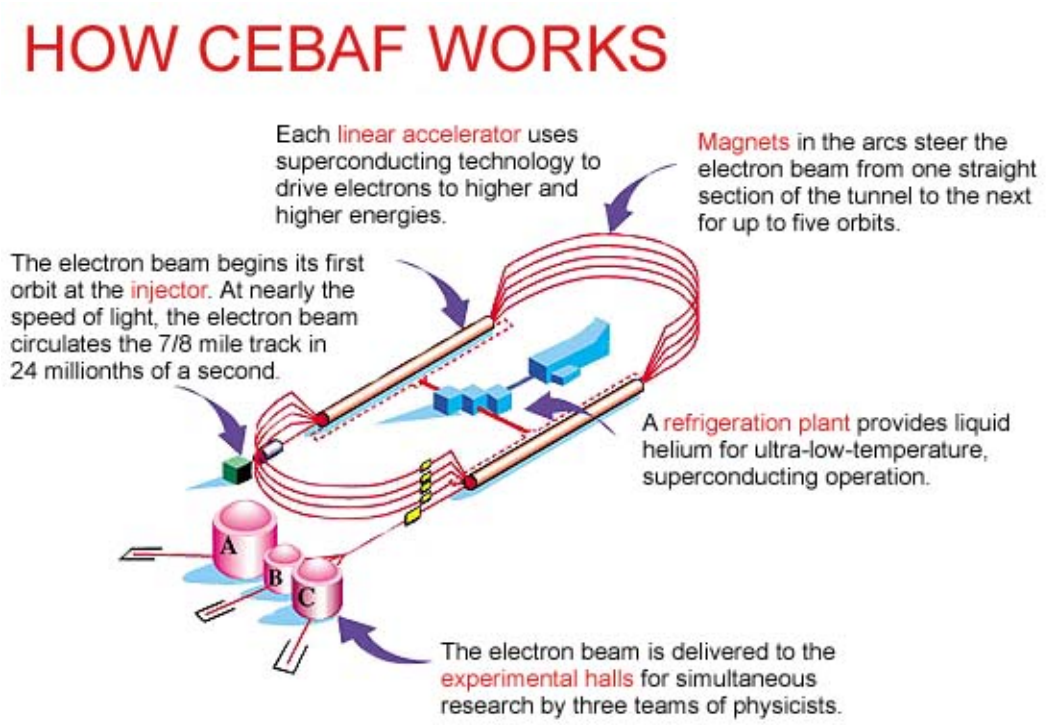


**Figure 3.1:** *Walk through of Jefferson Lab's CEBAF at the time of $Q_{weak}$ data-taking. Image provided by Jefferson Lab [7].*

Jefferson Lab shut down for the 12 GeV upgrade immediately after the end of $Q_{weak}$.

### 3.2.1 Source

CEBAF produced an electron beam by utilizing the photoelectric effect via circularly polarized light incident on a strained gallium arsenide (GaAs) photocathode source. [46] There was a laser assigned to each of the three original Halls(A,B,C) that provides the light. Hall D now shares Hall B's laser. These lasers emit 1560 nm light, pulsing at 499 Hz, $\frac{1}{3}$ of the operating frequency [47]. The lasers were 120° out of phase in order to allow the beam to be sent to all three adjacent Halls simultaneously. Jefferson Lab could produce high polarizations of the beam($\sim 90\%$) via treated crystals and optical pumping [8]. Optical pumping refers to exciting electrons to higher levels via circularly polarized light which, due to selection rules, caused a polarized electron to be produced [48]. Figure 3.2 shows the injector.

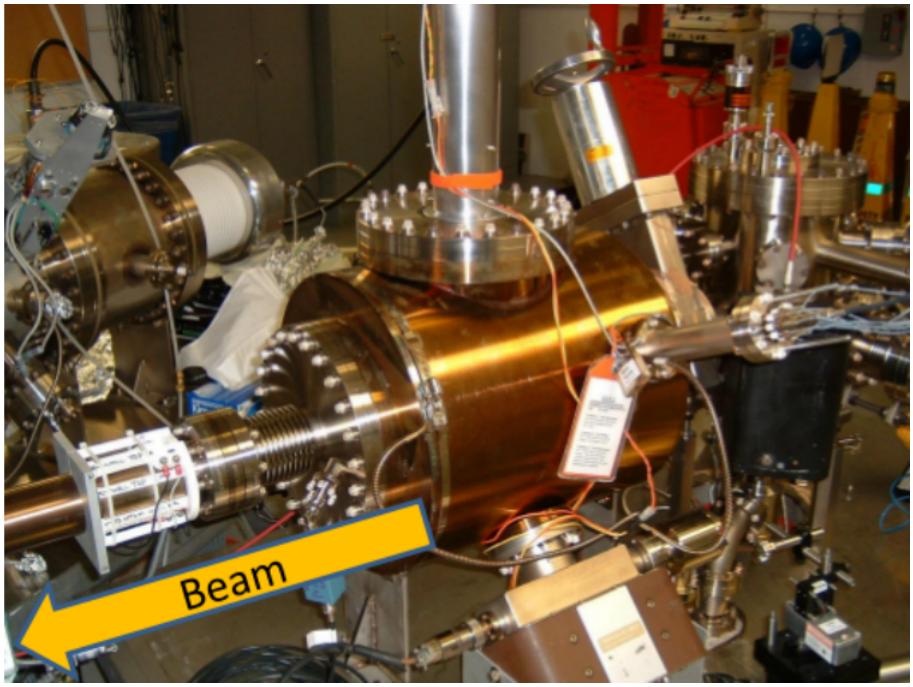


**Figure 3.2:** *Jefferson Lab's inverted injector gun at the time of $Q_{weak}$. Photo taken from the dissertation of Wade Duvall [2].*

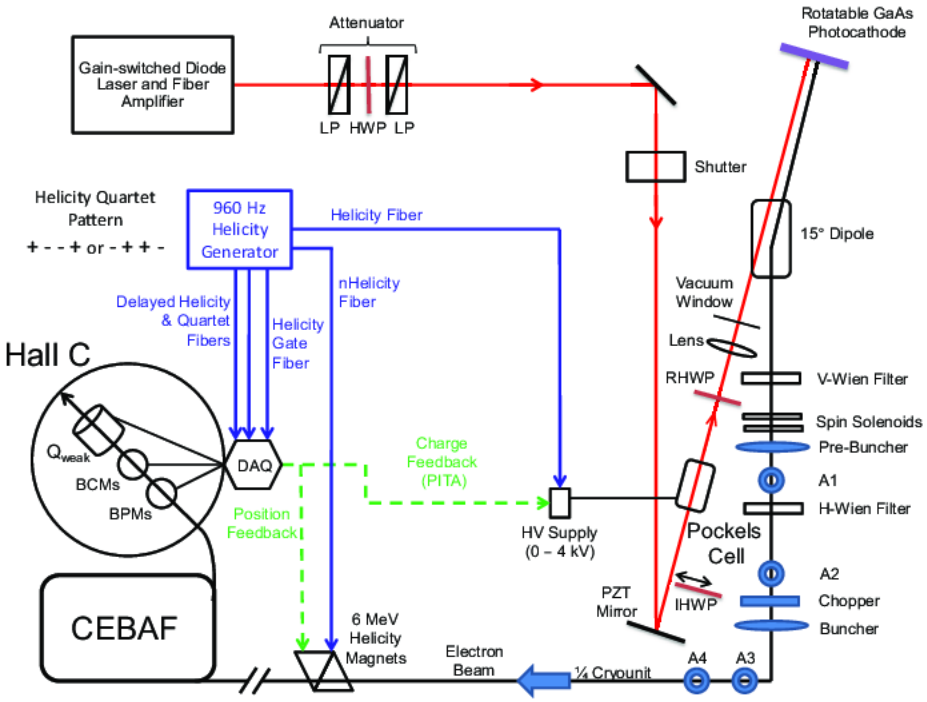


**Figure 3.3:** *Schematic of polarized source. Pockels Cell is visible in the red path before the photocathode,as is the IHWP. The two Wien filters are in the path of electron produced by photocathode. Image taken from $Q_{weak}$ NIM paper [8].*

$Q_{weak}$ required both fast and slow helicity reversals of the polarized electron beam. The fast helicity reversal was built into the source, as can be seen in Figure 3.3. The Hall C laser's light was passed through a Pockels cell before hitting the photocathode. By applying voltage to the Pockels Cell, it acted as a quarter-wave plate [8] and caused the polarization of the laser to be reversed. This resulted in flipping the helicity of the produced electrons. During $Q_{weak}$ the helicity was flipped at 960 Hz, with each helicity state being referred to as a macropulse(MPS).

There were two sets of slow helicity controls for the electron beam. The first one consisted of an insertable half-wave plate (IHWP) which is present in Figure 3.3 right before the

Pockels Cell. The IHWP flipped the polarization of the laser separately from Pockels Cell. The state of the IHWP was changed every 8 hours, with the 8 hours of data taken being referred to as a slug.

The second control was a pair of Wien filters (vertical and horizontal), located after the electron beam is produced from the photocathode in Figure 3.3. The double Wien filter rotated the polarization of the electron beam which $Q_{weak}$ used to flip the polarization on the timescale of weeks. The data taken for the specific Wien settings was referred to as a wien. The Wien filters were also used to create transverse polarization in order to quantify the transverse asymmetry and take several sets of ancillary data.

These helicity controls were necessary for several reasons. The rapid helicity reversal was used to set up the MPS so that quartets of either $+--+$ or $-++-$ could be pseudorandomly selected to measure the asymmetry [44]. The pseudorandom selection of quartets was a method to reduce helicity correlated noise. The slow helicity changes, performed by the IHWP and Wien filters, were used as checks for false asymmetries that are not associated with polarization.

### 3.2.2 Accelerator

The initial acceleration to the electrons is applied within the injector, before being injected into the main accelerator. A superconducting radio frequency (SRF) cavity accelerates the electrons to 45 MeV. There are two main linear accelerators (linacs), generally referred to as

the north and south linacs, that are part of the CEBAF. These two linacs use SRF cavities to add 600 MeV per accelerator, making a full loop add 1200 MeV [8]. The two linacs are connected via arcs in the east and west that consist of steering magnets. At the time of $Q_{weak}$ data-taking, the arcs could handle 5 passes of electrons through the linacs resulting in a maximum beam energy of 6 GeV. Electrons with different energies required different magnetic fields to bend properly. Therefore, the arcs would separate the beam into electrons of different energies and then recombine the electrons to be sent through the linacs.

The three original experimental halls receive simultaneous beam which is directed into the individual halls via the beam switchyard (BSY) separating electron bunches from the individual hall's laser, aka beam buckets, and directing them into the hall in question. The beam buckets can be sent through the loop a different number of times for the individual halls, allowing the halls to have simultaneous electron beam with varying energies.

### 3.2.3 Beam Monitors

There were two types of continuous beam monitors, beam position monitors(BPMs) and beam charge monitors(BCMs), pictured in Figure 3.4. BPMs used four antennas arranged to be parallel to the beam and 45° off the horizontal and vertical. The antennas were designed such that the beam's frequencies were harmonic of the electromagnetic response, allowing the position of the beam to be determined via the magnitude of the signal in each antenna. The BCMs were toroidal cavities shaped such that the magnitude of the resonance caused

by the beam passing through the center was proportional to the charge passing through, allowing a measurement of beam intensity. While the BCMs were able to measure relative charge well, they required calibration via the UNSER monitor which determines charge via electromagnetic induction in a paramagnetic current transformer.

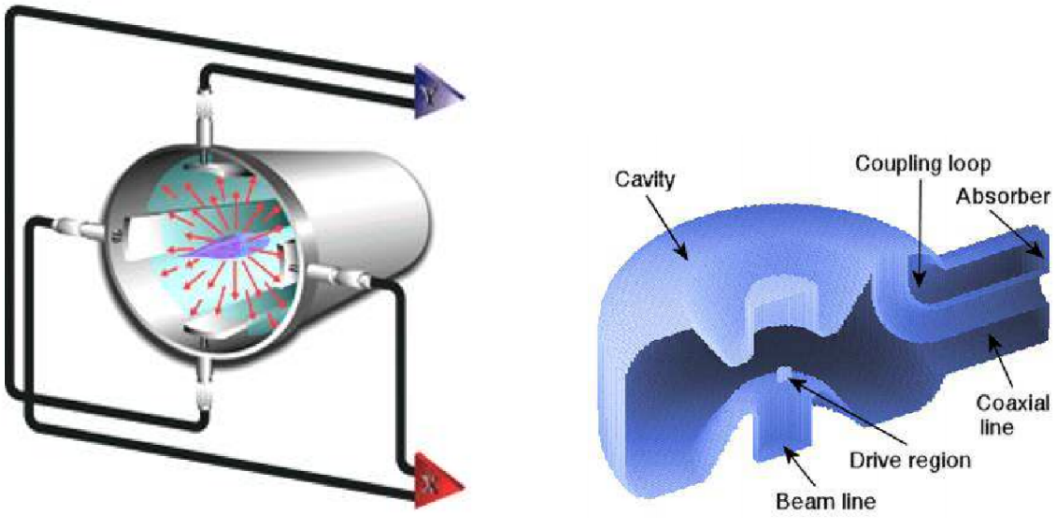


**(a)** *Beam Position Monitor(BPM)* **(b)** *Beam Current Monitor(BCM)*

**Figure 3.4:** *BPMs were used to measure the beam position and BCMs were used to determine the beam intensity. Images taken from the dissertation of John Leacock [4].*

These beam monitors are necessary because of the possibility of false asymmetries in the measured value. False asymmetries can be created via helicity-correlated beam motion causing the electron distribution to appear differently in the opposite helicity states. The false asymmetry generated by the beam properties that are correlated with the measured asymmetry is

$$A_{\text{beam}} = \sum_i \frac{1}{2Y}\frac{\partial Y}{\partial \chi_i}\Delta_{\chi_i} = -\sum_i \frac{\partial A}{\partial \chi_i}\Delta_{\chi_i} \tag{3.1}$$

where $Y$ represents the detector yield, $\chi_i$ is a beam parameter(position and angle differences),

$A$ is the measured asymmetry. The sensitivity of the yield to the specified parameter is given by $\frac{\partial Y}{\partial \chi_i}$, while $\frac{\partial A}{\partial \chi_i}$ gives the asymmetry's sensitivity to the beam parameter. The helicity-correlated mean of the specified beam parameter is defined to be

$$\Delta_{\chi_i} = \chi_{i+} - \chi_{i-}. \tag{3.2}$$

The BPMs monitor $X$ and $Y$ beam positions and $X'$ and $Y'$ angle differences between helicity states in order to determine the corrections applied. These values were recorded in the DAQ (explained in Section 3.8) and the detector sensitivities were determined for approximately hour long sets of data, which were then applied to the individual quartets that make up the data set. This systematic study was also used as verification for the final helicity-correlated beam motion correction, the beam modulation system which is discussed in Section 3.2.4.

The BPMs also characterized the beam energy. Specifically BPM3C12, which was the BPM at the highest dispersion of the beam, combined its $X$ position and angle information with standard beam position and angle data to extract the relative energy [8] via

$$\frac{\Delta P}{P} = \frac{\Delta X_{\text{3C12}}}{411} - \frac{\Delta X_{\text{target}}}{596} + \frac{\Delta X'_{\text{target}}}{0.443} \tag{3.3}$$

where the subscript of $\Delta X$ specifies which BPM along the beam line is being discussed. The denominators of Equation (3.3) come from the first order transport matrix used to propagate

the beam from BPM3C12 and the target. In order to calibrate these relative measurements of energy, invasive measurements were performed [8] using three wire scanners to determine the beam position and the accelerator arc magnets as a spectrometer [49].

Another possible source of false asymmetry in the detector signal is helicity-correlated charge asymmetry, as defined by

$$A_Q = \frac{Q_+ - Q_-}{Q_+ + Q_-}, \tag{3.4}$$

with $Q_\pm$ representing the charge in the relevant helicity state. This false asymmetry is related to a difference in the number of electrons found in the two possible helicity states. In order to minimize this value, by keeping the charge asymmetry below $\pm 10$ ppb [8], a charge feedback system was put in place. The detector signal was also normalized by charge as measured by the BCMs,

$$Y = \frac{S}{Q}. \tag{3.5}$$

This produces the normalized charge, $Y$, by using the integrated detector signal, $S$, and the BCM measured charge, $Q$.

### 3.2.4 Beam Modulation

Originally the natural jitter of the beam motion during data taking was used to determine the detector sensitivities, but it was determined that deliberately shifting the beam parameters in order to measure the effects resulted in more accurate sensitivities [8]. A beam modulation system was developed in order to induce larger beam motion than was seen during

normal running conditions. Changes in $X$, $X'$, $Y$, and $Y'$ were individually produced by manipulating the current in pairs of magnets along the beamline. There were two pairs in $X$ and two pairs in $Y$. Changing the beam energy was done via the accelerator's South Linac and monitored by the BPM3C12 as discussed in Section 3.2.3.

The final helicity-correlated beam motion correction was determined via the beam modulation system [50].

### 3.2.5 Halo Monitors

The halo monitors were photo multiplier tube (PMT) monitors that were used to tune the beam [8]. The monitors, which sat upstream of the $LH_2$ target, were pointed at a retractable halo "target" that was farther upstream (6 m from the $LH_2$ target). There were six halo monitors, four with lucite blocks and two with small scintillator blocks. The average scattering angle of the halo monitors was $\sim 12.4^\circ$. By using this system, the absolute halo fraction was calculated to a very high precision.

## 3.3 Polarization

Ideally, the $Q_{\text{weak}}$ Experiment would have used a 100% longitudinally polarized beam, but that was not possible. Instead, the measured asymmetry depends on the polarization as

$$A_{\text{msr}}^{\text{PV}} = P_L A_{\text{ep}}^{\text{PV}}. \tag{3.6}$$

This indicates that in addition to the asymmetry measurement $\left(A_{\rm msr}^{\rm PV}\right)$, the longitudinal polarization $(P_L)$ need to be measured $< 1\%$ in order to accurately extract the elastic asymmetry $\left(A_{\rm ep}^{\rm PV}\right)$. Table 3.1 included a beam polarization of 89%, which was the measured value of the polarization over the course of the experiment.

There were two methods of measuring the polarization over the course of the experiment. The first one involved an established Jefferson Lab Møller Polarimeter. This was an invasive measurement, due to the fact it could only be used at low current, and was able to measure the polarization to $\leq 1.5\%$ [8]. The Møller Polarimeter was the only source of polarimetry measurements for most of Run 1. The second method involved a Compton Polarimeter developed for $\rm Q_{weak}$ which was able to operate concurrently with normal data-taking and was able to obtain a precision of $< 1\%$ with an hour's worth of data [8]. The two independent polarization measurements were cross-checked by taking a measurement with the Compton Polarimeter directly before and directly after taking a Møller measurement at a current of 4.5 $\mu$A.

Figure 3.5 overlays both Møller and Compton Polarimeter results during run 2. Both sets of data are in good agreement.

### 3.3.1 Møller Polarimeter

To extract the polarization the Møller polarimeter used a precisely known cross-section, the $\vec{e}\,\vec{e}$ asymmetry. A 3.5 T superconducting solenoid was used to polarize a thin(1$\mu$m) iron foil

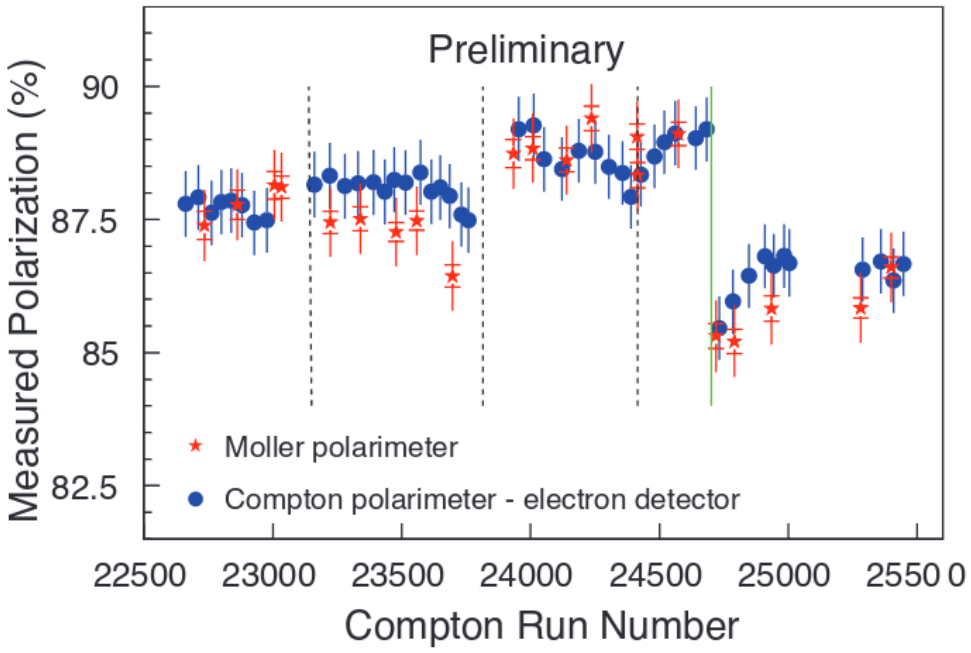


**Figure 3.5:** *The polarization measurements for run 2. The Compton(blue circles) and Møller(red stars) are shown to be in good agreement with each other. Each data point is averaged over 30 hours. The vertical lines represent when there were changes in the beam injector. Image taken from the $Q_{weak}$ NIM paper [8].*

that saturated at 2.2 T [8]. The thin iron foil was the target, and measurements were made by requiring both a scattered and recoil electron to be detected. Due to the invasiveness of the Møller measurement, a polarization value was only able to be obtained a few times a week. Figure 3.6 shows the layout of the thin lead foil(target), the solenoid, the electron detectors, and the quadrupole magnets(Q1, Q2, Q3) used to focus the electrons into the detectors. During $Q_{weak}$ data taking only Q1 and Q3 were being used to steer the electrons, as Q2 was installed in preparation for the 12 GeV upgrade.

There was an intermittent short in Q3 in Run 1 that caused an increase in the uncertainty in the polarization, but this was not present during Run 2.

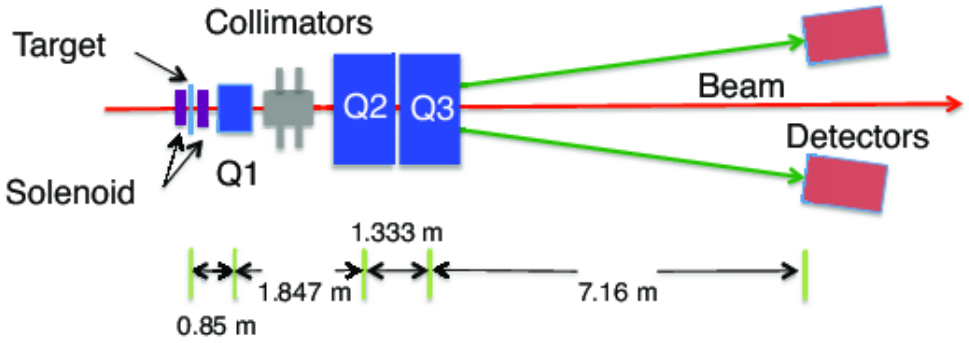


**Figure 3.6:** *Møller Polarimeter from Hall C, as shown in $Q_{weak}$ NIM paper [8].*

### 3.3.2 Compton Polarimeter

The Compton Polarimeter [51] relies on $\vec{\gamma}\vec{e} \rightarrow \vec{\gamma}\vec{e}$ scattering to extract the polarization. A chicane of four dipole magnets is used to deflect the beam down to a Fabry-Perot optical cavity and then back to the normal beamline after scattering off the 10 W 542 nm laser [8]. An electron detector is placed to monitor recoil electrons and a photon detector monitored the recoil photons. The locations of the various components can be seen in Figure 3.7.

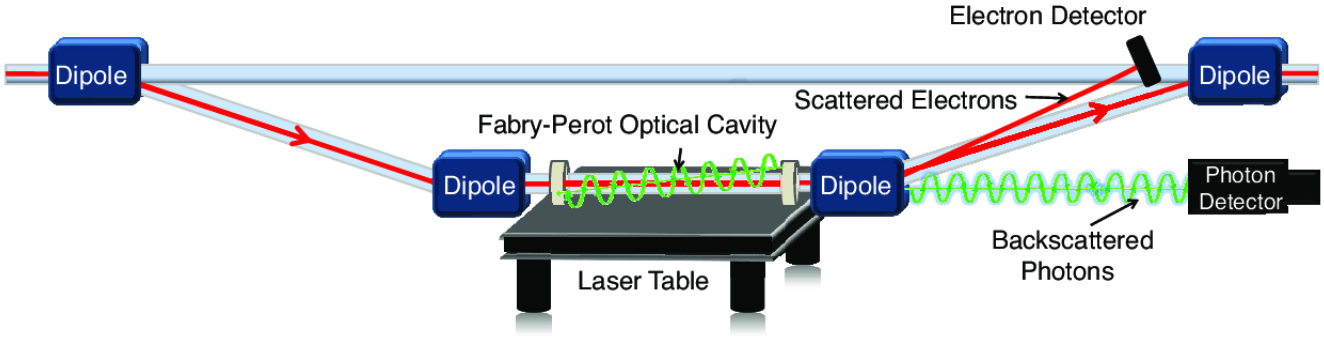


**Figure 3.7:** *Sketch of the Hall C Compton Polarimeter layout, as shown in $Q_{weak}$ NIM paper [8].*

In order to reach the photon detector, the backscattered electrons must pass through the dipole that deflects the beam upward. After that they enter the actual detector, a

lead tungstate (PbWO 4 ) crystal calorimeter connected to a single PMT. As yet, absolute polarizations have not been determined due to difficulty in determining the non-linearity measurements for this detector.

The third dipole of the chicane sent recoil electrons of a specific momentum range to the electron detector , as well as deflecting the beam upwards. The electron detector sat inside the beamline, though it could be moved out of the beam path when the chicane magnets were off, consisted of a diamond micro-strip detector. Hour long runs were used to collect data, both for laser off(background spectra) and laser on. The individual strips allowed a determination of asymmetry as a function of electron momentum which was then compared to QED calculations, as shown in Figure 3.8, to extract beam polarization.

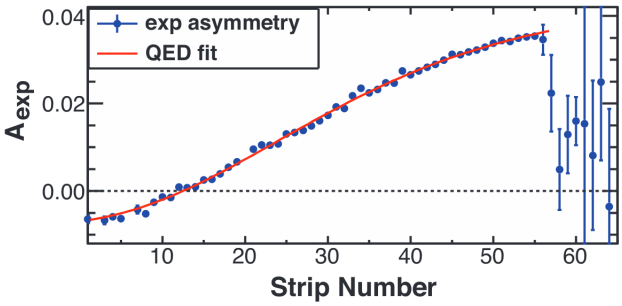


**Figure 3.8:** *Comparison of Compton Electron Detector Strip Asymmetries to QED calculated asymmetries. Image taken from $Q_{weak}$ NIM paper [8].*

## 3.4 Target System

The Jefferson Lab Target group was responsible for the design of the $Q_{weak}$ target system [8]. Figure 3.9 displays a schematic drawn in CAD of the structure of the liquid hydrogen

($LH_2$) target assembly. The solid target structure, schematic shown in Figure 3.12, was located beneath the hydrogen cell and in between the J-pipes. The $LH_2$ target provided the main measurement of $Q_{weak}$, while the solid targets allowed the extraction of the target window asymmetry. The solid targets also provided the opportunity for certain ancillary measurements.

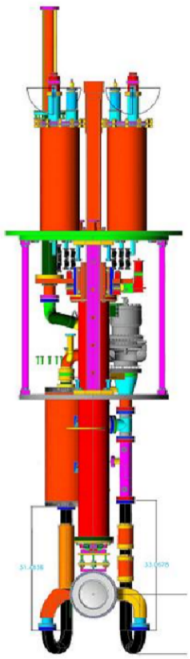

**Figure 3.9:** *CAD drawing of target. The solid target device is not shown but was located underneath the cell, between the protruding pipes. Image taken from the dissertation of Wade Duvall [2].*

### 3.4.1 Liquid Hydrogen Target

One of the technical challenges of $Q_{weak}$ was the requirement of a high power target with minimal localized density fluctuations(a major source of signal noise) [8]. This was overcome via the use of computational fluid dynamics(CFD) in determining the best geometry as seen

in Figure 3.10, a scattering chamber temperature simulation. The goal was to minimize boiling in $\sim$ 58 liters of $LH_2$ contained in the target and passed through a closed loop via centrifugal pump.

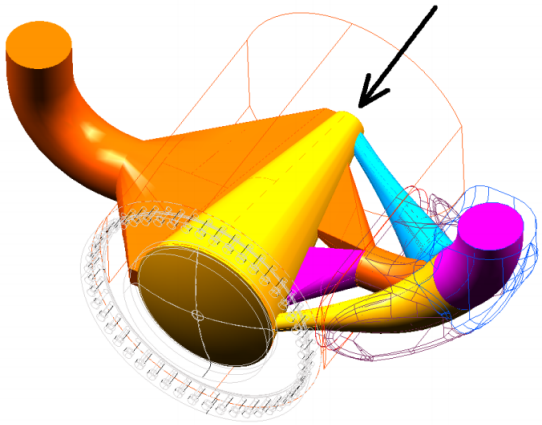

**Figure 3.10:** *Simulation of the computational fluid dynamics through the Hydrogen cell. The arrow indicates beam direction with $LH_2$ entering the cell from the right and leaving from the left. Image taken from the dissertation of Wade Duvall [2].*

The primary component of the closed loop was the 34.5 cm long scattering chamber where the beam interacted with the $LH_2$ [8]. The scattering chamber was constructed of aluminum and had thin entrance(0.10 mm) and exit(0.13 mm) windows made of 7075-T6 aluminum with the $LH_2$ flow transverse to the beam path. The exit window was designed so that electrons with a scattering angle of $< 14^\circ$ would pass through. The experiment's acceptance of $5.8^\circ < \theta < 11.6^\circ$ was in no way hampered by the exit window.

The next piece of the closed loop consisted of a hybrid counterflow heat exchanger which was designed to deal with the 2.1 kW of energy the beam deposited in the $LH_2$ [8]. This heat exchanger drew 5 K liquid helium from the Central Helium Liquefier (CHL) with a typical

flow of $\sim$ 14 g/s and 14 K liquid helium from the End Station Refrigerator(ESR) at $\sim$ 40 g/s in order to keep the $LH_2$ within the target at 20 K. A 3 kW heater was included in the loop to act as a equivalent heat source when the beam was off.

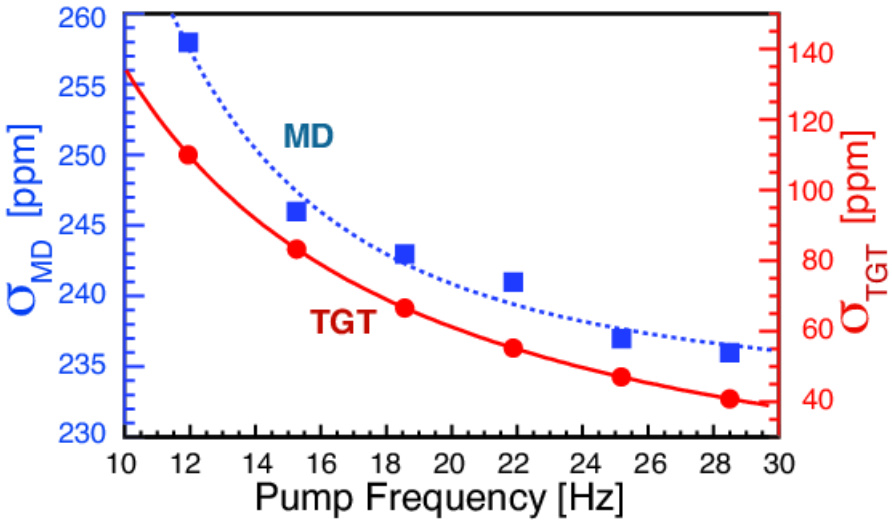


**Figure 3.11:** *Target boiling noise study. Figure taken from the $Q_{weak}$ NIM paper [8].*

Though the target was carefully designed to minimize noise via CFD, as discussed in relation to Figure 3.10, another measure used to keep any boiling under control involved using a raster, normally 4 mm $\times$4 mm, to diffuse the beam energy throughout more of the $LH_2$ [8]. This also prevented the aluminum windows from being damaged by the beam. Nonetheless, extensive studies were done on the noise contribution to the signal. Figure 3.11 shows one of the studies done, tracking the main detector widths (further explained in Section 3.7.1), $\sigma_{\mathrm{MD}}$, versus the pump frequency. Other studies consisted of plotting $\sigma_{\mathrm{MD}}$ versus beam current and rastered beam size. The studies were consistent, and in nominal

conditions the target noise contribution to the signal was $\sim$ 40 ppb.

### 3.4.2 Solid Targets

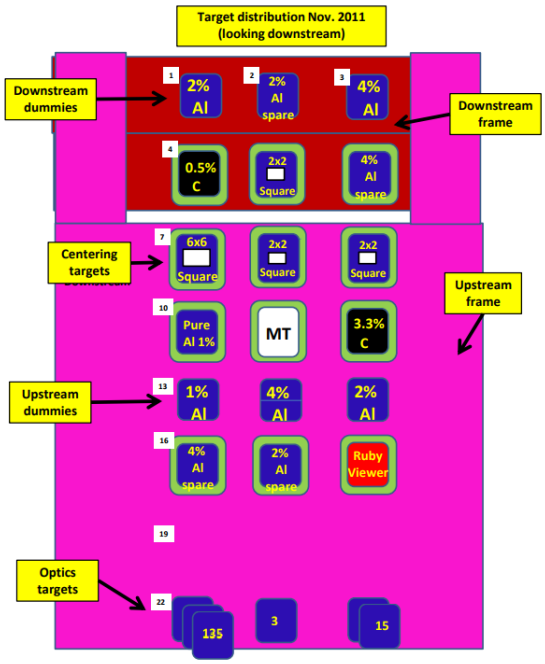


**Figure 3.12:** *Solid target device. Image taken from the dissertation of Wade Duvall [2].*

The solid targets of $Q_{weak}$ were housed on a set of two frames, one at the same Z-position as the downstream(DS) window of the scattering chamber and one at the same Z-position of the upstream(US) window [8]. There were also sets of "optics targets" that were actually positioned at 5 separate Z-positions between the US and DS windows. The purpose of these optics targets was to assist in vertex reconstruction algorithms at low beam energy(tracking mode). The run 2 layout of these solid targets is shown in Figure 3.12. The solid target arrays relied were placed in contact with the $LH_2$ vessel and took advantage of thermal

conductivity to remian at the correct temperature.

## 3.5 Toroidal Magnet Spectrometer

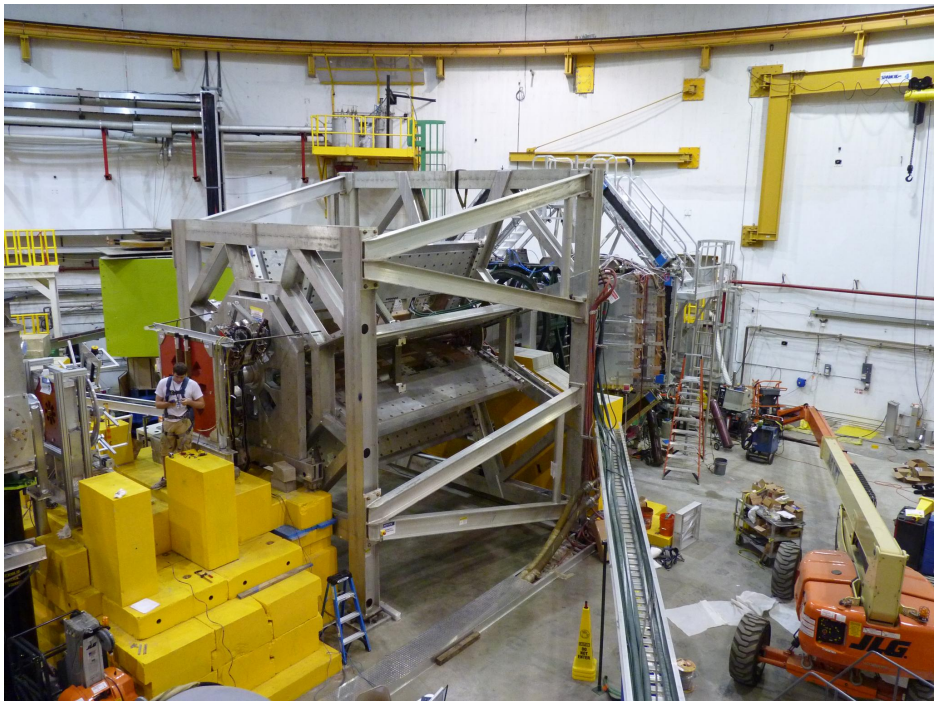


**Figure 3.13:** *Photo during installation of $Q_{weak}$ apparatus. Photo taken from the $Q_{weak}$ NIM paper [8].*

The toroidal magnet used in $Q_{weak}$(QTOR) is shown in Figure 3.13. Some of the eight copper coils that make up QTOR are visible within the aluminum structure. The red structures visible before QTOR are part of the triple collimator system that will be discussed in Section 3.6.1. Beyond QTOR, several of the main detector bars, discussed in Section 3.7.1 can be seen.

The copper coils of QTOR were made of very pure copper, with the goal of minimizing

iron content. As these coils provided the integrated magnetic field,

$$\int \mathbf{B} \cdot d\mathbf{l} = 0.67 \text{ T} \cdot \text{m}, \tag{3.7}$$

along the electron's path [8], any iron present within QTOR would become polarized due to the magnetic field. Any electrons scattering off this polarized iron would contaminate the elastic signal. Pure low conductivity water (LCW) was used to keep the coils from overheating.

QTOR was designed so that it would move lower energy electrons, such as ones caused by Møller scattering, away from the main detector bars [52]. It also focused the electrons that scattered elastically off the $LH_2$ target onto a 2 m by 10 cm image [10] on top of the main detector bars. This image was affected by fringe magnetic fields, causing the formation of a unique moustache shape [53].

## 3.6 Collimation and Shielding

The $Q_{weak}$ Experiment ran at very high beam currents($\sim 180\mu$A) for a long time, leading to very high radiation levels within the apparatus. Since this was known, designing shielding that would help isolate the signal was a very high priority. The three main materials used in the shielding were lead, tungsten, and concrete.

### 3.6.1 Triple Collimator

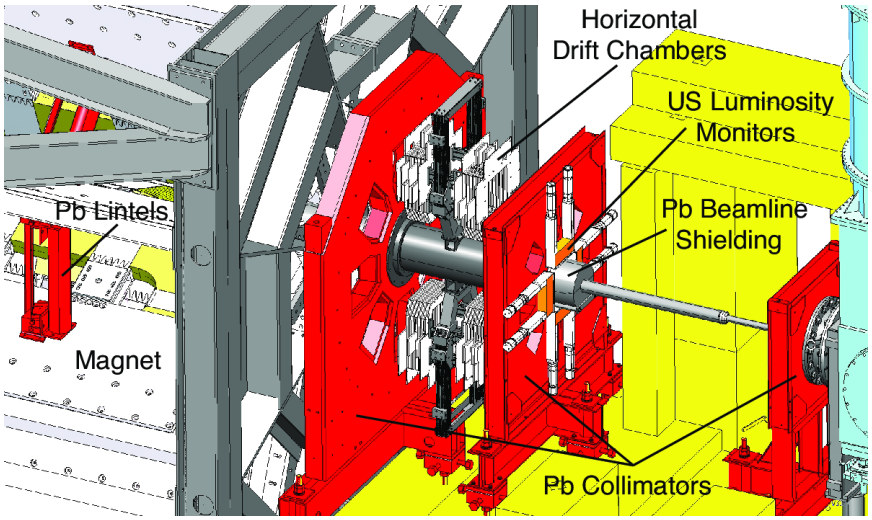


**Figure 3.14:** *Schematic of the beamline collimators. Image taken from the dissertation of Wade Duvall [2].*

The triple collimator, shown in red in Figure 3.14, were structures of lead antimony, a combination of 95.5% Pb and 4.5% Sb, which had eight six-sided holes that lined up with the eight main detectors [8]. In Figure 3.14, the beam would enter the array from the right and progress through the first collimator, then pass through the defining collimator, and finally pass through the third collimator before entering QTOR(see Section 3.4.1). The lintels(see Section 3.6.3 that reside within QTOR are also visible.

Two of the three collimators were referred to as clean-up collimators [8]. The first collimator, 15.2 cm wide and located only 0.74 m downstream of the target, was designed to allow all electrons that scattered off the target to pass through. There were also tungsten shutters that could be retracted on two of the eight octants at the first collimator in order to study backgrounds. The third collimator, 11.2 cm wide and located 3.82 m downstream

from the target, was also designed with several centimeters of clearance for elastic electrons.

The second collimator, 15.0 cm wide and 2.72 m downstream from the target, defined the acceptance for $Q_{weak}$ [8]. The downstream face allowed passage to elastic electrons from the upstream section of the target with scattering angles of $5.8^\circ < \theta < 10.2^\circ$. The downstream section of the target had an angular acceptance of $6.6^\circ < \theta < 11.6^\circ$.

### 3.6.2 Beam Collimator

It was necessary to attempt to isolate the target from the aluminum beamline as a method of reducing the backgrounds observed in the main detectors. Via simulation [54] [55], the best method of reducing these was determined to be using a 21 cm long tungsten-copper beam collimator that was placed in the center of the first collimator. A side view schematic(a) and photograph(b) of this water-cooled collimator can be seen in Figure 3.15. At normal running conditions, $\sim$ 1.6 kW of power was deposited in the collimator as determined via water flow and temperature change [8].

While the beam collimator did block a lot of the beamline backgrounds and successfully dissipated heat, late in run 2 it was discovered that it still had a contribution in the main detector signal. It was a large component of the upstream luminosity monitors due to the lack of shielding between them and the beam collimator. Simulations were done to characterize this effect, along with a systematic study. Section 5.2.3 describes how the results affect the final asymmetry.

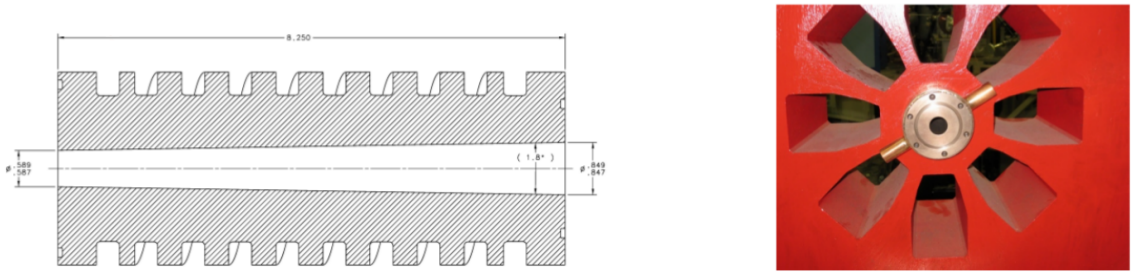

**(a)** *Side view of the tungsten beam collimator.*

**(b)** *Photo of the first collimator after installation of the tungsten beam collimator.*

**Figure 3.15:** *The tungsten beam collimator was installed on the first collimator to reduce beamline backgrounds. Images taken from the dissertation of Wade Duvall [2].*

Another measure used to reduce beamline backgrounds involved lead shielding clamped to the beamline upstream of the second collimator, visible in Figure 3.14. This extra shielding was added after setup runs demonstrated that steel parts of the beamline were causing additional backgrounds.

### 3.6.3 Lintels

Figure 3.14 shows the position of one of the eight lead lintels, which were installed in between QTOR coils [54]. A schematic of these lintels is shown in Figure 3.16. The lintels, 70 cm long and located 70 cm upstream of the target [8], were designed to prevent neutrals from reaching the detectors. Photons were being generated via Møller scattering on the inside of the second collimator. There was a 2 cm clearance built in for the elastically scattered electrons.

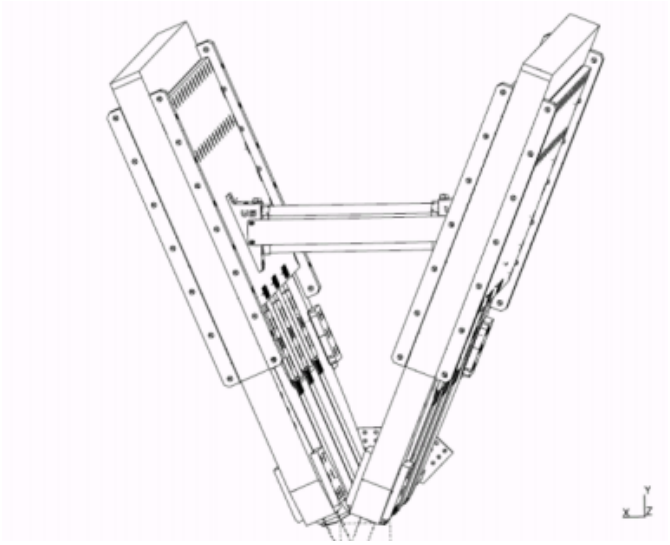

**Figure 3.16:** *A Pb lintel, the horizontal bar, is drawn here suspended between two toroidal spectrometer coils. These lintels were installed to prevent neutrals generated on the inner edge of the defining collimator being included in the signal. Image taken from the dissertation of Wade Duvall [2].*

### 3.6.4 Concrete Shielding

For further shielding, concrete structures were erected around several key areas of the $Q_{weak}$ apparatus. In Figure 3.13, the yellow blocks in front of QTOR show the start of a concrete hut 61 cm thick that was built over the space between the first and second collimators. This was not only to reduce backgrounds, but also in order to protect workers that needed to access various parts of the apparatus.

Simulations determined that another concrete structure(122 cm thick) was needed around the main detectors [54]. The structure was built with openings that included several centimeters of clearance for the elastically scattered electrons and was constructed of barite loaded concrete ($Ba_2SO_4$) and stainless steel fixtures [8].

## 3.7 Detectors

There were several sets of detectors that were designed and used for various purposes during $Q_{weak}$. The main detectors provided access to the asymmetry that was the primary measurement. The background detectors allowed various contributions to the asymmetry to be calculated and corrected. The final set of detectors consisted of the event mode tracking system which allowed the extraction of the kinematics.

### 3.7.1 Main Detectors

$Q_{weak}$ had eight quartz Čerenkov detectors that are referred to as the main detectors, two of which are shown in Figure 3.17. This photograph was taken prior to the lead preradiators being installed and so offers a clear picture of MD7(bottom) and MD8(left, angled). They were located immediately after QTOR and three of them(MD8, MD1, MD2) are also visible in Figure 3.13. The quartz bars and PMTs were responsible for measuring the asymmetry.

There were multiple challenges to overcome for $Q_{weak}$'s main detectors. They had to be able to measure the electrons elastically scattered off the target with minimal noise and background contributing to the signal. They also needed to respond linearly to the elastic signal and be radiation-hard. Finally, they had to have a high degree of azimuthal symmetry.

To decrease noise and low-energy backgrounds and boost the elastic signal in the detectors, 2 cm thick lead preradiators were placed in front of the main detectors [8]. This increased the light yield and caused the signal to background ratio to improve by a factor of

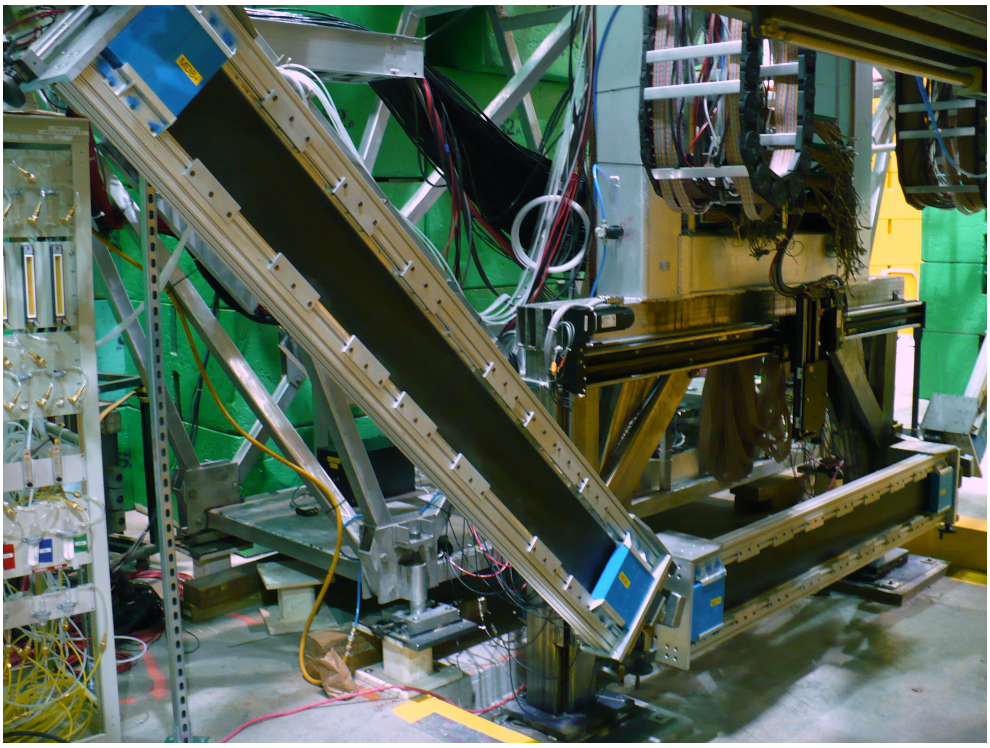

**Figure 3.17:** *A photograph of two main detectors prior to lead pre-radiators being installed. There were eight main detectors that were installed symmetrically around the beam line. Photo taken from the $Q_{weak}$ NIM paper [8].*

$\sim 20$. However, this did cause a noise increase of 10% due to electromagnetic showering that increased the width of the pulse height distribution of the events. It was later discovered that the inclusion of the preradiators lead to the lead interacting with transversely polarized electrons and causing a non-elastic asymmetry that contributed to the signal. This unpredicted asymmetry will be discussed in Section 5.2.6.

The material chosen for the main detectors was Spectrosil© 2000 fused quartz bars, chosen for the fact that it is non-scintillating, low-luminescent, and radiation hard up to 1MRad [8]. Each of the eight main detector bars consisted of two 1 m long bars glued together, with 18 cm long quartz light guides attached to either end. The photo multiplier tubes(PMTs),

Electron Tubes 9312WKB PMTs, were then attached to the light guides. All joins were made by gluing the respective surfaces together with UV transparent optical adhesive (SES-406).

In order to handle the two data-taking modes, two different sets of PMT bases were custom designed. The bases passed the PMT signal into the electronics chain. When $Q_{weak}$ was in event mode, the PMTs used high-gain bases ($2 \times 10^6$). While the experiment was in integration mode, low-gain bases ($\sim 440$) were used to reduce the PMTs' nonlinearity [8] [53].

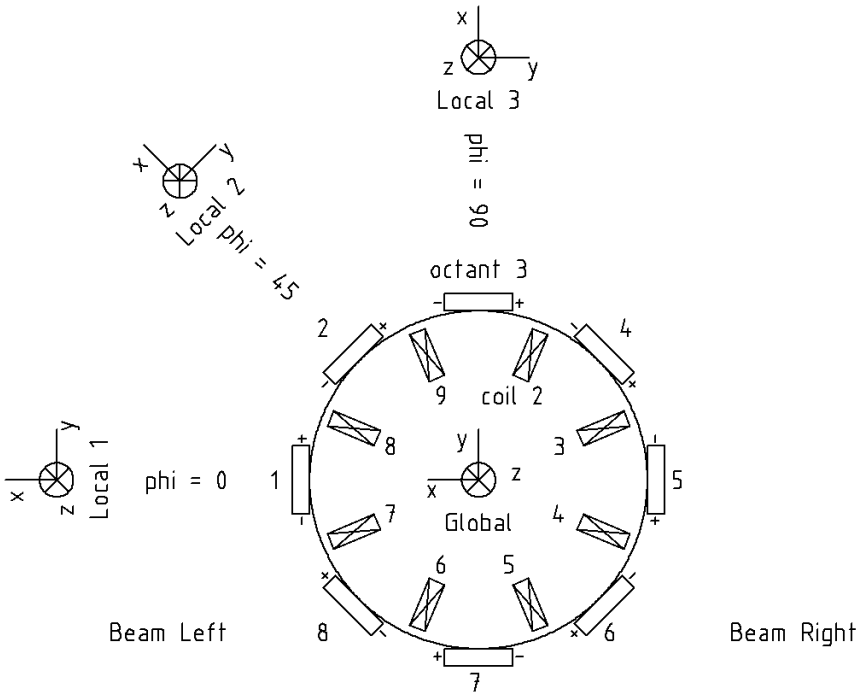


**Figure 3.18:** *Diagram of $Q_{weak}$'s azimuthal symmetry. The beam goes into page at the center. The main detectors are the empty rectangles labelled 1-8, with PMTs + and - at either end. The rectangles with an X labelled 2-9 represent the coils of the toroidal spectrometer. Image is taken from the dissertation of Wade Duvall [2].*

The science behind the Čerenkov detectors involves relativistic ($E_e > m_e$) electrons producing Čerenkov light when passing through the quartz. The light is channeled to the light guide thanks to the total internal reflection within the bar, and then the light guides pass the light into the PMTs. The PMTs then convert the photonic signal into an electrical signal which continues into the data acquisition system.

It was important to have the detectors positioned with azimuthal symmetry as this allowed various effects to cancel along the detectors. The detectors (labelled 1-8) and QTOR coils (labelled 2-9) were both arranged as shown in Figure 3.18. The PMTs were located at either end of the main detector bars, as described earlier, and were labelled either + or −. The main detector structures (composed of quartz bars, light guides, and PMTs) were placed in custom aluminum frames, visible in Figure 3.17, which were then held in the arrangement shown in Figure 3.18 via a large support structure, visible in Figures 3.17 and 3.13. This structure was nicknamed the Ferris wheel and had low-iron content in all parts. There was also mu-metal magnetic shielding on the PMTs.

### 3.7.2 Tracking Detectors

The event mode tracking system was made up of two sets of wire drift chambers, the horizontal drift chambers (HDCs) and the vertical drift chambers (VDCs). There were also trigger scintillator paddles developed for event mode data taking. Lastly there was a focal plane scanner that was placed behind the main detectors. The tracking detectors will be

discussed in great detail in Chapter 4.

### 3.7.3 Background Detectors

Every effort was made to reduce backgrounds via shielding, but it was impossible to remove them entirely. Therefore dedicated detectors were created in order to monitor the backgrounds so that their effect could be removed during analysis.

Two spare main detector PMTs were repurposed into background detectors [8]. One was only connected to an integration mode base and placed into a dark box along the beamline [56]. That detector was referred to as PMTONL. The second unused PMT was attached to a spare main detector light guide, and then connected to the integration mode base and placed in a dark box along the beamline. This monitor was referred to as PMTLTG. Figure 3.19 shows them in the two configurations used during data taking.

Figure 3.19a shows the original location of PMTLTG, placed between MD5 and MD6. PMTONL was in the mirror location between MD1 and MD8. This configuration was used during commisioning and the start of run 1. Partway through run 1, PMTONL and PMTLTG were moved to the location showing in Figure 3.19b, behind MD3 which was the bottom of the main detector bars. They remained in this configuration for the rest of data taking.

Halo monitors, discussed in Section 3.2.5, were not actually background monitors but the beam halo they tracked could cause backgrounds when interacting with beamline com-

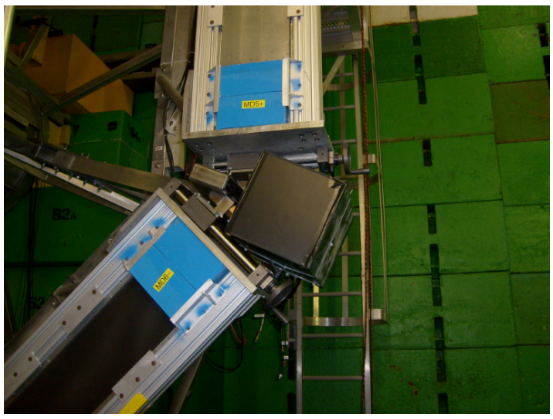

**(a)** *Original configuration for PMTLTG between MD5 and MD6. PMTONL is not visible, but is in the same location on the other side. Beam enters page.*

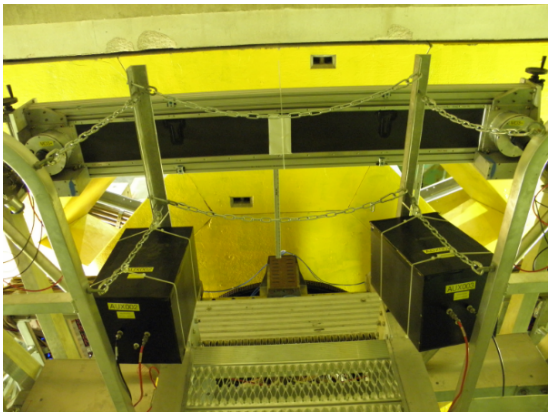

**(b)** *Final configuration for PMTLTG(left) and PMTONL(right) behind MD3 which is also visible. Beam would exit page.*

**Figure 3.19:** *There were two configurations of background detectors PMTLTG and PMTONL used in $Q_{weak}$. The original configuration is shown in (a) and the final configuration is shown in (b). Images taken from the dissertation of Wade Duvall [2].*

ponents. Therefore, they did provide information on backgrounds.

The final set of background detectors were two sets of luminosity monitors [8] [4]. They were placed at sites where the expected physics asymmetry was smaller and the scattered electron flux was higher than at the main detectors. The upstream luminosity monitors, shown in Figure 3.20a, were mounted on the second collimator's upstream face. The downstream luminosity monitors, shown in Figure 3.20b, were located downstream of the main detectors' shielding hut. Originally these were designed to act a null check on the asymmetry. The upstream luminosity monitors ended up assisting in the beamline background measurement

The luminosity monitors were all constructed of the same material as the main detectors, Spectrosil© 2000 fused quartz. The upstream luminosity monitors were placed in air-core

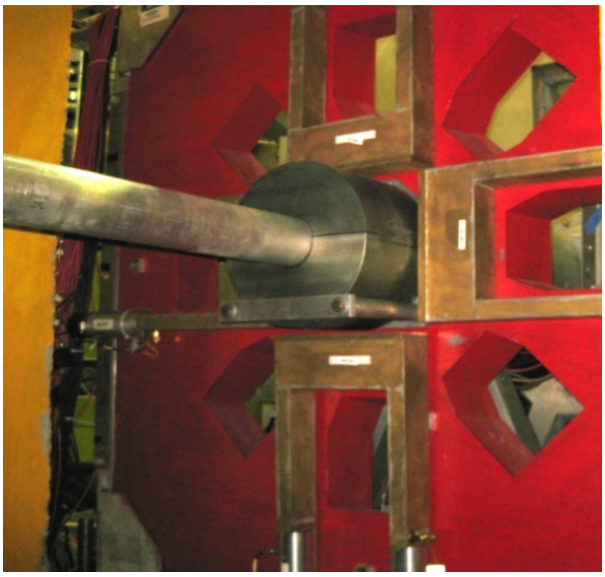

**(a)** *The second collimator with the upstream luminosity monitors installed. Beam enters image on the left and exits on the right.*

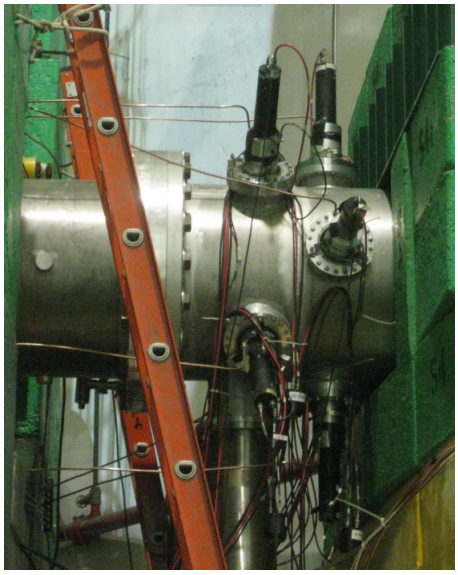

**(b)** *The end of the beamline with the downstream luminosity monitors installed. The orange ladders were permanent and used to maintain the luminosity monitors. Beam enters image on the left and exits on the right.*

**Figure 3.20:** *Photographs of Luminosity Monitors taken after they were installed on the beamline. Photographs taken from the dissertation of Wade Duvall [2].*

light guides made of highly reflective aluminum (Alanod Miro-Silver 27). These were placed in the odd octants, as shown in Figure 3.20a. The downstream luminosity monitors were placed one per octant, as see in Figure 3.20b.

## 3.8 Data Acquisition System

The data acquisition(DAQ) system was designed to handle the two running modes of $Q_{weak}$. Integration mode and event mode mostly consisted of different sets of detectors though there were some that were shared between modes. Integration mode handled production data,

usually with beam currents as high as 180 $\mu$A, and would average signals over intervals. Event mode included the event mode detectors and therefore was limited to currents $< 1\mu$A. It was used to extract trajectory information for the individual scattered electrons. The electronics for the two modes were separate. The software for $Q_{weak}$'s DAQ was written using a Jefferson Lab DAQ framework referred to as CODA [57] [58].

### 3.8.1 Integration mode DAQ

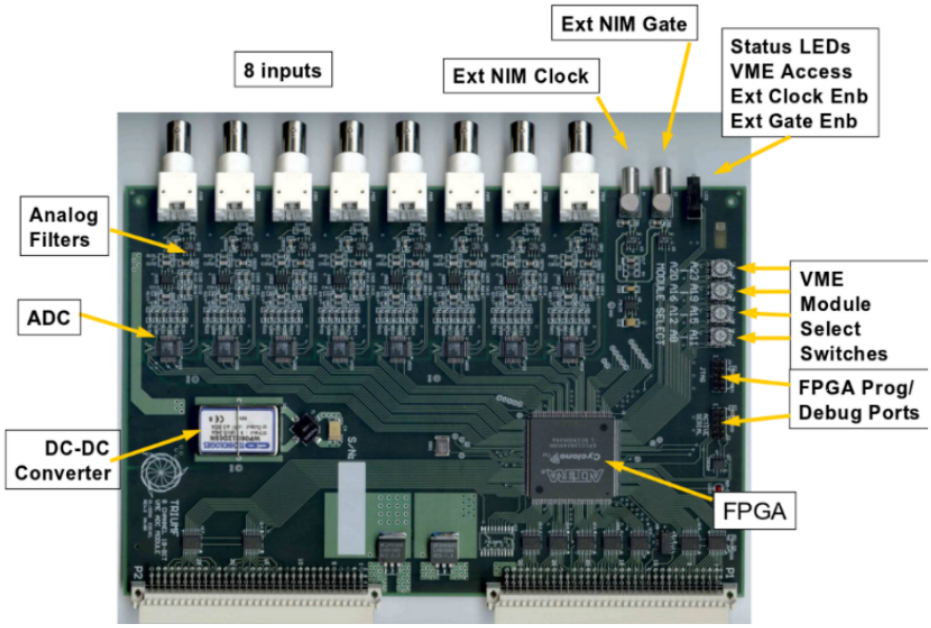


**Figure 3.21:** *The VQWK analog-to-digital converters(ADCs) were used to digitize detector signals in $Q_{weak}$. Photograph taken from the dissertation of Wade Duvall [2].*

Low-noise current-to-voltage preamplifiers were used to digitize the current that the PMTs produced [8]. The PMT current was proportional to the light generated in the quartz, which was proportional to the number of electrons passing through the quartz. The preampli-

fiers were tested for radiation-hardness up to 1 kRad with no decrease in performance being seen.

$Q_{weak}$ required custom sampling-integration analog-to-digital converters(ADCs) [8], pictured in Figure 3.21. These ADCs were called VQWK modules and were designed by a Canadian national laboratory, TRIUMF. The VQWK modules were application-specific integrated circuits (ASIC) that were specifically designed to be low noise. They were used to collect data from the eight main detector bars, the background detectors, and the beam monitors.

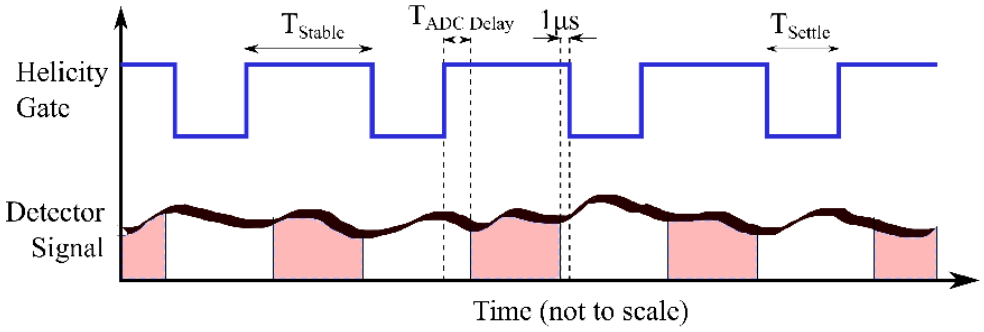


**Figure 3.22:** *Integration mode ADC input. Shaded areas indicate when the ADCs were digitizing signal associated with the helicity gate being open(blue line being elevated). Image taken from the $Q_{weak}$ NIM paper [8].*

The accelerator had a helicity reversal rate of 960 Hz (see Section 3.2.1). Figure 3.22 shows the helicity gate window [8], where an up-down combination is equivalent to one MPS. The shaded section of the detector signal would be the data actually recorded by the ADCs. The helicity is stable for $T_{Stable} = 971.65$ $\mu$s, and within that time period the ADCs start taking data after $T_{ADC\ Delay} = 42.5$ $\mu$s. This delay is due to computer dead time. Approximately 1 $\mu$s before the helicity flips again the last sample is taken. There is

then a $T_{Settle} = 70$ $\mu$s period for the system to stabilize before the pattern repeats.

### 3.8.2 Event Mode DAQ

While integration mode had helicity-based triggers, event mode required a detector trigger [8]. The helicity-based trigger was set to a 10 Hz clock. A Jefferson Lab Trigger Supervisor module was used to control which detector would trigger data-taking and the threshold of the trigger. The options for the trigger in event mode were the main detector bars, the trigger scintillator paddles, the focal plane scanner, and a background detector.

The VQWK modules were not used in event mode data-taking. Both the HDCs and VDCs were read out into Jefferson Lab F1TDC modules. The ADCs digitized analog current pulse heights and similarly the time-to-digital converters(TDCs) digitized time pulses.

# Chapter 4

# Tracking Apparatus and Analysis

The goal of $Q_{weak}$'s tracking system was designed to measure the kinematic variables involved in the elastic and inelastic reactions occurring during data-taking to be used as a benchmark to compare to the simulation used to extract the final $Q_{weak}$ $Q^2$. The measurement of the proton's weak charge requires a precise value of the four-momentum transfer, $Q^2$, as defined

$$Q^2 = 2E^2 \frac{1 - \cos\theta}{1 + \frac{E}{m_p}(1 - \cos\theta)} \tag{4.1}$$

with incident beam energy E and lab scattering angle $\theta$.

The $Q_{weak}$ tracking apparatus operated at 50 pA -100 nA of beam current, with the components inserted into the beam line during tracking runs. The tracking apparatus was designed in order to register hits where individual pulses of electrons passed through the detectors. A software package used to analyze these hits, called the tracking analyzer,

was developed in order to extract kinematic information about the path of the electrons via fitting tracks to the recorded hits.

In this chapter, each section of the tracking apparatus will be touched upon, both the physical description and the purpose. Then the horizontal drift chambers(HDCs) will be discussed in detail, as the HDCs were built and maintained by Virginia Tech. An overview of the tracking analyzer will follow, including the discovery and solution of a problem in the geometry file for the HDCs. The final part of the chapter will discuss the tracking simulations used to extract the final $Q_{\text{weak}}$ $Q^2$.

## 4.1 Apparatus

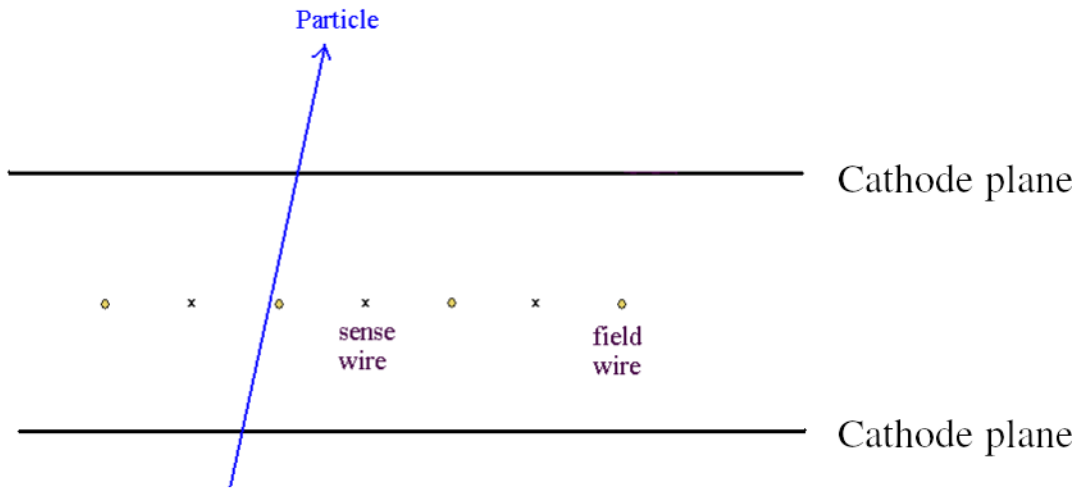


**Figure 4.1:** *This is a diagram of a single drift chamber plane. The plane is sandwiched between cathode planes and is composed of alternating sense(grounded) and field wires suspended in ionizing gas that were used to shape the electric potential. A particle, an electron in the case of $Q_{weak}$, would pass through the gas, generating ions that the electric potential would direct towards the nearest sense wire.*

The $Q_{\text{weak}}$ tracking apparatus can be broken down into four main components. The

horizontal drift chambers(HDCs), the vertical drift chambers(VDCs), the trigger scintillators(TSs), and the scanner. While the scanner was a single unit, the other components were made to be split into two packages placed into opposite octant pairs. The two sets of drift chambers(HDCs and VDCs) were mounted on rotators that allowed them to be shifted into the various octant pairs. The default octant setting was 5-1, but they could be shifted into the other octant pairs as well.

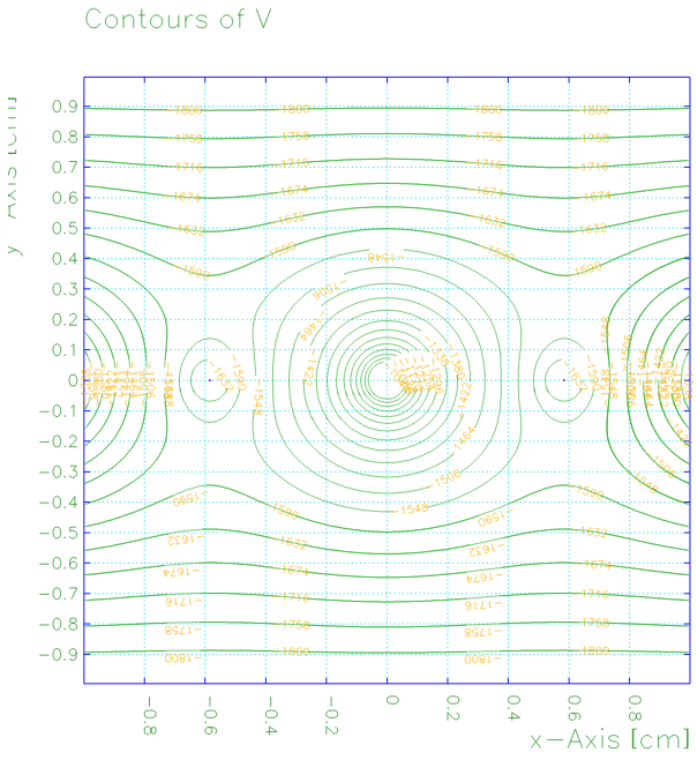


**Figure 4.2:** *Electric potential contours in the HDC drift cell centered on a sense wire. The cathode planes are found at* $y = \pm 0.996$ *cm while field wires are found at* $(\pm 0.585\ cm, 0)$*. Image from the senior thesis of Kevin Finelli [9].*

Two of the four components of the tracking apparatus are wire drift chambers(HDCs and VDCs), which are a type of detector composed of alternating sense and field wires immersed in a gas, with particles passing through. A simplified sketch of the set up is shown in Figure

4.1.

The sense wires are grounded, while the field wires and cathode planes had a voltage applied to set up an electric potential in the vicinity of the sense wires. As an electron passes through the drift chamber, it ionizes the gas. The resulting ionized particles are then drawn to the nearest sense wiring, causing it to fire. The field wires and cathodes are tuned such that the ionized particles pass through a relatively constant drift velocity region. Figure 4.2 shows an example of the electric potential centered around a sense wire in the HDCs. This drift cell was repeated around every sense wire in the HDCs.

To increase the resolution of drift chambers, a relation between the drift time and drift position can be determined. This relation is a property of the gas mixture. By stacking multiple planes with different wire orientations, multiple hits are found which can be used to determine a particle's track.

### 4.1.1 Horizontal Drift Chambers

The primary purpose of the horizontal drift chambers(HDCs) was to identify the scattering vertex and lab scattering angle($\theta$) via determining the scattered electron vector. The $\theta$ was required to determined the four momentum transfer($Q^2$).

The horizontal drift chambers(HDCs) were located between the second and third lead collimators, prior to the scattered electrons entering the toroidal spectrometer. The supporting structure consisted of two arms in opposite octants(180° apart) attached to a rotator

that allowed access to five octants for each arm as shown in Figure 4.3. All eight octants were accessible to at least one of the arms, and two of the octants could be accessed in both a normal and reverse configuration. The HDCs were mounted on a radial track, allowing them to be placed in the beam line during tracking periods and removed from the beamline during primary data-taking. [8]

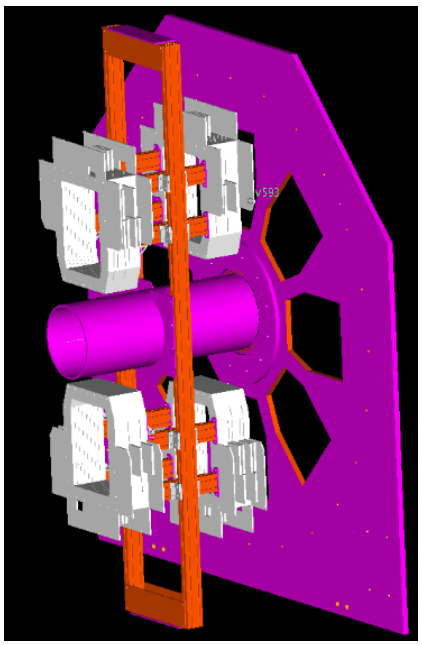

**Figure 4.3:** *Four of the HDCs shown as they were mounted on the HDC rotator apparatus. In the CAD drawing, they cover octants 3 and 7. Figure taken from the dissertation of John Leckey [10].*

Five HDCs were built(shown in Figure 4.4), two were mounted on each arm of the HDC rotator and one was a spare. When the chambers were in the beamline, the center of the upstream(US) HDC was located 3.15 m downstream of the center of the target and the center of the downstream(DS) HDC was located 3.57 m downstream of the center of the target. The DS chamber was 42 cm farther down the beamline than the US chamber. [8]

Each chamber was composed of six wire planes, with the first and fourth planes having the

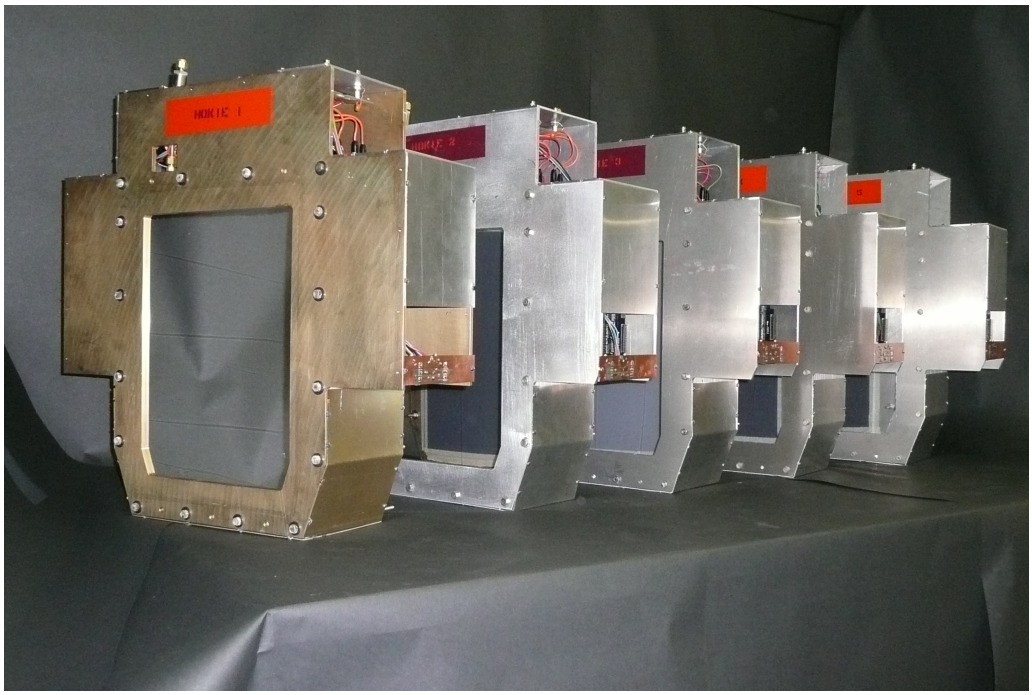

**Figure 4.4:** *The five Horizontal Drift Chambers(HDCs) prior to being installed in the apparatus. Photograph taken by Elizabeth Bonnell [11].*

wires oriented along the X-direction. The second and fifth planes were oriented along what was called the U-direction while the third and sixth were oriented along what was called the V-direction. The U and V oriented planes were at a $\pm 53.1^\circ$ angle to the X oriented planes. The first planes in the given directions were referred to as X, U, and V while the second planes in the given directions were referred to as X', U', and V'. The chambers were intended to be perpendicular to the beam line, with scattered electrons intersecting the planes at an angle of $\sim 83^\circ$. [8]

A mix of 65% argon-35% ethane filled the HDC chambers during Run 2. Aluminized mylar foil cathode planes isolated each wire plane in a chamber from the others. There were 33 field wires made of 75 $\mu$m diameter gold-plated beyllium-copper on each plane, with both

the field wires and cathode planes held at a ∼2150 V. In between the field wires, there were 32 grounded sense wires made of 20 $\mu$m diameter gold-plated tungsten per plane. [8]

### 4.1.2 Vertical Drift Chambers

The primary purpose of the vertical drift chambers(VDCs) was to correctly classify elastically scattered electrons by their scattered momentum. The tracks determined by the VDCs were swum in software through the magnetic field of the toroidal spectrometer and connected with the HDC-determined tracks to do this.

The VDCs were found between the toroidal spectrometer and prior to the main detectors. The supporting structure consisted of two arms in opposite octants(180° apart) attached to a rotator that allowed access to five octants for each arm. All eight octants were accessible to at least one of the arms, and two of the octants could be accessed in both a normal and reverse configuration. The VDCs were mounted on a radial track, allowing them to be placed in the beam line during tracking periods and removed from the beamline during primary data-taking. While the HDCs positioning system was operated manually(both radially and rotationally), the VDCs positioning system was motorized. The rotational motion was done via a Sumitomo Drive Technology motor while the radial motion was done via an electric cylinder. [8]

Five VDCs were built, two were mounted on each arm of the VDC rotator and one was a spare. As the VDCs were located after the toroidal spectrometer bent the electron paths,

the incoming electrons had an average lab angle of 22.5°. GEANT simulation was used to determine that the VDCs performance was best when held at a 24.4° angle to the vertical. Both VDCs on a rotator arm were held at this angle by stainless steel plates. There was a spacing of 53 cm between the US and DS VDC, with the center point between the two 107 cm US of the main detectors. [8]

A photo of two of the VDCs taken while they were installed in the apparatus is found in Figure 4.5.

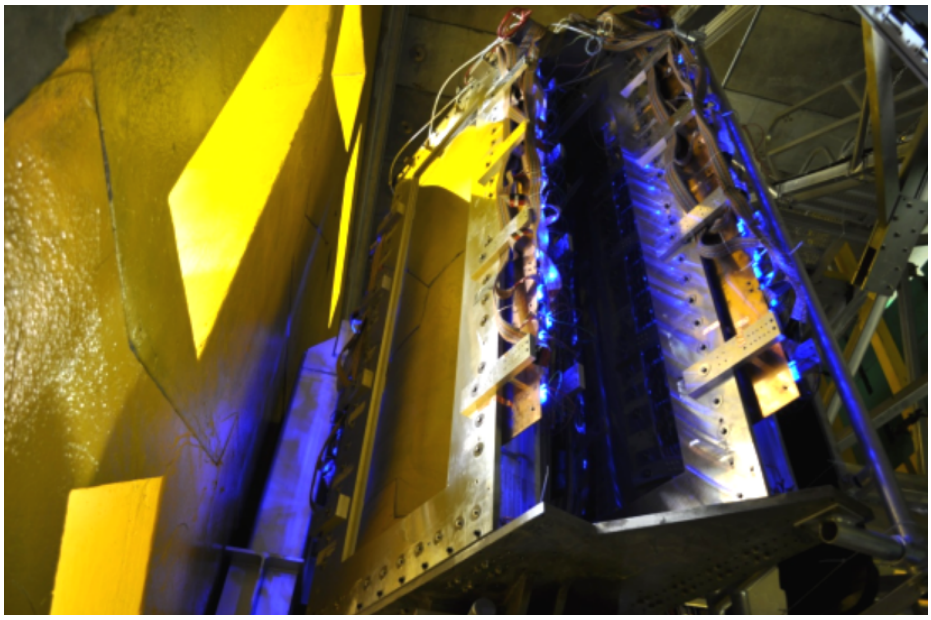

**Figure 4.5:** *A photo of two of the VDCs taken while installed in the $Q_{weak}$ apparatus. Photo taken from the dissertation of John Leckey [10].*

While the HDCs held six wire planes per chamber, the VDCs had two wire planes per chamber. The first wire plane(U) had the wires oriented 26.56° from the long axis of the chamber, while the second wire plane(V) had the wires oriented -26.56° from the same axis. The 279 sense wires that composed each plane were made of 25 $\mu$m diameter gold-plated

tungsten. The anode planes were grounded and sandwiched between high voltage cathode planes(∼3800 V) located ±12.7 mm around the anode planes. [8]

The outside cathode planes were made of 12.7 $\mu$m thick Mylar foils and were aluminized on the inside faces. The inside cathode plane was made of the same Mylar foils, but both sides were aluminized. The VDC chambers were filled with a gas mixture of 50% argon and 50% ehtane. [8]

### 4.1.3 Trigger Scintillators

The necessary trigger for this system was provided by a pair of trigger scintillators. These trigger scintillators were used to act as a fast timing trigger with the electronics, and were also necessary to the neutral background studies performed by the tracking system.

Two scintillators made of Bicron BC-409 plastic were placed on the VDC rotator such that the electrons would pass through the scintillators immediately after passing through the VDCs. These scintillators were connected to light guides that transmitted the signal generated by an electron passing through to a photo multiplier tube, which then passed the signal along to a CAEN N842 discriminator. This served as the trigger for the tracking system data acquisition.

### 4.1.4 Scanner

The focal plane scanner could operate at both 180 $\mu$A(current mode) and 50 pA(tracking mode), allowing comparison between the extremes of beam energy used in $Q_{weak}$. It consisted of two 1 $cm^3$ quartz cubes with a 1 x 1 $cm^2$ overlap. A coincidence between the two quartz cubes was required to reduce accidental triggers caused by background sources. [8]

The scanner was located by the Octant 7 main detector. A linear motion system moved the scanner in two dimensions, covering the main detector's active region. This allowed the beam profile on Octant 7 at both high and low energies to be compared. [8]

## 4.2 Tracking Analyzer

The kinematics for scattered electrons in $Q_{weak}$'s apparatus were determined using software referred to as the tracking analyzer. Three components were needed to determine the electron kinematics:the partial track through the horizontal drift chambers(HDCs) prior to entering the toroidal spectrometer, the magnetic field of the toroidal spectrometer, and the partial track through the vertical drift chambers(VDCs) after exiting the toroidal spectrometer. All three of these were necessary to fully reconstruct the scattered particle trajectory(track) and determine its kinematics.

### 4.2.1 Track Reconstruction

When an electron passed through a plane of the HDCs, the gas contained within would ionize. The ionized particles would be pulled via the tuned electric potential of the plane into a sense wire which would then fire. A relation between the drift time and drift distance, characteristic of the ionizing gas, allowed more precise understanding of where the particle passed in the chamber than the distance between the wires. Each chamber had the planes in a XUVX'U'V' arrangement and there were two chambers in a single electron's path. If the electron triggered a hit on each plane, there were twelve hits with which to construct a straight line partial track trhough the HDCs. This partial track provided a measurement of the scattering angle of the particle.

The electron did not have to trigger every plane for a partial track to be generated. A minimum of nine hits was necessary. The analyzer grouped each set of planes with the same wire directions(X, U, and V) to form what the analyzer referred to as treelines. There were four possible hits per treeline(XX'XX') and a minimum requirement of three hits for the analyzer to proceed. Each of the three treelines(X, U, V) defined a plane orientated along the wire direction that the electron moved in. The analyzer then combined these planes to define the straight-line HDC partial track.

The magnetic field of the toroidal spectrometer was mapped out as discussed in the Master's thesis and dissertation of Peiqing Wang [52] [59]. The magnitude of the field could be adjusted for various studies and input into the analyzer.

The VDCs act similarly to the HDCs in identifying tracks. An electron passes through the ionizing gas resulting in the ionized particles to be pulled to sense wires due to the electric potential in the chamber. Unlike the HDCs where only one wire hit is kept per wire plane, the VDCs use multiple wire hits. A drift time to drift distance relation is used to determine the location of the hits within the wire plane. [10]

A single electron will pass through two VDCs, composed of 2 wire planes apiece. The first wire planes in a VDC has wire direction U and the second has wire direction V. The wire planes are grouped by direction, so the two U planes are paired to determine a treeline in the U direction and the V planes are paired to determine a treeline in the V direction. These treelines are then combined to generate a straight-line VDC partial track. [10]

With all three components(HDC partial track, magnetic field, VDC partial track), the analyzer could project an electron along the HDC partial track through the magnetic field into the VDCs region. If the projected track matched the VDC partial track within error, the analyzer would save the track and all related information. This would include the $Q^2$, the scattering angle($\theta$), the hit information, the treeline information, and the partial track information.

### 4.2.2 Problem with Geometry

During the analysis of the horizontal drift chamber(HDC) data, it was deemed necessary to check on the internal and external geometry of the HDCs. The internal geometry refers to

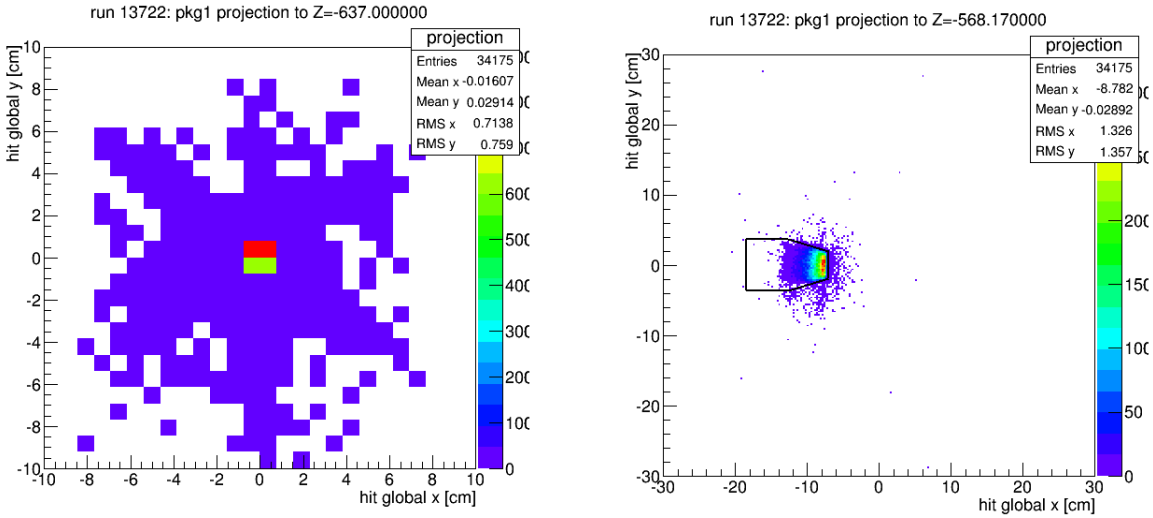


**(a)** *Pointing run projected to the downstream 4% radiation length aluminum dummy target.*

**(b)** *Pointing run projected to the first collimator.*

**Figure 4.6:** *These projections show the hit distribution for a pointing run example at two locations along the beamline.*

the relative positioning and orientation of the two drift chambers on the same side of the beamline, while the external geometry referes to the positioning of the package of the two drift chambers relative to the rest of the $Q_{weak}$ apparatus. This required using a data set referred to as pointing runs. This data set was taken during tracking periods at low current and was taken using the downstream 4% radiation length aluminum dummy target($\sim$ 0.36 cm [54]). The use of the dummy target was to limit the origin of the observed tracks to a specific position along the beamline instead of the 35 cm length of the $LH_2$ target. To further limit the origin of the observed tracks to a specific position in space, the raster was reduced to 1 x 1 $cm^2$ for the pointing runs.

The tracks recorded by the pointing runs could be projected along the beamline(Z-axis) and used to see the hit distribution at various positions. Two examples are shown in Figure

4.6, where (a) shows the tracks projected to the downstream 4% radiation length aluminum dummy target(the scattering vertex for these tracks) and (b) shows the tracks projected to the first collimator.

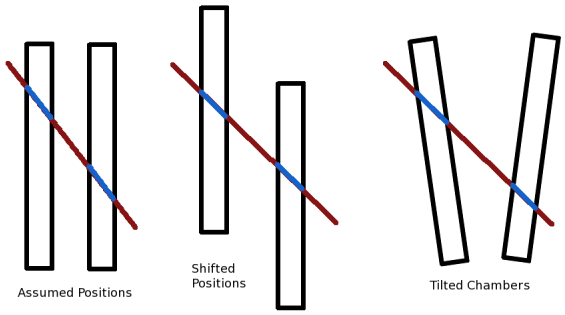


**(a)** *Diagrams showing some of the possible deviations from the assumed positions for the HDCs.*

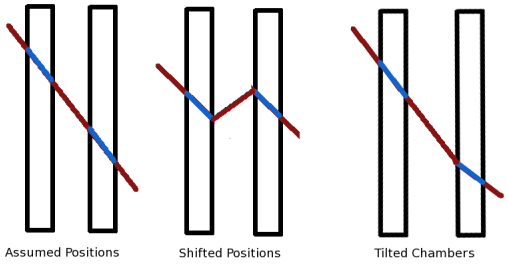


**(b)** *Diagrams showing how the possible deviations from the assumed positions could affect track projection through the HDCs.*

**Figure 4.7:** *Diagrams outlining the possible geometry issues and effects of these issues between the two HDC chambers. These diagrams are not to scale.*

One major use of the pointing runs was as a check on the external geometry of the HDCs. By looking at a pointing run, the location of the HDCs after being inserted into the beam line could be assessed. This allowed confirmation of the reproducibility of the HDC locations.

The pointing runs were also used to check on the internal geometry of the HDCs. By adjusting a private version of the tracking analyzer so that it did not require three hits per

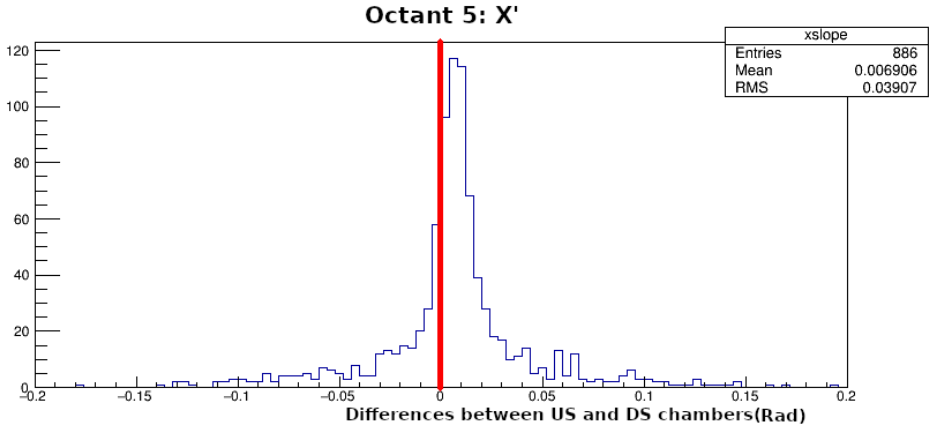


**(a)** *The differences between X' seen by the upstream(US) and downstream(DS) HDCs for a single pointing run.*

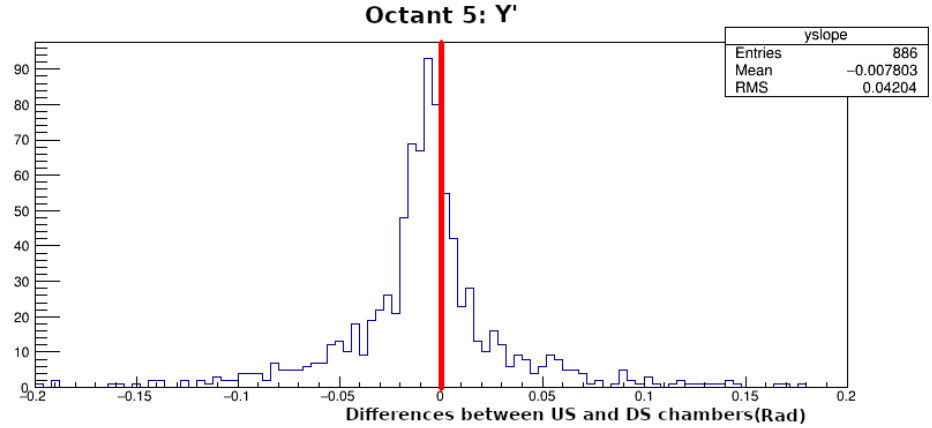


**(b)** *The differences between Y' seen by the upstream(US) and downstream(DS) HDCs for a single pointing run.*

**Figure 4.8:** *A representative pointing run was used to show the differences observed between the angles seen by the US and DS HDC chambers. The results are shown for Octant 5, but similar results were seen in the horizontal and vertical octants. The red line in both plots indicates the location of $\Delta X' = 0$, where the two chambers would see the same slope.*

wire direction, HDC partial tracks defined by a single chamber could be analyzed. During this study, it was discovered that the HDC partial track scattering angles disagreed between the US and DS chambers by 7 mrad.

It was concluded that while the analyzer assumed ideal positions(perpendicular to beam

line), it was possible that the physical geometry of the HDCs did not match the ideal. Two possibilities were presented: that the HDCs were shifted in position or that they were tilted in relation to each other. These possibilities are illustrated in Figure 4.7(a) with the effects on tracks shown in Figure 4.7(b). The observed difference between scattering angle seen in the individual chamber HDC partial tracks, as shown in Figure 4.8, confirmed that a tilt was present between the two chambers and needed to be corrected.

### 4.2.3 Correcting the HDC Geometry

Since the data showed a relative tilt was present between the HDC chambers, it was clear that there was an issue with the internal geometry. There was also an issue with the external geometry shown by pointing runs taken in different octants projecting to different points at the downstream 4% radiation length aluminum dummy target. A three-step method was developed to correct both the internal and external HDC geometry. The first step was to correct the relative tilt between the two HDC chambers via rotating the downstream chamber to match the upstream chamber. The second step was to correct any radial and tangential shifts between the upstream(US) and downstream(DS) chambers. The final step was to correct the overall orientation(involving both rotation and shifts) of the set of two HDCs.

The mean values shown in Figure 4.8 provided the approximate rotations necessary to match the DS chamber with the US chamber. These were implemented via the analyzer, and

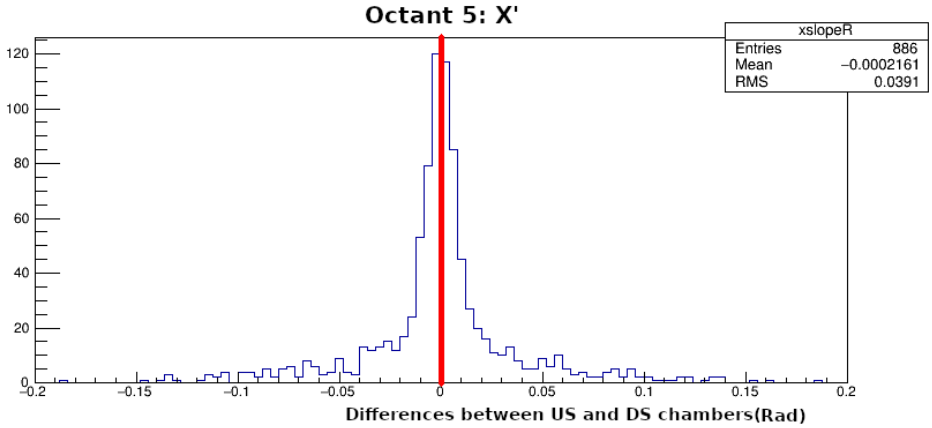


**(a)** *The differences between X' seen by the upstream(US) and downstream(DS) HDCs for a single pointing run.*

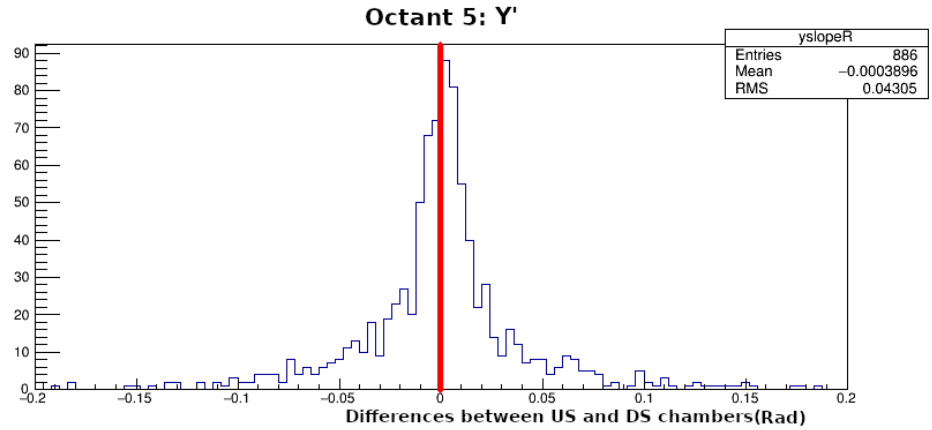


**(b)** *The differences between Y' seen by the upstream(US) and downstream(DS) HDCs for a single pointing run.*

**Figure 4.9:** *A representative pointing run was used to show the differences observed between the angles seen by the US and DS HDC chambers after the DS chamber was rotated to match the US chamber. The results are shown for Octant 5, but similar results were seen in the horizontal and vertical octants. The red line in both plots indicates the location of $\Delta X' = 0$, where the two chambers would see the same slope.*

the resulting differences between US and DS slopes is shown in Figure 4.9. The improvement in the agreement between the US and DS chambers is obvious. This was checked for the vertical(3 and 7) and horizontal octants(5 and 1), as shown in Figure 4.10.

After the US and DS HDC chambers were parallel, it was necessary to align the two

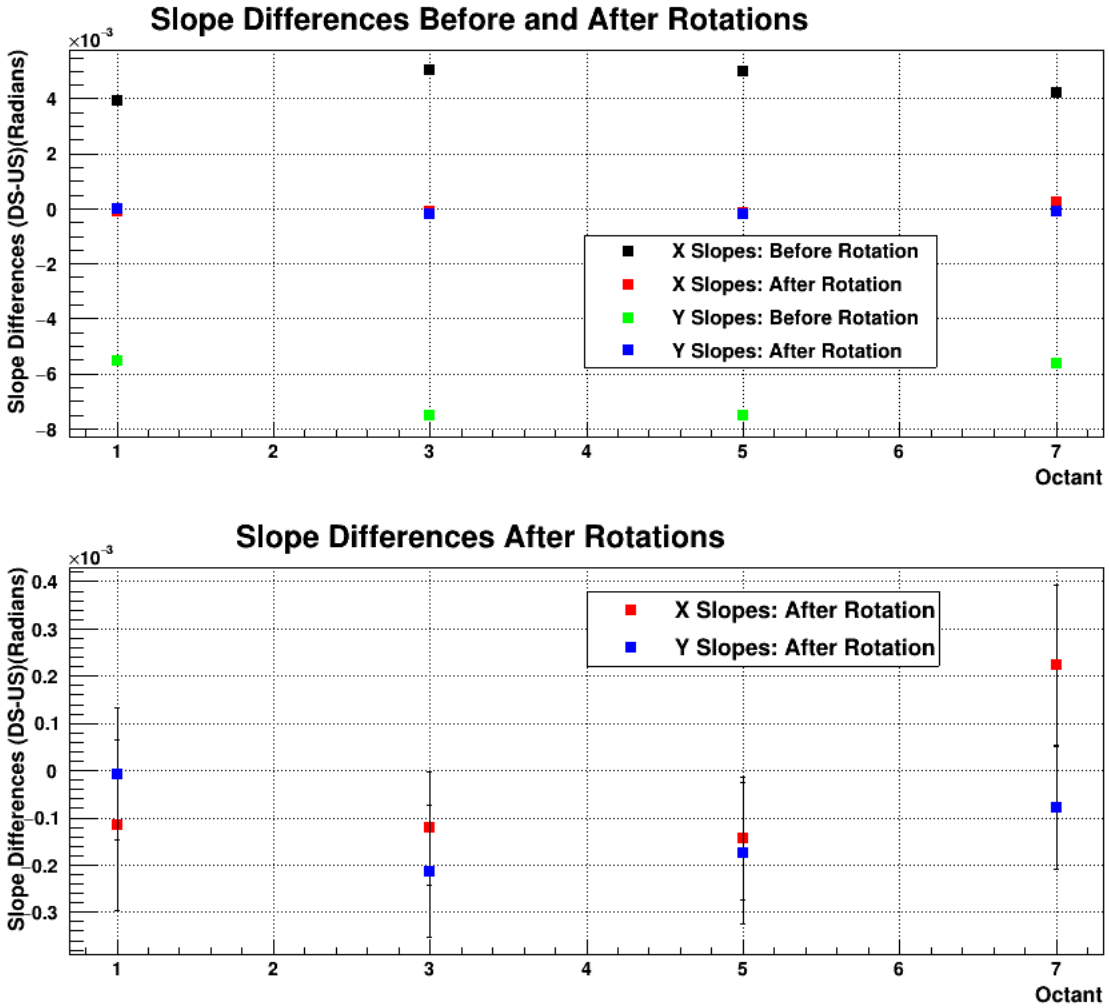


**Figure 4.10:** *The top plot shows the vertical and horizontal octants before and after rotating the DS chamber to match with the US chamber. The bottom plot shows only the after rotation values. The agreement between the US and DS chamber was clearly improved by the rotation.*

chambers. In this context, aligning refers to shifting the chambers in the radial and tangential directions so that a particle track passing through both matches up while holding the relative angles between the two chambers constant. A gradient search pattern was used to minimize the residual between the recorded hit on a plane($x_{\text{hit}}$) and the point where the determined track passed through the same plane($x_{\text{track}}$). The $\chi^2$ of a track was proportional to the sum

of the residuals as

$$\chi^2 \propto \left(x_{\text{track}} - x_{\text{hit}}\right)^2 . \tag{4.2}$$

The gradient search method worked by taking the base rootfile and applying two test shifts($\Delta x$ and $\Delta y$), one in the X direction and one in the Y direction. The $\chi^2$ would be extracted for both test rootfiles $\left(\chi^2_x \text{ and } \chi^2_y\right)$ and the base rootfile($\chi^2_0$). A pair of gradients,

$$\frac{\Delta\chi^2}{\Delta x} = \frac{\chi^2_0 - \chi^2_x}{\Delta x} \qquad \text{and} \qquad \frac{\Delta\chi^2}{\Delta y} = \frac{\chi^2_0 - \chi^2_y}{\Delta y}, \tag{4.3}$$

were extracted from the three rootfiles. A step of 0.05 cm was applied in the direction of the larger gradient and a step of 0.05 cm times the ratio of the two gradients applied in the direction of the smaller gradient. The resulting rootfile became the new base rootfile and the process was repeated until the gradients were sufficiently close to zero.

The last step to obtain the final geometry for the HDCs was to check the alignment of the system of both HDCs relative to well-surveyed fixed points in the apparatus. The two fixed points used were the downstream 4% radiation length target(position known to less than one mm [8]) and the first collimator. Using the corrected internal geometry for the HDCs, the tracks were projected both to the Z position of the 4% downstream aluminum target(Figure 4.6(a))($Z_{\text{al}}$) and the first collimator(Figure 4.6(b))($Z_{\text{c1}}$). From these the radial($R_{\text{al}}$ and $R_{\text{c1}}$) and tangential($T_{\text{al}}$ and $T_{\text{c1}}$) coordinates of the centers could be extracted. The extracted

coordinates were then written out in terms of the radial slope($R'$) and offset($R_{\rm off}$),

$$R_{\rm al} = R' \times Z_{\rm al} + R_{\rm off} \qquad \text{and} \qquad R_{\rm c1} = R' \times Z_{\rm c1} + R_{\rm off}, \tag{4.4}$$

as well as the tangential slope($T'$) and offset($T_{\rm off}$).

$$T_{\rm al} = T' \times Z_{\rm al} + T_{\rm off} \qquad \text{and} \qquad T_{\rm c1} = T' \times Z_{\rm c1} + T_{\rm off}. \tag{4.5}$$

To determine the rotation and shift values for the system of HDCs, it is necessary to look at an idealized track as two equations, one defining the radial motion and one defining the tangential motion of a particle in the track, parameterized by the Z position of the particle. In the ideal situation, the tracks would pass through the origin at the downstream 4% radiation length aluminum dummy target, leading to $R_{\rm al,ideal} = T_{\rm al,ideal} = 0$. At the first collimator the tangential coordinate would still be zero($T_{\rm c1,ideal} = 0$), but the radial coordinate would be the average value of the projections to the collimator ($R_{\rm c1,ideal} = R_{\rm c1,avg}$). The ideal coordinates can be written out in terms of the ideal radial slope($R'_{\rm ideal} = R' + R_{\rm rot}$) and offset($R_{\rm off,ideal} = R_{\rm off} + R_{\rm shift}$),

$$R_{\rm al,ideal} = 0 = R'_{\rm ideal} \times Z_{\rm al} + R_{\rm off,ideal} \qquad \text{and} \qquad R_{\rm c1,ideal} = R_{\rm c1,avg} = R'_{\rm ideal} \times Z_{\rm c1} + R_{\rm off,ideal}, \tag{4.6}$$

where $R_{\rm rot}$ and $R_{\rm shift}$ are the rotation and shift values necessary to obtain the corrected geometry. The ideal tangential coordinates can be written in terms of the ideal tangential

slope($T'_{\text{ideal}} = T' + T_{\text{rot}}$) and offset($T_{\text{off,ideal}} = T_{\text{off}} + T_{\text{shift}}$),

$$T_{\text{al,ideal}} = 0 = T'_{\text{ideal}} \times Z_{\text{al}} + T_{\text{off,ideal}} \quad \text{and} \quad T_{\text{c1,ideal}} = 0 = T'_{\text{ideal}} \times Z_{\text{c1}} + T_{\text{off,ideal}}, \tag{4.7}$$

where $T_{\text{rot}}$ and $T_{\text{shift}}$ are the rotation and shift values necessary to obtain the corrected geometry.

One more value needs definition before determining the rotation and shift values. That is $Z_{\text{rot}}$, the Z position of the center point between the two HDC chambers. It is the point that the HDC chambers will be rotated around.

The next step is to determine the rotation value for both radial and tangential directions. The tangential direction is simpler as both ideal tangential points are zero. The ideal tangential values, Equation (4.7), are subtracted from the relevant actual tangential values, Equation (4.5):

$$\begin{gathered} T_{\text{al}} - T_{\text{al,ideal}} = T_{\text{al}} = -T_{\text{rot}} \times Z_{\text{al}} - T_{\text{shift}} \\ \text{and} \\ T_{\text{c1}} - T_{\text{c1,ideal}} = T_{\text{c1}} = -T_{\text{rot}} \times Z_{\text{c1}} - T_{\text{shift}}. \end{gathered} \tag{4.8}$$

Then $T_{\text{c1}}$ is subtracted from $T_{\text{al}}$ to isolate $T_{\text{rot}}$:

$$T_{\text{rot}} = -\left(\frac{T_{\text{al}} - T_{\text{c1}}}{Z_{\text{al}} - Z_{\text{c1}}}\right). \tag{4.9}$$

The radial rotation value, $R_{\text{R}}$, is determined via the same method. First the ideal positions

are subtracted from the actual positions:

$$\begin{gathered} R_{\mathrm{al}} = -R_{\mathrm{rot}} \times Z_{\mathrm{al}} - R_{\mathrm{shift}} \\ \text{and} \\ R_{\mathrm{c1}} = -R_{\mathrm{rot}} \times Z_{\mathrm{c1}} - R_{\mathrm{shift}} + R_{\mathrm{c1,avg}}. \end{gathered} \tag{4.10}$$

Unlike in the tangential direction, the ideal position at the first collimator in the radial direction does not equal zero. This introduces an extra component to $R_{\mathrm{rot}}$ when it is isolated by subtracting $R_{\mathrm{c1}}$ from $R_{\mathrm{al}}$:

$$R_{\mathrm{rot}} = -\left(\frac{R_{\mathrm{al}} - R_{\mathrm{c1}} + R_{\mathrm{c1,avg}}}{Z_{\mathrm{al}} - Z_{\mathrm{c1}}}\right). \tag{4.11}$$

Now that the rotaion values have been defined, the shift values need to be determined. This can be done by looking at Equations (4.8) and (4.10). The Z position needs corrected for rotating around the defined rotation point at $Z_{\mathrm{rot}}$, so $Z_{\mathrm{al}} \rightarrow (Z_{\mathrm{rot}} - Z_{\mathrm{al}})$ in the equations. That leads to the shift values for the tangential and radial directions of

$$\begin{gathered} T_{\mathrm{shift}} = -T_{\mathrm{rot}} \times (Z_{\mathrm{rot}} - Z_{\mathrm{al}}) - R_{\mathrm{al}} \\ \text{and} \\ R_{\mathrm{shift}} = -R_{\mathrm{rot}} \times (Z_{\mathrm{rot}} - Z_{\mathrm{al}}) - R_{\mathrm{al}}. \end{gathered} \tag{4.12}$$

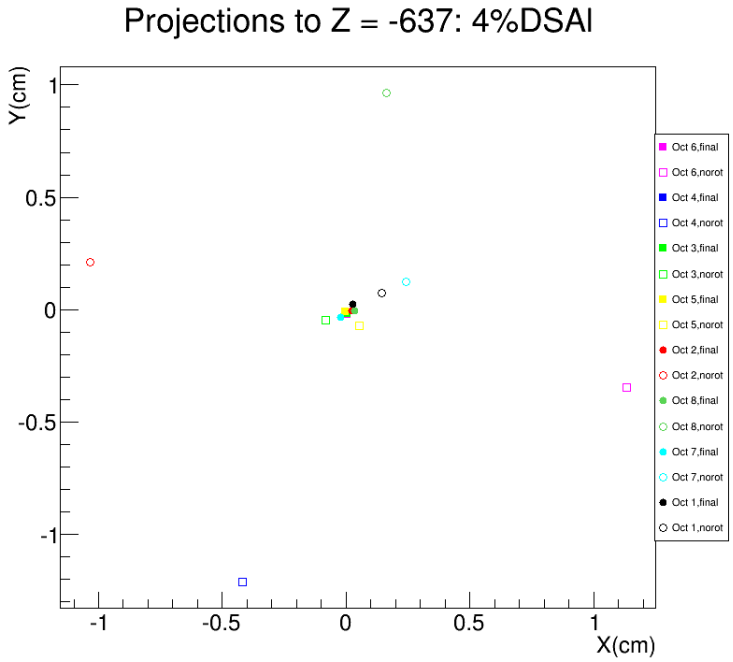


**(a)** *The centroids of projections of pointing runs to the downstream 4% radiation length aluminum dummy target are shown here.*

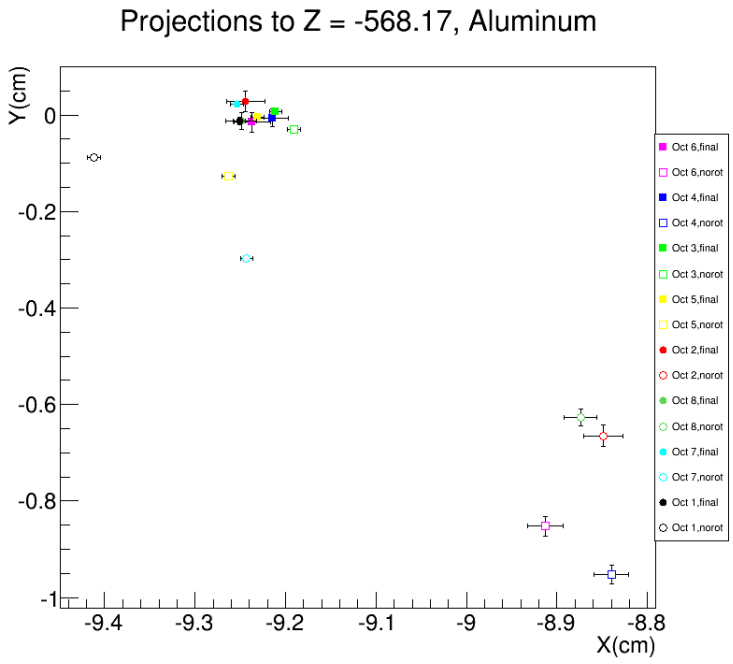


**(b)** *The centroids of projections of pointing runs to the first collimator are shown here.*

**Figure 4.11:** *The centroids of projections of pointing runs both prior to and after implementing the correction to the HDC geometry are shown for all eight octants. The open symbols represent the data prior to the geometry correction while the closed symbols represent the data after the geometry correction. The improvement in agreement between octants is clear after the correction.*

The final rotation and shift values were implemented and, as shown in Figure 4.11, significant improvement was seen in all octants. Figure 4.11(a) shows the centroids of the projections to the downstream 4% radiation length aluminum dummy target both prior(open symbols) and after(solid symbols) the correction was implemented. Figure 4.11(b) shows the same for the projections to the first collimator. It is clear in both figures that all octants are in far better agreement after the correction was implemented.

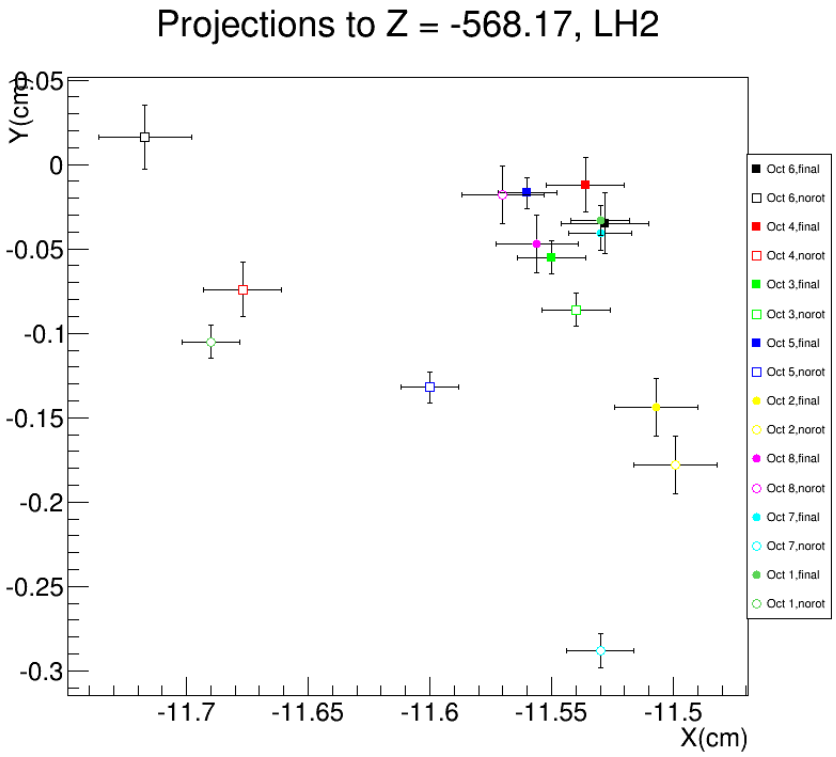


**Figure 4.12:** *The centroids of projections to the downstream window of the $LH_2$ target runs both prior to and after implementing the correction to the HDC geometry are shown for all eight octants. The open symbols represent the data prior to the geometry correction while the closed symbols represent the data after the geometry correction. The improvement in agreement between octants is clear after the correction.*

While the improvement for the pointing runs was obvious, it was necessary to check how implementing the geometry corrections affected the $LH_2$ data. Figure 4.12 shows the

same type of data as Figure 4.11 for $LH_2$ projections to the first collimator. Again, the improvement after the correction was implemented is clear.

## 4.3 Tracking Simulation

The tracking simulation was used determine the final kinematic values for the $Q_{weak}$ Experiment. The simulation was done by Valerie Gray [60] using the C++ libraries of GEANT4 [61], and included detailed geometry of many detectors(main detectors, HDCs, VDCs), a realistic magnetic field for the toroidal spectrometer, idealized collimators, targets($LH_2$, the various aluminum dummy targets,etc), the beamline, and the various shielding and supporting structures [60]. The dissertation of Valerie Gray [60] discusses details of the simulations.

## 4.4 Tracking Data vs. Simulation

As was stated previously, the simulation was used to extract the final kinematics for $Q_{weak}$ while the tracking data was used to benchmark the simulation. One of the primary reasons for this was that the measured kinematics, referred to as the visible kinematics($Q^2_{\text{visible}}$ and $\theta_{\text{visible}}$), can be extracted from the tracking data but those values are not the true kinematics of the interaction. The true kinematics of the interaction, $Q^2_{\text{vertex}}$ and $\theta_{\text{vertex}}$, occur at the scattering vertex, where the electron and proton interact.

It was not possible in $Q_{weak}$ to measure the vertex kinematics directly because of energy

loss and bremsstrahlung as the scattered electron travelled to the main detector. Instead simulation was used to extract both visible and vertex kinematics. The visible kinematics extracted by the tracking system were compared to the visible kinematics produced by the simulation. When the kinematics matched sufficiently in shape, the vertex kinematics of the simulation were used as the final kinematics for $Q_{weak}$.

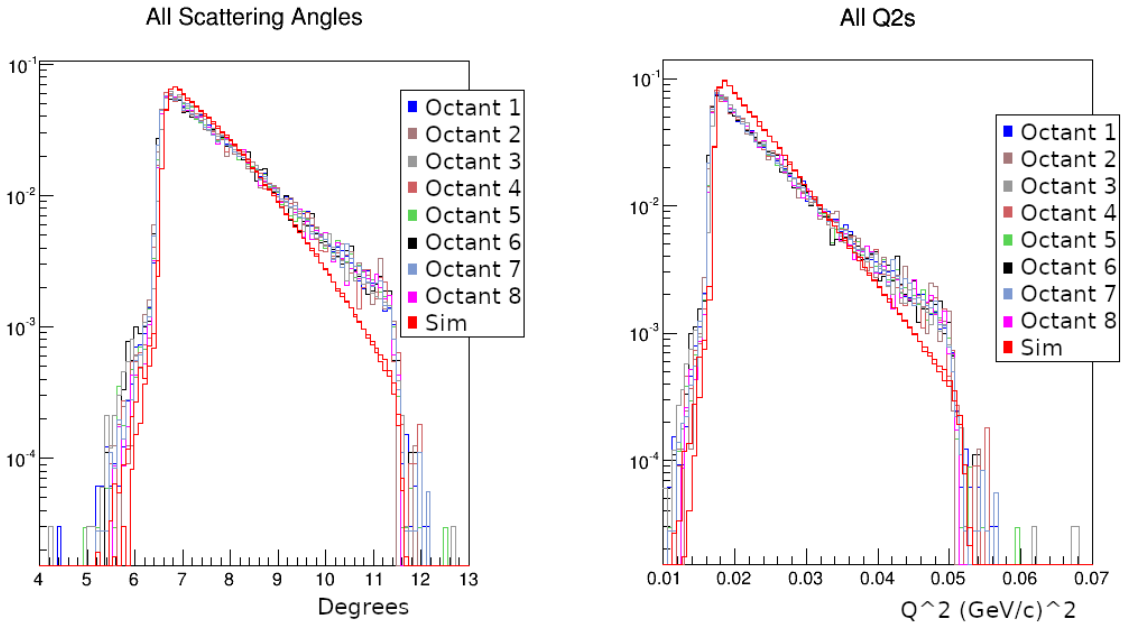


**(a)** *Comparison of scattering angle($\theta$) between simulation and data.*

**(b)** *Comparison of 4-momentum transfer($Q^2$) between simulation and data.*

**Figure 4.13:** *The comparison between simulated visible kinematics and measured kinematics in the downstream 4% radiation length aluminum dummy target revealed a problem with the aluminum simulation.*

An example of how benchmarking the simulation with the data identified problems with the simulation is shown in Figure 4.13. The simulation of the visible kinematics of the downstream 4% radiation length aluminum dummy target was compared with the measured kinematics, and the shapes were clearly different.

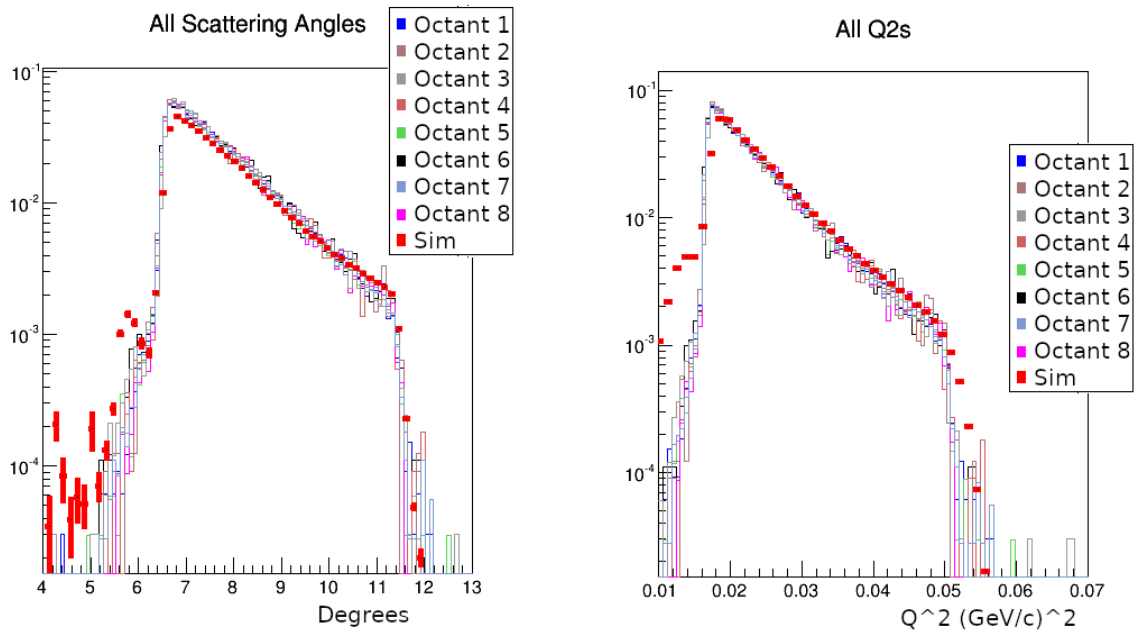


**(a)** *Comparison of scattering angle($\theta$) between simulation and data.*

**(b)** *Comparison of 4-momentum transfer($Q^2$) between simulation and data.*

**Figure 4.14:** *The comparison between simulated visible kinematics and measured kinematics in the downstream 4% radiation length aluminum dummy target after the other processes had been added to the simulation.*

This discrepancy was investigated and the simulation was found to be solely elastic aluminum. Further simulations were performed of the various other processes that would contribute to the aluminum signal: quasi-elastic, inelastic, etc. When these simulations were added to the elastic aluminum, the agreement was greatly improved though the higher angles as shown in Figure 4.14. Further improvement may be possible with more work on the pointing runs. [62]

Unlike the aluminum, the $LH_2$ data showed good agreement in the shape of the visible $Q^2$ and $\theta$ values as shown in Figure 4.15. This allowed the extraction of the vertex kinematics

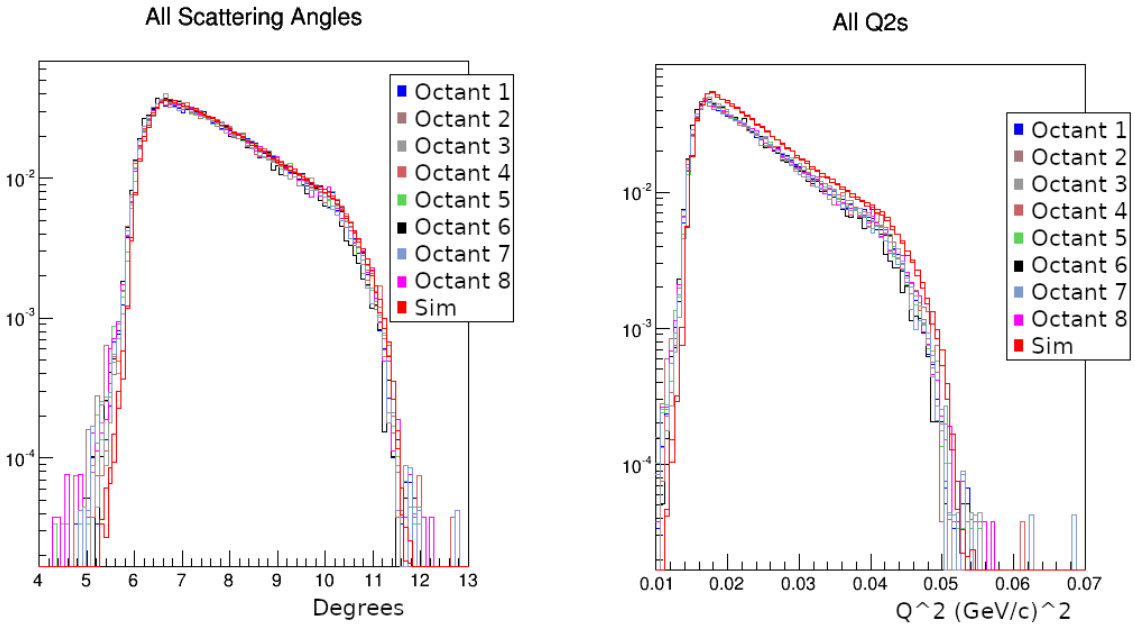


**(a)** *Comparison of scattering angle($\theta$) between simulation and data.*

**(b)** *Comparison of 4-momentum transfer($Q^2$) between simulation and data.*

**Figure 4.15:** *The comparison between simulated visible kinematics and measured kinematics in the liquid hydrogen target showed good agreement in the shape allowing the extraction of the vertex kinematics.*

from the simulation. The final extracted kinematics for the $Q_{weak}$ Experiment are

$$\langle Q^2 \rangle = 0.0248\,(\mathrm{GeV}/c)^2$$

and (4.13)

$$\langle \theta \rangle = 7.90^{\circ}.$$

# Chapter 5

# $Q_{weak}$ Experiment: Main Result

The $Q_{weak}$ Collaboration consisted of 101 people over 27 institutions, of which 26 were graduate students and 11 were postdoctoral scholars. This chapter will cover the analyses performed by the collaborators in order to extract a final elastic electron-proton parity-violating asymmetry, which has been published in Nature [17]. The author's personal contributions are summarized in Appendix A.

To determine a final result, the raw asymmetry($A_{raw}$) must be extracted from the data. This asymmetry is then corrected for false asymmetries to determine a measured asymmetry($A_M$), which is then corrected for the polarization, backgrounds, and multiplicative corrections to extract a final elastic asymmetry($A_{ep}$). The implications of the elastic asymmetry are then examined.

## 5.1 Extracting the Raw Elastic Asymmetry

The raw elastic asymmetry is determined via combining the integrated yields in each PMT of the MD for both helicity states (+ and −),

$$A^i_{\text{tube}} = \frac{Y^{+,i}_{\text{MD}} - Y^{-,i}_{\text{MD}}}{Y^{+,i}_{\text{MD}} + Y^{-,i}_{\text{MD}}}. \tag{5.1}$$

Then the 16 PMTs need to be combined in order to extract the raw elastic asymmetry, via averaging the PMTs,

$$A_{\text{raw}} = \frac{\sum_{i=1}^{16} A^i_{\text{tube}}}{16}. \tag{5.2}$$

The individual PMT values are determined by running the data through the $Q_{weak}$ analyzer.

The $Q_{weak}$ analyzer went through multiple revisions over the years. The goal of the collaboration was to define a consistent dataset, as well as improving the analysis of the data as the code evolved. The revisions of the analyzer that were used to analyze the full dataset at a given time were named with their pass number. Each pass was associated with changes to the analyzer that had the possibility of affecting the final result which have been documented [58]. There were also smaller corrections to the analyzer that were denoted with a letter added to the pass number. These changes were focused on correcting errors in the detector and parameter definitions. The final analysis was performed with pass5c+, the plus signifying the addition of some beam modulation data [50] [63] .

The final $Q_{weak}$ elastic asymmetry is drawn from the two main running periods, referred

to as run 1 and run 2. In an ideal world, there would have been no changes to the apparatus between the two running periods but that was not the case. As such, the two sets of data have to be treated separately for the corrections. The results of both periods will then be combined at the end. The raw asymmetries for the two running periods are

$$\begin{gathered} \text{run 1: } A_{\text{raw}} = -192.7 \pm 13.2 \text{ (stat) ppb} \\ \text{and} \\ \text{run 2: } A_{\text{raw}} = -170.7 \pm 7.3 \text{ (stat) ppb.} \end{gathered} \tag{5.3}$$

The apparent significant difference between the two run periods is due to corrections(including a different blinding factor for each period) that were not the same during the two running periods.

## 5.2 Extracting the Measured Asymmetry

The $Q_{weak}$ apparatus was designed to minimize false asymmetries, but it was not possible to completely eliminate them. Instead these false asymmetries need to be measured and taken into account. The raw asymmetry($A_{\text{raw}}$) seen by the apparatus is actually the value after the false asymmetries($A_{\text{false}}$) have affected the measured asymmetry($A_{\text{M}}$),

$$A_{\text{raw}} = A_{\text{M}} - A_{\text{false}}, \tag{5.4}$$

which can be expanded to include the individual false asymmetries: the beam current monitor correct($A_{\mathrm{BCM}}$), the helicity-correlated beam motion correction($A_{\mathrm{beam}}$), the beamline background correction($A_{\mathrm{BB}}$), the linearity correction($A_{\mathrm{L}}$), the transverse leakage correction($A_{\mathrm{T}}$), the rescattering bias correction($A_{\mathrm{bias}}$), and the blinding factor($A_{\mathrm{blinding}}$). Written out explicitly, the measured asymmetry becomes

$$A_{\mathrm{M}} = A_{\mathrm{raw}} + A_{\mathrm{BCM}} + A_{\mathrm{beam}} + A_{\mathrm{BB}} + A_{\mathrm{L}} + A_{\mathrm{T}} + A_{\mathrm{bias}} - A_{\mathrm{blinding}}. \tag{5.5}$$

This section will expand on each correction and determine a value. At the end a final value for $A_{\mathrm{M}}$ will be extracted.

### 5.2.1 Beam Current Monitor Correction

Beam Current Monitors(BCMs), as discussed in Section 3.2.3, were used to noninvasively measure the charge. The correction $A_{\mathrm{BCM}}$ is defined to be zero due to the normalization of the main detector signals to the charge normalization with the error on it coming from the BCM resolution, where the resolution is the random noise in the charge measurement process. The BCM resolution is determined by the differences between a pair of BCMs in similar positions.

During the run 1 running period, there were two BCM pairs active. The first pair(bcm1 and bcm2) were averaged and the result was defined as the charge, which was the initial value used to normalize the main detectors. The other pair were bcm5 and bcm6. Using the

charge led to a 30% residual charge correlation in the normalized main detector asymmetries that defied explanation, and the decision was made to renormalize using the average of bcm5 and bcm6. This removed the unexplained correlation and also improved the $\chi^2$ for null asymmetries. [64]

The run 2 running period had 3 pairs of BCMs active, but only five of the BCMs were included in the analysis. The active BCMs were bcm1, bcm2, bcm5, bcm6, bcm7, and bcm8. The analysis did not include bcm7. For run 2, charge was defined as bcm8 and was used for the initial normalization of the main detectors. The final normalization of the detector signal was determined via a combination of bmc5, bcm6, and bcm8(charge). [64]

The raw physics asymmetries with different BCM normalizations are shown in Figure 5.1.

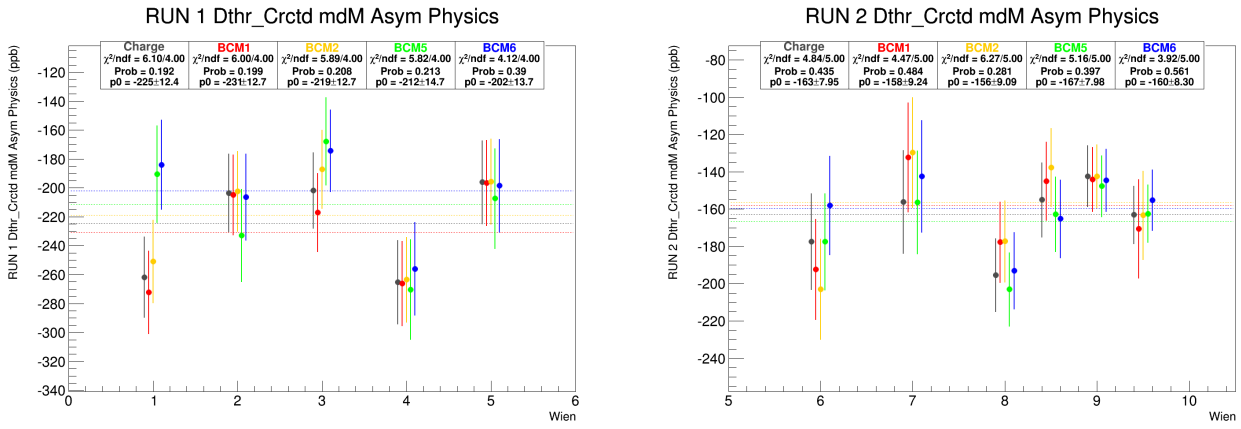


**Figure 5.1:** *The above plots show raw physics asymmetries for the two running periods with different BCM normalizations. The right plot(run 1) has the normalization for the average of bcm1 and bcm2 represented by charge(black), bcm1(red), bcm2(yellow), bcm5(green), and bcm6(blue). The final normalization involved the average of bcm5 and bcm6. The left plot(run 2) has the normalization for bcm8 represented by charge(black), bcm1(red), bcm2(yellow), bcm5(green), and bcm6(blue). The final normalization involved the combination of bcm5, bcm6, and bcm8. Plots produced by Peng Zang [12].*

Using the average of bcm1 and bcm2 for run 1 and the combination of bcm5, bcm6, and

bcm8 for run 2, the final BCM normalization corrections were determined to be

$$\begin{gathered} \text{run 1: } A_{\text{BCM}} = 0 \pm 4.4 \text{ ppb} \\ \text{and} \\ \text{run 2: } A_{\text{BCM}} = 0 \pm 2.1 \text{ ppb.} \end{gathered} \tag{5.6}$$

As stated previously, the actual correction is zero by definition and the error is determined by the variation found in the BCMs charge asymmetries used in the two analyses.

### 5.2.2 Helicity-Correlated Beam Motion Correction

There were five beam properties that were helicity correlated and therefore generated false asymmetries in the signal. These five beam parameters were X(beam x position), Y(beam y position), X'(beam x angle), Y'(beam y angle), and E(energy). One of $Q_{weak}$'s two methods for correcting for these false asymmetries was to use natural motion in the beam to determine the sensitivity of the signal to changes in the parameters. This used linear regression of the natural beam motion and is described in Section 3.2.3. The second method of correcting the false asymmetries generated by helicity-correlated beam motion was to drive the beam motion via beam modulation, as described in Section 3.2.4.

While this correction is now referred to as $A_{\text{beam}}$, it has previously been referred to as $A_{\text{reg}}$ in the previously published commissioning result [65].

The fact that linear regression used natural motion to determine the sensitivity of the

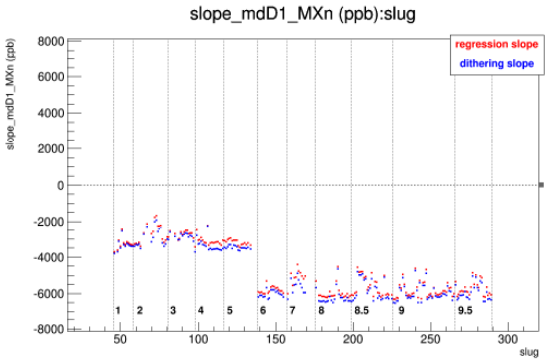


**(a)** *Sensitivity to natural monitor X.*

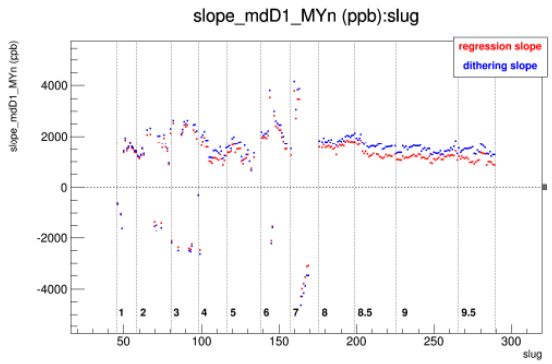


**(b)** *Sensitivity to natural monitor Y.*

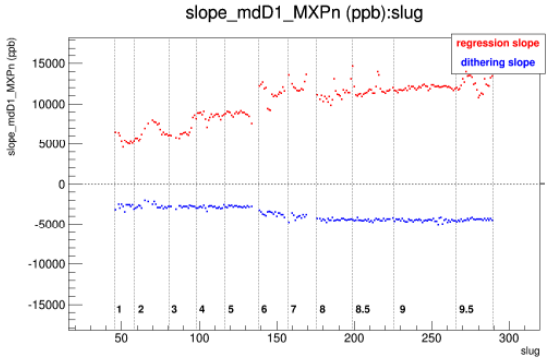


**(c)** *Sensitivity to natural monitor X'.*

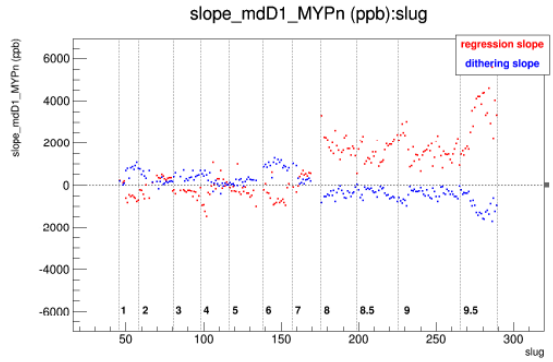


**(d)** *Sensitivity to natural monitor Y'.*

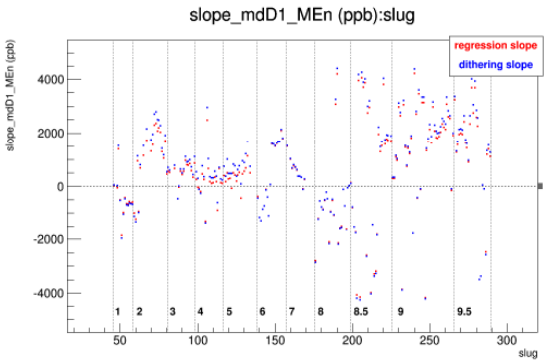


**(e)** *Sensitivity to natural monitor E.*

**Figure 5.2:** *The above plots show the sensitivities of the detector signal to variations in the helicity-correlated beam properties(X, Y, X', Y', E) on a eight-hour timescale. The red represents the sensitivities as seen by linear regression of natural beam motion while the blue shows the sensitivities as seen by the beam modulation system. Plots produced by Peng Zang [13].*

detector signal had a weakness. If the beam was very stable over a period of time, noise in the beam monitors could affect the determined sensitivities. Beam modulation used imposed beam motion with a large amplitude to determine the sensitivities, which led to an immunity to beam monitor noise. [66] It was decided to use beam modulation to determine the helicity-correlated beam motion correction, with the exception of times during which no beam modulation data was taken.

When the beam modulation data was analyzed, there was a beam dithering response that was not fully explained by the beam position monitors(BPMs) in place. This response has still not been understood. There is a systematic error, referred to as the scheme dependent error, applied to account for this. [13] [66]

Beam modulation was chosen as the primary beam correction method, but during the analysis the agreement between beam monitoring and beam modulation was checked as well [13]. To eliminate correlations in the beam monitors, a set of monitors was created and normalized to the noise. These were referred to as the natural monitors [67].

Figure 5.2 shows the sensitivities to beam monitoring and beam modulation of the main detector to the natural monitors(X,Y,X',Y',E). Significant differences between beam monitoring and modulation were found [13] [68]. Specifically the main detector sensitivities to X'(beam x angle) and Y'(beam y angle) were very different between the two methods.

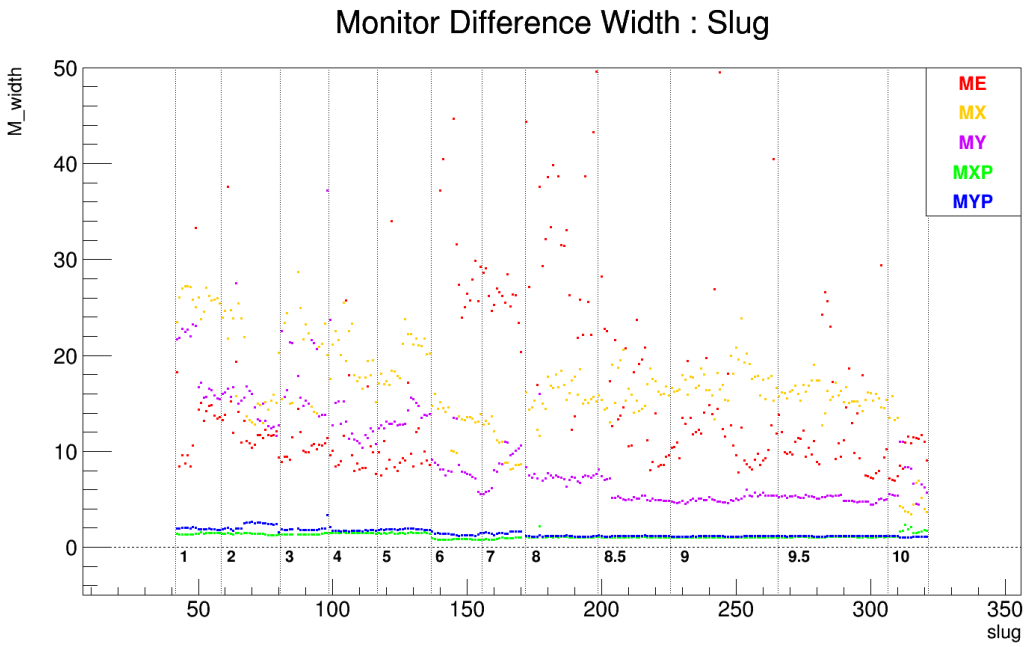


**(a)** *Natural BPM widths for the helicity-correlated beam parameters.*

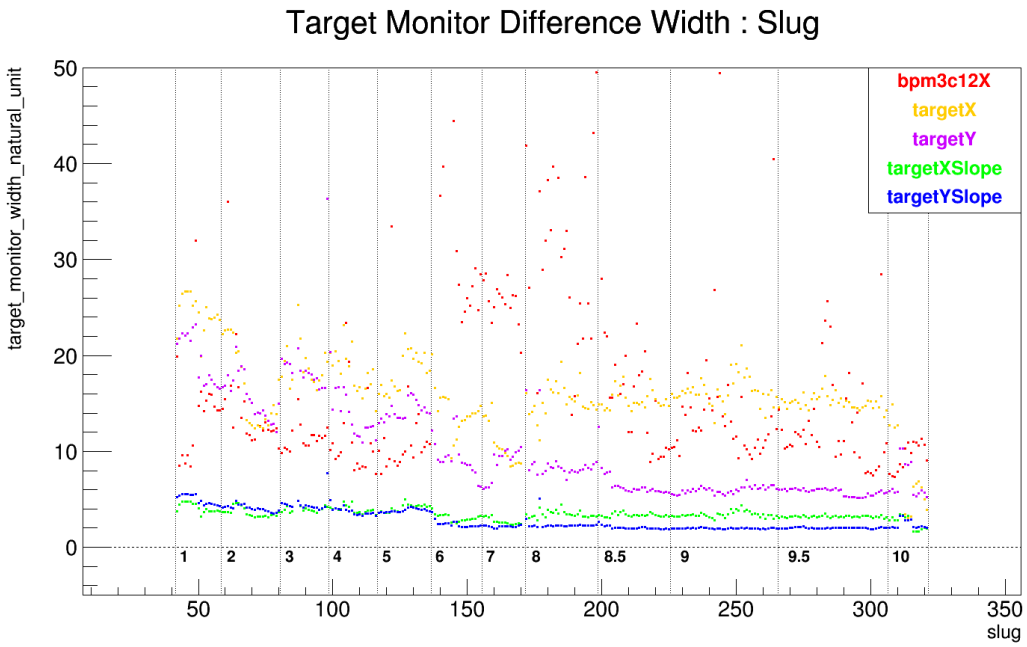


**(b)** *Physical BPM widths for the helicity-correlated beam parameters.*

**Figure 5.3:** *The top plot shows the natural BPM widths on an eight-hour time scale. The bottom plot shows the physical BPM widths associated with the respective natural monitors on an eight-hour time scale. All five of the helicity-correlated beam parameters are shown in both plots: X(yellow), Y(purple), X'(green), Y'(blue), and E(red). Plots produced by Peng Zang [14].*

The differences between the two methods for these two parameters can be explained by looking at the stability of the monitors. Figure 5.3 shows the monitor widths for both natural and physical monitors. It is clear that X' and Y' varied only slightly during data-taking [14] [69]. The reason beam modulation was chosen as the primary beam correction method was because when the beam was stable over time, the sensitivities determined by linear regression were often inaccurate. That was what caused the differences between beam modulation and beam monitoring [66].

As was mentioned earlier, a beam dithering response unexplained by the beam position monitors was found during analysis. To account for this a systematic scheme dependent error was included in the beam motion correction [66]. A second systematic error was included to account for the resolution of the sensitivities when beam modulation was used. The final corrections for helicity-correlated beam motion are

$$\begin{aligned} &\text{run 1: } A_{\text{beam}} = 18.5 \pm 4.1 \text{ (scheme) } \pm 0.1 \text{ (sensitivity) ppb} = 18.5 \pm 4.1 \text{ ppb} \\ &\qquad\qquad\qquad\qquad \text{and} \\ &\text{run 2: } A_{\text{beam}} = 0.0 \pm 1.1 \text{ (scheme) } \pm 0.3 \text{ (sensitivity) ppb} = 0.0 \pm 1.1 \text{ ppb.} \end{aligned} \tag{5.7}$$

### 5.2.3 Beamline Background Asymmetry Correction

As was described in Section 3.6.2, a tungsten-copper beam collimator was introduced into the beamline in order to limit background signal in the detectors. However, there was some beam that scattered off of this collimator and the beamline with a large asymmetry and

contributed to the signal in the main detectors.

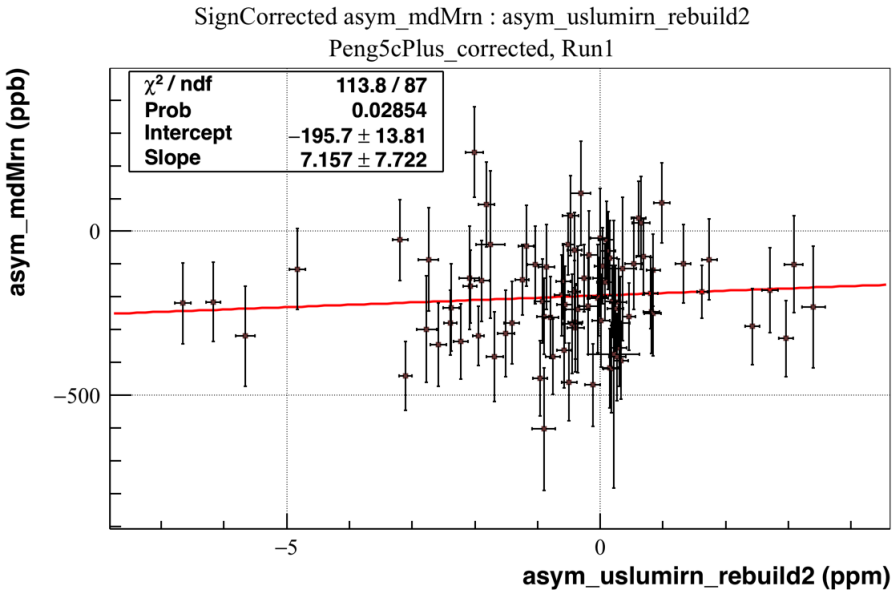


**(a)** *Run 1 main detector asymmetries(ppb) correlated with the US luminosity monitor asymmetries(ppm).*

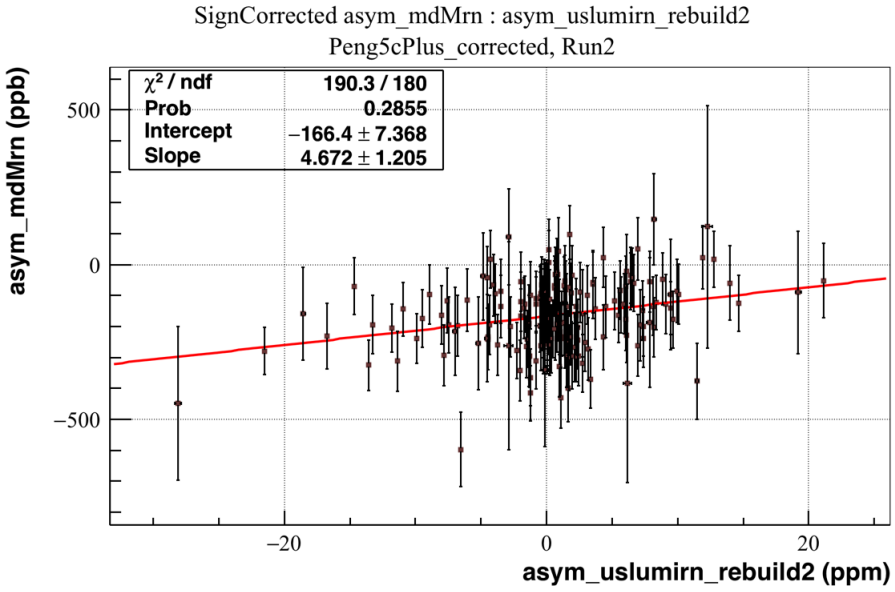


**(b)** *Run 2 main detector asymmetries(ppb) correlated with the US luminosity monitor asymmetries(ppm).*

**Figure 5.4:** *The averaged asymmetries of the main detector(ppb) per eight hours of data were correlated with the US luminosity monitor asymmetries(ppm) which were highly correlated with the beamline background for both run 1 and run 2. Plots produced by E. Kargiantoulakis [15] [16].*

Via the use of two inch tungsten shutters that blocked the beam in octants 1 and 5, this beamline background could be measured. It was found to be highly correlated with the upstream(US) luminosity monitors, to the point where the asymmetry of the US luminosity monitors could be used to find the beamline background correction for the main detector asymmetry.

In order to determine the correction, two quantities were needed. The first was the correlation between the main detector asymmetry and the asymmetry of the US luminosity monitors, shown in Figure 5.4 for both run 1 and run 2. The second was the average value over six minutes of data taking(a runlet) for the asymmetry of the US luminosity monitors. Doing this for every six minutes of data was to take into account variations over time. [17]

By combining these two values over both the run 1 and run 2 data, final net corrections can be determined [17],

$$\begin{gathered} \text{run 1: } A_{\text{BB}} = 3.9 \pm 4.5 \text{ ppb} \\ \text{and} \\ \text{run 2: } A_{\text{BB}} = -2.4 \pm 1.1 \text{ ppb.} \end{gathered} \tag{5.8}$$

### 5.2.4 Linearity Correction

The linearity referred to in this section refers to the ideal situation where the output voltage of the detector would have a linear relationship with the beam signal. In reality, there was nonlinearity introduced into the electronics chain both in the Beam Charge Monitor(BCM) and in the Cherenkov detector itself.

In order to measure this nonlinearity, bench tests were performed with a spare phototube and the full $Q_{weak}$ electronics chain. These bench tests used three light-emitting diodes of different colors and at different frequencies to develop a relationship between the detector output voltage and the nonlinearity present in the electronics chain. A full discussion of these bench tests can be found in the thesis of Wade Duvall [2]. The results for nominal $Q_{weak}$ running conditions are shown in Figure 5.5.

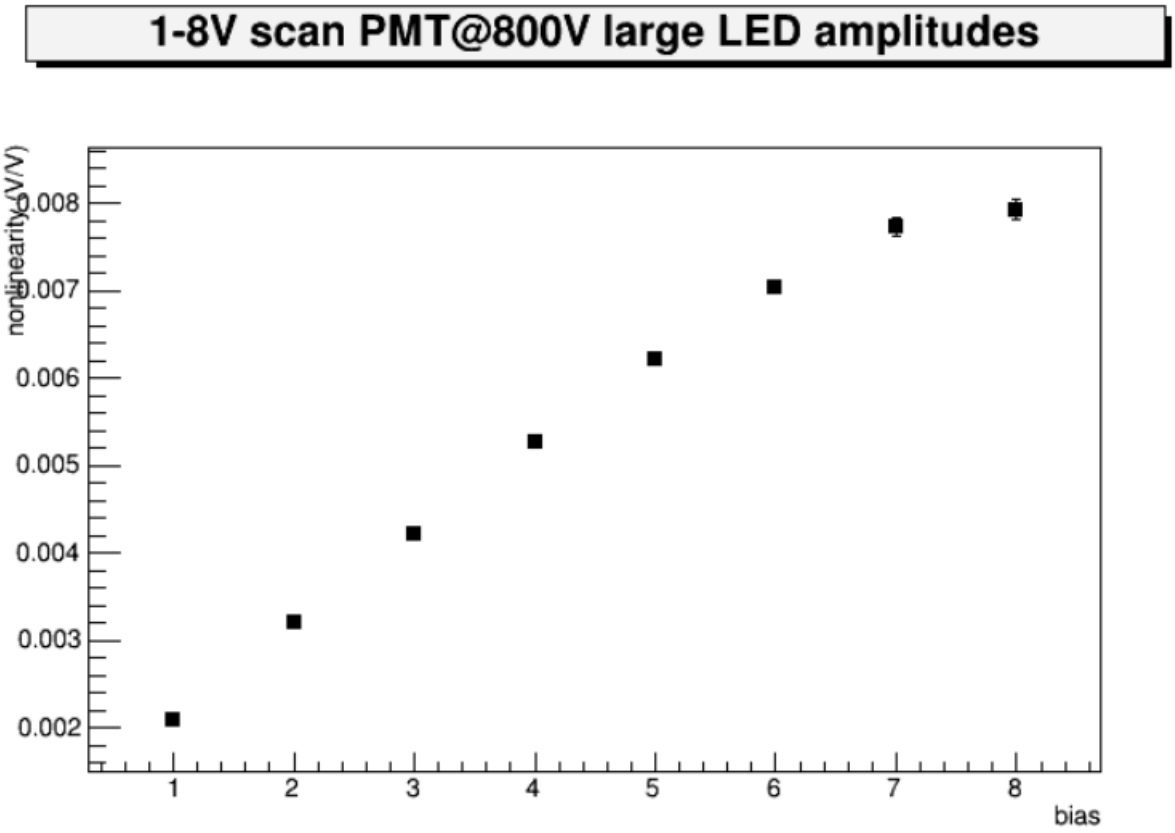


**Figure 5.5:** *Various detector output voltages(bias) was mimicked in a series of bench tests. The resulting nonlinearities have a mostly linear relationship with these values. Image taken from the dissertation of Wade Duvall [2].*

For nominal $Q_{weak}$ running, the detector output voltage was $\sim 6.2$ volts for both run 1

and run 2 [2]. This voltage is associated with a nonlinearity of $x = (0.7 \pm 0.5)\%$. This is combined with the raw asymmetries for run 1 and run 2 to determine the linearity corrections,

$$\begin{gathered} \text{run 1: } A_{\mathrm{L}} = 1.3 \pm 1.0 \text{ ppb} \\ \text{and} \\ \text{run 2: } A_{\mathrm{L}} = 1.2 \pm 0.9 \text{ ppb.} \end{gathered} \tag{5.9}$$

### 5.2.5 Transverse Asymmetry Correction

The $\mathrm{Q_{weak}}$ apparatus was designed with strong azimuthal symmetry to reduce the effect of any transverse leakage. There was a small transverse component($\sim 2\%$) in the electron beam that was mostly suppressed thanks to the azimuthal symmetry. However, this transverse component still needed to be measured. The transverse leakage, driven by parity-conserving two-photon-exchange [70], is referred to as the transverse asymmetry correction, $A_{\mathrm{T}}$.

To investigate the transverse leakage, pure transversely polarized beam was used . The beam can be transversely polarized either horizontally (parallel to floor of hall) or vertically (perpendicular to the floor of hall). This was used to determine the maximum broken symmetry seen by the eight main detectors [71]. A full discussion of this analysis is found in the thesis of B. Waidyawansa. [44]

The correction value was chosen to be zero as there was minimal direct effect of the transverse leakage, but an error was applied to take the leakage into consideration. The

final values,

$$\begin{gathered}\text{run 1: } A_{\mathrm{T}} = 0.0 \pm 1.1 \text{ ppb} \\ \text{and} \\ \text{run 2: } A_{\mathrm{T}} = 0.0 \pm 0.7 \text{ ppb.}\end{gathered} \tag{5.10}$$

were determined by B. Waidyawansa, P. Zang, and P. King [72].

### 5.2.6 Rescattering Bias Correction

The rescattering bias was a systematic effect that was discovered in the data after data taking had finished. Lead preradiators had been placed in front of the eight main detectors to minimize low energy beamline backgrounds. The longitudinally polarized scattered electrons precessed while being transported through the magnetic field, gaining a transverse polarization. These electrons then caused showers within the lead preradiators. The lead imparted a parity conserving asymmetry between the left and right PMTs mounted on the main detector, introducing a difference between the asymmetries seen by the two PMTs. This effect was hidden by the averaging of the PMTs during data taking, but as the symmetry of the main detectors is not perfect there was a bias in the asymmetry.

The final value was the same for both run 1 and run 2,

$$A_{\text{bias}} = 4.3 \pm 3.0 \text{ ppb.} \tag{5.11}$$

It was determined via a Gaussian process regression model using simulated microscopic

model results of the asymmetry versus the scattering angles of the shower electrons. A full discussion of the analysis of the rescattering bias correction can be found in the thesis of Wade Duvall [2].

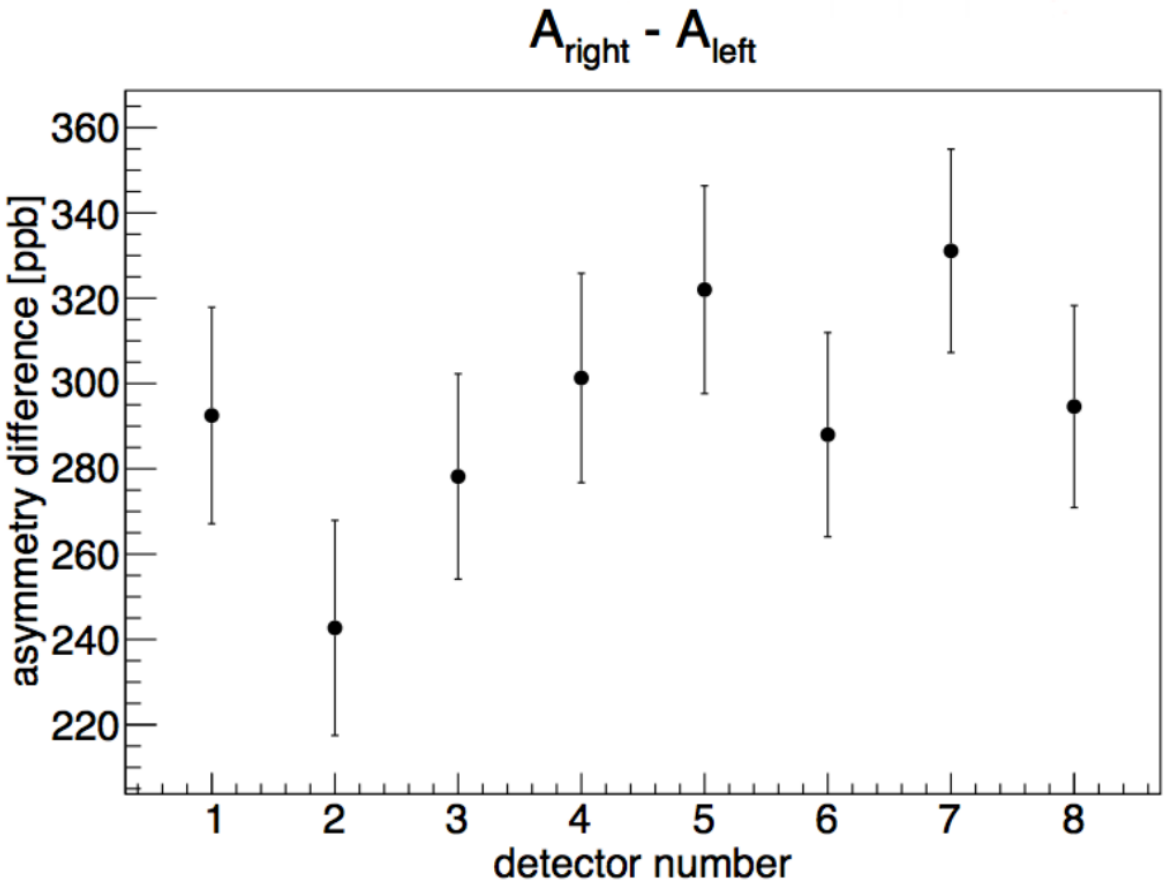


**Figure 5.6:** *Each main detector has a photomultiplier tube on both ends. The rescattering bias is visible when the difference between the right PMT and the left PMT for each main detector is compared. Image taken from the dissertation of Wade Duvall [2].*

### 5.2.7 Blinding Factor Correction

A blinding factor was applied to the raw data in order to prevent bias in the analysis. Different blinding factors were applied for the three main running periods: commissioning.

run 1, and run 2. These factors were applied by the software during analysis.

There were a few considerations to be dealt with in regards to the blinding factors. A limit of ±60 ppb was applied to the blinding factor. The sign of the blinding factor changed with the insertable half-wave plate state, the wien setting, and any other condition that would affect the sign of the asymmetry. It was also limited to production runs, when the liquid hydrogen target was in the path of longitudinally polarized beam. [73]

The blinding factors for run 1 and run 2 are

$$\begin{gathered} \text{run 1: } A_{\text{blinding}} = -25.34 \pm 0 \text{ ppb} \\ \text{and} \\ \text{run 2: } A_{\text{blinding}} = 6.669 \pm 0 \text{ ppb.} \end{gathered} \tag{5.12}$$

### 5.2.8 $A_{\text{M}}$

**Table 5.1:** *The final false asymmetry corrections to the raw elastic asymmetry for nominal $Q_{weak}$ running.*

| Correction | | Run 1 | Run 2 |
|---|---|---|---|
| Beam Monitor Correction | $A_{\text{BCM}}$ | $0 \pm 4.4$ ppb | $0 \pm 2.1$ ppb |
| Helicity Correlated Beam Correction | $A_{\text{beam}}$ | $18.5 \pm 4.1$ ppb | $0.0 \pm 1.1$ ppb |
| Beamline Background Correction | $A_{\text{BB}}$ | $3.9 \pm 4.5$ ppb | $-2.4 \pm 1.1$ ppb |
| Linearity Correction | $A_{\text{L}}$ | $1.3 \pm 1.0$ ppb | $1.2 \pm 0.9$ ppb |
| Transverse Asymmetry Correction | $A_{\text{T}}$ | $0.0 \pm 1.1$ ppb | $0.0 \pm 0.7$ ppb |
| Rescattering Bias Correction | $A_{\text{bias}}$ | $4.3 \pm 3.0$ ppb | $4.3 \pm 3.0$ ppb |
| Blinding Factor Correction | $A_{\text{blinding}}$ | $-25.34 \pm 0.0$ ppb | $6.669 \pm 0.0$ ppb |

Now that the false asymmetry corrections have been quantified, the measured asymmetry($A_{\mathrm{M}}$) can be determined from the false asymmetry, as shown in Equation (5.5). The final values for the false asymmetry corrections can be found in Table 5.1, and the final values of the measured asymmetry are

$$\begin{gathered}\text{run 1: } A_{\mathrm{M}} = -165.6 \pm 13.2 \text{ (stat)} \pm 8.2 \text{ (syst) ppb} \\ \text{and} \\ \text{run 2: } A_{\mathrm{M}} = -167.5 \pm 7.3 \text{ (stat)} \pm 8.2 \text{ (syst) ppb.}\end{gathered} \tag{5.13}$$

With the removal of the false asymmetries, the two run periods more clearly agree than the raw asymmetries originally suggested.

## 5.3 Extracting the Elastic Asymmetry

Now that the false asymmetries have been removed from the signal, the measured asymmetry($A_{\mathrm{M}}$) needs to be corrected for the polarization, the various backgrounds, and a few multiplicative factors to determine the elastic asymmetry($A_{\mathrm{ep}}$). This is done by

$$A_{\mathrm{ep}} = R_{\mathrm{tot}} \frac{A_{\mathrm{M}}/P - A_{\mathrm{bkgd}}}{1 - f_{\mathrm{tot}}}. \tag{5.14}$$

The backgrounds that need to be accounted for consist of the aluminum signal from the entrance and exit windows($f_{\mathrm{al}}A_{\mathrm{al}}$), the neutral beamline signal($f_{\mathrm{nb}}A_{\mathrm{nb}}$), and the inelastic

signal($f_{\rm in}A_{\rm in}$). The sum of these backgrounds explicitly written out is

$$A_{\rm bkgd} = f_{\rm al}A_{\rm al} + f_{\rm nb}A_{\rm nb} + f_{\rm in}A_{\rm in}. \tag{5.15}$$

In the published results the aluminum background is referred to with the subscript 1, the neutral beamline background is referred with the subscript 3, and the inelastic background with the subscript 4 [17].

The dilution factors($f_i$) for the various backgrounds contributed to $f_{\rm tot}$, as does the dilution factor for the beamline background($f_{\rm BB}$) resulting in

$$f_{\rm tot} = f_{\rm ep} + f_{\rm al} + f_{\rm nb} + f_{\rm pn} + f_{\rm BB}. \tag{5.16}$$

In the published results the beamline background dilution factor is referred to with the subscript 2 [17].

The multiplicative factors consist of the electromagnetic radiative correction($R_{\rm RC}$), the detector response correction($R_{\rm det}$), the acceptance correction($R_{\rm acc}$), and the $Q^2$ correction($R_{Q^2}$). These are combined to form $R_{\rm tot}$,

$$R_{\rm tot} = R_{\rm RC}R_{\rm det}R_{\rm acc}R_{Q^2}. \tag{5.17}$$

All of the above values are required to determine the final elastic parity-violating electron-proton scattering asymmetry that is required to extract the weak charge of the proton($Q_W^p$).

### 5.3.1 Polarization

There were two methods used to track the polarization during the $Q_{weak}$ Experiment. The first used the established Møller polarimeter(Section 3.3.1) but this was an invasive process and was limited to very low beam currents. It involved measuring the parity-conserving asymmetry of electrons scattered on a polarized iron foil target. The second method involved a new Compton polarimeter. The Compton polarimeter(Section 3.3.2) was noninvasive and continuously monitored the beam polarization at full beam energy. For the main $Q_{weak}$ measurement, these two methods were in good agreement. Figure 3.5 shows both the Møller and Compton measurements overlaid, illustrating the agreement between the two. [8] [51]

An important goal of the $Q_{weak}$ Experiment was to very accurately measure($< 1\%$) the polarizations due to the dependence of the parity-violating asymmetry on the value. Both run periods succeeded at having very precise measurements,

$$\begin{gathered} \text{run 1: } P = (87.66 \pm 1.05)\% \\ \text{and} \\ \text{run 2: } P = (88.71 \pm 0.55)\%. \end{gathered} \tag{5.18}$$

### 5.3.2 Inelastic Background

The amount of inelastic background, made up of the radiative peak of the $N \rightarrow \Delta$ transition [17] [4], in the signal was calculated by simulation, with the resulting shown in Equation 5.19.

While it is a very small percentage of the signal, the expected asymmetry was large in comparison to the expected asymmetry of the elastic signal. Therefore dedicated measurements were made at the inelastic kinematics to measure the inelastic asymmetry [4], summarized in Section 6.5. The inelastic asymmetry found for the inelastic kinematics was then scaled by $Q^2$ to determine the inelastic asymmetry at the elastic kinematics. The dilution factor and asymmetry, neither of which changed between run 1 and run 2, are

$$f_{\text{in}} = (0.018 \pm 0.004)\% \text{ and } A_{\text{in}} = -3.0 \pm 1.0 \text{ ppm}. \tag{5.19}$$

### 5.3.3 Aluminum Background

The dominant background($\sim 2.5\%$) contaminating the elastic signal was due to scattering off aluminum nuclei. When the beam passed through the $LH_2$ target, it entered and exited through thin aluminum windows. These windows were the source of the aluminum background. The entrance window (0.11 mm) and exit window (0.13 mm) were made from same block of aluminum 7075 alloy, as was the dummy target (3.7 mm) used to determine the aluminum asymmetry for both run 1 and run 2, shown in Equation (5.20). The dummy target was thicker than the windows so as to match the radiation length of the normal beam path, the hydrogen target.

Simulation was used to take into account the acceptances of the entrance and exit windows [74]. Data was taken at a low current while the $LH_2$ target was empty and simulation

was done on the radiative effects to determine the dilution factor [75], which differed between run 1 and run 2. The final values for the aluminum dilution factors and asymmetries for the two run periods are

$$\begin{aligned} &\text{run 1: } f_{\text{al}} = (2.471 \pm 0.056)\% \text{ and } A_{\text{al}} = 1.514 \pm 0.077 \text{ ppm} \\ &\text{and} \\ &\text{run 2: } f_{\text{al}} = (2.516 \pm 0.059)\% \text{ and } A_{\text{al}} = 1.515 \pm 0.077 \text{ ppm.} \end{aligned} \tag{5.20}$$

### 5.3.4 Beamline Background Dilution Factor

The $Q_{weak}$ result has already been corrected for the beamline background when the false asymmetries were removed from the raw asymmetry($A_{\text{raw}}$) to determine the measured asymmetry($A_{\text{M}}$). However, the beamline background was carried by neutral particles that composed part of the signal seen by the main detectors. Therefore, while the false asymmetry due to the beamline backgroun($A_{\text{BB}}$) is not considered in the background asymmetries($A_{\text{bkgd}}$), the dilution factor($f_{\text{BB}}$) still contributes to the total non-elastic dilution factor($f_{\text{tot}}$).

It is possible to isolate the beamline background dilution factor by using two inch tungsten shutters placed in octants 1 and 5. These shutters block out the particles that would pass through the main detectors, except for the ones caused by the beamline background. Therefore by comparing the average yields of the blocked and unblocked) octants, a dilution

factor for the beamline background can be determined to be

$$f_{\mathrm{BB}} = (0.193 \pm 0.064)\%. \tag{5.21}$$

The error was assigned as the difference seen between good halo and bad halo periods.

### 5.3.5 Neutral Background

While scattering off the tungsten plug and beamline caused the beamline background, there were other sources of possible scattering. The primary scattered electrons can have secondary interactions with the concrete shielding(collimators) and the toroidal spectrometer structure [56]. The resulting neutral particles are low-energy and form the neutral background.

The neutral signal in the main detectors was determined by using thin scintillators to identify the charged particles passing through the detectors in event mode, where the beam current was kept to 100 nA or below, and calculating what percentage of the signal was left. Simulation of neutral events was used to determine the final neutral beamline asymmetry($A_{\mathrm{nb}}$). The asymmetries and final dilution factors($f_{\mathrm{nb}}$) for the two run periods are

$$\begin{gathered}\text{run 1: } f_{\mathrm{nb}} = (0.12 \pm 0.20)\% \text{ and } A_{\mathrm{nb}} = -0.39 \pm 0.16 \text{ ppm} \\ \text{and} \\ \text{run 2: } f_{\mathrm{nb}} = (0.06 \pm 0.12)\% \text{ and } A_{\mathrm{nb}} = -0.39 \pm 0.16 \text{ ppm}.\end{gathered} \tag{5.22}$$

### 5.3.6 Electromagnetic Radiative Correction

Bremsstrahlung can occur before and after the primary scattering of the electron. However, there is also a difference in how internal and external bremsstrahlung can affect the kinematics at the point of primary scattering. Bremsstrahlung can cause depolarization of the incident electron and change its energy resulting in the $Q^2$ of the vertex changing. Internal bremsstrahlung occurs in the field of the primary proton being scattered from, while external bremsstrahlung occurs elsewhere in the target. Geant3 simulation was used to determine the radiative correction factor $R_{\mathrm{RC}}$ that accounts for the effects of both. The resulting correction is

$$R_{\mathrm{RC}} = 1.010 \pm 0.005. \tag{5.23}$$

### 5.3.7 Detector Response Correction

In an ideal situation, the summed signal seen by the two photomultiplier tubes attached to each main detector would be the same no matter where on the bar the scattered electron impacted. However, that was not the case, with the position of the interaction between the main detector and scattered electron having an effect on both the momentum transfer and light generated of that electron. The interaction of those two factors led to a weighted response in the main detectors. The tracking system was used to determine how the main

detectors responded, measuring the detector response correction to be

$$R_{\text{det}} = 0.9895 \pm 0.0021. \tag{5.24}$$

### 5.3.8 Acceptance Correction

The average momentum transfer($\langle Q^2 \rangle$) is treated as a singular value associated with the final asymmetry, but in actuality represents a range of kinematics. The acceptance correction acts to shift the average over $Q^2$ to a value for the average vertex $Q^2$,

$$R_{\text{acc}} = \frac{A\left(\langle Q^2 \rangle\right)}{\langle A\left(Q^2\right) \rangle}. \tag{5.25}$$

This correction takes into account the limited acceptance of the toroidal spectrometer and energy loss in the liquid hydrogen target. Simulation was used to determine the correction value,

$$R_{\text{acc}} = 0.977 \pm 0.002. \tag{5.26}$$

### 5.3.9 $Q^2$ Correction

The tracking system measured a $\langle Q^2 \rangle$ that was used to benchmark a Geant4 simulation. The Geant4 simulation $\langle Q^2 \rangle$ value was not identical between run 1 and run 2 due to differences between the two run periods. Run 2 was chosen as the default, and the run 1 $\langle Q^2 \rangle$ value was

scaled. The decision was made to treat $\langle Q^2 \rangle$ as an exact value. The sensitivity $\partial A_{\rm ep}/\partial Q^2$ was used to rotate the error on $Q^2$ to an effective error on the asymmetry for each run period [17],

$$\begin{gathered} \text{run 1: } R_{Q^2} = 0.9928 \pm 0.0055 \\ \text{and} \\ \text{run 2: } R_{Q^2} = 1.0 \pm 0.0055. \end{gathered} \tag{5.27}$$

### 5.3.10 Final $A_{\rm ep}$

Now that all the variables have been determined, the final elastic electron-proton asymmetry can be determined. The first step is to determine the background correction, as shown in Equation (5.15). The combination of the aluminum, neutral beamline, and inelastic background corrections is

$$\begin{gathered} \text{run 1: } A_{\rm bkgd} = 0.036 \pm 0.002 \text{ ppm} \\ \text{and} \\ \text{run 2: } A_{\rm bkgd} = 0.037 \pm 0.002 \text{ ppm}. \end{gathered} \tag{5.28}$$

The next step is to combine the five dilution factors, as directed by Equation (5.16). The results of this is

$$\begin{gathered} \text{run 1: } f_{tot} = (2.80 \pm 0.22)\% \\ \text{and} \\ \text{run 2: } f_{tot} = (2.78 \pm 0.15)\%. \end{gathered} \tag{5.29}$$

The final intermediate step is to combine the multiplicative corrections, as directed by Equation (5.17). The results of this is

$$\begin{gathered}\text{run 1: } R_{tot} = 0.9693 \pm 0.0080 \\ \text{and} \\ \text{run 2: } R_{tot} = 0.9764 \pm 0.0090.\end{gathered} \tag{5.30}$$

Now all the components of can be put into Equation (5.14) in order to determine the final parity-violating asymmetries for the two run periods. These are

$$\begin{gathered}\text{run 1: } A_{\text{ep}} = -223.5 \pm 15.0 \text{ (stat)} \pm 10.1 \text{ (syst) ppb} \\ \text{and} \\ \text{run 2: } A_{\text{ep}} = -227.2 \pm 8.3 \text{ (stat)} \pm 5.6 \text{ (syst) ppb.}\end{gathered} \tag{5.31}$$

Now that all the corrections have been applied, the agreement between run 1 and run 2 has improved significantly from the raw asymmetries(Equation (5.3)). The two run periods are now combined together to determine the final $Q_{\text{weak}}$ elastic parity-violating electron-proton asymmetry,

$$A_{\text{ep}} = -226.5 \pm 7.3 \text{ (stat)} \pm 5.8 \text{ (syst) ppb.} \tag{5.32}$$

## 5.4 Implications

Now that a parity-violating electron scattering(PVES) asymmetry($A_{ep}$) has been determined for the $Q_{weak}$ Experiment, this value can be used to look at physical quantities that result from the standard model. The physical quantities that will be discussed are the weak charge of the proton($Q_w^p$), the weak charge of the neutron($Q_w^n$), and the weak mixing angle($\sin^2\theta_W$). There will also be discussion of the current mass reach in the search for new physics.

### 5.4.1 Weak Charge of the Proton

The weak charge of the proton($Q_w^p$) was determined via a global fit of the reduced asymmetry,

$$\frac{A_{ep}^{PV}}{A_0} = Q_w^p + Q^2 B\left(Q^2,\theta\right) \qquad \text{where} \qquad A_0 = \left[\frac{-G_F Q^2}{4\pi\alpha\sqrt{2}}\right], \tag{5.33}$$

of the world's PVES data. The $B\left(Q^2,\theta\right)$ term represents the hadronic effects and is determined via the world's PVES data, after being corrected for the energy-dependent part of the electroweak radiative correction ($\Box_{\gamma Z}$). This correction comes from axial-vector coupling at the electron vertex, shown in the Feynman diagram in Figure 5.7, and is the dominant energy-dependent correction to $A_{ep}/A_0$. The details of this correction are found in the published $Q_{weak}$ paper on the commissioning data [65]. For the $Q_{weak}$ kinematics, the electroweak radiative correction was $0.00459 \pm 0.00044$ [76].

The $\Box_{\gamma Z}$ correction was the only electroweak correction necessary for the PVES data

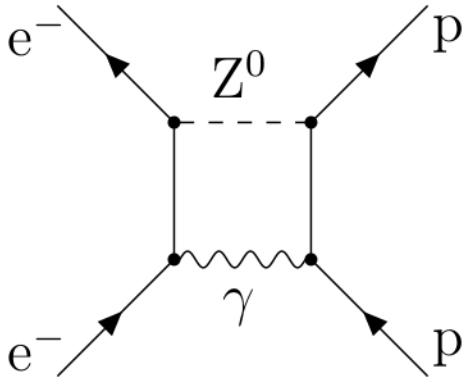


**Figure 5.7:** *The Feynman diagram for the electroweak radiative interaction* ($\Box_{\gamma Z}$).

being used in the global fit, and the asymmetries being used in the fit were already corrected for ordinary electromagnetic corrections [17]. The three dimensional fitting procedure over $Q^2$ and $\theta$ was published previously [77]. Five free parameters used in the fitting procedure are the neutral weak quark coupling constants ($C_{1\mathrm{u}}$ and $C_{1\mathrm{d}}$), the strange charge radius ($\rho_s$), the strange magnetic moment ($\mu_s$), and the isovector weak axial form factor ($G_A^{Z(T=1)}$). The data was then rotated into the forward angle limit ($\theta = 0$) using

$$A_{\mathrm{ep}}^{\mathrm{data}}\left(\theta = 0, Q^2\right) = A_{\mathrm{ep}}^{\mathrm{data}}\left(\theta, Q^2\right) - \left[A^{\mathrm{fit}}\left(\theta, Q^2\right) - A^{\mathrm{fit}}\left(0, Q^2\right)\right] \tag{5.34}$$

in order to be displayed in two dimensions. $A_{\mathrm{ep}}^{\mathrm{data}}$ is the asymmetry seen in data taken at $Q^2$ and $\theta$, while $A_{\mathrm{ep}}^{\mathrm{fit}}$ is the fit-determined asymmetry seen at $Q^2$ and $\theta$.

The resulting plot from the rotation into the forward angle limit is shown in Figure 5.8. This plot combined the world PVES data on hydrogen, deuterium, and helium [78] [79] [80] [81] [82] [83] [84] [85] [86] [87] [88] [89]. A value for the weak charge of the proton was

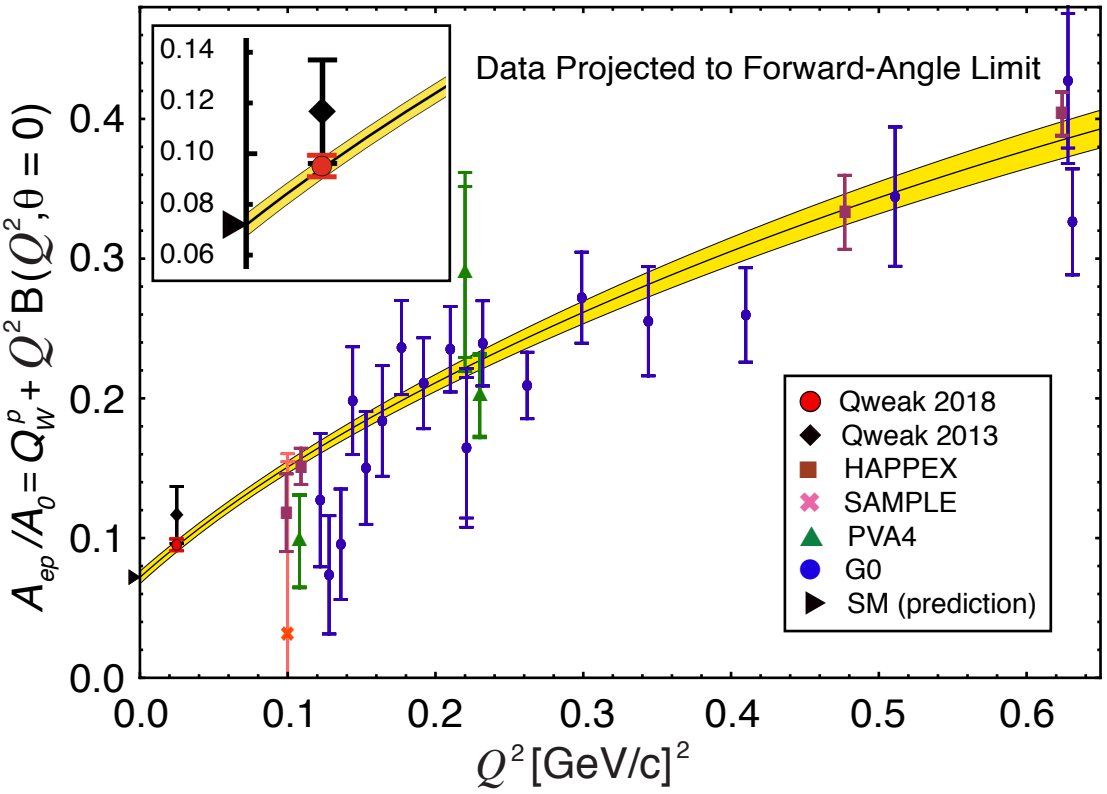


**Figure 5.8:** *The reduced asymmetries(Equation 5.33) of the world PVES data rotated to the forward angle limit($\theta = 0$), with the global fit shown by the black line and the uncertainty represented by the yellow. The Standard Model value is shown by the black arrow at $Q^2 = 0$ and the inset box shows the preliminary $Q_{weak}$ result in black and the final $Q_{weak}$ result in red. Figure is from the $Q_{weak}$ Nature paper [17].*

determined by looking at $A^{\text{fit}}(0,0)$,

$$Q_w^p\,(\text{PVES}) = 0.0719 \pm 0.0045. \tag{5.35}$$

Experimental values of the strange form factor are much less precise than the lattice QCD(LQCD) determination. By taking the strange form factor determined by LQCD over

the measured values, the weak chage value becomes

$$Q_w^p\,(\text{PVES + LQCD}) = 0.0684 \pm 0.0039. \tag{5.36}$$

Both Equation (5.35) and Equation (5.36) should be compared to the weak charge of the proton as predicted by the Standard Model,

$$Q_w^p\,(\text{SM}) = 0.0708 \pm 0.0003. \tag{5.37}$$

There is strong agreement between the Standard Model and the experimentally determined values for $Q_w^p$.

### 5.4.2 Weak Charge of the Neutron

A second physical quantity that the $\text{Q}_{\text{weak}}$ data provides information on is the weak charge of the neutron. To access this quantity, it is necessary to first look at the neutral weak quark coupling constants, $C_{1\text{u}}$ and $C_{1\text{d}}$. Both the weak charges of the proton($Q_w^p$) and the neutron($Q_w^n$) depend on these values,

$$\begin{gathered} Q_w^p = -2\,(2C_{1\text{u}} + C_{1\text{d}}) \\ \text{and} \\ Q_w^n = -2\,(C_{1\text{u}} + 2C_{1\text{u}})\,. \end{gathered} \tag{5.38}$$

As discussed in the previous section, $Q_{weak}$ and the rest of the world parity violating electron scattering(PVES) data have determined a very precise measurement of $Q_w^p$ which provides constraints on the coupling constants, but it is obvious in Equation (5.38) that more information is necessary to isolate them.

Atomic parity violation(APV) data provides constraints on the coupling constraints that are nearly orthogonal to the PVES constraints. Specifically the $^{133}$Cs measurements of the weak charge [90] [91] are combined with the PVES data to extract values for the coupling constants. Both the PVES(blue band) and APV(gold band) 95% level constraints are shown in Figure 5.9.

The combined constraints, represented by the black ellipse, are in agreement with the Standard Model value represented by the red square. The values for the neutral weak quark coupling constants are

$$C_{1u} = -0.1874 \pm 0.0022$$
$$\text{and} \tag{5.39}$$
$$C_{1d} = 0.3389 \pm 0.0025.$$

By combining the coupling constants in Equation (5.39) with the formula for $Q_w^n$ shown in Equation (5.38), the weak charge of the neutron can be determined. The final value is

$$Q_w^n \,(\text{PVES} + \text{APV}) = -0.9808 \pm 0.0063. \tag{5.40}$$

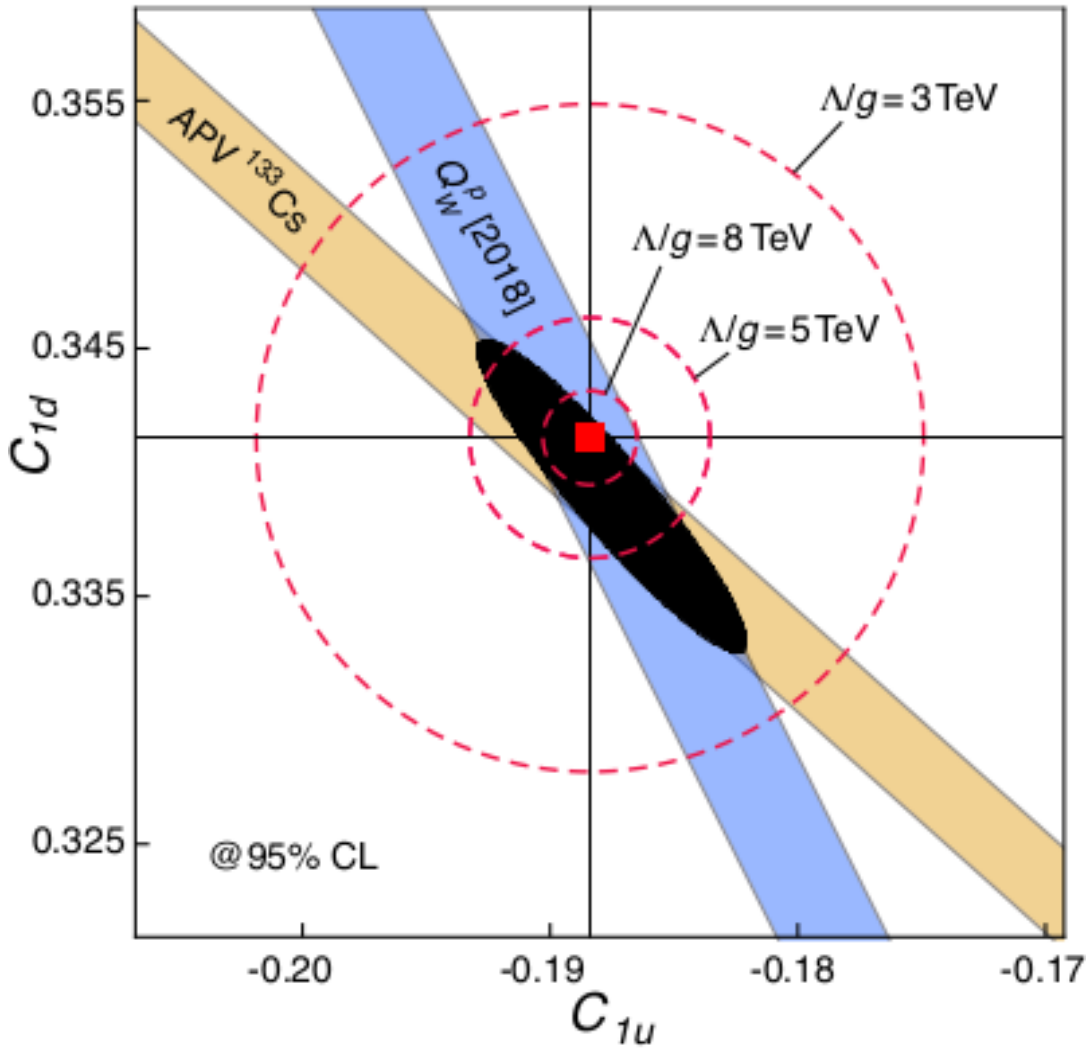


**Figure 5.9:** *The blue band represents the PVES data constraints on the coupling constants, while the gold band represents the APV constraints. The black ellipse at the intersection of the two bands represents the combined constraints(95% confidence level). The dashed red circles represent mass reach($\Lambda/g$) contours for new physics, centered at the Standard Model predicted values shown by the red square. Figure is from the $Q_{weak}$ Nature paper [17].*

This value is in strong agreement with the $Q_w^n$ value predicted by the Standard Model,

$$Q_w^n\,(\mathrm{SM}) = -0.975 \pm 0.0063. \tag{5.41}$$

### 5.4.3 Weak Mixing Angle

A key parameter of the Standard Model is the weak mixing angle $\left(\sin^2\theta_{\mathrm{W}}\right)$. This value is associated with how the electromagnetic and weak interactions mix, as described in Section 2.2. The weak mixing angle is related to the weak charge of the proton ($Q_w^p$) [76] via

$$Q_w^p = (\rho + \Delta_{\mathrm{e}})\left(1 - 4\sin^2\theta_{\mathrm{W}} + \Delta'_{\mathrm{e}}\right) + \Box_{\mathrm{WW}} + \Box_{\mathrm{ZZ}} + \Box_{\gamma\mathrm{Z}}(0)\,, \tag{5.42}$$

which includes the WW and ZZ radiative corrections($\Box_{\mathrm{WW}}$ and $\Box_{\mathrm{ZZ}}$), the low-energy renormalization($\rho$) of the weak neutral-current($\mathrm{Z}^0$) to charged current($\mathrm{W}^{\pm}$) interactions, the electron vertex correction($\Delta_{\mathrm{e}}$), the electron anapole moment($\Delta'_{\mathrm{e}}$), and the energy-independent part of the previously discussed $\Box_{\gamma\mathrm{Z}}$ [17]. While the full relation is used to extract the $\mathrm{Q}_{\mathrm{weak}}$ value for the weak mixing angle, to leading order Equation (5.42) can be simplified to

$$Q_w^p \approx 1 - 4\sin^2\theta_{\mathrm{W}}. \tag{5.43}$$

The Standard Model predicts that $\sin^2\theta_{\mathrm{W}}$ will be dependent on $M_{\mathrm{W}}$ and $M_{\mathrm{Z}}$ [29] [30],

$$\sin^2\theta_{\mathrm{W}} = 1 - \left(\frac{M_{\mathrm{W}}}{M_{\mathrm{Z}}}\right)^2 \approx \frac{1}{4}\,. \tag{5.44}$$

This leads to the suppression of $Q_w^p$ in the Standard Model, which means that the $Q_w^p$ is very sensitive to $\sin^2\theta_{\mathrm{W}}$. This means that the $\mathrm{Q}_{\mathrm{weak}}$ Experiment's 6.25% precision on the measurement of $Q_w^p$ becomes a 0.46% precision on the measurement of $\sin^2\theta_{\mathrm{W}}$, the final

value of which is

$$\sin^2\theta_{\mathrm{W}}\,(Q=0) = 0.2384 \pm 0.0011. \tag{5.45}$$

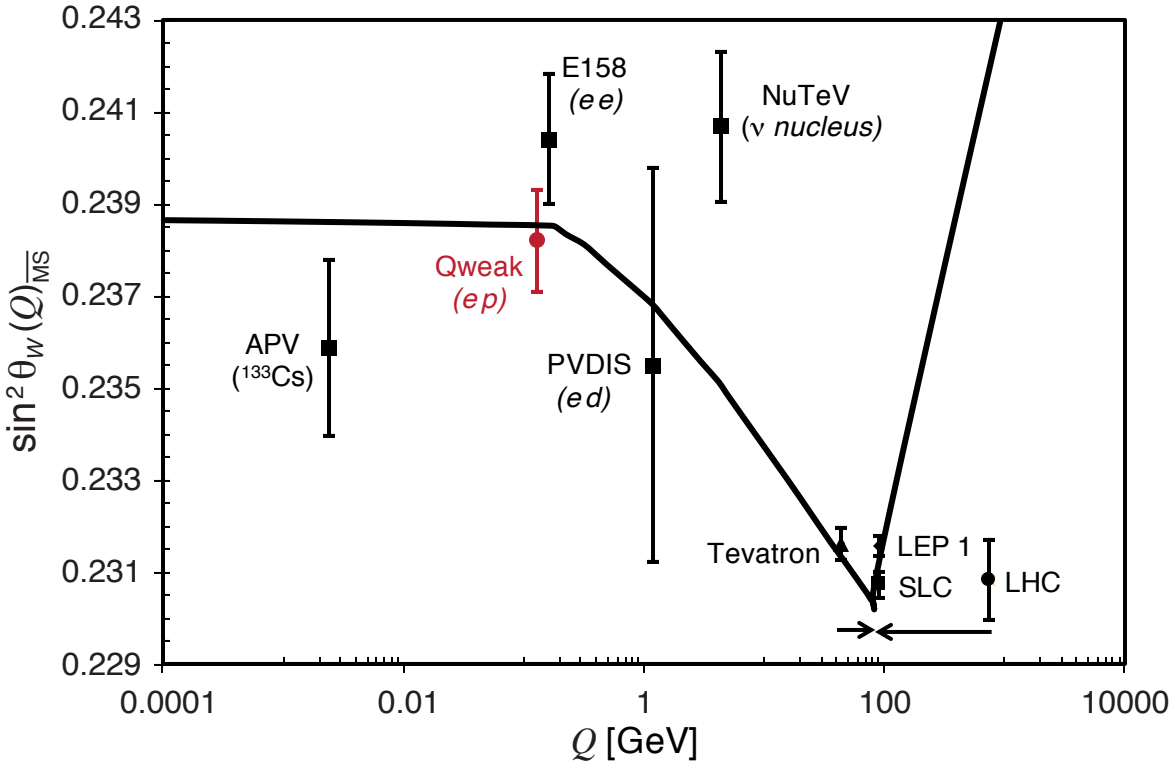


**Figure 5.10:** *The Standard Model predicted running of the weak mixing angle($\sin^2\theta_W$) over the 4-momentum transfer(black line) with experimental data plotted. With the addition of the $Q_{weak}$ data(red point), the weak charge of the proton completes the weak charge triad as E158 provides the electron and APV provides the neutron. Figure is from the $Q_{weak}$ Nature paper [17].*

The $Q_{weak}$ result, as well other experimental results, is plotted along the Standard Model prediction in Figure 5.10.

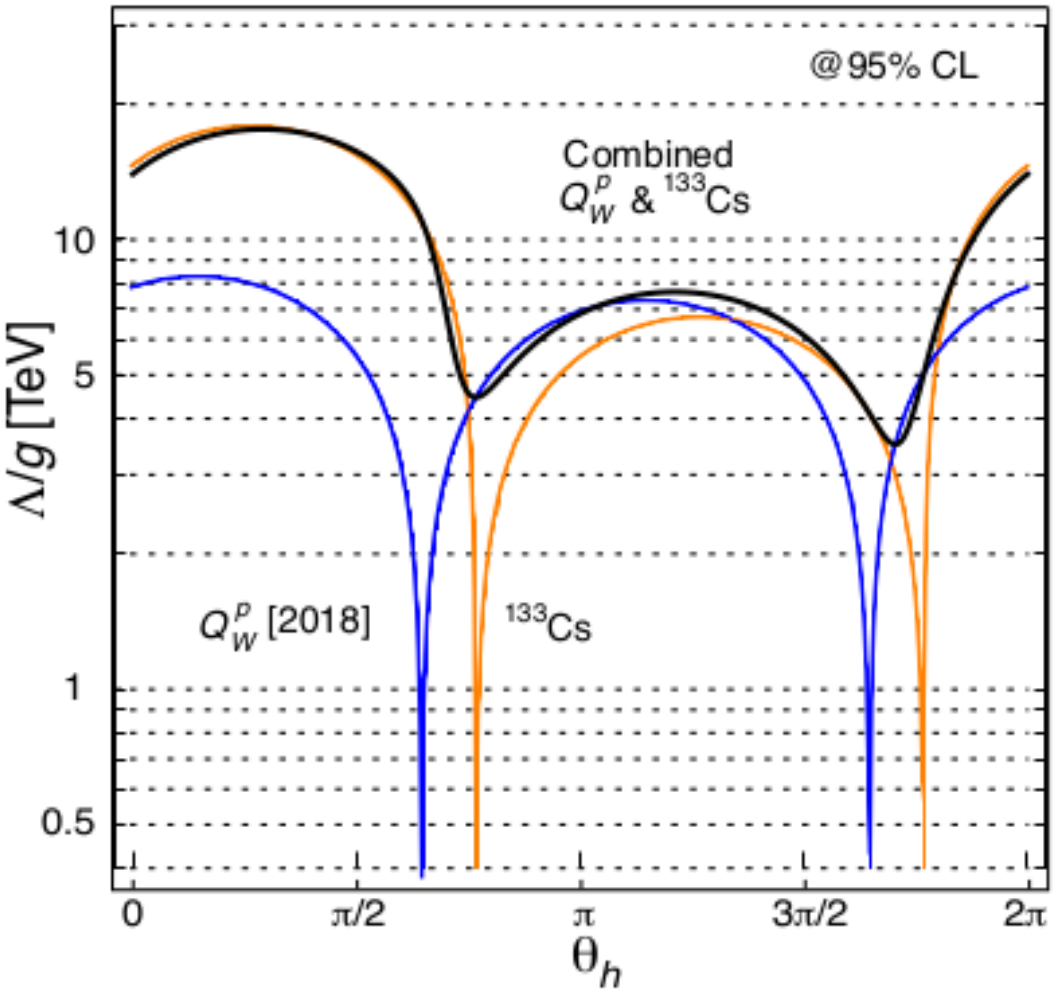


**Figure 5.11:** *The phase space of the "new physics term" $\Lambda/g$ and the quark-flavour mixing angle $\theta_h$. The 95% confidence-level of the PVES determined $Q_w^p$ is represented by the blue line and the APV data($^{133}Cs$) is represented by the gold line. The combined 95% confidence-level is represented by the black line. Figure is from the $Q_{weak}$ Nature paper [17].*

### 5.4.4 Mass Reach

A standard method [31] of looking at the sensitivity for new physics beyond the Standard Model(BSM) involves manipulating the Standard Model Lagrangian,

$$\mathcal{L}^{\mathrm{PV}}_{\mathrm{SM}} = -\frac{G_F^2}{\sqrt{2}}\bar{e}\gamma_\mu\gamma_5 e\sum_q C_1\bar{q}\gamma^\mu q. \tag{5.46}$$

A "new physics term" [31] of $g^2/\Lambda^2$ is added to this Lagrangian, resulting in the BSM Lagrangian

$$\mathcal{L}^{\mathrm{PV}}_{\mathrm{BSM}} = -\frac{g^2}{\Lambda^2}\bar{e}\gamma_\mu\gamma_5 e\sum_q h_v^q\bar{q}\gamma^\mu q. \tag{5.47}$$

The new term consists of the coupling $g$ and the mass scale for any new physics $\Lambda$. Both Lagrangians are summed over the up and down quarks $q$. The projections $h_v^u$ and $h_v^d$ depend on the quark-flavour mixing angle($\theta_h$) as

$$h_v^u = \cos\theta_h \quad \text{and} \quad h_v^d = \sin\theta_h. \tag{5.48}$$

The APV data on $^{133}$Cs and the PVES data previously discussed can be used to look at the phase space of $\Lambda/g$ and $\theta_h$. This phase space is depicted in Figure 5.11 where the 95%-confidence level for the APV data is represented by the gold curve, the PVES data is represented by the blue curve, and the combined result is represented by the black curve.

The PVES data(blue curve) has maxima at $\theta_h = 26.6°$ and $\theta_h = 206.6°$. At these values

of the quark-flavour mixing angle, new physics is ruled out below $\Lambda_-/g = 8.4$ TeV and $\Lambda_+/g = 7.4$ TeV [17] at the 95% confidence level.

# Chapter 6

# Ancillary Topic: N$\rightarrow \Delta$ transition

**Table 6.1:** *$Q_{weak}$'s inelastic data taken at both nominal(1165 MeV) kinematics and 877 MeV.*

| Beam Energy | $< \theta >$ | $< Q^2 >$ | $< W >$ |
|---|---|---|---|
| 1165 MeV | 8.3° | 0.021 GeV$^2$ | 1205 MeV |
| 877 Mev | 8.4° | 0.011 GeV$^2$ | 1189 MeV |

The $Q_{weak}$ Experiment's main measurement was of the elastic electron-proton asymmetry. Within the measured $Q_{weak}$ asymmetry, there was a inelastic electron-proton background. The dominant inelastic pathway involves the proton being excited to a $\Delta$, ie N$\rightarrow \Delta$. To correct for this background, data was taken at the inelastic peak. In addition, there was a longer period of time in Run 2 when Jefferson Lab's Hall A had priority and required a beam energy incompatible with $Q_{weak}$'s normal production energy. This provided an opportunity to obtain an N$\rightarrow \Delta$ measurement at a second beam energy and different kinematics. The two sets of data are summarized in Table 6.1. The focus of this chapter will be on the 877 MeV

data, and will reference the previous analysis of the 1165 MeV data afterwards. A value of $d_\Delta$ will be determined for both beam energies, which will be combined with a previous value determined by the G0 experiment to provide a limit on $d_\Delta$.

## 6.1 877 MeV Data

During April 2012, Hall A became the priority hall at Jefferson Lab for a period of two weeks. Due to this, $Q_{weak}$ was unable to receive beam that could be used for the elastic asymmetry at 1165 MeV. The choice was made to use this opportunity to make ancillary measurements, one of which involved taking an inelastic asymmetry measurement at a smaller $< Q^2 >$. The beam energy for this time period was 877 MeV, and the results are summarized in Table 6.2.

**Table 6.2:** *Summary of the $A_{inel}$ information for 877 MeV running.*

| | |
|---|---|
| Date | Apr 2012 |
| Beamtime | 141 hours |
| $A_{raw}$ | $-76 \pm 75$ (stat) ppb |
| $A_M$ | $-110 \pm 75$ (stat) $\pm 52$ (syst) ppb |
| $A_{inel}$ | $-1.2 \pm 1.0$ (stat) $\pm 1.0$ (syst) ppm |

Due to Hall A being the priority during this data-taking, Jefferson Lab was unable to provide $Q_{weak}$ with the normal highly longitudinally polarized beam. The beam available during this time period was 43% transversely polarized. The azimuthal symmetry of the detectors allowed the majority of this signal to cancel out, but there is still a significant correction necessary due to this transverse beam component.

### 6.1.1 Simulation and Planning

As the beam was at a different energy than normal running, the spectrometer settings that maximized the inelastic signal would be different. To determine the optimal settings simulations were run in GEANT3, a well established simulation program, over multiple settings for the toroidal spectrometer(QTOR). The elastic and inelastic rates of these simulations are shown in Figure 6.1.

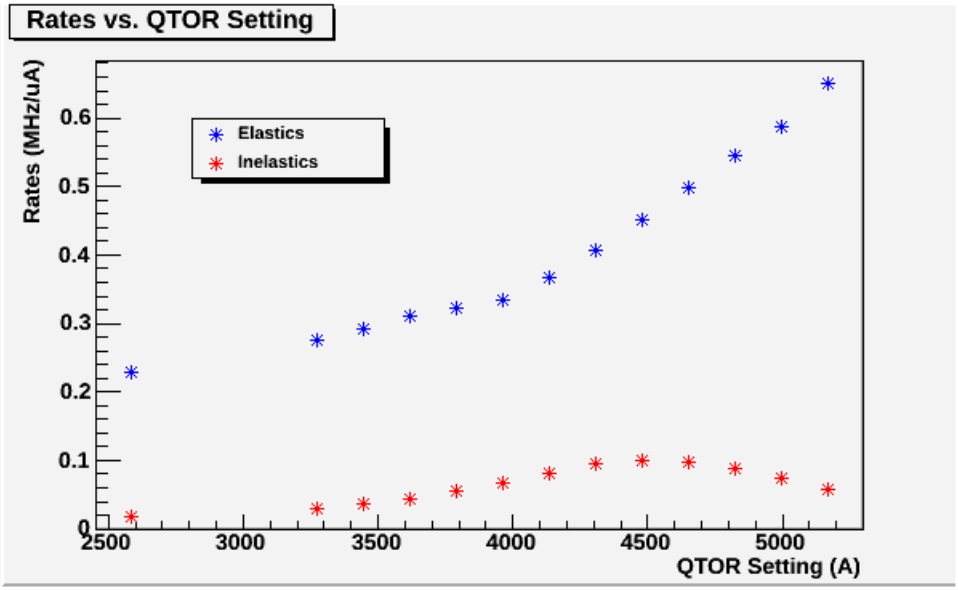


**Figure 6.1:** *Geant3 simulations of the inelastic(red) and elastic(blue) rates for 877 MeV running, performed prior to data taking. The inelastic peak is visible near the toroidal spectrometer(QTOR) setting of 4500 A.*

The goal of this data set was to extract the inelastic asymmetry. In order to do that, several factors needed to be taken into account. The first was the simulated inelastic dilution factor($f$),

$$f = \frac{R_{\text{in}}}{R_{\text{ep}} + R_{\text{in}}}, \tag{6.1}$$

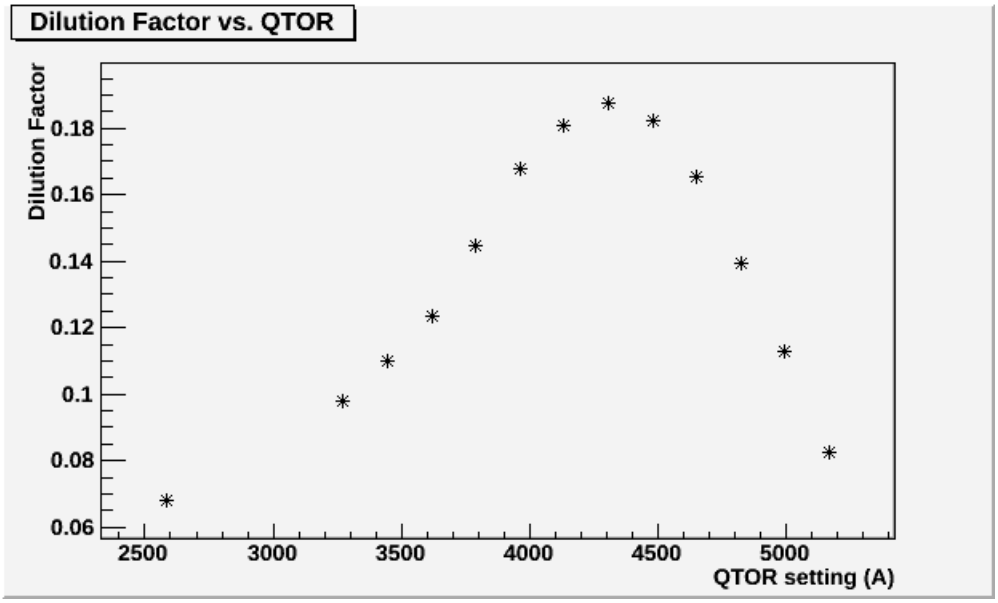


**Figure 6.2:** *Geant3 simulations of the inelastic dilution factors* $\left(\frac{R_{in}}{R_{ep}+R_{in}}\right)$ *for 877 MeV running over a range of settings for the toroidal spectrometer(QTOR).*

which is determined from the inelastic($R_{\rm in}$) and elastic($R_{\rm ep}$) rates.

Figure 6.2 shows the results of Equation (6.1) from the rates shown in Figure 6.1. It is clear that the maximum inelastic dilution factor, 18.8%, is at a toroidal spectrometer setting of 4300 A. However, there was another consideration involved in choosing the running conditions. There is a nonresonant process, two pion production, that can occur due to an inelastic collision. The two pion production process has a minimum threshold energy of 1215 MeV,

$$\mathrm{W} = \mathrm{M}_p + 2\mathrm{M}_\pi = 1215 \text{ MeV}. \tag{6.2}$$

This threshold is determined by the minimum missing mass(W) resulting from the mass of a proton($\mathrm{M}_p$) and two pions($\mathrm{M}_\pi$). Therefore if the inelastic collision has a missing mass above this threshold, it is possible for this reaction to occur. As the $\Delta$ resonance has a mass

of 1232 MeV with a width of ≈ 120 MeV, this was a possible background process with an unknown asymmetry. Figure 6.3 shows how the percentage of the simulation signal with a missing mass large enough for the two pion production process to occur varies with respect to the toroidal spectrometer setting.

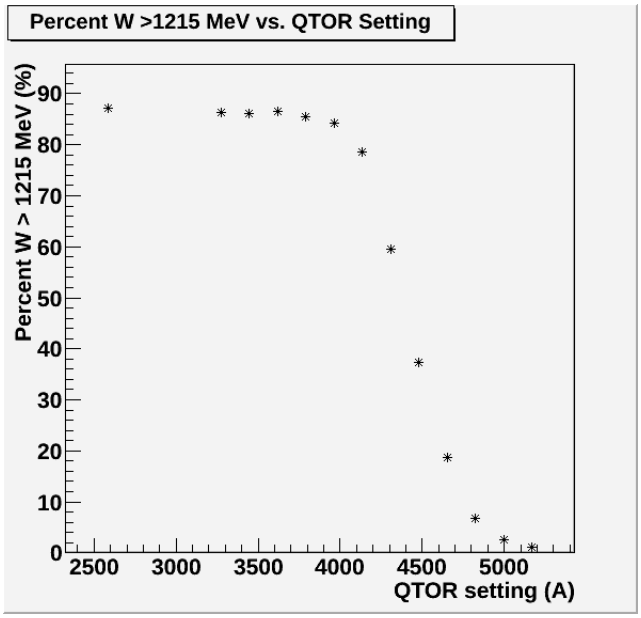


**Figure 6.3:** *Geant3 simulations of percentage of missing mass above the 1215 MeV threshold for two pion production over a range of settings for the toroidal spectrometer(QTOR).*

The maximum inelastic dilution factor (18.8%) occurred at a toroidal spectrometer setting with 60% of the signal larger than the two pion production threshold. That would present a significant possibility of the unknown asymmetry of this process contaminating the signal. In order to minimize that possibility, a spectrometer setting with a slightly smaller dilution factor (16.5%) was chosen. This setting had only 19% of the signal larger than the threshold. The maximum dilution factor spectrometer setting and the chosen spectrometer setting are highlighted in Figure 6.4 for both dilution factors and rates. Figure

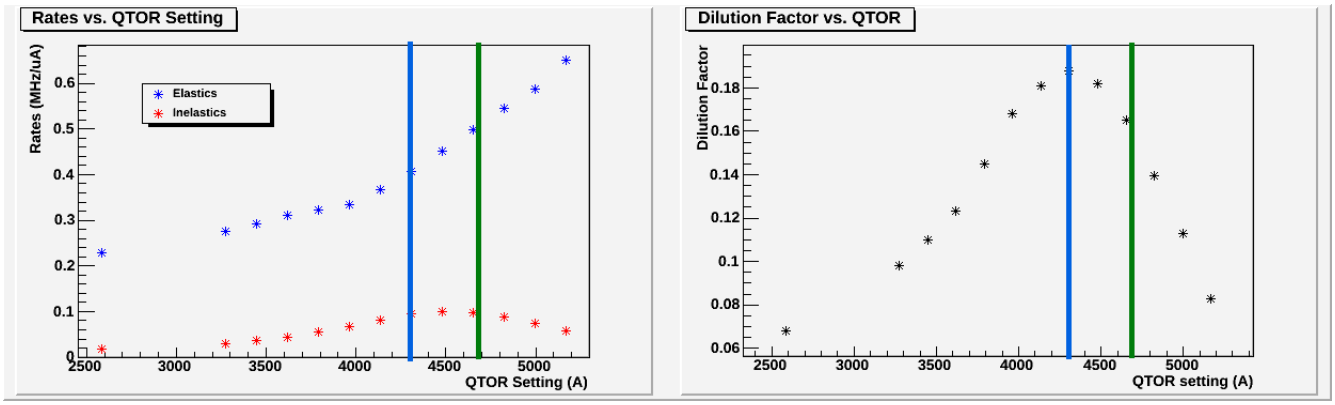


**Figure 6.4:** *Geant3 simulations of rates(Figure 6.1) and dilution factors(Figure 6.2) over a range of toroidal spectrometer settings(QTOR). The maximum inelastic dilution factor is highlighted in blue, but was not used due to high possibility of two pion production in the signal. The spectrometer setting highlighted in green was chosen for a large inelastic dilution factor as well as reducing the possible two pion production component.*

6.5 has the same spectrometer settings highlighted to show how the statistical error per day changes with relation to the toroidal spectrometer setting.

As the spectrometer setting was selected, it was necessary to confirm the simulations missing mass was within the Δ resonance (1232 ± 120 Mev). As shown in Figure 6.6b, the missing mass was 1189 MeV, comfortably within the Δresonance. The momentum, $Q^2 = 0.011\text{GeV}^2$, is shown in Figure 6.6a.

These values have since been confirmed by Geant4 simulations as well, with the momentum($Q^2$), scattering angle($\theta$), and missing mass(W) shown in Figure 6.7 and summarized in Table 6.3.

**Table 6.3:** *Nominal 877 Kinematics*

| $Q^2$ | $\theta$ | W |
|---|---|---|
| 11.081 m($\text{GeV}^2$) | 8.346° | 1.1909 GeV |

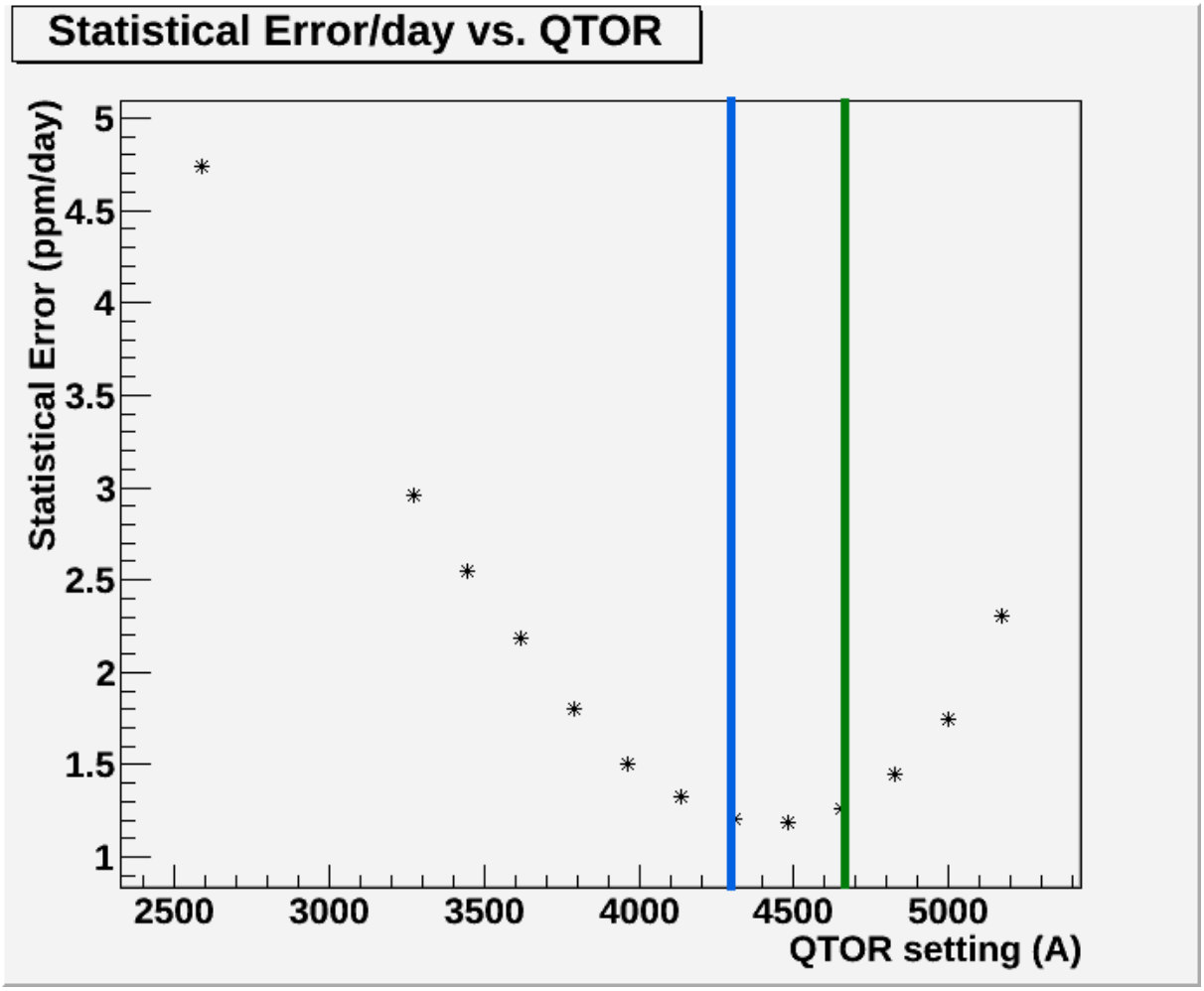


**Figure 6.5:** *As the beam current during the 877 MeV running was 90 μA, the statistical error for each day of running could be estimated with Geant3 over a range of the toroidal spectrometer settings(QTOR). The blue highlighted line is the maximum inelastic dilution factor, while the green highlighted line is the setting chosen to balance maximizing inelastic dilution factor with minimizing two pion production. The statistical error per day for the two settings are comparable.*

### 6.1.2 Data Quality

Once the 877 MeV data was taken, the first task was to confirm that all the data was of acceptable quality. This was done via a series of checks of both external parameters and data values on runlets, which were on average about six minutes of data taking. Analyzing the data required a clean data set to be identified first. In the end only 35 runlets were

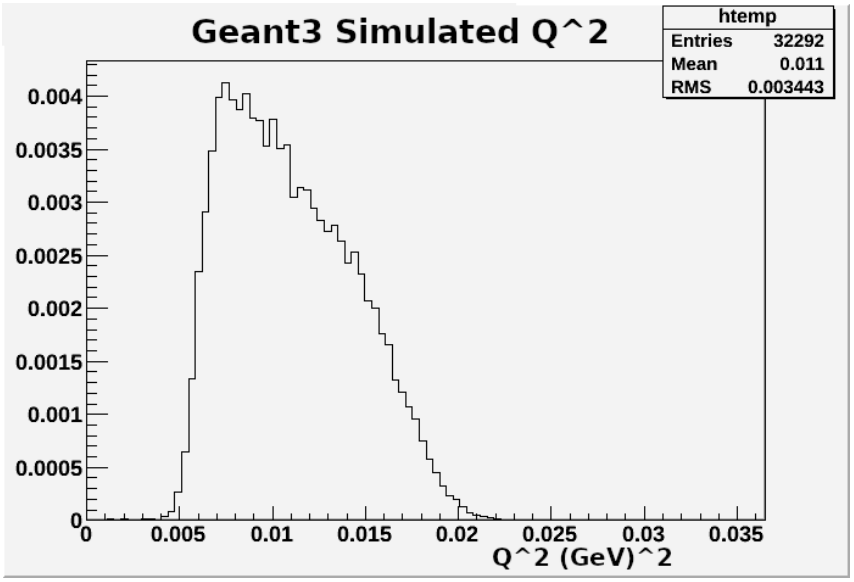


**(a)** $Q^2$.

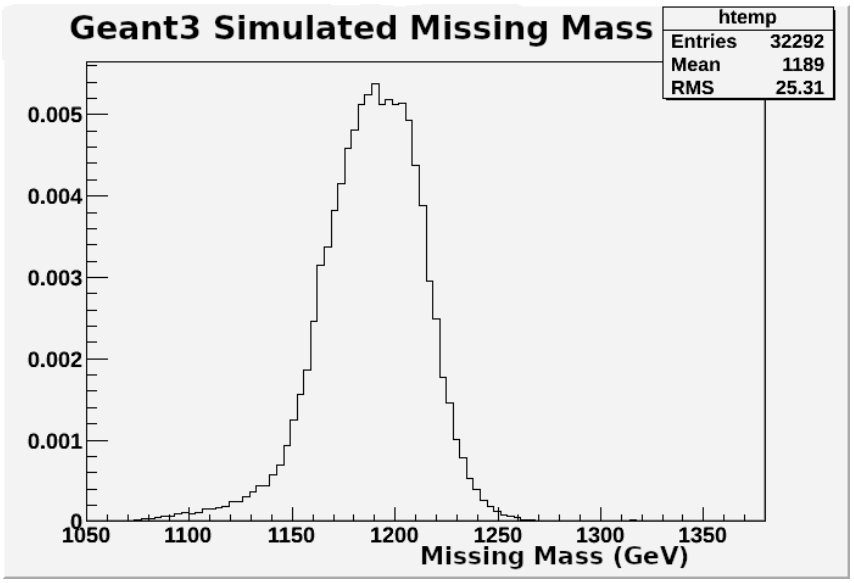


**(b)** *Missing mass.*

**Figure 6.6:** *The Geant3 simulation results for QTOR = 4652 A, the toroidal spectrometer setting chosen for the 877 MeV running. These were determined during the planning stage.*

removed from a data set of 2000+ runlets.

The first check consisted of checking the consistency of toroidal spectrometer(QTOR) setting. The first thing of note was two off-peak runs were taken in order to check back-

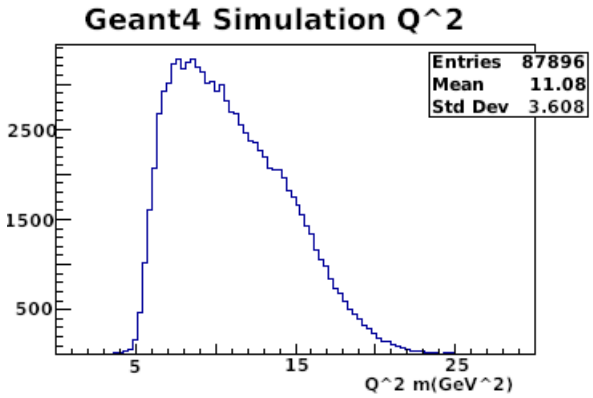


**(a)** $Q^2$.

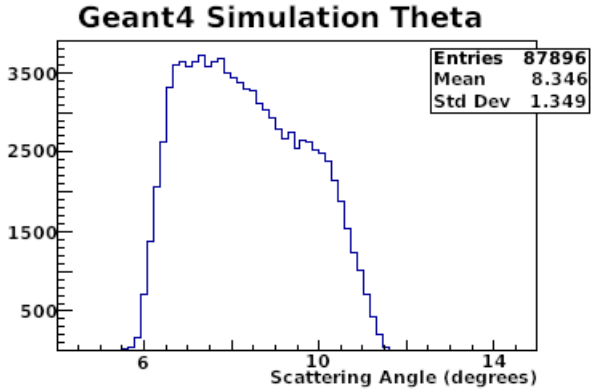


**(b)** *Scattering Angle*($\theta$).

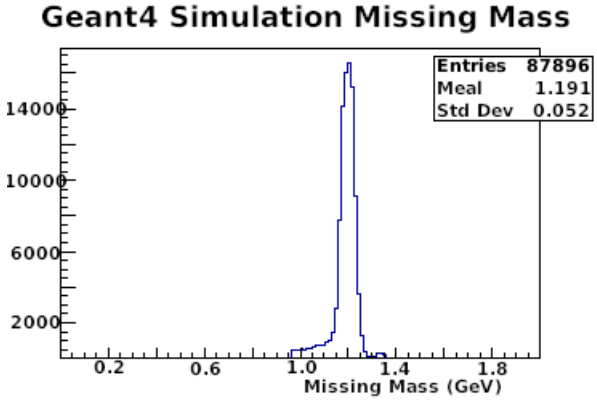


**(c)** *Missing mass.*

**Figure 6.7:** *The Geant4 Simulation results for QTOR = 4652 A, the toroidal spectrometer setting chosen for the 877 MeV running. These were determined after the data taking was complete. Images produced by Valerie Gray [18].*

grounds. This data clearly could not be included within the main data set as the kinematics would not match with the inelastic interaction. Due to these two runs, 28 runlets were removed from the data set. There were also 5 QTOR trips that caused single runlets to have incorrect magnetic fields. These runlets were also removed.

The next consideration was the BCM charge asymmetries. The relevant BCMs during this time period were 5, 6, and 8. There were six runlets identified having abnormally large values for the important BCMs over the course of the 877 MeV running. Of these six runlets, only two ended up being removed from the data set due to being associated with IHWP changes. IHWP changes were known to cause large BCM charge asymmetries.

Helicity-correlated beam parameters were also checked. These variables include beam position X and Y, beam angle X' and Y', beam energy, and beam charge. While there were multiple runlets with oddly large values for these parameters, there was no external justification for removing these runlets from the dataset.

To check for any overall effect of leaving in the questionable data, a study where all the runs that contained questionable data were removed from the data set. This study showed no obvious change in the data set's mean values and spread for various quantities. Therefore the majority of the questionable data was kept in the data set, except for questionable data associated with external reasons. The off-peak QTOR runs, QTOR trips, and the runlets associated with IHWP changes made up the data removed from the 877 MeV data, and the remaining data was defined as the clean data set.

**Table 6.4:** *877 MeV Inelastic Data Running Conditions*

| Beam Current | Magnetic Field |
|---|---|
| 90.64 $\mu$A | 4649 A |

**Table 6.5:** *877 MeV Inelastic Data Helicity Correlated Beam Parameters.*

| Helicity Correlated Variable | Mean(IN) | Mean(OUT) |
|---|---|---|
| X [nm] | $-9.49 \pm 5.62$ | $45.94 \pm 3.70$ |
| Y [nm] | $-0.7385 \pm 10.82$ | $-35.34 \pm 4.20$ |
| X' [$\mu$rad] | $0.0765 \pm 0.1276$ | $0.7267 \pm 0.0923$ |
| Y' [$\mu$rad] | $0.0040 \pm 0.3653$ | $-0.8161 \pm 0.2058$ |
| Energy [ppm] | $0.0031 \pm 0.0011$ | $-0.0043 \pm 0.0006$ |
| Charge [ppm] | $-0.0233 \pm 0.6150$ | $0.1235 \pm 0.1591$ |

### 6.1.3 Beam Conditions

During the 877 MeV running, the running conditions were significantly different than the nominal $Q_{weak}$ running. Table 6.4 shows the running conditions for the 877 MeV dataset.

The helicity-correlated beam parameters for the 877 MeV data set are found in Table 6.5. The ideal set of beam parameters would have all the values being consistent with zero. The 877 MeV parameters are sufficiently close to zero to be able to rely on the data. The parameters fall within the normal constraints of linear regression and beam modulation system.

As was previously mentioned, the 877 MeV running had a large ($\sim 43\%$) transverse component. This component is demonstrated in Figure 6.8, where the IN(blue) and OUT(red)

states have clear sinusoidal shapes of the form

$$A = B_0 \cos\left(\frac{\pi}{180}\left(45\left(N_{\text{Octant}} - 1\right) + \phi_0\right)\right) + C. \tag{6.3}$$

This fit defines the transverse asymmetry ($B_0$), the longitudinal asymmetry($C$), and the phase ($\phi_0$). It fits the asymmetry ($A$) using the angular position of the octants. The IN and OUT components can be combined for a null check,

$$\text{NULL} = \frac{\text{IN} + \text{OUT}}{2}. \tag{6.4}$$

The null check is the green line in Figure 6.8, where it is clearly in agreement with zero. This demonstrates how the azimuthal symmetry of the $\text{Q}_{\text{weak}}$ apparatus allowed the transverse component to be averaged out.

## 6.2 Extracting the Raw Inelastic Asymmetry

The raw inelastic asymmetry is determined via combining the integrated yields in each PMT of the MD for both helicity states (+ and −),

$$A^i_{\text{tube}} = \frac{Y^{+,i}_{\text{MD}} - Y^{-,i}_{\text{MD}}}{Y^{+,i}_{\text{MD}} + Y^{-,i}_{\text{MD}}}. \tag{6.5}$$

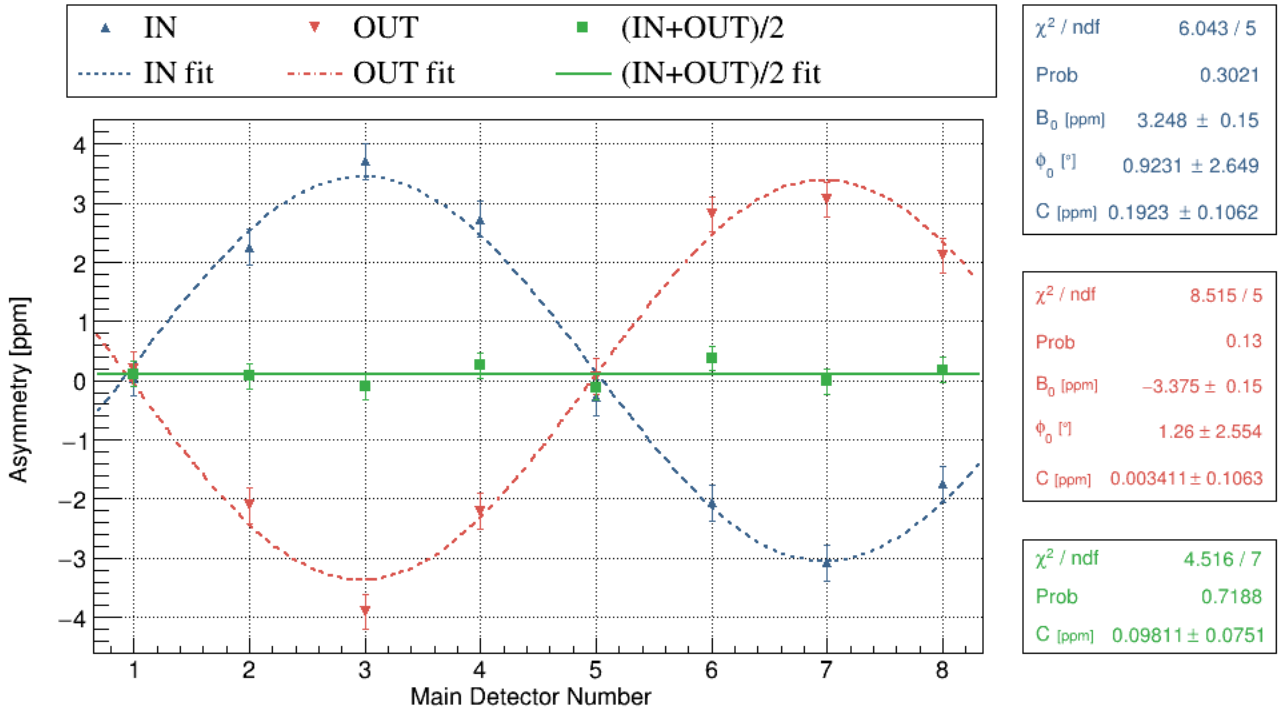


**Figure 6.8:** *An insertable half-wave plate was used as a slow helicity check. The blue data represents the data for which the plate was in the beamline, while the red represents the data for which the plate was not in the beamline. The green line is the average of the two, and is in agreement with zero as is expected.*

The 16 PMTs need to be combined in order to extract the raw inelastic asymmetry. The simplest way to combine them is an average of the PMTs,

$$A_{\text{raw}} = \frac{\sum_{i=1}^{16} A^i_{\text{tube}}}{16}. \tag{6.6}$$

However, due to the large transverse component in the 877 MeV data, it is not quite as simple as a straight average. To obtain a better asymmetry, the individual PMT asymmetries need to be fitted with the fit shown in Equation (6.3). The result of fitting the PMT+, the PMT-, and the PMTAVG for each MD is shown in Figure 6.9 where $B_0$ is the parity-

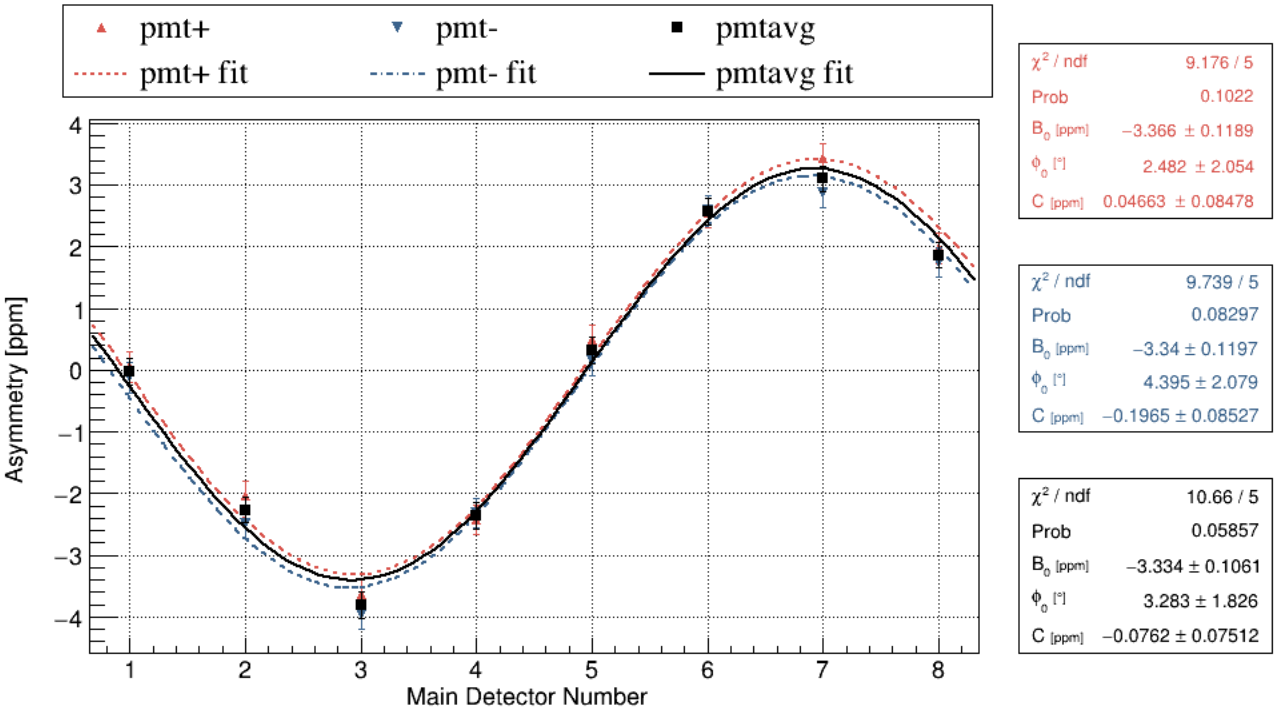


**Figure 6.9:** *Each main detector had two PMTs attached to it. The raw asymmetries recorded by the left(red) and right(blue) PMTs are shown, as is the combined PMT asymmetry(black). The asymmetries are then fit using Equation (6.3). The combined PMT asymmetry gives the raw longitudinal asymmetry as C and the raw transverse asymmetry as* $B_0$.

conserving transverse asymmetry and C is the parity-violating longitudinal asymmetry.

**Table 6.6:** *Raw 877 MeV Asymmetries*

| Type | Asymmetry |
|---|---|
| Longitudinal | $-76 \pm 75$ ppb |
| Transverse | $-3.3 \pm 0.1$ ppm |

The raw transverse and longitudinal asymmetries are displayed in Table 6.6. The raw asymmetry can be written out as a combination of the measured asymmetry and false asym-

metries contributing to the signal,

$$A_{\text{raw}} = A_{\text{M}} - A_{\text{false}}. \tag{6.7}$$

The next step involves isolating the measured asymmetries from any false asymmetries that are contributing to the signal.

## 6.3 Extracting the Measured Inelastic Asymmetry

While the $Q_{\text{weak}}$ apparatus was designed to minimize false asymmetries, it was not possible to eliminate them. Equation (6.7) can be rewritten to account for them,

$$A_{\text{M}} = A_{\text{raw}} + A_{\text{BCM}} + A_{\text{beam}} + A_{\text{BB}} + A_{\text{L}} + A_{\text{T}} + A_{\text{bias}} - A_{\text{blinding}}. \tag{6.8}$$

Due to the large transverse component of the signal during the 877 MeV data taking, there will be discussion of both transverse and longitudinal asymmetry components for each correction. The determinations of these shall be discussed over the course of this chapter.

### 6.3.1 Beam Current Monitor Correction

Beam Current Monitors(BCMs), as discussed in Section 3.2.3, were used to noninvasively measure the charge. At the time of 877 MeV data taking, there were three BCMs being used

to track the beam current. The correction $A_{\mathrm{BCM}}$ is defined to be zero due to the normalization of the main detector signal to average of the BCM signals, as shown in Equation (3.5).

Disagreement between the BCMs is the source of the systematic error for this correction. To account for this, the differences between the charge asymmetries in the various combinations of BCMS are calculated,

$$\delta\mathrm{BCM}_{ij} = A_{\mathrm{BCM,i}} - A_{\mathrm{BCMi,j}}. \tag{6.9}$$

The average values of these differences over the 877 MeV running is summarized in Table 6.7, while the values over the 877 MeV running are shown in Figure 6.10.

**Table 6.7:** *BCM Differences for BCM5, BCM6, and BCM8 over the 877 MeV data taking.*

| $\delta\mathrm{BCM}_{56}$ | $\delta\mathrm{BCM}_{58}$ | $\delta\mathrm{BCM}_{68}$ |
|---|---|---|
| $-5.2 \pm 7.8$ ppb | $0.9 \pm 5.4$ ppb | $6.9 \pm 7.6$ ppb |

An error bar of 10 ppb was selected to take into account the precision with which the differences between the BCM charge asymmetries were determined, leading to a final correction of

$$A_{\mathrm{BCM}} = 0 \pm 10 \text{ ppb}. \tag{6.10}$$

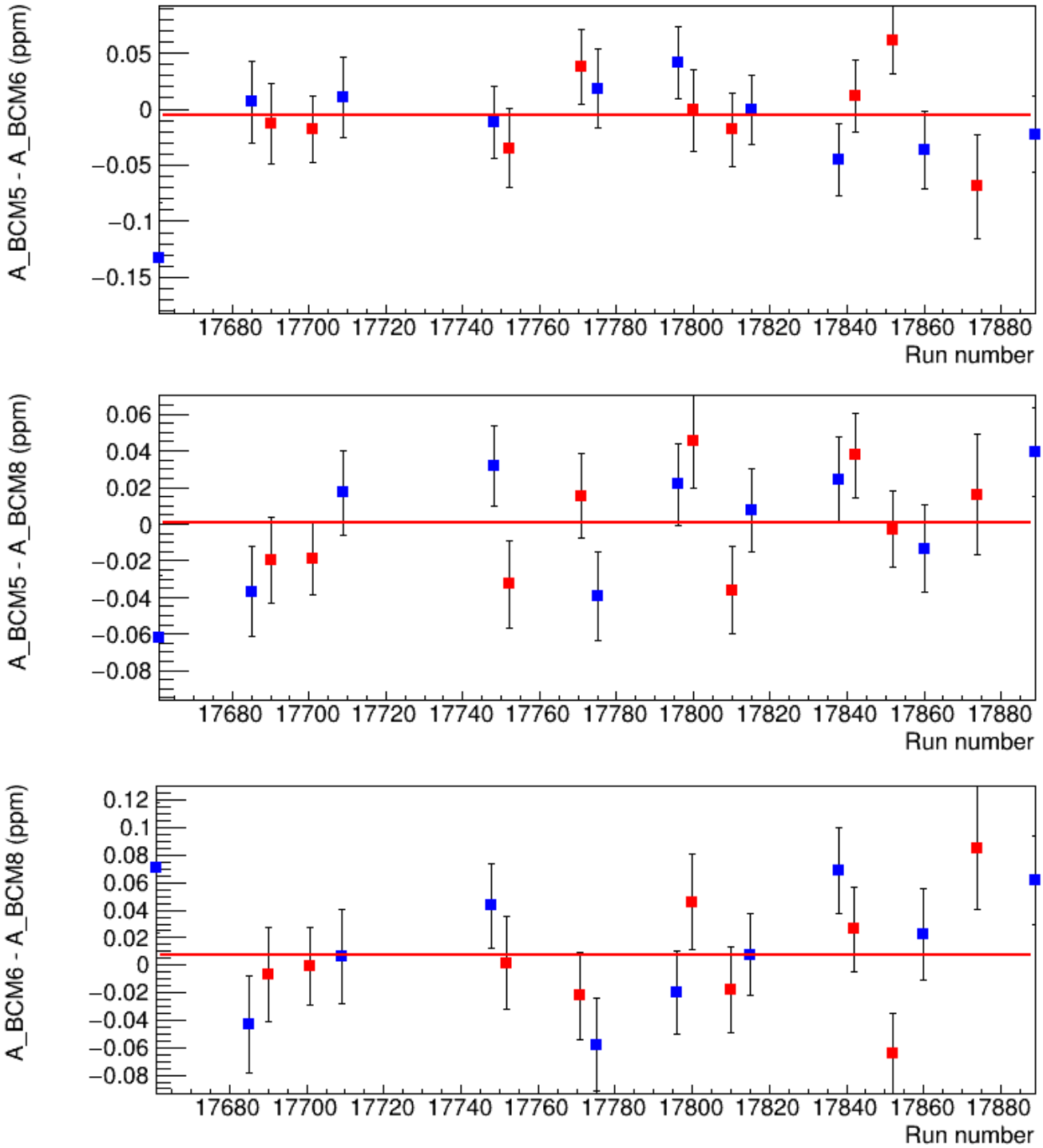


**Figure 6.10:** *The average charge asymmetry differences between two beam current monitors(BCMs) as calculated per eight hours of data over the course of the 877 MeV running. The blue data points represent the insertable half-wave plate being in the path of the laser, while the red points represent the plate being out. The average values represented by the red lines are found in Table 6.7.*

### 6.3.2 Helicity-Correlated beam motion correction

There were five beam properties that were helicity correlated and therefore generated false asymmetries in the signal. These five beam parameters were X position, Y position, X' angle, Y' angle, and energy. Natural motion in the beam parameters provided a method to determining the degree to which the change in parameter affected the signal. A process referred to as regression was used to determine the correction. The correction combined the helicity-correlated beam differences ($\Delta X_i$) with sensitivities of the signal to the beam parameter changes ($\delta A/\delta X_i$) determined through regression,

$$A_{\text{beam}} = -\sum_{i=1}^{5} \left(\frac{\delta A}{\delta X_i}\right) \Delta X_i. \tag{6.11}$$

When this correction was applied on the runlet time scale, the resulting data was referred to as "on" regression($A_{\text{on}}$) shown in Figure 6.11. The raw data, without including this correction, was referred to as "off" regression ($A_{\text{off}}$). To obtain the correction for the 877 MeV running, the difference between $A_{\text{on}}$ and $A_{\text{off}}$ is taken. The correction between the regressed value and the raw values is referred to as $A_{\text{beam}}$. The correction value is

$$A_{\text{beam}} = A_{\text{on}} - A_{\text{off}} = -0.095 \text{ ppm } + 0.076 \text{ ppm } = -18 \text{ ppb}. \tag{6.12}$$

As the error bars on both $A_{\text{on}}$ and $A_{\text{off}}$ are due to the same data, the error bar for $A_{\text{beam}}$ cannot be easily determined from them. Instead, a cross-check on the regression can be done

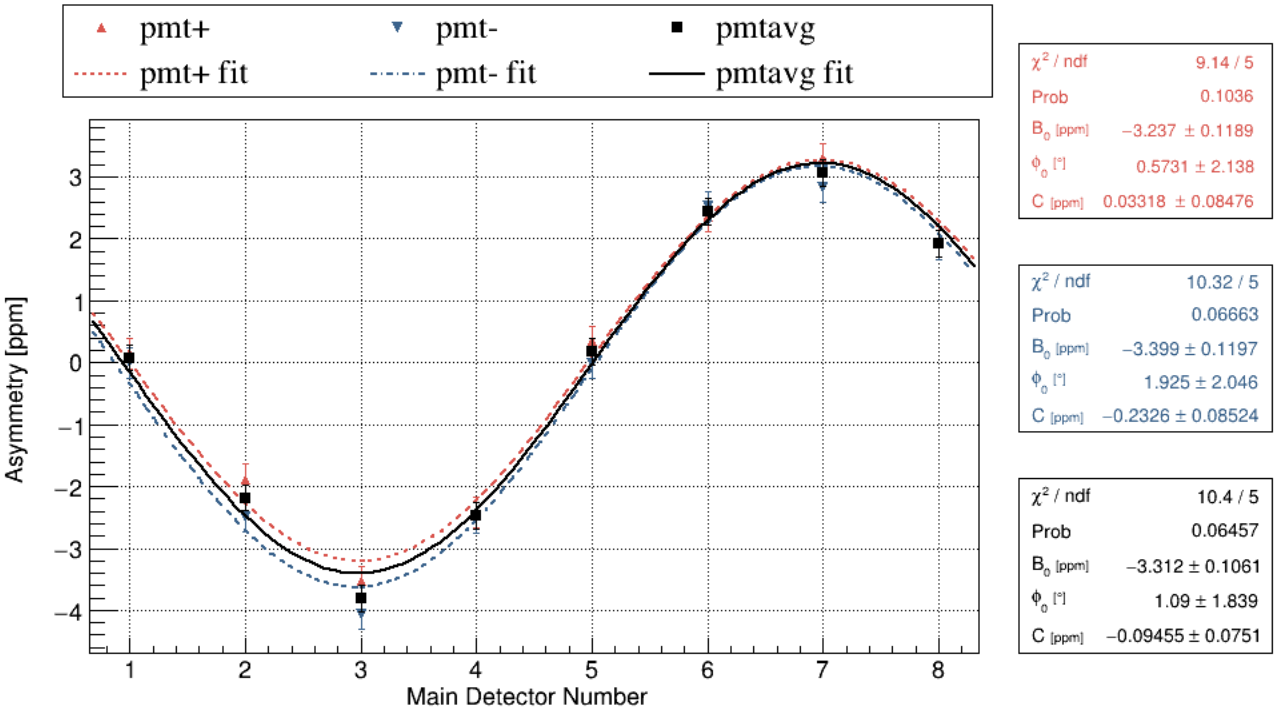


**Figure 6.11:** *Each main detector had two PMTs attached to it. The regressed asymmetries recorded by the left(red) and right(blue) PMTs are shown, as is the combined PMT asymmetry(black). The asymmetries are then fit using Equation 6.3. The combined PMT asymmetry gives the regressed longitudinal asymmetry as $C$ and the regressed transverse asymmetry as $B_0$ for the 877 MeV running.*

by looking at the beam sensitivites over the full 877 MeV running. Figure 6.12 shows that these values are constant over the running period. That allows an estimate of $A_{\text{beam}}$ to be determined by using Equation (6.11) on the averaged values. This data is summarized in Table 6.8.

Averaging over the 877 MeV run period gives a correction of $A_{\text{beam}} = -0.026 \pm 0.003$ ppm. While that provides an error bar of 3 ppb, the differences between the runlet time scale $A_{\text{beam}}$ and this one suggests that a more conservative error bar (10 ppb) should be imposed,

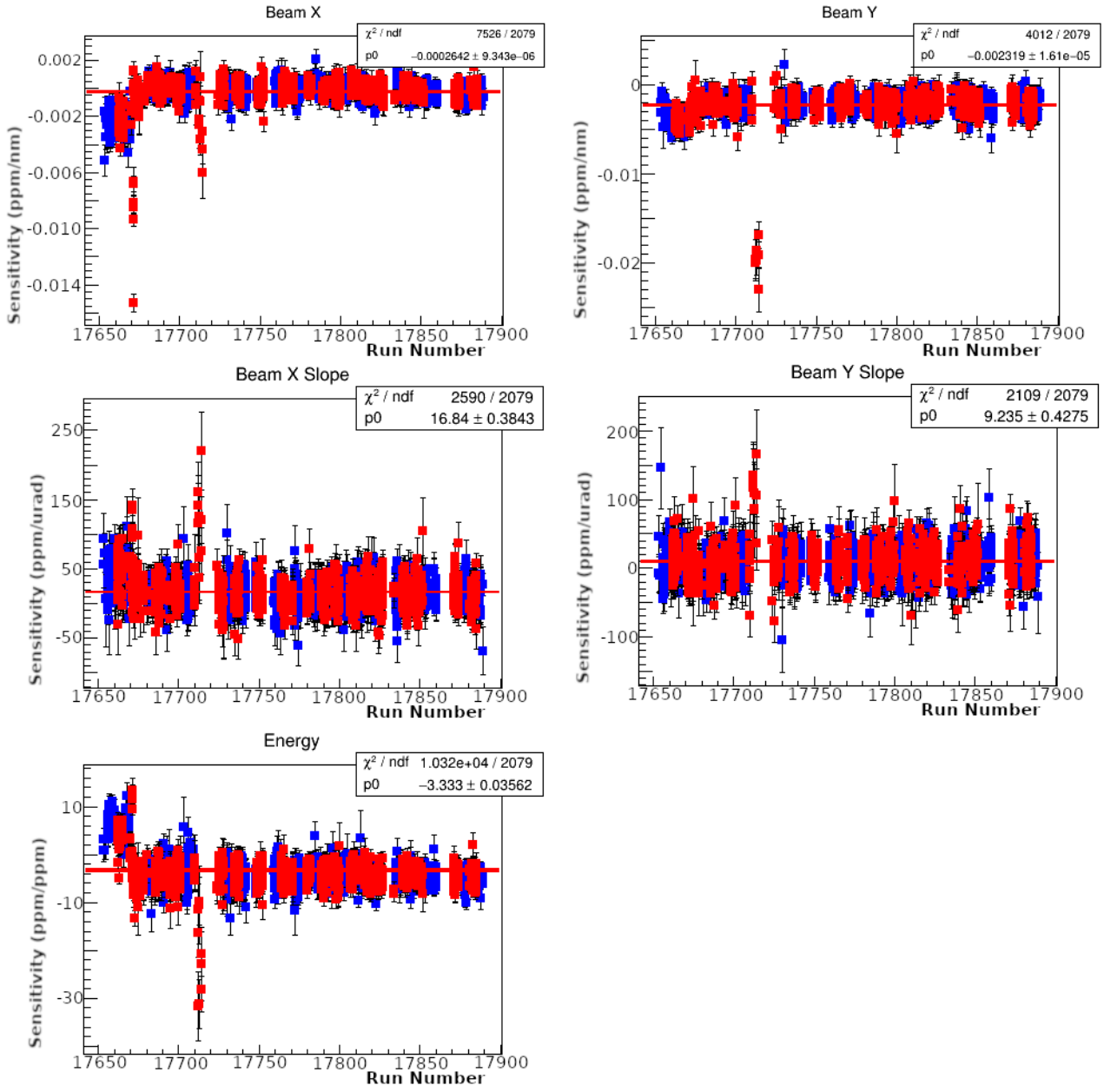


**Figure 6.12:** *The sensitivities of the five helicity correlated beam parameters(beam x, beam y, beam x', beam y', and energy) as calculated for each runlet. The blue data points represent the insertable half-wave plate being in the path of the laser, while the red points represent the plate being out.*

**Table 6.8:** *The helicity correlated beam parameters and the asymmetry's sensitivity to them.*

| Parameter | $X_i$ | $\delta A/\delta X_i$ | $\left(\frac{\delta A}{\delta X_i}\right)\Delta X_i$ |
|---|---|---|---|
| X | $27 \pm 1$ nm | $-0.00026 \pm 0.00001$ ppm/nm | $-0.0071 \pm 0.0004$ ppm |
| Y | $-9.5 \pm 1.0$ nm | $-0.0023 \pm 0.0000$ ppm/nm | $0.022 \pm 0.002$ ppm |
| X' | $0.26 \pm 0.02$ nrad | $17 \pm 0.0$ ppm/nrad | $0.0044 \pm 0.0004$ ppm |
| Y' | $-0.35 \pm 0.04$ nrad | $9.2 \pm 0.4$ ppm/nrad | $-0.0032 \pm 0.0004$ ppm |
| Energy | $-3.1 \pm 0.3$ ppb | $-3.3 \pm 0.0$ ppm/ppb | $0.010 \pm 0.001$ ppm |
| Total | | | $-0.026 \pm 0.003$ ppm |

leading to the final correction of

$$A_{\text{beam}} = -18 \pm 10 \text{ ppb}. \tag{6.13}$$

### 6.3.3 Beamline Background Asymmetry Correction

As was described in Section 3.6.2, a tungsten-copper beam collimator was introduced into the beamline in order to limit background signal in the detectors. However, there was some beam that scattered off of this collimator and the beamline with a large asymmetry and contributed to the signal in the main detectors.

Via the use of two inch tungsten shutters that blocked the beam in octants 1 and 5, this beamline background could be measured. It was found to be highly correlated with the upstream(US) luminosity monitors. The correlation is shown in Figure 6.13. The US luminosity monitor asymmetry($A_{\text{USLumi}}$) is also required in order to determine the false

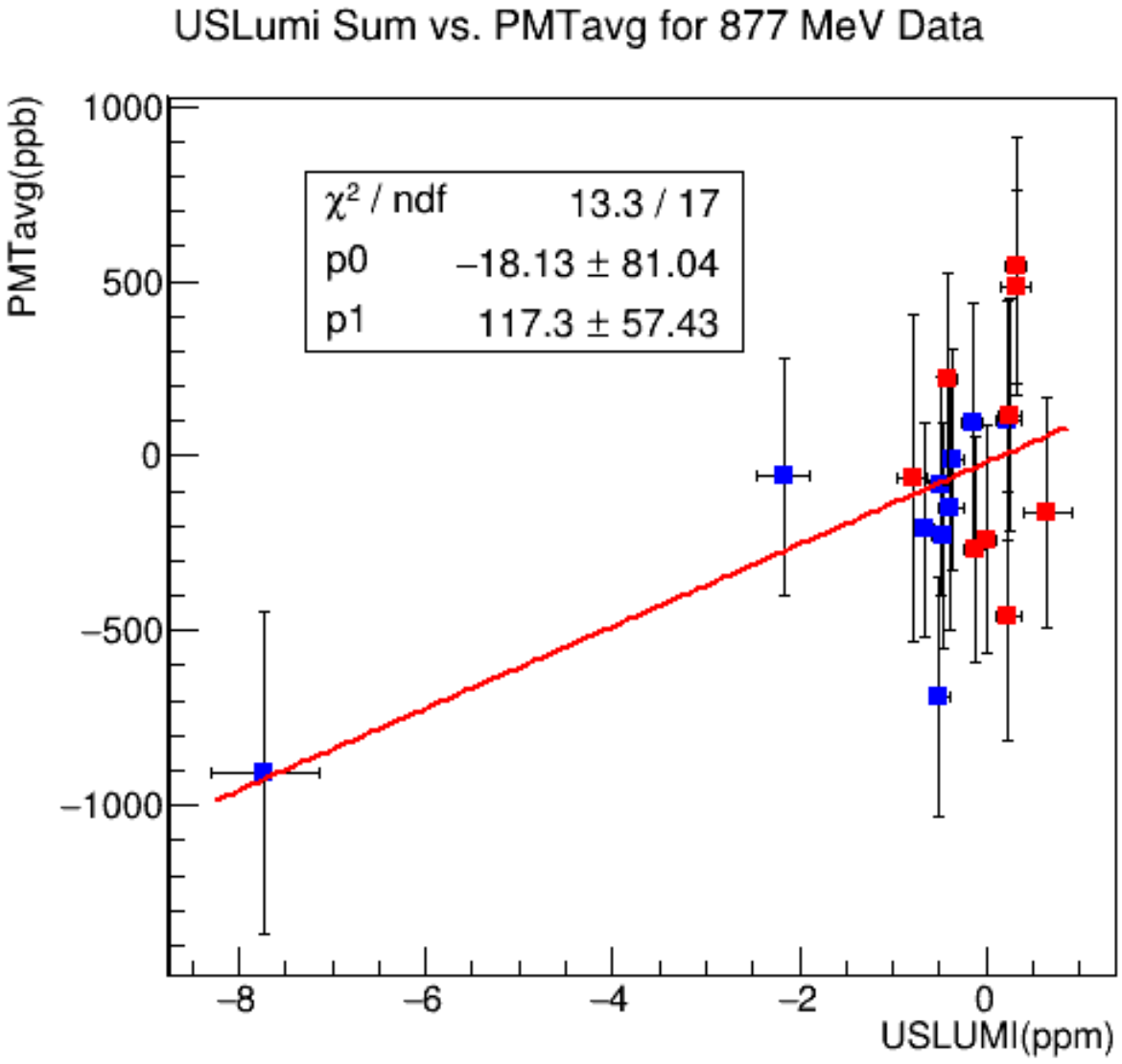


**Figure 6.13:** *The averaged asymmetries of the main detector photomultiplier tubes per eight hours of data were correlated with the US luminosity monitor asymmetries which were highly correlated with the beamline background. The blue data points represent the insertable half-wave plate being in the path of the laser, while the red points represent the plate being out. Removing the outlier does not significantly change the fit.*

asymmetry. This is shown in figure 6.14.

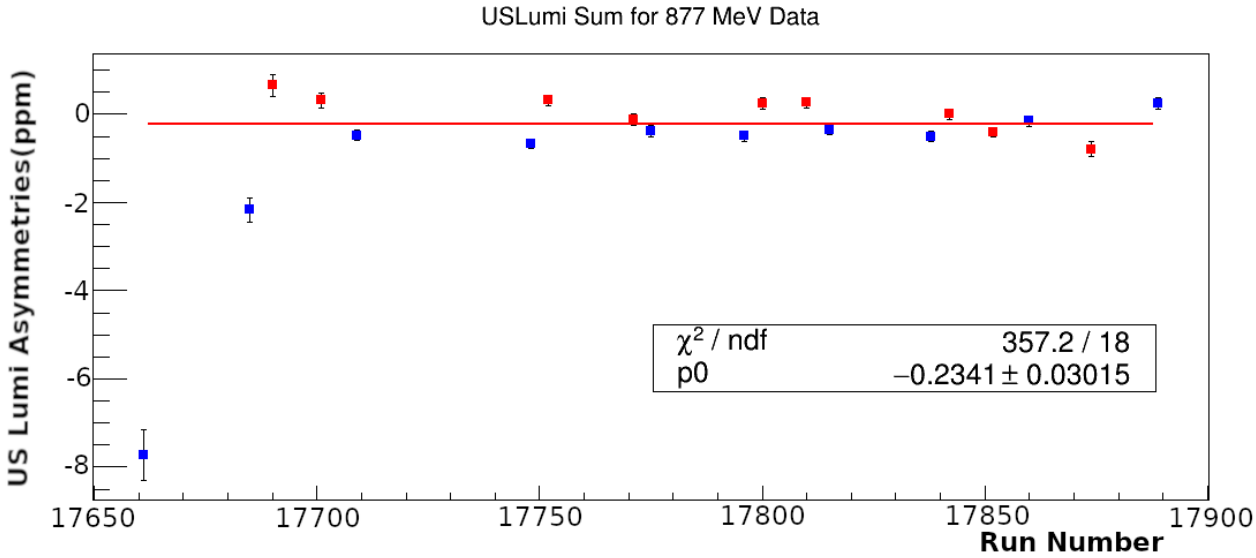


**Figure 6.14:** *The US luminosity monitor asymmetries, which were highly correlated to the beamline background, per eight hours of data over the 877 MeV running. The blue data points represent the insertable half-wave plate being in the path of the laser, while the red points represent the plate being out.*

The beamline background false asymmetry($A_{\mathrm{BB}}$) can be determined via

$$\begin{aligned} A_{\mathrm{BB}} &= -\frac{dA_{\mathrm{PMTavg}}}{dA_{\mathrm{USLumi}}} \times A_{\mathrm{USLumi}} \\ &= -\left(117.3 \pm 57.43 \frac{\mathrm{ppb}}{\mathrm{ppm}}\right) \times (-0.2341 \pm 0.0301 \text{ ppm}) \\ &= 27.46 \pm 13.90 \text{ ppb}. \end{aligned} \tag{6.14}$$

### 6.3.4 Linearity Correction

The linearity referred to in this section refers to the ideal situation where the output voltage of the detector would have a linear relationship with the beam signal. In reality, there was nonlinearity introduced into the electronics chain both in the Beam Charge Monitor(BCM)

and in the Cherenkov detector itself.

In order to document this nonlinearity, bench tests were performed with a spare photo-tube and the full $Q_{weak}$ electronics chain. These bench tests used three light-emitting diodes of different colors and at different frequencies to develop a relationship between the detector output voltage and the nonlinearity present in the electronics chain. The results for the 877 MeV running conditions are shown in Figure 6.15. [2]

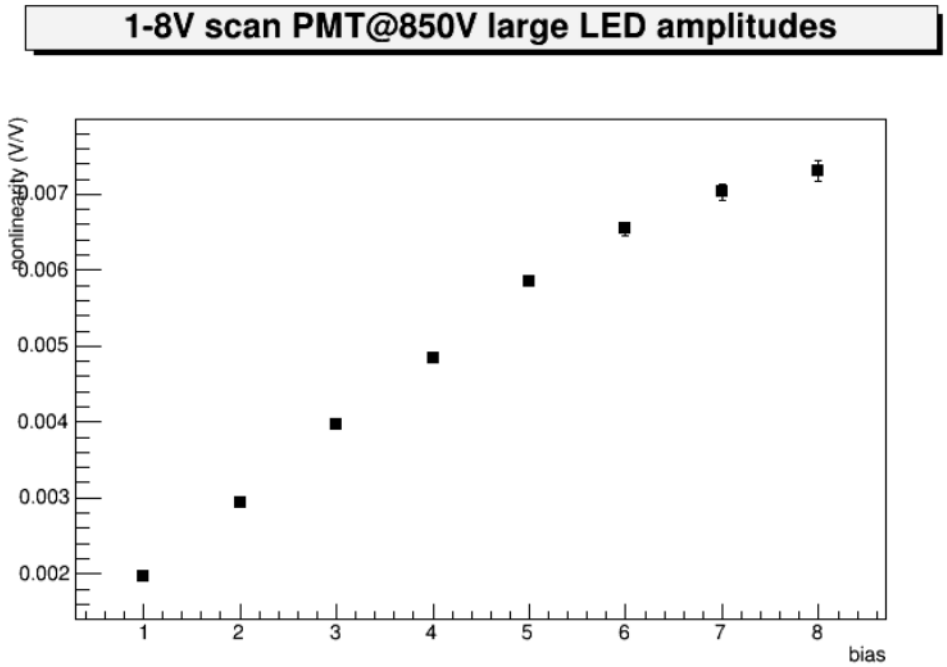


**Figure 6.15:** *Various detector output voltages(bias) was mimicked in a series of bench tests. The resulting nonlinearities have a mostly linear relationship with these values. Image taken from the dissertation of Wade Duvall. [2]*

The detector output voltage for the 877 MeV running was 0.23 V. The linear nature of Figure 6.15 between 0-6 V allows the extrapolation of the curve down to the 877 MeV running detector output voltage, which gives a nonlinearity of $x = 0.0013 \pm 0.0050$. The linearity correction($A_L$) depends on the determined nonlinearity($x$) of the electronics chain

and the raw asymmetry ($A_{\text{raw}} = -0.076 \pm 0.075$ ppm) via

$$\begin{aligned} A_L &= -x * A_{\text{raw}} \\ &= -\left(0.0013 \pm 0.0050\right)\left(-0.076 \pm 0.075 \text{ ppm}\right) \\ &= 0.099 \pm 0.393 \text{ ppb}. \end{aligned} \tag{6.15}$$

### 6.3.5 Transverse Asymmetry Correction

Unlike in the main $Q_{\text{weak}}$ measurement, the 877 MeV running had a large transverse component. This was due to Hall A having priority, leading to a non-integer number of turns for the beam before entering Hall C causing the g-2 precession of the Jefferson Lab Accelerator to not be optimized for maximum longitudinal polarization.

The transverse asymmetry($A_{\text{T}}$), driven by parity-conserving two-photon-exchange [70], is mostly compensated for by the azimuthal symmetry of the apparatus. The asymmetries of the various main detectors can be fit via Equation (6.3), as seen in Figures 6.9 and 6.11.

However the azimuthal symmetry was not perfect, and survey data on the actual placement of the detectors relative to the ideal positions was used to determine a correction. The beam can be transversely polarized either horizontally (parallel to floor of hall) or vertically (perpendicular to the floor of hall). Survey results revealed no breakage of the symmetry in the vertical direction, but the horizontal symmetry was broken. [44] The 877 MeV transverse signal was purely horizontal, and therefore a nonzero correction is required.

To correct for the known broken asymmetry, a symmetry factor is required. A symmetry factor is determined by comparing the offset(false parity-violating asymmetry) seen by the detectors caused by a purely transverse beam, in this case horizontal, and the amplitude of the measured transverse asymmetry. The 877 MeV transverse asymmetry correction accounts for the survey determined broken horizontal symmetry factor of 92.

It is possible that there other, unknown sources of transverse signal in the $Q_{weak}$ apparatus. To account for this possibility, data taken with purely horizontal transverse beam at nominal $Q_{weak}$ kinematics can be used. This data had a transverse asymmetry of 4.8 ppm with an offset of $0.0110 \pm 0.0610$ ppm, leading to a symmetry factor of 70. It gives a lower limit of how much transverse beam affects the longitudinal measurement, and therefore is used as the error bar for this correction. The final transverse asymmetry correction is

$$A_T = -\frac{A_{\text{trans}}}{92} \pm \frac{A_{\text{trans}}}{70} = -\frac{3.3 \text{ ppm}}{92} \pm \frac{3.3 \text{ ppm}}{70} = -36 \pm 47 \text{ ppb}. \tag{6.16}$$

### 6.3.6 Rescattering Bias Correction

The rescattering bias was a systematic effect that was discovered in the data after data taking had finished. Lead preradiators had been placed in front of the eight main detectors to minimize low energy beamline backgrounds. The longitudinally polarized scattered electrons precessed while swimming through the magnetic field, gaining a transverse polarization. These electrons then caused showers within the lead preradiators. The lead imparted a parity

conserving asymmetry between the left and right PMTs mounted on the main detector, introducing a difference between the asymmetries seen by the two PMTs. This effect was hidden by the averaging of the PMTs during data taking, but as the symmetry of the main detectors is not perfect there was a bias in the asymmetry.

The best way to observe this effect in the data involves plotting the difference between the right and left PMTs for each main detector. The $Q_{weak}$ main measurement saw an asymmetry of 300 ppb in this data(Figure 5.6). As seen in Figure 6.16, the 877 MeV asymmetry for this is $A_{\text{pmtdd}} = 260 \pm 120$ ppb, which is in agreement with the nominal $Q_{weak}$ kinematics.

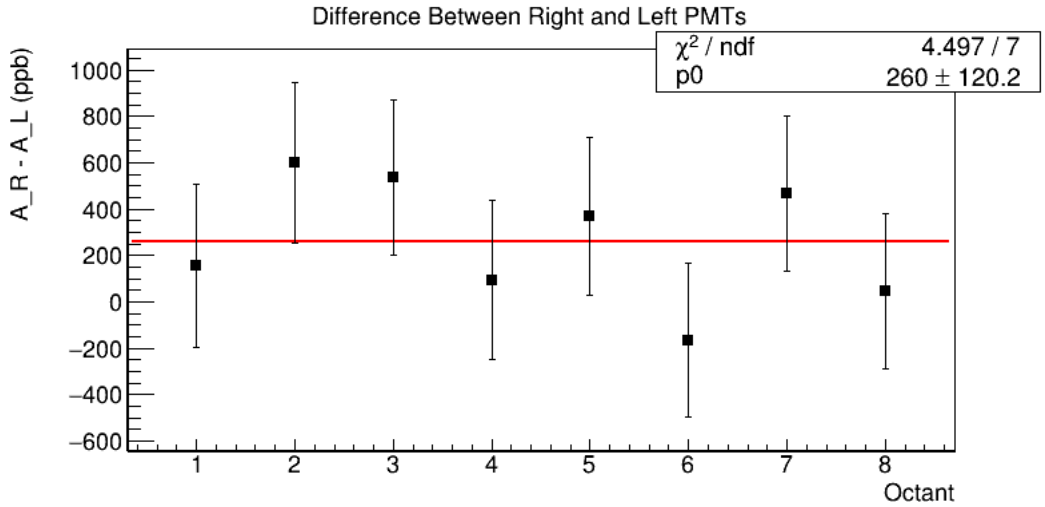


**Figure 6.16:** *Each main detector has a photomultiplier tube on both ends. The rescattering bias is visible when the difference between the right PMT and the left PMT for each main detector is compared.*

As the 877 MeV running value for the double difference, a term used to refer to the difference between two asymmetries, of the right and left PMTs is in agreement with $Q_{weak}$'s main measurement value, the 877 MeV running can use the rescattering bias correction

developed for the main measurement. The correction,

$$A_{\text{bias}} = 4.3 \pm 10 \text{ ppb}, \tag{6.17}$$

was determined via a Guassian process regression model using simulated microscopic model results of the asymmetry versus the scattering angles of the shower electrons.

### 6.3.7 Blinding Factor Correction

A blinding factor was applied to the raw data in order to prevent bias in the analysis. Different blinding factors were applied for the three main running periods: commissioning. run 1, and run 2. These factors were applied by the software during analysis.

As the 877 MeV data was taken during run 2, it shares the same blinding factor

$$A_{\text{blinding}} = 6.669 \pm 0 \text{ ppb}. \tag{6.18}$$

Due to it being applied via software, there is no error associated with it.

### 6.3.8 $A_{\mathbf{M}}$

Now that the false asymmetry corrections have been quantified, the measured asymmetry($A_{\text{M}}$) can be determined from the false asymmetry, as shown in Equation (6.8). The final values for the false asymmetry corrections can be found in Table 6.9, and the resulting measured

**Table 6.9:** *The final false asymmetry corrections to the raw inelastic asymmetry for 877 MeV running.*

| Correction | | Value |
|---|---|---|
| Beam Monitor Correction | $A_{\mathrm{BCM}}$ | $0 \pm 10$ ppb |
| Helicity Correlated Beam Correction | $A_{\mathrm{beam}}$ | $-18 \pm 10$ ppb |
| Beamline Background Correction | $A_{\mathrm{BB}}$ | $27 \pm 14$ ppb |
| Linearity Correction | $A_{\mathrm{L}}$ | $0.099 \pm 0.393$ ppb |
| Transverse Asymmetry Correction | $A_{\mathrm{T}}$ | $-36 \pm 47$ ppb |
| Rescattering Bias Correction | $A_{\mathrm{bias}}$ | $4.3 \pm 10$ ppb |
| Blinding Factor Correction | $A_{\mathrm{blinding}}$ | $6.669 \pm 0$ ppb |

asymmetry is

$$\begin{aligned} A_{\mathrm{M}} =& A_{\mathrm{raw}} + A_{\mathrm{BCM}} + A_{\mathrm{beam}} + A_{\mathrm{BB}} + A_{\mathrm{L}} + A_{\mathrm{T}} + A_{\mathrm{bias}} - A_{\mathrm{blinding}} \\ =& (-76 \pm 75 \text{ ppb}) + (0 \pm 10 \text{ ppb}) + (-18 \pm 10 \text{ ppb}) \\ &+ (27 \pm 14 \text{ ppb}) + (0.099 \pm 0.393 \text{ ppb}) + (-36 \pm 47 \text{ ppb}) \\ &+ (4.3 \pm 10 \text{ ppb}) - (6.669 \pm 0 \text{ ppb}) \\ =& -105 \pm 75 \text{ (stat)} \pm 52 \text{ (syst) ppb.} \end{aligned} \tag{6.19}$$

## 6.4 Extracting the Inelastic Asymmetry

Now that the false asymmetries have been removed from the signal, the measured asymmetry($A_{\mathrm{M}}$) needs to be corrected for the polarization, the various backgrounds, and a few multiplicative

factors to determine the inelastic asymmetry($A_{\rm inel}$) via

$$A_{\rm inel} = R_{\rm tot}\frac{A_{\rm M}/P - A_{\rm bkgd}}{1 - f_{\rm tot}}. \tag{6.20}$$

The backgrounds that need to be accounted for consist of the elastic signal($f_{\rm ep}A_{\rm ep}$), the aluminum signal from the entrance and exit windows($f_{\rm al}A_{\rm al}$), the neutral transport signal($f_{\rm nt}A_{\rm nt}$), and the pion contribution to the signal($f_{\rm pn}A_{\rm pn}$). These corrections are combined to get the background asymmetry,

$$A_{\rm bkgd} = f_{\rm ep}A_{\rm ep} + f_{\rm al}A_{\rm al} + f_{\rm nt}A_{\rm nt} + f_{\rm pn}A_{\rm pn} = C_{\rm ep} + C_{\rm al} + C_{\rm nt} + C_{\rm pn}. \tag{6.21}$$

The dilution factors($f_i$) for the various backgrounds contributed to $f_{\rm tot}$, as does the dilution factor for the beamline background($f_{\rm BB}$). The total dilution factor for the backgrounds is determined by summing these components,

$$f_{\rm tot} = f_{\rm ep} + f_{\rm al} + f_{\rm nt} + f_{\rm pn} + f_{\rm BB}. \tag{6.22}$$

The multiplicative factors consist of the electromagnetic radiative correction($R_{\rm RC}$), the detector response correction($R_{\rm det}$), the acceptance correction($R_{\rm acc}$), and the $Q^2$ correction($R_{Q^2}$). These are combined to form $R_{\rm tot}$,

$$R_{\rm tot} = R_{\rm RC}R_{\rm det}R_{\rm acc}R_{Q^2}. \tag{6.23}$$

These values are all required before an inelastic asymmetry for the 877 MeV running can be determined.

### 6.4.1 Polarization

There were two methods used to track the polarization during the $Q_{weak}$ Experiment. The first used the established Møller polarimeter(Section 3.3.1) but this was an invasive process and was limited to very low beam currents. It involved measuring the parity-conserving asymmetry of electrons scattered on a polarized iron foil target. The second method involved a new Compton polarimeter. The Compton polarimeter(Section 3.3.2) was noninvasive and continuously monitored the beam polarization at full beam energy. For the main $Q_{weak}$ measurement, these two methods were in good agreement. [8] [51]

The 877 MeV running occurred during wien9 of the main $Q_{weak}$ measurement. The polarization for that running period was $P_{\text{wien9}} = (87.71 \pm 0.62)\%$. However there was a second factor to take into account for the 877 MeV running. When the electrons are sent through the accelerator, the electron spins precess due to the magnetic moment of the electron which is referred to as the $g$ factor. If $g = 2$ the spin precession would match the momentum precession of the electron, but $g - 2 \neq 0$ so the spin precesses faster than the momentum of the electron. Therefore part of the selection of the nominal $Q_{weak}$ kinematics was confirming that the electrons would precess an integer multiple of $\pi$ before entering Hall C, allowing the large longitudinal polarization.

However during the 877 MeV running, Hall C was not the primary hall and the spin precession of the electrons before entering the hall was not an integer of $\pi$, which lead to the large transverse polarization, as is visible in Figure 6.17. The longitudinal precession polarization($P_{\text{prec}}$) was (89.9±1.7)%. These two polarizations need to be combined to extract the final polarization,

$$P_{877\text{ MeV}} = P_{\text{wien9}} \times P_{\text{prec}} = (87.71 \pm 0.62)\% \times (89.9 \pm 1.7)\% = (78.9 \pm 1.6)\%. \tag{6.24}$$

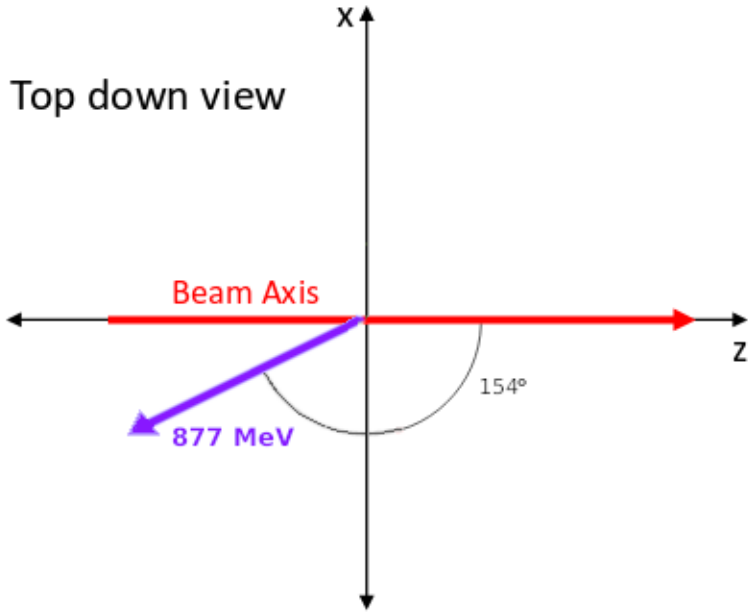


**Figure 6.17:** *The spin precession of the electrons during the 877 MeV running period led to a polarization angle of $\theta = 154°$, which had a large transverse component that was opposite of the standard transverse set up.*

### 6.4.2 Elastic Background

The main $Q_{weak}$ measurement tracked the elastic signal, but the 877 MeV running was focused on the inelastic signal. However, there was still a large component of elastically scattered electrons present in the 877 MeV signal due to the elastic radiative tail. Therefore, just as the main measurement had to compensate for the inelastic background, the 877 MeV running had to compensate for the elastic background.

To determine the effect of the elastic background, two quantities are required: the fraction of signal that is elastic (dilution factor: $f_{\rm ep}$) and the elastic asymmetry ($A_{\rm ep}$). The dilution factor was determined via simulation, to be $f_{\rm ep} = 79.0\%$ [19] and had an error of 5% applied to it,

$$f_{\rm ep} = (79.0 \pm 4.0)\%. \tag{6.25}$$

The simulation of the contributions to the 877 MeV running signal over a range of scattered electron momenta is shown in Figure 6.18.

Due to the kinematic difference between the 877 MeV running and the main $Q_{weak}$ measurement, the final elastic asymmetry is not directly applicable to the elastic background. Also due to being firmly in the radiative tail, the bremsstrahlung radiation has to be taken into account. Bremsstrahlung radiation can occur before or after the primary scattering of the electron, so to estimate the asymmetry in this region two extreme situations were considered.

The first situation assumes that all bremsstrahlung radiation occurs before the electron

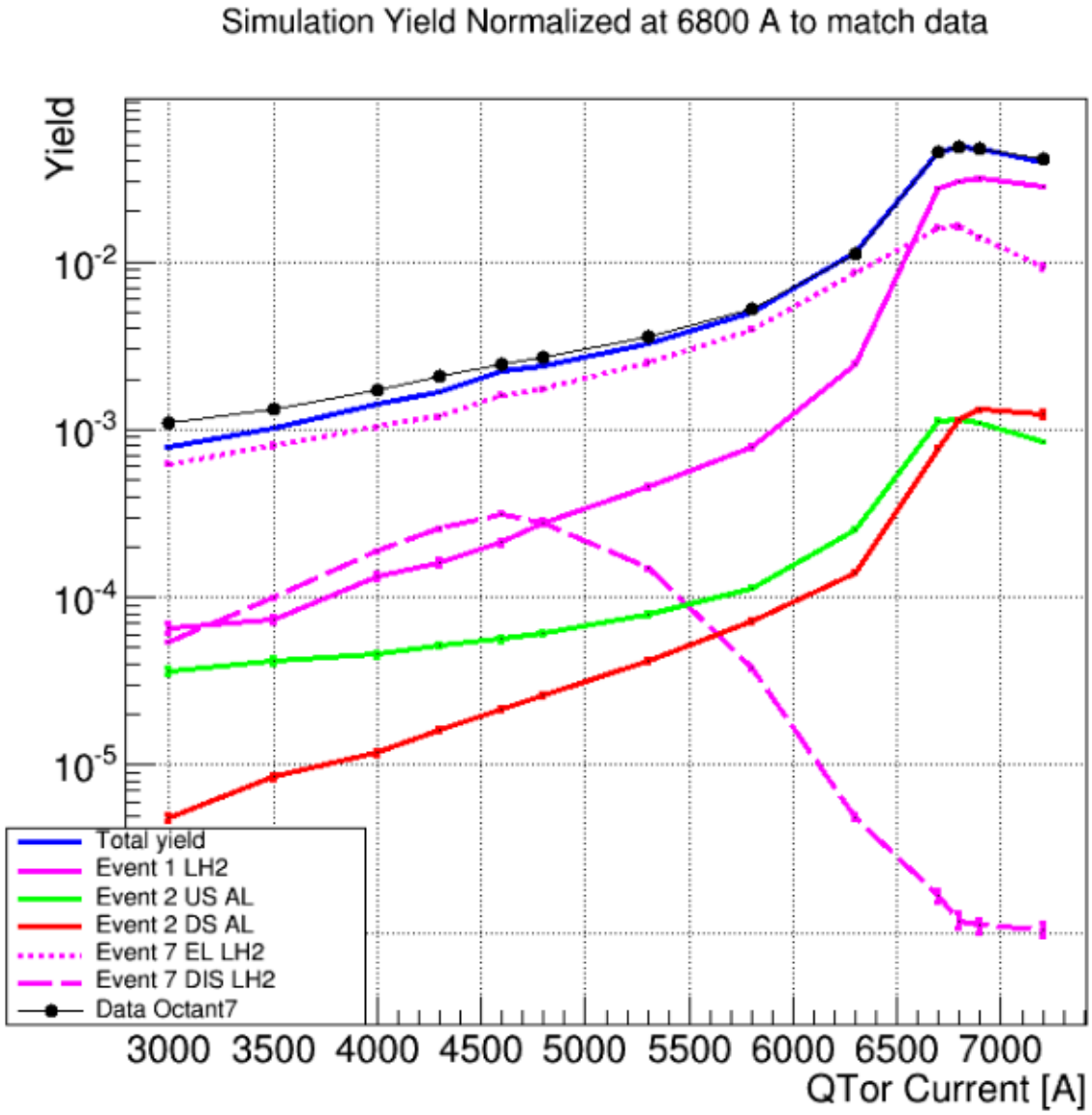


**Figure 6.18:** *This shows a scan of scattered electron momenta, done by varying the current to the toroidal spectrometer(QTOR). The 877 MeV data for Octant 7 is shown by the black dots, and the total simulated rate(shown in blue) has been normalized to match the 877 MeV data at the elastic peak of QTOR Current = 6800 A. The disagreement between data and simulation at the inelastic peak(4650 A) drives the chosen relative error bars for dilution factors. The other lines represent the various components of the simulated rate: Event 1 LH2 is elastic events within 15 MeV of the elastic peak, Event 2 US AL is the aluminum entrance window, Event 2 DS Al is the aluminum exit window, Event 7 EL LH2 is elastic events outside of 15 MeV of the elastic peak, and Event 7 DIS LH2 is the inelastics. The Δ peak is visible in Event 7 DIS LH2. The dilution factor for each component is determined by the ratio of it to the total rate including pions, not shown here, at a given QTOR. Image from the dissertation of Hend Nuhait [19].*

scatters off the primary proton. In that case, the phase space point of the average kinematics ($\langle Q^2 \rangle = 0.011$ GeV$^2$ and $\langle \theta \rangle = 8.346^\circ$) can be used to calculate an asymmetry of $A_{\mathrm{ep},1} = -81$ ppb.

The second situation assumes that all bremsstrahlung radiation occurs after the electron scatters off the primary proton. For this case, the scattering can be treated as if it was elastic scattering at 877 MeV. That means that the asymmetry should be computed at the phase space point of the average scattering angle($\theta$) found during nominal $\mathrm{Q}_{\mathrm{weak}}$ running $\langle \theta \rangle = 7.90^\circ$. This $\theta$ results in $Q^2 = 0.0145$ GeV$^2$. These kinematics result in an asymmetry of $A_{\mathrm{ep},2} = -111$ ppb.

In order to span both situations, the final $A_{\mathrm{ep}}$ is the average of the two extremes with an error bar that spans the full range,

$$\begin{aligned} A_{\mathrm{ep}} &= \frac{A_{\mathrm{ep},1} + A_{\mathrm{ep},2}}{2} \pm \left| \frac{A_{\mathrm{ep},1} - A_{\mathrm{ep},2}}{2} \right| \\ &= \frac{-81 + -111}{2} \pm \left| \frac{(-81) - (-111)}{2} \right| \text{ ppb} \\ &= -96 \pm 15 \text{ ppb}. \end{aligned} \tag{6.26}$$

The final correction for the elastic background is determined by combining the elastic dilution factor and the elastic asymmetry,

$$C_{\mathrm{ep}} = f_{\mathrm{ep}} A_{\mathrm{ep}} = (0.790 \pm 0.040)(-96 \pm 15 \text{ ppb}) = -76 \pm 12 \text{ ppb}. \tag{6.27}$$

### 6.4.3 Aluminum Background

When the beam passed through the $LH_2$ target, it entered and exited through thin aluminum windows. These windows were the source of the aluminum background. The entrance window (0.11 mm) and exit window (0.13 mm) were made from same block of aluminum 7075 alloy, as was the dummy target (3.7 mm) used to determine the aluminum asymmetry. The dummy target was thicker than the windows so as to match the radiation length of the normal beam path, the hydrogen target.

In order to determine the aluminum background correction to the measured asymmetry, both the aluminum dilution factor($f_{\rm al}$) and asymmetry($A_{\rm al}$) are required. The aluminum dilution factor was determined via simulation to be $f_{\rm al} = 6.9\%$ [19] and had a relative error of 5% applied to it,

$$f_{\rm al} = (6.9 \pm 0.3)\%. \tag{6.28}$$

There were five data runs taken on the thick aluminum dummy target in order to get a measurement of the aluminum asymmetry. The resulting data is shown in Figure 6.19 using the fit shown in Equation (6.3). Due to the large transverse component, the transverse leakage into the aluminum asymmetry must be corrected before determining a final $A_{\rm al}$ for the 877 MeV running.

The offset, $C = 341 \pm 703$ ppb, represents the raw aluminum longitudinal asymmetry while $B_0 = -5000 \pm 990$ ppb represents the aluminum transverse asymmetry($A_{\rm trans,al}$). The transverse asymmetry can be used to determine the transverse asymmetry correction($A_{\rm T,al}$)

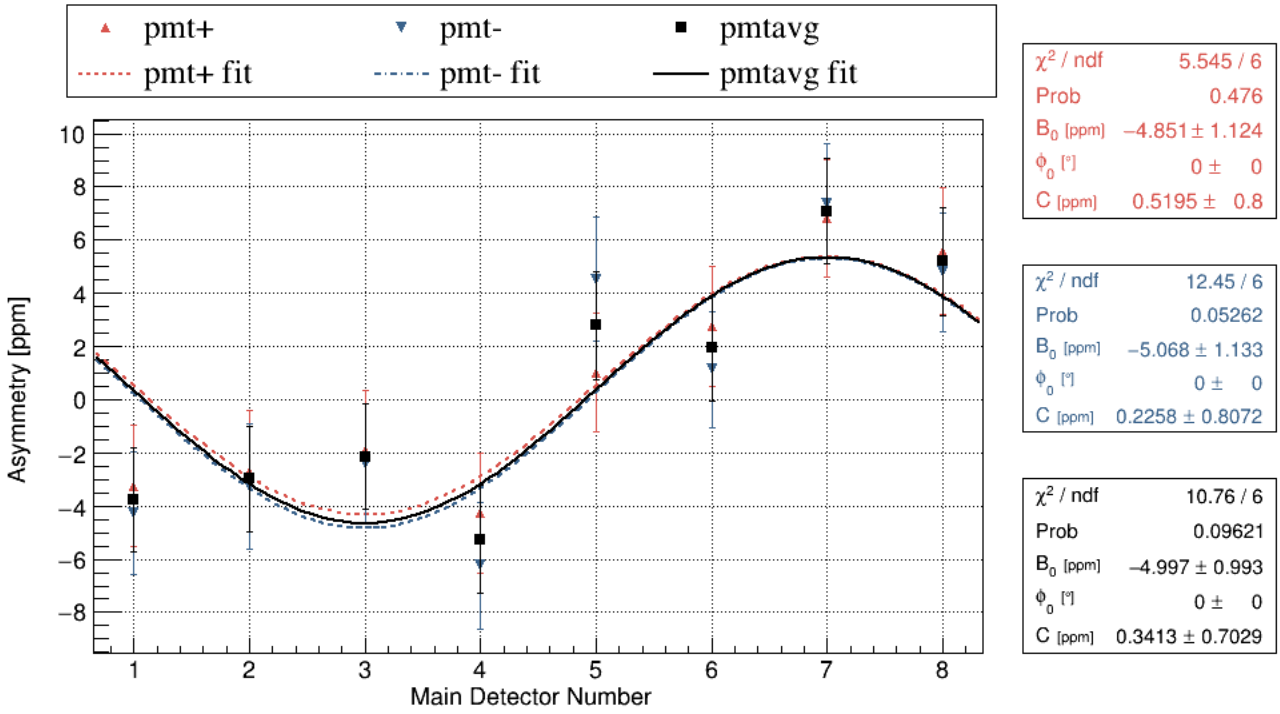


**Figure 6.19:** *The asymmetry for each detector when the beam was passing through the aluminum dummy target. The red data represents the right photomultiplier tube on the individual main detectors, while the blue represents the left tube. The black data is the average of the two photomultiplier tubes. The phase for all fits is set to be 0.*

to the aluminum longitudinal asymmetry in the manner described in Section 6.3.5. The determination of the aluminum transverse correction is

$$A_{\mathrm{T,al}} = -\frac{A_{\mathrm{trans,al}}}{92} \pm \frac{A_{\mathrm{trans,al}}}{70} = -\frac{5.0\ \mathrm{ppm}}{92} \pm \frac{5.0\ \mathrm{ppm}}{70} = -54 \pm 71\ \mathrm{ppb}. \tag{6.29}$$

To get the longitudinal aluminum asymmetry($A_{\mathrm{al,L}}$), the transverse correction($A_{\mathrm{T,al}}$) has to be applied to the raw longitudinal asymmetry($C$)

$$A_{\mathrm{al,L}} = C + A_{\mathrm{T,al}} = (341 \pm 703\ \mathrm{ppb}) + (-54 \pm 71\ \mathrm{ppb}) = 287 \pm 707\ \mathrm{ppb}. \tag{6.30}$$

To get the physics asymmetry for the aluminum($A_{\rm al}$), this longitudinal asymmetry needs to be corrected for the polarization(Equation (6.24)),

$$A_{\rm al} = \frac{A_{\rm al,L}}{P} = \frac{287 \pm 707 \text{ ppb}}{(78.9 \pm 1.6)\%} = 364 \pm 897 \text{ ppb}. \tag{6.31}$$

Now that a final value for the aluminum asymmetry has been determined, it needs to be combined with the dilution factor to extract the aluminum background correction via

$$C_{\rm al} = f_{\rm al} A_{\rm al} \quad = (0.069 \pm 0.003)(364 \pm 897 \text{ ppb}) = 25 \pm 62 \text{ ppb}. \tag{6.32}$$

### 6.4.4 Beamline Background Dilution Factor

The extraction of the Beamline Background Asymmetry was discussed in Section 6.3.3 where it contributes a false asymmetry to the signal. However unlike the other false asymmetry corrections, the beamline background is caused by neutral particles interacting with the main detector. Therefore, the presence of these particles must be taken into account when determining the various contributions to the signal.

It is possible to isolate the beamline background dilution factor by using two inch tungsten shutters placed in octants 1 and 5. These shutters block out the particles that would pass through the main detectors, except for the ones caused by the beamline background. Therefore by comparing the average yields of the blocked(Figure 6.20a) and unblocked(Fig-

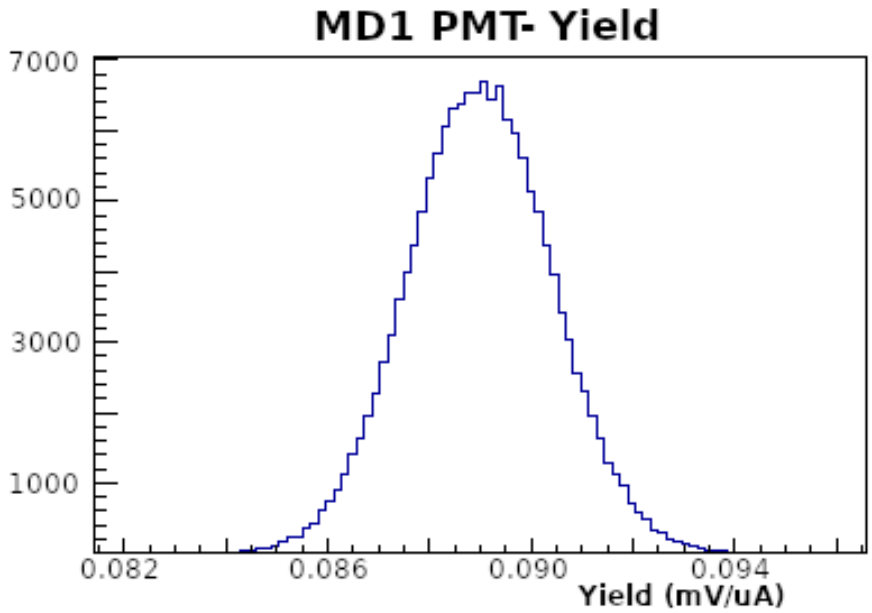


**(a)** *Yield from one of the blocked photo multiplier tube on main detector 1.*

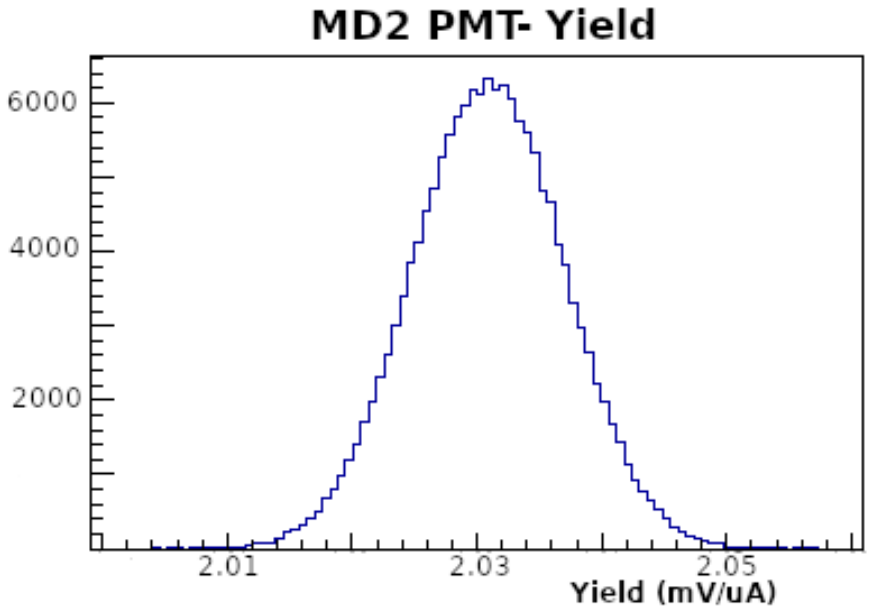


**(b)** *Yield from one of the unblocked photo multiplier tube on main detector 2.*

**Figure 6.20:** *Examples of blocked and unblocked main detector yields via the use of the tungsten shutters.*

ure 6.20b) octants, a dilution factor for the beamline background can be determined:

$$f_{\mathrm{BB}} = \frac{\langle Y_{\mathrm{blocked}} \rangle}{\langle Y_{\mathrm{unblocked}} \rangle} = \frac{0.088}{2.6} = 3.4\%. \tag{6.33}$$

Varying the size of the square the beam was swept across, referred to as a raster scan, provided the means of determining a reasonable error bar. Three sizes of raster were checked for the 877 MeV data while the tungsten shutters were in: 3 mm x 3 mm, 3.5 mm x 3.5 mm, and 4 mm x 4 mm. The resulting beamline background dilution factors are shown in Figure 6.21. The 877 MeV running was taken at a 3 mm x 3 mm raster which matches the dilution factor found in Equation (6.33). As can be seen in Figure 6.21, the variation in raster sizes causes a shift in dilution factor of 0.4%. This can be used as the error bar on the dilution factor, leading to the final beamline background dilution factor

$$f_{\mathrm{BB}} = (3.4 \pm 0.4)\%. \tag{6.34}$$

### 6.4.5 Neutral Background

While scattering off the tungsten plug and beamline caused the beamline background, there were other sources of possible scattering. The primary scattered electrons can have secondary interactions with the concrete shielding(collimators) and the toroidal spectrometer structure [56]. The resulting neutral particles are low-energy and form the neutral background.

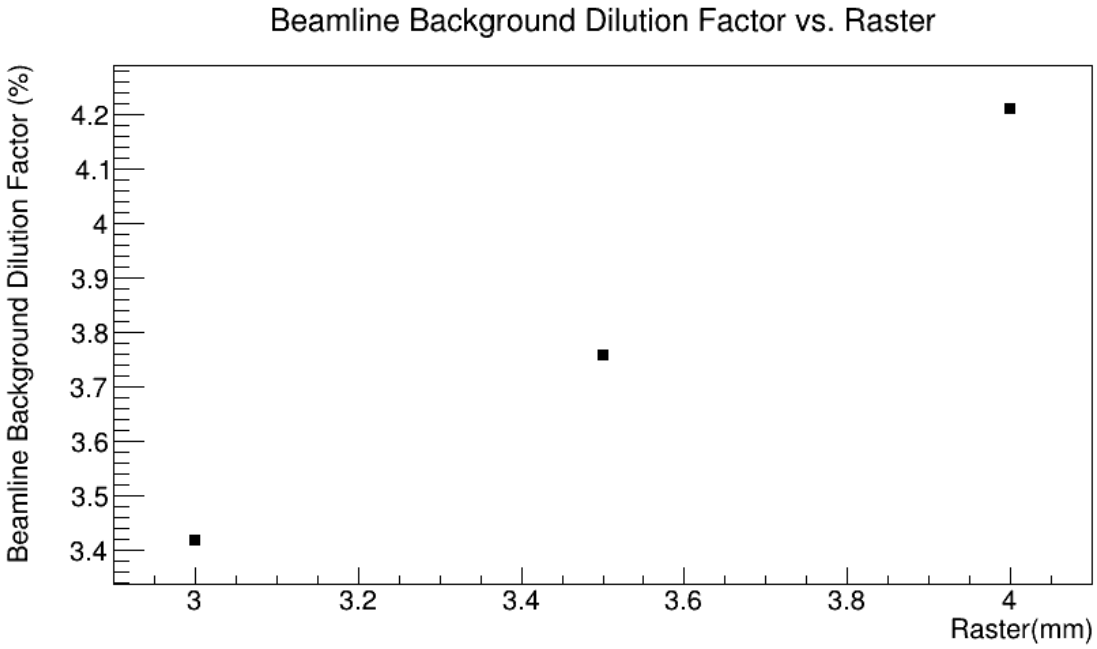


**Figure 6.21:** *The beamline background dilution factors, as determined by taking the ratio of averages of octants blocked by tungsten shutters to unblocked octants, for various square raster side lengths. The 877 MeV running used a 3 mm x 3 mm raster.*

The neutral signal in the main detectors was determined by using thin scintillators to identify the charged particles passing through the detectors in event mode, where the beam current was kept to 100 nA or below, and calculating what percentage of the signal was left. The measured neutral signal dilution factor for the liquid hydrogen target in 877 MeV running was $f_{\text{neutral}} = (3.6 \pm 0.6)\%$ [92]. However, this method does not distinguish between the beamline background and the neutral background, so $f_{\text{BB}}$ from Equation (6.34) must be removed to determine the neutral background dilution factor $f_{\text{nt}}$,

$$f_{\text{nt}} = f_{\text{neutral}} - f_{\text{BB}} = (3.6 \pm 0.6)\% - (3.4 \pm 0.4)\% = (0.2 \pm 0.7)\%. \tag{6.35}$$

The neutral background asymmetry($A_{\text{nt}}$) is composed of low-energy neutral particles

that were caused by high-energy electrons scattering off the shielding or magnet structure. These high-energy electrons were produced via one of three processes: inelastic scattering, aluminum scattering, or elastic radiative tail scattering. By renormalizing the dilution factors of these three processes(found in Equations (6.57), (6.28), (6.25)) and using the asymmetries for these values (found in Equations (6.59), (6.31), (6.26)), a neutral background asymmetry can be determined. Due to this value relying on the final inelastic asymmetry and dilution factor, this was a recursive calculation but only the final values are presented.

The renormalization of the inelastic, aluminum and elastic dilution factors is done via determining the sum of the three relevant dilution factors,

$$f_{\text{tot}}^{\text{nt}} = f_{\text{inel}} + f_{\text{al}} + f_{\text{ep}} = 9.5\% + 6.9\% + 79.0\% = 95.4\%, \tag{6.36}$$

and then taking the ratio of each one individually resulting in

$$\begin{aligned} f_{\text{inel}}^{\text{nt}} &= \frac{f_{\text{inel}}}{f_{\text{tot}}^{\text{nt}}} = \frac{9.5\%}{95.4\%} = 10.0\%, \\ f_{\text{al}}^{\text{nt}} &= \frac{f_{\text{al}}}{f_{\text{tot}}^{\text{nt}}} = \frac{6.9\%}{95.4\%} = 7.2\%, \text{ and} \\ f_{\text{ep}}^{\text{nt}} &= \frac{f_{\text{ep}}}{f_{\text{tot}}^{\text{nt}}} = \frac{79.0\%}{95.4\%} = 82.8\%. \end{aligned} \tag{6.37}$$

These new dilution factors are then used with the related asymmetry to determine a neutral

background asymmetry,

$$\begin{aligned} A_{\rm nt} &= f_{\rm inel}^{\rm nt} A_{\rm inel} + f_{\rm al}^{\rm nt} A_{\rm al} + f_{\rm ep}^{\rm nt} A_{\rm ep} \\ &= (10.0\%)(-1.2 \text{ ppm}) + (7.2\%)(364 \text{ ppb}) + (82.8\%)(-96 \text{ ppb}) \\ &= -174 \text{ ppb}. \end{aligned} \tag{6.38}$$

To account for possible variations, an error bar of 100 ppb is assigned to this asymmetry, leaving a final neutral background asymmetry

$$A_{\rm nt} = -174 \pm 100 \text{ ppb}. \tag{6.39}$$

A correction for the measured asymmetry can now be determined by combining the dilution factor and asymmetry for the neutral background:

$$C_{\rm nt} = f_{\rm nt} A_{\rm nt} \quad = ((0.2 \pm 0.7)\%)(-174 \pm 100 \text{ ppb}) = -0 \pm 1 \text{ ppb}. \tag{6.40}$$

### 6.4.6 Pion Background

The 877 MeV data was taken near the inelastic peak, with a missing mass of $W = 1.1909 \pm 0.0002$ GeV (shown in Figure 6.7c). The pion fraction of the signal is minimal at the elastic peak, but increases significantly at the inelastic peak. As such, both the dilution factor($f_{\rm pn}$) and asymmetry($A_{\rm pn}$) need to be determined. Simulation was used to determine the dilution

factor to be $f_{\rm pn} = 0.97\%$ [19]. It was later determined that the simulation for the pions was not properly performed. To take this into account a relative error of 50% was applied,

$$f_{\rm pn} = (0.97 \pm 0.49)\,\%. \tag{6.41}$$

Further simulation could reduce the size of this error bar.

A different $\rm Q_{weak}$ ancillary measurement determined the longitudinal pion asymmetry at a beam energy of 3.3 GeV, with a value of $22.06 \pm 7.79$ ppm [93]. A crude estimate of the pion asymmetry for a beam energy of 877 MeV can be determined via a few assumptions. Firstly, the 3.3 GeV pion asymmetry value needs to be corrected for the overall beam polarization at the time of running $P^{\rm 3GeV} = (87.0 \pm 0.6)\%$,

$$A_{\rm pn}^{\rm 3GeV} = \frac{22.06 \pm 7.79 \text{ ppm}}{(87.0 \pm 0.6)\%} = 25.36 \pm 8.96 \text{ ppm}. \tag{6.42}$$

The electron momentum for the 3.3 GeV running was $Q^2_{\rm e^-,3GeV} = 0.082\ (\text{GeV})^2$.

The first required assumption is in regards to the composition of the pion fraction. There are two production pathways for the pions that would be in the 877 MeV signal. Pion electroproduction is associated with electron proton scattering with virtual photon exchange. There is a 4-momentum associated with electron scattering events where an electron is detected($Q^2_{\rm e^-}$) and a 4-momentum associated with events where a pion is detected($Q^2_\pi$). The second pathway, pion photoproduction, is associated with real photons generated by

bremsstrahlung in the target. This pathway carries no 4-momentum($Q^2_{\text{photo}} = 0$) and has an asymmetry on the order of hadronic parity violation. The assumption is made that the proportion of pion electroproduction to photoproduction is independent of beam energy, at least within the range of 3.3 GeV and 877 MeV. While it is not done in this document, this assumption can be checked by looking at known pion electroproduction cross-sections.

The second and third assumptions are specific to pion electroproduction. The second assumption is that the total pion asymmetry is proportional to the squared 4-momentum transfer associated with the events where a pion is detected,

$$A_\pi = f_{\text{electro}} K Q^2_{\pi,\text{ electro}} \tag{6.43}$$

where $K$ is an unknown constant and $f_{\text{electro}}$ is the proportion of the pion signal that is electroproduced.

The $Q^2_\pi$ is unknown at both beam energies, but the $Q^2_{e^-}$'s are known. This leads to the final assumption: the ratio $Q^2_\pi/Q^2_{e^-}$ is constant over the range of beam energies.

The second assumption(Equation (6.43)) can be solved for the unknown constant $K$ at both beam energies,

$$K = \frac{A^{3\text{GeV}}_\pi}{f_{\pi,\text{electro,3GeV}} Q^2_{\pi,\text{electro,3GeV}}} = \frac{A^{877\text{MeV}}_\pi}{f_{\pi,\text{electro,877MeV}} Q^2_{\pi,\text{electro,877MeV}}}. \tag{6.44}$$

The first assumption shows that $f_{\pi,\text{electro,3GeV}} = f_{\pi,\text{electro,877MeV}}$, allowing the dilution factors

to be removed from Equation (6.44). Isolating the 877 MeV pion asymmetry leads to

$$A_{\pi}^{877\text{MeV}} = A_{\pi}^{3\text{GeV}} \frac{Q^2_{\pi,\text{electro},877\text{MeV}}}{Q^2_{\pi,\text{electro},3\text{GeV}}}. \tag{6.45}$$

The third assumption is now of use. If the ratio $Q^2_{\pi}/Q^2_{\text{e}^-}$ is a constant, then

$$\frac{Q^2_{\pi,\text{electro},877\text{MeV}}}{Q^2_{\pi,\text{electro},3\text{GeV}}} = \frac{Q^2_{\text{e}^-,877\text{MeV}}}{Q^2_{\text{e}^-,3\text{GeV}}} = \frac{0.011\ (\text{GeV})^2}{0.082\ (\text{GeV})^2} \tag{6.46}$$

is true. Given that $Q^2_{\text{e}^-,3\text{GeV}} = 0.082\ (\text{GeV})^2$ and $Q^2_{\text{e}^-,877\text{MeV}} = 0.011\ (\text{GeV})^2$, the ratio can be reduced to a number. Now Equations (6.42) and (6.46) can be inserted into Equation (6.45) to estimate a pion asymmetry for the 877 MeV running. The result is

$$\begin{aligned} A_{\pi}^{877\text{MeV}} &= A_{\pi}^{3\text{GeV}} \frac{Q^2_{\pi,\text{electro},877\text{MeV}}}{Q^2_{\pi,\text{electro},3\text{GeV}}} \\ &= (25.36 \pm 8.96\ \text{ppm}) \frac{0.011\ (\text{GeV})^2}{0.082\ (\text{GeV})^2} \\ &= 3.40 \pm 1.20\ \text{ppm}. \end{aligned} \tag{6.47}$$

With both a dilution factor and an asymmetry for the pions, the correction is calculated to be

$$C_{\text{pn}} = f_{\text{pn}} A_{\text{pn}} \quad = ((0.97 \pm 0.49)\%)(3.40 \pm 1.20\ \text{ppm}) = 33 \pm 20\ \text{ppb}. \tag{6.48}$$

The assumptions made here can be checked with more in depth studies at a later date.

### 6.4.7 Electromagnetic Radiative Correction

As discussed in Section 6.4.2, bremsstrahlung can occur before and after the primary scattering of the electron. However, there is also a difference in how internal and external bremsstrahlung can affect the kinematics at the point of primary scattering. Bremsstrahlung can cause depolarization of the incident electron and change its energy resulting in the $Q^2$ of the vertex changing. Internal bremsstrahlung occurs in the field of the primary proton being scattered from, while external bremsstrahlung occurs elsewhere in the target. Geant3 simulation was used to determine the radiative correction factor $R_{\mathrm{RC}}$ that accounts for the effects of both. The simulation was performed at the nominal $\mathrm{Q_{weak}}$ kinematics but given that the same target was used for the 877 MeV running and therefore had the same radiation length, the same radiative correction,

$$R_{\mathrm{RC}} = 1.010 \pm 0.005, \tag{6.49}$$

can be used.

### 6.4.8 Detector Response correction

In an ideal situation, the summed signal seen by the two photomultiplier tubes attached to each main detector would be the same no matter where on the bar the scattered electron impacted. However, that was not the case, with the position of the interaction between the main detector and scattered electron having an effect on both the momentum transfer and light generated of that electron. The interaction of those two factors led to a weighted

response in the main detectors. The impact of this effect,

$$R_{\text{det}} = 0.9857 \pm 0.0022, \tag{6.50}$$

was determined via simulation. The simulations compared the kinematics of the ideal situation with the kinematics of the situation weighted by the optical photons generated in the bar.

### 6.4.9 Acceptance correction

The average momentum transfer($\langle Q^2 \rangle$) is treated as a singular value associated with the final asymmetry, but in actuality represents a range of kinematics. The acceptance correction acts to shift the average over $Q^2$ to a value for the average vertex $Q^2$,

$$R_{\text{acc}} = \frac{A\left(\langle Q^2 \rangle\right)}{\langle A\left(Q^2\right) \rangle} \ . \tag{6.51}$$

This correction takes into account the limited acceptance of the toroidal spectrometer and energy loss in the liquid hydrogen target. For the 877 MeV kinematics, the dominant term of the asymmetry varies linearly in $Q^2$ causing $\langle A(Q^2) \rangle = A(\langle Q^2 \rangle)$ which leads to $R_{\text{acc}} = 1$. To take into account higher order terms, a 1% error bar is applied leading to

$$R_{\text{acc}} = 1.000 \pm 0.010. \tag{6.52}$$

### 6.4.10 $Q^2$ correction

A Geant4 simulation was used to determine the various kinematic values for the 877 MeV running. The results can be found in Table 6.3. An error of 0.45% has been applied to the $Q^2$ [94]. The $Q_{weak}$ approach to error on $Q^2$ is to use it as an exact value and use the $\delta A/\delta Q^2$ relation to apply the error on $Q^2$ directly to the asymmetry, via a multiplicative correction with a central value of 1.

For the 877 MeV running the theoretical inelastic asymmetry has two dominant components, one that depends on directly on $Q^2$ and one that depends on $d_\Delta$. The error inflation factor when shifting the error to the asymmetry is

$$\sigma_{R_{Q^2}} = \frac{\delta A/A}{\delta Q^2/Q^2}\sigma_{Q^2} \ . \tag{6.53}$$

In the case that $d_\Delta = 0$, the error inflation factor will simplify to 1, leading to the relative error on the asymmetry to be the same as the relative error on $Q^2$, 0.45%. In the case of $d_\Delta \neq 0$, the asymmetry will be larger than in the $d_\Delta = 0$ case causing the error inflation factor to decrease, meaning that 0.45% will be a safe error bar for this value [95]. The final value for $R_{Q^2}$ is

$$R_{Q^2} = 1.0000 \pm 0.0045. \tag{6.54}$$

**Table 6.10:** *Final Values for all variables to 877 MeV Inelastic Asymmetry*

| Variable | | Value |
|---|---|---|
| Measured Asymmetry | $A_{\mathrm{M}}$ | $-105 \pm 75$ (stat) $\pm 52$ (syst) ppb |
| Polarization | $P$ | $(78.9 \pm 1.6)\%$ |
| Elastic Background Correction | $C_{\mathrm{ep}} = f_{\mathrm{ep}} A_{\mathrm{ep}}$ | $-76 \pm 12$ ppb |
| Aluminum Background Correction | $C_{\mathrm{al}} = f_{\mathrm{al}} A_{\mathrm{al}}$ | $25 \pm 62$ ppb |
| Neutral Background Correction | $C_{\mathrm{nt}} = f_{\mathrm{nt}} A_{\mathrm{nt}}$ | $-0 \pm 1$ ppb |
| Pion Background Correction | $C_{\mathrm{pn}} = f_{\mathrm{pn}} A_{\mathrm{pn}}$ | $33 \pm 20$ ppb |
| Total Dilution factor | $f_{\mathrm{tot}}$ | $(90.5 \pm 4.1)\%$ |
| Total Multiplicative Correction | $R_{\mathrm{tot}}$ | $0.9956 \pm 0.0501$ |

### 6.4.11 Final $A_{\mathrm{inel}}$

Now that the various contributions to the final inelastic asymmetry have been determined, Equation (6.20) can be solved for a final $A_{\mathrm{inel}}$. The first step to solving the equation is to determine the background asymmetry correction $A_{\mathrm{bkgd}}$, shown in Equation (6.21). The final result is

$$\begin{aligned} A_{\mathrm{bkgd}} &= C_{\mathrm{ep}} + C_{\mathrm{al}} + C_{\mathrm{nt}} + C_{\mathrm{pn}} \\ &= (-76 \pm 12 \text{ ppb}) + (25 \pm 62 \text{ ppb}) + (-0 \pm 1 \text{ ppb}) + (33 \pm 20 \text{ ppb}) \\ &= -18 \pm 66 \text{ ppb}. \end{aligned} \tag{6.55}$$

The next required number is the total dilution factor $f_{\text{tot}}$, shown in Equation (6.22). The calculation is

$$\begin{aligned} f_{\text{tot}} &= f_{\text{ep}} + f_{\text{al}} + f_{\text{BB}} + f_{\text{nt}} + f_{\text{pn}} \\ &= (79.0 \pm 4.0)\% + (6.9 \pm 0.3)\% + (3.4 \pm 0.4)\% + (0.2 \pm 0.7)\% + (0.97 \pm 0.49)\% \\ &= (90.5 \pm 4.1)\%. \end{aligned} \tag{6.56}$$

This leads to an inelastic dilution factor

$$f_{\text{inel}} = 1 - f_{\text{tot}} = 1 - (90.5 \pm 4.1)\% = (9.5 \pm 4.1)\%. \tag{6.57}$$

The last required component to solve for the inelastic asymmetry is the combined value of the multiplicative corrections $R_{\text{tot}}$, shown in Equation (6.23). The value is determined to be

$$\begin{aligned} R_{\text{tot}} &= R_{\text{RC}} R_{\text{det}} R_{\text{acc}} R_{Q^2} \\ &= (1.0100 \pm 0.0050)(0.9857 \pm 0.0022)(1.0000 \pm 0.0100)(1.0000 \pm 0.0045) \\ &= 0.9956 \pm 0.0501. \end{aligned} \tag{6.58}$$

Table 6.10 summarizes all the inputs into Equation (6.20). The final $A_{\text{inel}}$ for the 877 MeV running is

$$\begin{aligned} A_{\text{inel}} &= R_{\text{tot}} \frac{A_{\text{M}}/P - A_{\text{bkgd}}}{1 - f_{\text{tot}}} \\ &= (0.9955 \pm 0.0501) \frac{(-105 \pm 75 \pm 52 \text{ ppb})/(78.9 \pm 1.6)\% + (18 \pm 66 \text{ ppb})}{1 - (90.5 \pm 4.1)\%} \\ &= -1.2 \pm 1.0 \text{ (stat)} \pm 1.1 \text{ (syst) ppm.} \end{aligned} \tag{6.59}$$

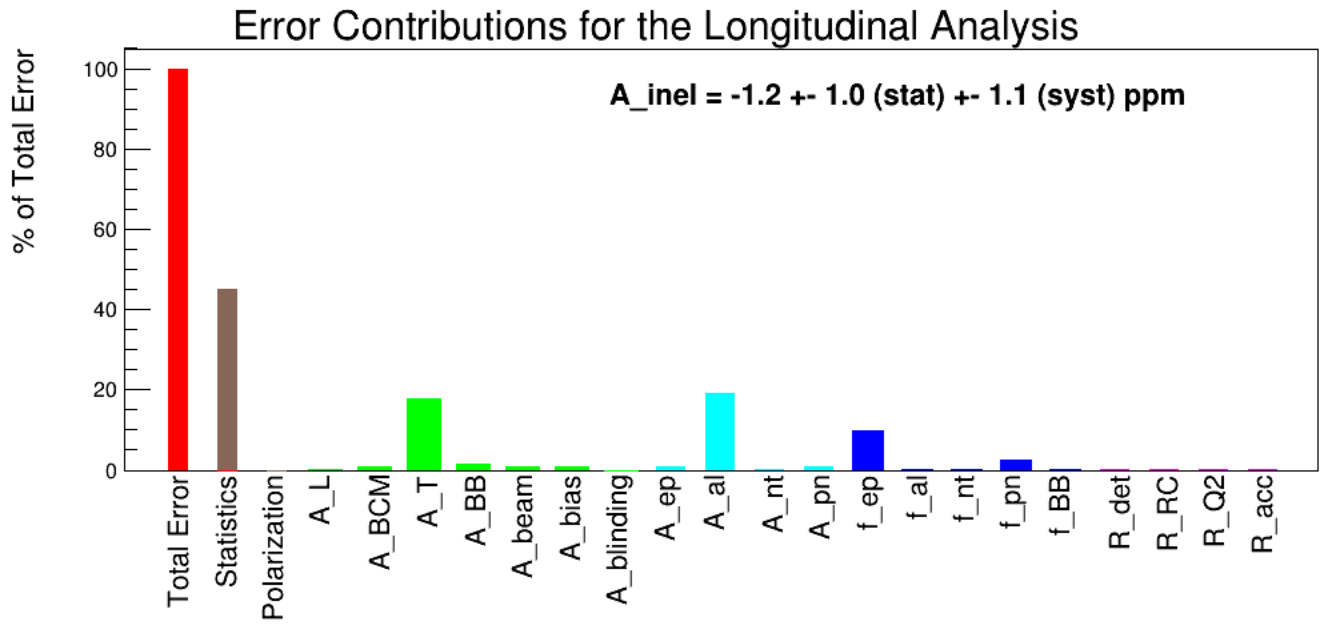


**Figure 6.22:** *The fractional quadrature contributions* $(\sigma_i/\sigma_{tot})^2$ *of all the various quantities are pictured above. As is obvious, the largest source of error is the statistics, followed by the transverse asymmetry leakage, the aluminum asymmetry, and the elastic dilution factor.*

The fractional quadrature contributions to the final error bar of $A_{\text{inel}}$ can be found in Figure 6.22.

## 6.5 1165 MeV Data and $A_{\mathbf{inel}}$

The primary purpose of taking 1165 inelastic data was to correct the measured asymmetry for the inelastic background and allow the isolation of the elastic asymmetry. For this reason, there were three sets of 1165 MeV inelastic data taken, as shown in Table 6.11. The 1165 MeV data was taken at nominal beam energy and running conditions with the exception of the spectrometer. QTOR was set to 6700 A, 75% of the normal current(8921 A).

**Table 6.11:** *Available 1165 MeV Inelastic Data.*

| Date | Beamtime | $dA_M$ | $dA_{inel}$ |
|---|---|---|---|
| Feb 2011 | 3 hours | 0.6 ppm | 2.7 ppm |
| Apr 2011 | 48 hours | 0.2 ppm | 0.9 ppm |
| Dec 2011 | 60 hours | 0.156 ppm | 0.7 ppm |

The initial dataset, taken in Feb 2011, was in essence a test of the inelastic data-taking. In order to not take too much beam time away from the main measurement only a few hours were taken as a proof of concept.

The second dataset, taken in Apr 2011, had a major issue. The null check $\left(\frac{IN+OUT}{2}\right)$ was not in agreement with zero. In fact it was $7\sigma$ away from zero. For this reason, this set of data was not included in the final calculation. More recent studies have shown that this is likely due to the beamline background. Thamraa <last name> is working on analyzing this and will produce an updated result for the 1165 MeV inelastic asymmetry including this data.

The third dataset, taken in Dec 2011, was taken due to the issue with the second dataset to get a strong inelastic measurement. This was the dataset that was used to extract the inelastic contribution to the elastic asymmetry. It was taken during a period of time when the QTOR power supply was having issues and unable to produce the high current necessary for elastic data taking.

The inelastic asymmetry has been previously extracted for the 1165 MeV data by John Leacock [4]. He determined the final inelastic asymmetry to be

$$A_{\text{inel}}(1165\text{ MeV}) = -3.03 \pm 0.65\text{ (stat)} \pm 0.73\text{ (syst)} \pm 0.07\text{ (blinding) ppm} \tag{6.60}$$

for $\langle Q^2 \rangle = 0.02078 \pm 0.0005$ GeV$^2$.

## 6.6 Extracting $d_\Delta$ From $A_{\text{inel}}$

As shown in Equation (2.41) and (2.50), there is a contribution to the inelastic asymmetry known as the Siegert term. This term, shown in Equation (2.51), is non-zero at $Q^2 = 0$ and is dependent on the low energy constant $d_\Delta$ which has a natural scale of $g_\pi$. However, a puzzle in Weak Hyperon Decay suggests possible values up to $100 g_\pi$. Due to the forward angle nature of the $Q_{\text{weak}}$ Experiment, the Siegert term is a major contributing factor to the inelastic asymmetry, allowing various values of $d_\Delta$ to have a significant effect on the predicted value.

Both the 877 MeV inelastic asymmetry(blue), found in Equation (6.59), $A_{\text{inel,877MeV}} = -1.2 \pm 1.0\ (\text{stat}) \pm 1.1\ (\text{syst})$ ppm and the 1165 MeV inelastic asymmetry(red), found in Equation (6.60), $A_{\text{inel,1165MeV}} = -3.03 \pm 0.65\ (\text{stat}) \pm 0.73\ (\text{syst}) \pm 0.07\ (\text{blinding})$ ppm are plotted against their respective 4-momentum transfers in Figure 6.23. Via comparison with calculated inelastic asymmetries for increasing values of $d_\Delta$, values for $d_\Delta$ can be extracted from these asymmetries. The $d_\Delta$ curves plotted on the same figure were determined for a beam energy of 424 MeV, but the $d_\Delta$ values are reasonably constant with regards to beam energy [5]. From an estimate of the dependence of the asymmetry on beam energy, a conservative error of $3g_\pi$ was estimated. This was applied to the final determination of $d_\Delta$ values to take into account the difference in beam energies.

The measured 877 and 1165 MeV inelastic asymmetries lead to extracted values for $d_\Delta$ of

$$d_\Delta(877\ \text{MeV data}) = (-8 \pm 22\ (\text{stat}) \pm 24\ (\text{syst}) \pm 3\ (\text{theory}))\, g_\pi \tag{6.61}$$

and

$$d_\Delta(1165\ \text{MeV}) = (5.8 \pm 15\ (\text{stat}) \pm 16\ (\text{syst}) \pm 1.5\ (\text{blinding}) \pm 3\ (\text{theory}))g_\pi. \tag{6.62}$$

The 1165 MeV $d_\Delta$ was extracted by John Leacock [4].

A $d_\Delta$ result was determined by the G0 Experiment, $d_\Delta = (8.1 \pm 23.7 \pm 8.3 \pm 0.7)g_\pi$ at $Q^2 = 0.0032\ \text{GeV}^2$, with the dominant process being pion photoproduction off the neutron near the $\Delta^0$ resonance [20].

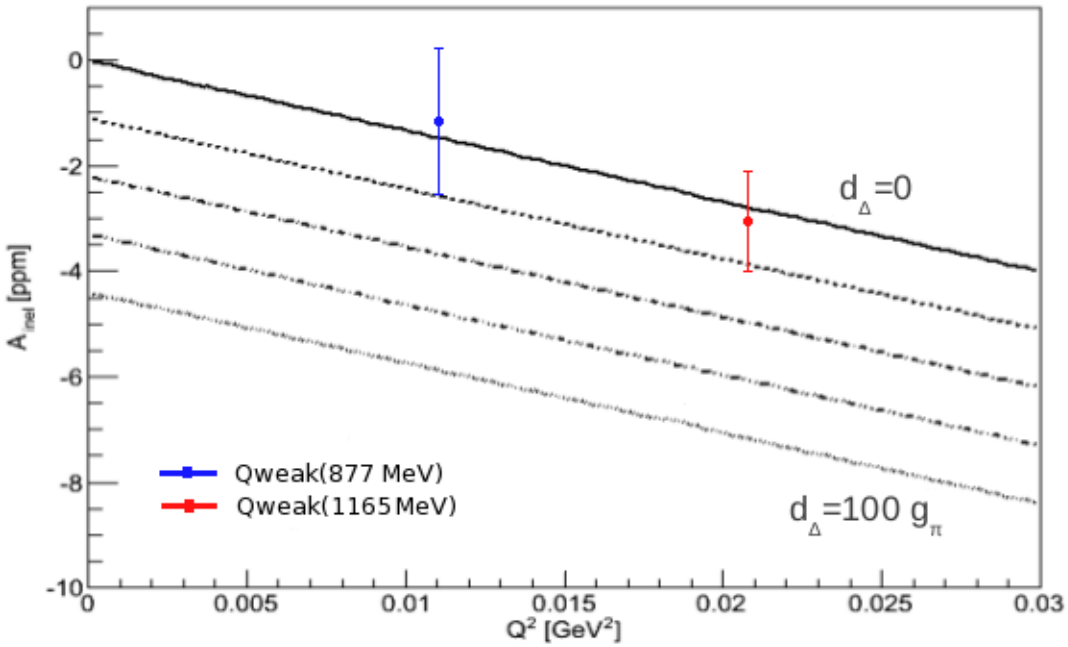


**Figure 6.23:** *$Q_{weak}$'s 1165 MeV(red) and 877 MeV(blue) inelastic asymmetries are plotted against the average momentum of the scattered electrons on top of curves representing the theoretical inelastic asymmetry for a beam energy of 424 MeV with various values of $d_\Delta$. The solid line represents $d_\Delta = 0$ and each consecutive line has $d_\Delta$ increased by a factor of $25g_\pi$, up to a total of $d_\Delta = 100g_\pi$. Figure is adapted from the dissertation of John Leacock [4].*

This value can be combined with the $Q_{weak}$ values, as shown in Figure 6.24, to extract a final determination of $d_\Delta$. A constant fit line was used, as $d_\Delta$ is defined to be constant. The resulting constraint is

$$d_\Delta = (3.8 \pm 14.7)g_\pi. \tag{6.63}$$

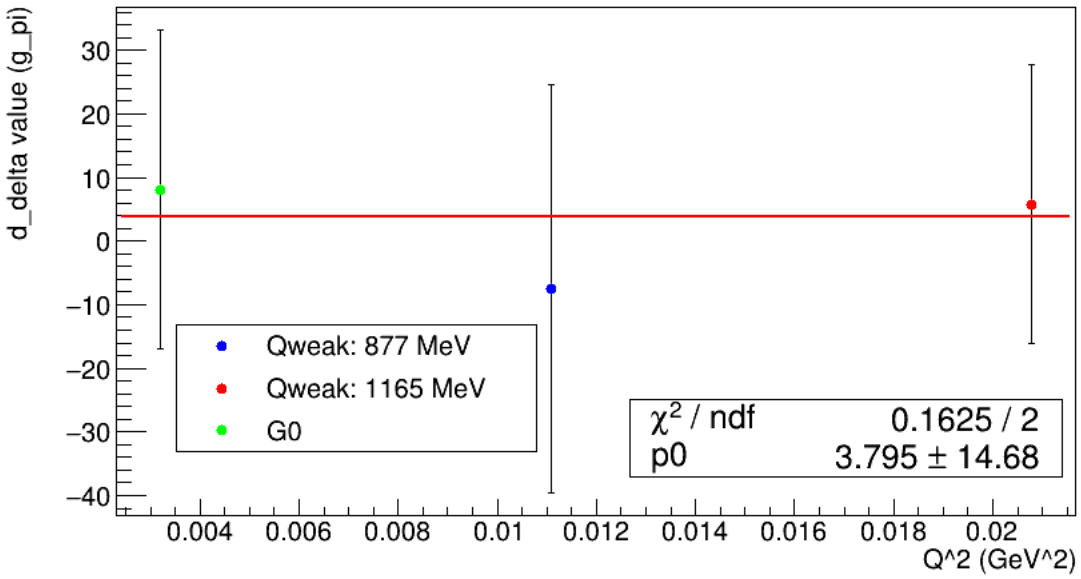


**Figure 6.24:** *The three measured values for $d_\Delta$ are combined via a constant fit due to the nature of $d_\Delta$. The $Q_{weak}$ values, 877 MeV(blue) and 1165 MeV(red), were determined from their respective $A_{inel}$s, but the G0(green) value has been previously published [20].*

## 6.7 Inelastic Beam-Normal Single-Spin Asymmetry for the 877 MeV Running

The transverse asymmetry is also referred to as the beam-normal single-spin asymmetry (BNSSA). Previous analyses using purely transverse beam have extracted this value for the inelastic [96] and elastic [44] at $Q_{weak}$'s nominal beam kinematics, as well as for the aluminum [97] and carbon [56]. There was no purely transverse running at the 877 MeV kinematics, but due to large transverse component of the beam, the inelastic BNSSA can be extracted via a similar process.

### 6.7.1 Extracting the Measured BNSSA

The measured BNSSA($B_{\mathrm{M}}$) depends on the raw BNSSA($B_{\mathrm{raw}}$), the detector acceptance correction($\beta_{\mathrm{acc}}$), the regression correction on the BNSSA($B_{\mathrm{reg}}$), the fit correction($B_{\mathrm{fit}}$), the linearity correction($B_{\mathrm{L}}$), and the rescattering bias($B_{\mathrm{bias}}$) as

$$B_{\mathrm{M}} = \frac{B_{\mathrm{raw}}}{\beta_{\mathrm{acc}}} + B_{\mathrm{reg}} + B_{\mathrm{fit}} + B_{\mathrm{L}} + B_{\mathrm{bias}}. \tag{6.64}$$

The raw BNSSA is equivalent to the opposite of the raw transverse asymmetry, which was determined in Figure 6.9. It is the opposite of this due to the transverse polarization of the 877 MeV running(shown in Figure 6.17) was along the negative transverse axis. The raw BNSSA value is

$$B_{\mathrm{raw}} = 3.334 \pm 0.106 \text{ ppm}. \tag{6.65}$$

The detector acceptance correction accounts for the fact that only 49% of the azimuthal angle is covered, leading to a 22° azimuthal acceptance for each octant. A transverse asymmetry, such as the BNSSA, is "flattened" by the large acceptance causing a lower amplitude of the sinusoidal asymmetry to be measured. Simulations were performed for the $^{12}$C BNSSA analysis [56] to extract the light-weighted average of the sine of the azimuthal angle ($\langle \sin\phi \rangle_i$). These simulations were compared to the idealized scenario for fully polarized beam. The idealized scenario gives

$$A_i = -B_n \langle \sin\phi \rangle_i. \tag{6.66}$$

The acceptance correction for each detector is determined by comparing simulations to this idealized scenario:

$$\beta_i = \frac{\langle \sin\phi \rangle_i}{\sin\phi_i}. \tag{6.67}$$

The individual detector comparisons were consistent, so the average value becomes the correction and the standard deviation becomes the error. The final value [56] is

$$\beta_{\text{acc}} = 0.9862 \pm 0.0036. \tag{6.68}$$

The regression correction for BNSSA is determined in the same manner as the longitudinal helicity-corrected beam motion correction(Section 6.3.2), by subtracting the "off" regression data(found in Figure 6.9) from the "on" regression data(found in Figure 6.11). A conservative error bar of 10 ppb is applied, resulting in a correction of

$$B_{\text{reg}} = B_{\text{on}} - B_{\text{off}} \quad = 3.312 \text{ ppm} - 3.334 \text{ ppm} = -0.022 \pm 0.010 \text{ ppm}. \tag{6.69}$$

In the longitudinal result, a beamline background correction was required to find the measured asymmetry. However, the beamline background asymmetry is isotropic and affects all the detectors in the same manner. Therefore the fit equation(Equation (6.3)) limits the effect of the beamline background to the longitudinal asymmetry while the transverse asymmetry is unaffected.

While the fit found in Equation (6.3) is the proper fitting algorithm to extract the BNSSA

and longitudinal asymmetry, it was worthwhile to check how varying the fit would affect the BNSSA. The various fits and resulting asymmetries are found in Table 6.12. These fits were done on the regressed data, but the resulting correction is applicable to the raw data.

**Table 6.12:** *Varying fits for the regressed BNSSA.*

| Fit | BNSSA(ppm) |
|---|---|
| $A = B_0 \cos\left(\frac{\pi}{180}\left(45\left(N_{\text{Octant}} - 1\right) + \phi_0\right)\right) + C$ | $-3.312 \pm 0.106$ |
| $A = B_0 \cos\left(\frac{\pi}{180}\left(45\left(N_{\text{Octant}} - 1\right) + \phi_0\right)\right)$ | $-3.311 \pm 0.106$ |
| $A = B_0 \cos\left(\frac{\pi}{180}\left(45\left(N_{\text{Octant}} - 1\right)\right)\right) + C$ | $-3.311 \pm 0.106$ |
| $A = B_0 \cos\left(\frac{\pi}{180}\left(45\left(N_{\text{Octant}} - 1\right)\right)\right)$ | $-3.311 \pm 0.106$ |

Table 6.12 shows that the varying fits only have a 1 ppb effect on the resulting BNSSA. To take this into account, a zero correction is applied to the measurement with an error that is half the maximum difference between the fits,

$$B_{\text{fit}} = 0 \pm 0.5 \text{ ppb.} \tag{6.70}$$

The linearity correction is determined in the same manner as the longitudinal linearity correction(Section 6.3.4). The determined nonlinearity is the same as in the longitudinal, but it is now multiplied by $B_{\text{raw}}$,

$$B_{\text{L}} = -x * B_{\text{raw}} \quad = -\left(0.0013 \pm 0.0050\right)\left(3.334 \pm 0.106 \text{ ppm}\right) = -4.3 \pm 16.7 \text{ ppb.} \tag{6.71}$$

As discussed in Section 6.3.6, the rescattering bias was an effect discovered post data

taking that was generated by the transverse polarization, gained via precession while passing through the magnetic field, of the longitudinally polarized scattered electrons generating showers in the lead preradiators placed in front of the main detector bars. The effect of this process on the BNSSA is still being studied via simulation, but simulations have shown the maximum correction(including uncertainty) is less than 100 ppb though the sign is still under discussion. For this analysis, the maximum correction will be treated as the uncertainty on a correction of zero:

$$B_{\text{bias}} = 0 \pm 0.1 \text{ ppm}. \tag{6.72}$$

The above corrections can all be combined with $B_{\text{raw}}$ in order to extract the measured BNSSA $B_{\text{M}}$,

$$\begin{aligned} B_{\text{M}} &= \frac{B_{\text{raw}}}{\beta_{\text{acc}}} + B_{\text{reg}} + B_{\text{fit}} + B_{\text{L}} + B_{\text{bias}} \\ &= \frac{3.334 \pm 0.106 \text{ ppm}}{0.9862 \pm 0.0036} + (-0.022 \pm 0.010 \text{ ppm}) + (0 \pm 0.0005 \text{ ppm}) \\ &\qquad + (-0.004 \pm 0.017 \text{ ppm}) + (0 \pm 0.1 \text{ ppm}) \\ &= 3.354 \pm 0.106 \text{ (stat)} \pm 0.102 \text{ (syst) ppm}. \end{aligned} \tag{6.73}$$

### 6.7.2 Extracting the Inelastic BNSSA

Now that the measured beam-normal single-spin asymmetry has been extracted($B_{\text{M}}$), the inelastic BNSSA($B_{\text{n}}$) can be determined. To access $B_{\text{n}}$, there are multiple variables that need to be evaluated. The relation between $B_{\text{n}}$ and the polarization($P$), background corrections($B_{\text{bkgd}}$),

total dilution factor of other contributions($f_{\rm tot}$), and the multiplicative corrections($R_{\rm tot}$) is

$$B_{\rm n} = R_{\rm tot}\frac{B_{\rm M}/P_{\rm T} - B_{\rm bkgd}}{1 - f_{\rm tot}}. \tag{6.74}$$

As was mentioned for the longitudinal polarization(Section 6.4.1), Hall C was not the primary hall and there was spin precession of the electrons leading to a longitudinal precession polarization of $P_{\rm prec} = (89.9 \pm 1.7)\%$. The transverse precession polarization can be determined from this value. During wien9, when the 877 MeV running occured, the polarization of the beam leaving the source was $P_{\rm wien9} = (87.71 \pm 0.62)\%$. The transverse precession polarization is combined with the polarization of the beam leaving the source to determine the transverse polarization,

$$\begin{aligned} P_{\rm T} &= P_{\rm wien9} \times \sqrt{1 - P_{\rm prec}^2} \\ &= (87.71 \pm 0.62)\% \times \sqrt{1 - (89.9 \pm 1.7)\%^2} \\ &= (38.4 \pm 3.4)\%. \end{aligned} \tag{6.75}$$

The background corrections can be broken down into four pieces, as in the longitudinal analysis. The breakdown is

$$B_{\rm bkgd} = C_{\rm ep,T} + C_{\rm al,T} + C_{\rm nt,T} + C_{\rm pn,T}, \tag{6.76}$$

where the corrections for the elastic background($C_{\rm ep,T}$), the aluminum background($C_{\rm al,T}$), the

neutral background($C_{\mathrm{nt,T}}$), and the pion background($C_{\mathrm{pn,T}}$) are combined to determine $B_{\mathrm{bkgd}}$. As in the longitudinal analysis, each correction is determined by combining the dilution factor and the asymmetry of the respective background. The dilution factors are unchanged from the longitudinal analysis and can be found in Equations (6.25), (6.28), (6.35), and (6.41). While the beamline background does not generate a false BNSSA, the dilution factor still contributes to $f_{\mathrm{tot}}$ and is also unchanged from the longitudinal analysis(Equation (6.33)). The $f_{\mathrm{tot}}$ value is unchanged from the longitudinal analysis and is found in Equation (6.56).

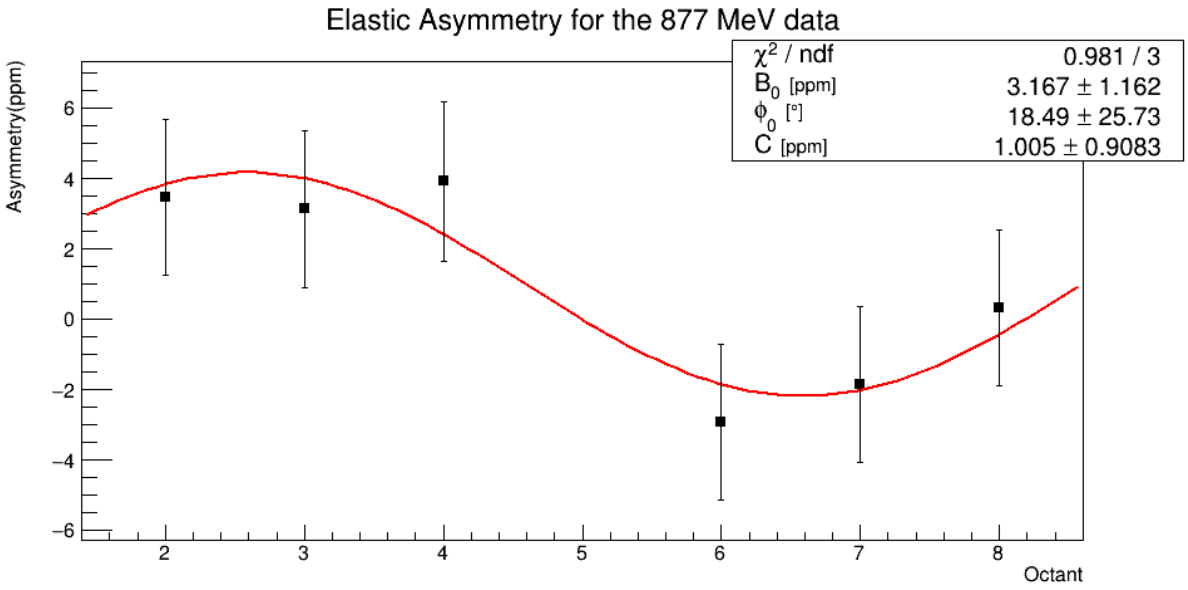


**Figure 6.25:** *A small amount of data was taken on the elastic peak at the 877 MeV kinematics. This data was taken while the lead shutters were inserted in the beamline, resulting in Octants 1 and 5 being excluded from the fit.*

The only data that exists for the elastic asymmetry at the 877 MeV kinematics was taken during a scan in which the setting of the toroidal spectrometer was varied around the elastic peak. Only a small amount of data was taken, as shown in Figure 6.25. The data showed a BNSSA at the elastic peak of $B^{\mathrm{ep}}_{\mathrm{ep,raw}} = 3.167 \pm 1.162$ ppm. In the standard convention

the transverse polarization was along the negative transverse axis, thus this value needs to be multiplied by $-1$ to get $B^{\rm ep}_{\rm ep,raw} = -3.167 \pm 1.162$ ppm. This needs to be corrected for the polarization(Equation (6.75)) which results in $B^{\rm ep}_{\rm ep} = -8.244 \pm 3.113$ ppm for the elastic kinematics at 877 MeV.

A cross-check of the elastic asymmetry involves taking the established BNSSA for the 1165 MeV data, $B_{\rm n}^{1165\ \rm MeV} = -5.350 \pm 0.067 \pm 0.137$ ppm [44], and scaling it by $\frac{1}{E}$,

$$\begin{aligned} B_{\rm n}^{877\ \rm MeV} &= B_{\rm n}^{1165\ \rm MeV} \frac{1/E_{877\ \rm MeV}}{1/E_{1165\ \rm MeV}} = B_{\rm n}^{1165\ \rm MeV} \frac{E_{1165\ \rm MeV}}{E_{877\ \rm MeV}} \\ &= (-5.350 \pm 0.153\ \text{ppm}) \frac{1165\ \text{MeV}}{877\ \text{MeV}} \\ &= -7.107 \pm 0.203\ \text{ppm}. \end{aligned} \tag{6.77}$$

As the cross-check agrees with $B^{\rm ep}_{\rm ep}$, this value needs to be scaled by $\sqrt{Q^2}$ to extract the elastic BNSSA at the inelastic kinematics($B^{\rm in}_{\rm ep}$),

$$\begin{aligned} B^{\rm in}_{\rm ep} &= B^{\rm ep}_{\rm ep} \sqrt{\frac{Q^2_{\rm in}}{Q^2_{\rm ep}}} \\ &= (-8.244 \pm 3.113\ \text{ppm}) \sqrt{\frac{0.01258\ \text{GeV}^2}{0.01424\ \text{GeV}^2}} \\ &= -7.748 \pm 2.926\ \text{ppm}. \end{aligned} \tag{6.78}$$

The $Q^2$ values are taken from Geant3 simulations done prior to running.

Now that the elastic BNSSA at the inelastic kinematics has been determined, it can be

combined with the dilution factor to extract the correction,

$$C_{\mathrm{ep,T}} = f_{\mathrm{ep}} B_{\mathrm{ep}}^{\mathrm{in}} \quad = ((79.9 \pm 4.0)\%)(-7.748 \pm 2.926 \text{ ppm}) = -6.121 \pm 2.332 \text{ ppm}. \tag{6.79}$$

The aluminum BNSSA can be found from the same plot the longitudinal aluminum background asymmetry was found, Figure 6.19. The fit found in Equation (6.3) gives $B_{\mathrm{al,raw}} = -4.997 \pm 0.993$ ppm. Correcting for the sign of the transverse polarization results in $B_{\mathrm{al,raw}} = 4.997 \pm 0.993$ ppm. This value needs to be corrected for the polarization(Equation (6.75)) to extract the physics asymmetry,

$$B_{\mathrm{al}} = \frac{B_{\mathrm{al,raw}}}{P} = \frac{4.997 \pm 0.993 \text{ ppm}}{(38.4 \pm 3.4)\%} = 13.007 \pm 2.834 \text{ ppm}. \tag{6.80}$$

Combining this with the dilution factor found in Equation (6.28) gives the aluminum background correction,

$$C_{\mathrm{al,T}} = f_{\mathrm{al}} B_{\mathrm{al}} \quad = (6.9 \pm 0.3)\%(13.007 \pm 2.834 \text{ ppm}) = 0.898 \pm 0.201 \text{ ppm}. \tag{6.81}$$

The neutral background BNSSA follows the same procedure as in longitudinal(Section 6.4.5). The elastic, aluminum, and inelastic dilution factors are renormalized(Equations (6.36) and (6.37)) as they compose the neutral background signal. The asymmetries are

then combined to determine the BNSSA,

$$\begin{aligned} B_{\rm nt} &= f_{\rm inel}^{\rm nt} B_{\rm n} + f_{\rm al}^{\rm nt} B_{\rm al} + f_{\rm ep}^{\rm nt} B_{\rm ep} \\ &= (10.0\%)\,(151.843 \text{ ppm}) + (7.2\%)\,(13.007 \text{ ppm}) + (82.8\%)\,(-7.748 \text{ ppm}) \\ &= 9.705 \pm 9.705 \text{ ppm}, \end{aligned} \tag{6.82}$$

with an arbitrary error of 100% added to the final neutral background BNSSA on the final line.

The neutral background BNSSA is then combined with the neutral background dilution factor to determine the correction,

$$C_{\rm nt,T} = f_{\rm nt} B_{\rm nt} \quad = ((0.2 \pm 0.7)\%)\,(9.705 \pm 9.705 \text{ ppm}) = 0.018 \pm 0.072 \text{ ppm}. \tag{6.83}$$

The pion background BNSSA is determined via the same process as the longitudinal pion background asymmetry(Secton 6.4.6). As in the longitudinal, a different $Q_{\rm weak}$ ancillary measurement determined the transverse pion asymmetry($-52.28 \pm 16.85$ ppm) at a beam energy of 3.3 GeV [93]. This asymmetry, which should be equivalent to the beam-normal single-spin asymmetry at those kinematics, still needs corrected for polarization

$$B_{\rm pn}^{\rm 3Gev} = \frac{B_{\rm pn,raw}^{\rm 3GeV}}{P} \quad = \frac{-52.28 \text{ ppm}}{(87.0)\%} = -60 \text{ ppm}. \tag{6.84}$$

As this for the transverse direction, the transverse polarization is determined from the lon-

gitudinal polarization. To account for the uncertainity on this, it was decided to apply a 100% uncertainty to the final asymmetry.

Similar assumptions can be made to determine the pion BNSSA for the 877 MeV running as were made in the longitudinal measurement. The difference is that $B$ depends on $\sqrt{Q^2}$, so the final value is solved for by

$$\begin{aligned} B_\pi^{877\text{MeV}} &= B_\pi^{3\text{GeV}} \sqrt{\frac{Q^2_{\pi,\text{electro},877\text{MeV}}}{Q^2_{\pi,\text{electro},3\text{GeV}}}} \\ &= (-60 \text{ ppm}) \sqrt{\frac{0.011 \text{ (GeV)}^2}{0.082 \text{ (GeV)}^2}} \\ &= -22.0 \pm 22.0 \text{ ppm}, \end{aligned} \tag{6.85}$$

which is similar to Equation (6.47). The 100% uncertainty is applied on the final line of Equation (6.85).

Now that a BNSSA for pions at 877 MeV kinematics has been determined, it can be combined with the dilution factor to obtain the pion background correction,

$$C_{\text{pn,T}} = f_{\text{pn}} B_{\text{pn}} \quad = ((0.97 \pm 0.49)\%)(-22.0 \pm 22.0 \text{ ppm}) = -0.213 \pm 0.239 \text{ ppm}. \tag{6.86}$$

Unlike in the longitudinal case, $R_{\text{tot}}$ only has three contributing factors for the BNSSA case, due to the acceptance correction being applied directly to $B_{\text{raw}}$. The breakdown of $R_{\text{tot}}$ is

$$R_{\text{tot}} = R_{\text{RC}} R_{\text{det}} R_{Q^2}. \tag{6.87}$$

For the longitudinal 877 MeV analysis, the weak charge value for the electromagnetic radiative correction($R_{\mathrm{RC}}$) was used(Section 6.4.7). The logic for this was that the same target was used in both measurements and therefore the radiation length was unchanged. Since the 877 MeV BNSSA analysis works off the same data, the logic is unchanged leading to

$$R_{\mathrm{RC}} = 1.010 \pm 0.005. \tag{6.88}$$

In the longitudinal analysis the detector response correction was determined via comparing simulations of the ideal(non-lightweighted) kinematics($Q^2_{\mathrm{ideal}}$) and the optical photon weighted(lightweighted) kinematics($Q^2_{\mathrm{lw}}$). However, while the longitudinal asymmetry depends directly on $Q^2$ ($A \propto Q^2$) theory suggests that the BNSSA depends on the square root of the 4-momentum transfer$\left(B_n \propto \sqrt{Q^2}\right)$ [98]. The detector response correction for the inelastic BNSSA can be determined by taking the square root of the longitudinal correction(Equation (6.50)), leading to

$$R_{\mathrm{det}} = 0.9928 \pm 0.0011. \tag{6.89}$$

As according to theory $B_n \propto \sqrt{Q^2}$ [98], this can be treated as $B_n = m\sqrt{Q^2}$. By doing so the $Q^2$ correction for the inelastic 877 MeV BNSSA can be determined. Using $B_{\mathrm{M}} = 3.354$ ppm and the measured $Q^2 = 0.01108$ GeV$^2$, a value for $m$ can be calculated

$$m = \frac{B_{\mathrm{M}}}{\sqrt{Q^2}} = \frac{3.354 \text{ ppm}}{\sqrt{0.01108 \text{ GeV}^2}} = 31.86 \frac{\text{ppm}}{\text{GeV}}. \tag{6.90}$$

Using the relation $B_{\mathrm{M}} = m\sqrt{Q^2}$, the error on the measured BNSSA($B_{\mathrm{M}}$) can be propagated from the error on $Q^2(0.45\%)$

$$\partial B_{\mathrm{M}} = \pm\frac{1}{2}\frac{m}{\sqrt{Q^2}}\partial Q^2 = \pm\frac{1}{2}\frac{31.86\ \frac{\mathrm{ppm}}{\mathrm{GeV}}}{\sqrt{0.01108\ \mathrm{GeV}^2}}(0.00004986\ \mathrm{GeV}^2) = \pm 0.0075\ \mathrm{ppm}. \tag{6.91}$$

Now the multiplicative $Q^2$ correction for $B_{\mathrm{M}}$ can be calculated by looking at how $\partial B_{\mathrm{M}}$ compares to $B_{\mathrm{M}}$ and using it as the error for a unity correction,

$$R_{Q^2} = 1.0000 \pm \frac{\partial B_{\mathrm{M}}}{B_{\mathrm{M}}} = 1.0000 \pm \frac{0.0075\ \mathrm{ppm}}{3.354\ \mathrm{ppm}} = 1.0000 \pm 0.0022. \tag{6.92}$$

Now that all the individual components have been calculated, the final inelastic BNSSA at 877 MeV can be determined. First, the background correction($B_{\mathrm{bkgd}}$) as defined in Equation (6.76) is calculated from the four background components,

$$\begin{aligned} B_{\mathrm{bkgd}} &= C_{\mathrm{ep,T}} + C_{\mathrm{al,T}} + C_{\mathrm{nt,T}} + C_{\mathrm{pn,T}} \\ &= (-6.121 \pm 2.332\ \mathrm{ppm}) + (0.898 \pm 0.201\ \mathrm{ppm}) \\ &+ (0.018 \pm 0.072\ \mathrm{ppm}) + (-0.213 \pm 0.239\ \mathrm{ppm}) \\ &= -5.420 \pm 2.354\ \mathrm{ppm}. \end{aligned} \tag{6.93}$$

The total dilution($f_{\mathrm{tot}}$) is the same as in the longitudinal analysis, and was given in Equation (6.56). The final necessary calculation is for the total multiplicative correction as defined in

Equation (6.87). This combination of the three multiplicative corrections is

$$\begin{aligned} R_{\text{tot}} &= R_{\text{RC}} R_{\text{det}} R_{Q^2} \\ &= (1.010 \pm 0.005)(0.9928 \pm 0.0011)(1.0000 \pm 0.0022) \\ &= 1.0028 \pm 0.0056. \end{aligned} \tag{6.94}$$

Now that all the components of Equation (6.74) have been determined, the final inelastic BNSSA for 877 MeV is

$$\begin{aligned} B_{\text{n}} &= R_{\text{tot}} \frac{B_{\text{M}}/P_{\text{T}} - B_{\text{bkgd}}}{1 - f_{\text{tot}}} \\ &= (1.0028 \pm 0.0056) \frac{\frac{(3.354 \pm 0.147 \text{ ppm})}{(38.4 \pm 3.4)\%} - (-5.420 \pm 2.354 \text{ ppm})}{1 - (90.5 \pm 4.1)\%} \\ &= 149 \pm 3 \text{ (stat)} \pm 72 \text{ (syst) ppm}. \end{aligned} \tag{6.95}$$

The fractional quadrature contributions to the final error bar of $B_{\text{n}}$ can be found in Figure 6.26.

### 6.7.3 Comparison with Theory and Implications

Carlson et al [21] determined the BNSSA for $e+p \rightarrow e+\Delta$ via summing up the contributions of various intermediate states for the two-photon exchange. This calculation was not done at the same kinematics as the 877 MeV data, but Marc Vanderhaeghen and the writing team of the paper provided calculations for the 877 MeV kinematics in a private communication to Mark Dalton. These calculations are used to provide a comparison for the value quoted in

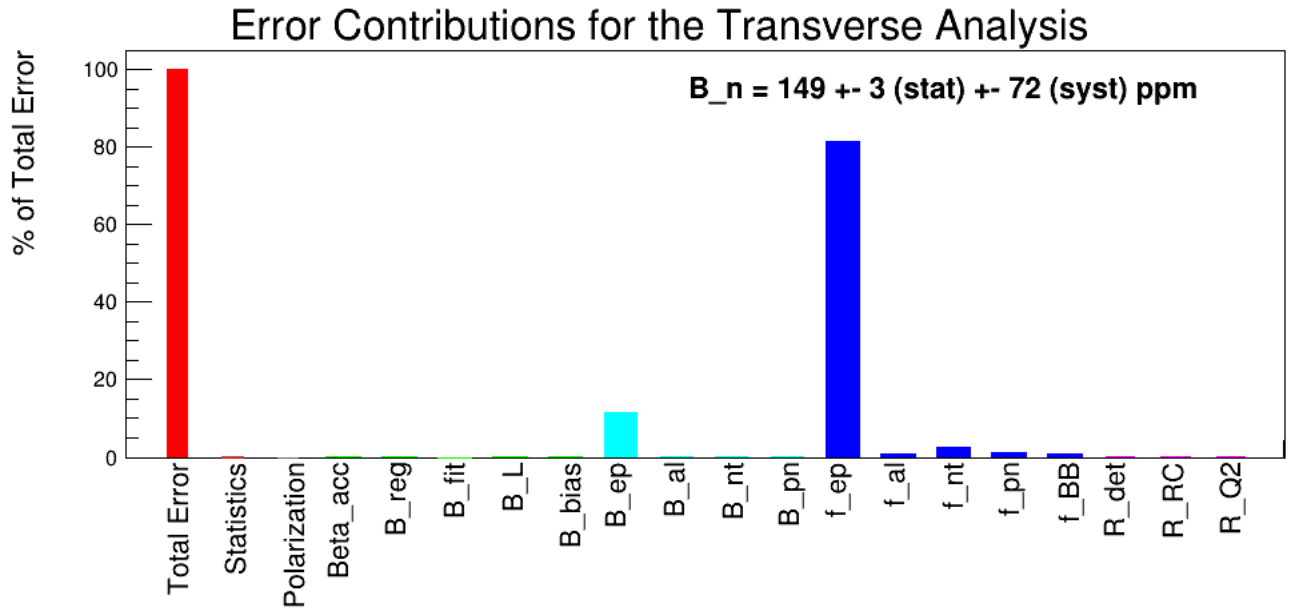


**Figure 6.26:** *The fractional quadrature contributions* $(\sigma_i/\sigma_{tot})^2$ *of all the various quantities are pictured above. The error is clearly dominated by the elastic dilution factor.*

Equation (6.95) in Figure 6.27 where it shows good agreement with the theoretical prediction.

As discussed in Section 2.5, one of the main motivations for the extraction of $B_n$ for the N→ Δ transition was to contribute to the future measurement of the electromagnetic form factors of the Δ. The measurement of the BNSSA for the N→ Δ transition is one of the only measurable observables related to the form factors. Therefore, the 877 MeV measurement combined with the previously measured 1165 MeV value provide a starting point for a data set that will hopefully lead to the extraction of these form factors. Future measurements and more theoretical work will both be required before they can be revealed.

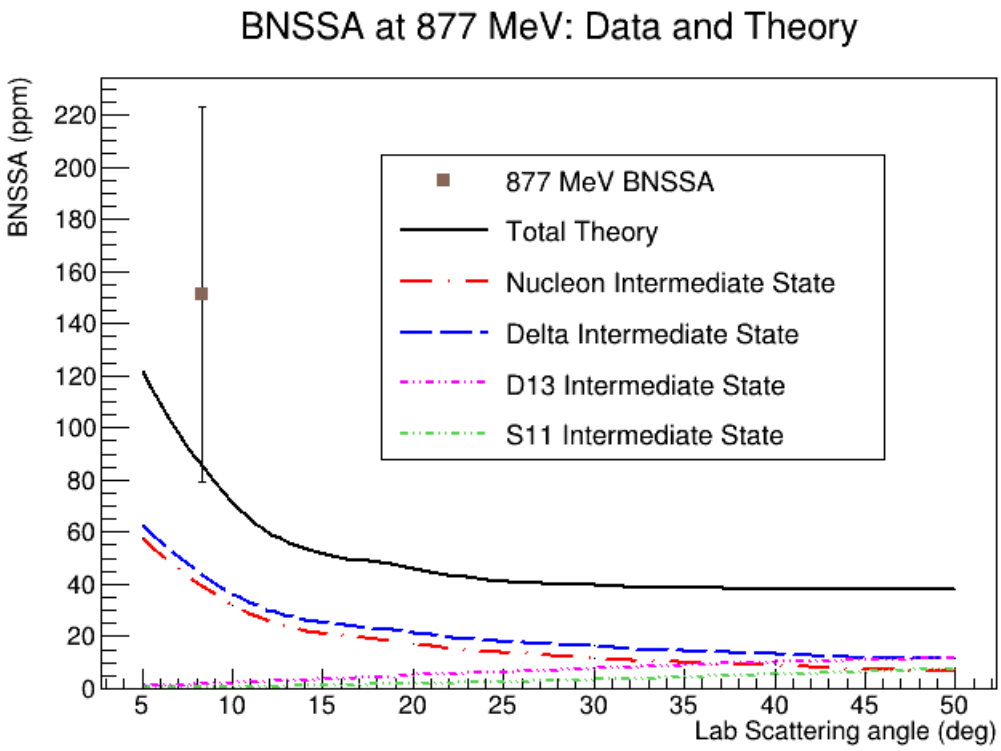


**Figure 6.27:** *Carlson et al [21] combined the theoretical calculations for various intermediate states of the two-photon exchange to determine an overall theoretical value(black). The values shown here are from a private communication applying these calculations to the 877 MeV kinematics. The possible intermediate states for the $e + p \rightarrow e + \Delta$ are a nucleon(red), the $\Delta$ resonance(blue), the $D_{13}$ resonance(fuschia), and the $S_{11}$ resonance(green). The $B_n$(brown) for the 877 MeV data is plotted alongside these calculation and is in agreement with theory.*

# Chapter 7

# Conclusion

There were two sets of data discussed in this dissertation. The first set of data consists of the primary measurement of the $Q_{weak}$ Experiment and the second set consists of an ancillary measurement taken using the $Q_{weak}$ apparatus. The analysis of the $Q_{weak}$ primary result can be found in Chapter 5 and the analysis of the inelastic N$\rightarrow \Delta$ transition can be found in Chapter 6. The results and implications of both measurements will be summarized here.

## 7.1 Primary Measurement: Elastic $\vec{e} + p \rightarrow e + p$

The primary measurement was the parity-violating asymmetry of elastic electron-proton scattering at extreme forward angle. The full analysis of this result was discussed in Chapter 5. This result had some broad implications for particle physics that are discussed in Section 5.4. The analysis and implications are summarized below.

### 7.1.1 Elastic Parity-Violating Asymmetry($A_{\mathbf{ep}}$)

The final elastic parity-violating asymmetry determined by the $Q_{weak}$ Experiment is listed in Equation (5.32) which is found in Section 5.3.10. The value is $A_{ep} = -226.5 \pm 7.3$ (stat) $\pm$ 5.8 (syst) ppb. The analysis was performed in three parts. The first part, Section 5.1, involves extracting the raw asymmetry from the data gathered. The second part, Section 5.2, determines the measured asymmetry by correcting for false asymmetries. The third part, Section 5.3, takes the measured asymmetry and corrects for the polarization, removes various backgrounds, and applies several multiplicative corrections to extract the final $A_{ep}$.

### 7.1.2 Weak Charge of the Proton($Q_w^p$)

The primary purpose of the $Q_{weak}$ Experiment was to use the final $A_{ep}$ with other parity-violating electron scattering(PVES) data to obtain a precise measurement of the $Q_w^p$ which could be compared with the Standard Model predicted value of $Q_w^p$ (SM) $= 0.0708 \pm 0.0003$.

The process of extracting the measured $Q_w^p$ is discussed in detail in Section 5.4.1, but summarized here. To obtain a value of $Q_w^p$, reduced asymmetries from the world's PVES data, as shown in Equation (5.33),are plotted against their $Q^2$. The extreme forward angle nature of $Q_{weak}$ and the precision of the $Q_{weak}$ measurement of $A_{ep}$ leads to to it being a defining point in identifying the y-intercept($Q^2 = 0$), which is the weak charge of the proton. This fit can be seen in Figure 5.8 and leads to a value of $Q_w^p$ (PVES) $= 0.0719 \pm 0.0045$. This is in strong agreement with the previously mentioned SM predicted value, $Q_w^p$ (SM).

### 7.1.3 Weak Charge of the Neutron($Q_w^n$)

As discussed in Section 5.4.2 and explicitly stated in Equation(5.38), both $Q_w^p$ and $Q_w^n$ depend on the neutral weak vector quark coupling constants, $C_{1\mathrm{u}}$ and $C_{1\mathrm{d}}$. The precise measurement of $Q_w^p$ discussed both in the previous section and Section 5.4.1 puts constraints on the possible values for these coupling constants. There are additional constraints on the coupling constants, nearly orthogonal to the PVES constraints, from Atomic Parity Violation(APV) data. The coupling constants allowed by both sets of data are shown in Figure 5.9, where the 95% confidence level constraints from the PVES data are represented by the blue band and constraints from the APV data are represented by the gold band. The overlap of the two sets of data is represented by the black ellipse and in agreement with the Standard Model predicted values shown by the red square.

By using the measured values of these coupling constraints, Equation (5.39), and Equation (5.38) a value for the weak charge of the neutron of $Q_w^n\,(\mathrm{PVES} + \mathrm{APV}) = -0.9808 \pm 0.0063$ can be determined. This value is in strong agreement with the Standard Model predicted value of $Q_w^n\,(\mathrm{SM}) = -0.976 \pm 0.0063$.

### 7.1.4 Weak Mixing Angle($\sin^2\theta_W$)

The weak mixing angle($\sin^2\theta_W$) parametrizes the mixing between the neutral electromagnetic and weak interactions, as shown in Equations (2.10) and (2.11). It is a key parameter of the Standard Model that is related to the weak charge of the proton via Equation (5.42)

as discussed in Section 5.4.3.

The Standard Model "accidentally" surpresses the $Q_w^p$ as it predicts $\sin^2\theta_W \approx \frac{1}{4}$ as shown in Equation (5.44) and the simplified dependence $Q_w^p \approx 1 - 4\sin^2\theta_W$ as shown in Equation (5.43) leading to $Q_w^p$ being very sensitive to $\sin^2\theta_W$. This results in a high precision(0.46%) on the value of $\sin^2\theta_W$ given the precision(6.25%) of the measurement of $Q_w^p$ by $\mathrm{Q_{weak}}$.

The final $\sin^2\theta_W$ value for $\mathrm{Q_{weak}}$, $0.2384 \pm 0.0011$, is plotted along the Standard Model prediction in Figure 5.10.

### 7.1.5 Mass Reach

As discussed in Section 5.4.4, a "new physics term"($g^2/\Lambda^2$) can be added to the Standard Model Lagrangian to create the Beyond Standard Model(BSM) Lagrangian. This new term, which depends on coupling $g$ and mass scale $\Lambda$ for possible new physics, provides a way of quantifying the sensitivity to new physics BSM. [31]. The PVES(blue) and APV(gold) data, previously used to extract the neutral weak vector coupling constants to determine the weak charge of the neutron, can be mapped on the phase space of $\Lambda/g$ and the quark-flavour mixing angle($\theta_h$) as shown in Figure 5.11. The black line represents the combined 95% confidence-level and local maxima at $\theta_h = 26.6^\circ$ and $\theta_h = 206.6^\circ$, corresponding with mass reaches of $\Lambda_-/g = 8.4$ TeV and $\Lambda_+/g = 7.4$ TeV.

## 7.2 Ancillary Result: N$\rightarrow \Delta$ Transition

The original purpose of investigating the N$\rightarrow \Delta$ transition was to measure a background present in the primary $Q_{weak}$ measurement of the elastic parity-violating asymmetry. However this inelastic measurement is interesting in its own right as well. The original inelastic data set, aimed at obtaining the background correction, was taken at the same kinematics as the primary $Q_{weak}$ measurement and has been previously analyzed [4]. This data set and its results are discussed in Section 6.5.

This dissertation focused on the analysis of a second set of data taken during a period when nominal beam conditions were unavailable. This data set was taken at a beam energy of 877 MeV. The planning and conditions of the 877 MeV data set are described in Section 6.1. As described there, the data taken during this time had a large transverse component. This meant that the analysis of the 877 MeV data is broken into the longitudinal analysis(Sections 6.2, 6.3, and 6.4) and the transverse analysis(Section 6.7). The longitudinal analysis results in an inelastic asymmetry that grants access to a low-energy constant, $d_\Delta$, associated with hadronic parity violation. By combining the 877 MeV data set with previously measured values of $d_\Delta$, a limit on $d_\Delta$ can be extracted. The transverse analysis results in the measurement of the beam-normal single-spin asymmetry(BNSSA) for N$\rightarrow \Delta$.

### 7.2.1 Longitudinal Inelastic Asymmetry($A_{\mathbf{inel}}$)

The final value for the longitudinal 877 MeV inelastic asymmetry, $-1.2 \pm 1.0$ (stat) $\pm$ 1.0 (syst) ppm, of the 877 MeV data is found in Equation (6.59) in Section 6.4.11. As in the primary measurement, the analysis was performed in three parts. The first part, Section 6.2, extracted the raw asymmetry from the data gathered. The second part, Section 6.3, removed false asymmetries from the raw value to extract the measured asymmetry. The final part, Section 6.4, corrected for polarization, backgrounds, and several multiplicative corrections.

### 7.2.2 Extraction of $d_\Delta$

The inelastic 877 MeV asymmetry, as well as the same value extracted at nominal $\mathrm{Q_{weak}}$ kinematics(described in Section 6.5), can be used to extract a low energy constant $d_\Delta$. The theory connecting $d_\Delta$ to the Siegert term of the inelastic asymmetry can be found in Section 2.4.2, but in summary it parametrizes the nonzero component of the asymmetry at $Q^2 = 0$. While $d_\Delta$ has a natural scale of $g_\pi$, the hadronic coupling constant for PV charged current interactions, a puzzle in Weak Hyperon decay exists whose possible solutions suggests that $d_\Delta$ could be as large as $100 g_\pi$ making this a value of interest.

The extraction of $d_\Delta$ for the two measured inelastic asymmetries taken on the $\mathrm{Q_{weak}}$ apparatus is found in Section 6.6. The two asymmetries are plotted against $Q^2$ in Figure 6.23 alongside lines representing the theoretical inelastic asymmetries for values of $d_\Delta$ that

vary from 0 to $100g_\pi$ in units of $25g_\pi$. The extracted $d_\Delta$ value for the 877 MeV data, $(-8 \pm 22\ (\text{stat}) \pm 22\ (\text{syst}) \pm 3\ (\text{theory}))\ g_\pi$, is found in Equation (6.61). A linear fit of the two $Q_{weak}$ values of $d_\Delta$ and a third previously published value from the G0 Experiment, shown in Figure 6.24, allows the extraction of a constraint on the $d_\Delta$ value, $d_\Delta = (3.8 \pm 14.7)g_\pi$, as seen in Equation (6.63).

### 7.2.3 Transverse Analysis($B_n$)

Section 2.5 describes the theory behind the beam-normal single-spin asymmetryi(BNSSA). In summary, a transversely polarized beam of electrons scattering off an unpolarized target leads to a BNSSA being observed. Dedicated measurements were taken to document this background for the primary $Q_{weak}$ measurement, but the 877 MeV data had a large enough transverse polarization that the analysis of the transverse component resulted in another measurement at the 877 MeV kinematics.

The transverse analysis of the 877 MeV data is discussed in Section 6.7, broken into extracting the measured BNSSA(Section 6.7.1) and correcting the measured value to extract the final BNSSA(Section 6.7.2). The final value of $B_n$ for the 877 MeV data set, $149 \pm 3\ (\text{stat}) \pm 72\ (\text{syst})$ ppm, is shown in Equation (6.95).

One of the motivations of the 877 MeV transverse analysis is to contribute to the future extraction of the electromagnetic form factors of the $\Delta$, as discussed in Section 6.7.3. The N$\rightarrow$ $\Delta$ measurements of $B_n$ taken with the $Q_{weak}$ apparatus, both at 877 MeV and 1165

MeV, will hopefully be the foundation of a data set devoted to extracting these form factors.

# Bibliography

[1] Wikipedia. Standard Model of Elementary Particles. [Online]. Available: https://commons.wikipedia.org/wiki/File:Standard_Model_of_Elementary_Particles.svg

[2] W. S. Duvall, "Precision Measurement of the Proton's Weak Charge using Parity-Violating Electron Scattering," Ph.D. dissertation, Virginia Polytechnic Institute and State University, 2017.

[3] F. Halzen and A. D. Martin, *Quarks and Leptons: An Introductory Course in Modern Particle Physics*. John Wiley & Sons Inc., 1984.

[4] J. D. Leacock II, "Measuring the weak charge of the proton and the hadronic parity violation of the $N \rightarrow \Delta$ transition," Ph.D. dissertation, Virginia Polytechnic Institute and State University, 2012.

[5] S.-L. Zhu, C. M. Maekawa, G. Sacco, B. R. Holstein, and M. J. Ramsey-Musolf, "Electroweak radiative corrections to parity violating electroexcitation of the Delta," *Phys. Rev.*, vol. D65, p. 033001, 2002.

[6] M. M. Dalton, "Accessing the Elastic Form-Factors of the $\Delta(1232)$ Using the Beam-Normal Asymmetry," in *Proceedings, 12th Conference on the Intersections of Particle and Nuclear Physics (CIPANP 2015): Vail, Colorado, USA, May 19-24, 2015*, 2015. [Online]. Available: https://misportal.jlab.org/ul/publications/view_pub.cfm?pub_id=14090

[7] J. Lab. How CEBAF Works. [Online]. Available: https://www.jlab.org/visitors/science/works.html

[8] T. Allison *et al.*, "The Qweak experimental apparatus," *Nuclear Instruments and Methods in Physics Research Section A: Accelerators, Spectrometers, Detectors and Associated Equipment*, vol. 781, no. 0, pp. 105 – 133, 2015.

[9] K. Finelli, "Calibration and Performance Characterization of $Q^p_{Weak}$ Region II Drift Chambers," B.S. Thesis, Virginia Polytechnic Institute and State University, 2009.

[10] J. P. Leckey IV, "The first direct measurement of the weak charge of the proton," Ph.D. dissertation, College of William & Mary, 2012.

[11] E. Bonnell. 5 completed drift chambers. [Online]. Available: https://www1.phys.vt.edu/elog/DRIFT_CHAMBER/78

[12] P. Zang. Renormalized Main Detector - Null and Physics Asymmetries. [Online]. Available: https://qweak.jlab.org/elog/Analysis+%26+Simulation/1558

[13] ——. Natural Monitor Variables III - Regression and Dithering Correction Comparison. [Online]. Available: https://qweak.jlab.org/elog/Analysis+Simulation/1454

[14] ——. Natural Monitor Variables I - Monitor Width Comparison. [Online]. Available: https://qweak.jlab.org/elog/Analysis+Simulation/1444

[15] E. Kargiantoulakis. Proposed Beamline Background Corrections, Run1 and Run2. [Online]. Available: https://qweak.jlab.org/elog/Analysis+Simulation/1652

[16] ——, "Beamline Backgrounds Correction." [Online]. Available: https://qweak.jlab.org/DocDB/0023/002390/001/16-11-14_BeamlineBackgrounds.pdf

[17] D. Androić *et al.*, "Precision measurement of the weak charge of the proton," *Nature*, vol. 557, no. 7704, pp. 207–211, 2018.

[18] V. Gray. N-> Delta - 877 MeV - high statistics simulation. [Online]. Available: https://dilbert.physics.wm.edu/Physics/233

[19] H. A. Nuhait, "Full Simulation for the Qweak Experiment at 1.16 and 0.877 GeV and their impact on extracting the PV Asymmetry in the N -> Transition," Ph.D. dissertation, Louisiana Tech University, 2017.

[20] D. Androic *et al.*, "Measurement of the parity-violating asymmetry in inclusive electroproduction of $\pi^-$ near the $\Delta^0$ resonance," *Phys. Rev. Lett.*, vol. 108, p. 122002, 2012.

[21] C. E. Carlson, B. Pasquini, V. Pauk, and M. Vanderhaeghen, "Beam normal spin asymmetry for the $ep \to e\Delta(1232)$ process," *Phys. Rev.*, vol. D96, no. 11, p. 113010, 2017.

[22] C. Burgess and G. Moore, *The Standard Model: A Primer*. Cambridge, 2007.

[23] B. C. Rislow, "Low energy tests of the standard model," Ph.D. dissertation, The College of William and Mary, 2013.

[24] T. D. Lee and C.-N. Yang, "Question of Parity Conservation in Weak Interactions," *Phys. Rev.*, vol. 104, pp. 254–258, 1956.

[25] C. S. Wu, E. Ambler, R. W. Hayward, D. D. Hoppes, and R. P. Hudson, "Experimental Test of Parity Conservation in Beta Decay," *Phys. Rev.*, vol. 105, pp. 1413–1414, 1957.

[26] D. S. Armstrong and R. D. McKeown, "Parity-Violating Electron Scattering and the Electric and Magnetic Strange Form Factors of the Nucleon," *Ann. Rev. Nucl. Part. Sci.*, vol. 62, pp. 337–359, 2012.

[27] C. Patrignani *et al.*, "Review of Particle Physics," *Chin. Phys.*, vol. C40, no. 10, p. 100001, 2016.

[28] H. Davoudiasl, H.-S. Lee, and W. J. Marciano, "Muon anomaly and dark parity violation," *Phys. Rev. Lett.*, vol. 109, p. 031802, Jul 2012. [Online]. Available: https://link.aps.org/doi/10.1103/PhysRevLett.109.031802

[29] J. Erler and M. J. Ramsey-Musolf, "The Weak mixing angle at low energies," *Phys. Rev.*, vol. D72, p. 073003, 2005.

[30] K. S. Kumar, S. Mantry, W. J. Marciano, and P. A. Souder, "Low Energy Measurements of the Weak Mixing Angle," *Ann. Rev. Nucl. Part. Sci.*, vol. 63, pp. 237–267, 2013.

[31] J. Erler, C. J. Horowitz, S. Mantry, and P. A. Souder, "Weak polarized electron scattering," *Annual Review of Nuclear and Particle Science*, vol. 64, no. 1, pp. 269–298, 2014. [Online]. Available: https://doi.org/10.1146/annurev-nucl-102313-025520

[32] N. C. Mukhopadhyay, M. J. Ramsey-Musolf, S. J. Pollock, J. Liu, and H. W. Hammer, "Parity violating excitation of the Delta (1232): Hadron structure and new physics," *Nucl. Phys.*, vol. A633, pp. 481–518, 1998.

[33] H. W. Hammer and D. Drechsel, "Parity violating pion electroproduction off the nucleon," *Z. Phys.*, vol. A353, pp. 321–331, 1995.

[34] C. L. Capuano, "Parity-violating asymmetry in the nucleon to $\Delta$ Transition," Ph.D. dissertation, The College of William and Mary, 2012.

[35] L. M. Nath, K. Schilcher, and M. Kretzschmar, "Parity Violating Effects in Electroproduction of the $\Delta$ (1232) by Polarized Electrons," *Phys. Rev.*, vol. D25, p. 2300, 1982.

[36] V. Bernard, L. Elouadrhiri, and U.-G. Meissner, "Axial structure of the nucleon: Topical Review," *J. Phys.*, vol. G28, pp. R1–R35, 2002.

[37] P. A. Schreiner and F. Von Hippel, "Neutrino production of the Delta (1236)," *Nucl. Phys.*, vol. B58, pp. 333–362, 1973.

[38] S. L. Adler, "Photoproduction, electroproduction and weak single pion production in the (3,3) resonance region," *Annals Phys.*, vol. 50, pp. 189–311, 1968.

[39] ——, "Application of Current Algebra Techniques to Soft Pion Production by the Weak Neutral Current: V,a Case," *Phys. Rev.*, vol. D12, p. 2644, 1975.

[40] S.-L. Zhu, S. J. Puglia, B. R. Holstein, and M. J. Ramsey-Musolf, "The Nucleon anapole moment and parity violating e p scattering," *Phys. Rev.*, vol. D62, p. 033008, 2000.

[41] A. J. F. Siegert, "Note on the interaction between nuclei and electromagnetic radiation," *Phys. Rev.*, vol. 52, pp. 787–789, 1937.

[42] J. L. Friar and S. Fallieros, "Extended Siegert theorem," *Phys. Rev.*, vol. C29, pp. 1645–1655, 1984.

[43] B. Borasoy and B. R. Holstein, "Resonances in radiative hyperon decays," *Phys. Rev.*, vol. D59, p. 054019, 1999.

[44] D. B. P. Waidyawansa, "A 3% measurement of the beam normal single spin asymmetry in forward angle elastic electron-proton scattering using the Qweak setup," Ph.D. dissertation, Ohio University, 2013.

[45] C. W. Leemann, D. R. Douglas, and G. A. Krafft, "The Continuous Electron Beam Accelerator Facility: CEBAF at the Jefferson Laboratory," *Ann. Rev. Nucl. Part. Sci.*, vol. 51, pp. 413–450, 2001.

[46] T. Nishitani, T. Nakanishi, M. Yamamoto, S. Okumi, F. Furuta, M. Miyamoto, M. Kuwahara, N. Yamamoto, K. Naniwa, O. Watanabe, Y. Takeda, H. Kobayakawa, Y. Takashima, H. Horinaka, T. Matsuyama, K. Togawa, T. Saka, M. Tawada,

T. Omori, Y. Kurihara, M. Yoshioka, K. Kato, and T. Baba, "Highly polarized electrons from gaas–gaasp and ingaas–algaas strained-layer superlattice photocathodes," *Journal of Applied Physics*, vol. 97, no. 9, p. 094907, 2005. [Online]. Available: http://dx.doi.org/10.1063/1.1886888

[47] C. Sinclair, P. Adderley, B. Dunham, J. Hansknecht, P. Hartmann, M. Poelker, J. Price, P. Rutt, W. Schneider, and M. Steigerwald, "Development of a high average current polarized electron source with long cathode operational lifetime," *Physical Review Special Topics - Accelerators and Beams*, vol. 10, p. 023501, 2007.

[48] R. J. Celotta and D. Pierce, "Sources of polarized electrons," *Advances in Atomic and Molecular Physics*, vol. 16, p. 101, 1980.

[49] C. Yan, R. Carlini, and D. Neuffer, "Conference Proceedings CC930517," p. 2136, 1993.

[50] P. Zang, "Main Detector Asymmetry Summary." [Online]. Available: https://qweak.jlab.org/DocDB/0023/002373/014/MD_Asymmetries_Summary.pdf

[51] A. Narayan *et al.*, "Precision Electron-Beam Polarimetry at 1 GeV Using Diamond Microstrip Detectors," *Phys. Rev.*, vol. X6, no. 1, p. 011013, 2016.

[52] P. Wang, "A measurement of the proton's weak charge using an integration Čerenkov detector system," Ph.D. dissertation, University of Manitoba, 2011.

[53] J. Pan, "Towards a precision measurement of parity-violating e-p elastic scattering at low momentum transfer," Ph.D. dissertation, University of Manitoba, 2012.

[54] K. E. Myers, "The first determination of the proton's weak charge through parity-violating asymmetry measurements in elastic e + p and e + Al scattering," Ph.D. dissertation, The George Washington University, 2012.

[55] J. Mammei, "Parity-Violating Elastic Electron Nucleon Scattering: Measurement of the Strange Quark Content of the Nucleon and Towards a Measurement of the Weak Charge of the Proton," Ph.D. dissertation, Virginia Polytechnic Institute and State University, 2010.

[56] M. J. McHugh III, "A Measurement of the Transverse Asymmetry in Forward-Angle Electron-Carbon Scattering Using the $Q_{weak}$ Apparatus," Ph.D. dissertation, The George Washington University, 2017.

[57] W. A. Watson III, J. Chen, G. Heyes, E. Jastrzembski, and D. Quarrie, "Coda: A scalable, distributed data acquisition system," in *Proceedings of the Real Time Conference, 1993*, 1993, p. 296.

[58] R. S. Beminiwattha, "A measurement of the weak charge of the proton through parity violating electron scattering using the Qweak apparatus: A 21% result," Ph.D. dissertation, Ohio University, 2013.

[59] P. Wang, "Magnetic field simulation and mapping for the qweak experiment," Master's thesis, University of Manitoba, 2007.

[60] V. M. Gray, "Determination of the kinematics of the $Q_{weak}$ experiment and investigation of an atomic hydrogen møller polarimeter," Ph.D. dissertation, College of William & Mary, 2018.

[61] S. Agostinelli *et al.*, "GEANT4: A Simulation toolkit," *Nucl. Instrum. Meth.*, vol. A506, pp. 250–303, 2003.

[62] K. Bartlett. Aluminum 4p DS Simulation Theta and Q2 Distribution Comparison to Pass 7 Tracking Run 13722. [Online]. Available: https://qweak.jlab.org/elog/Tracking/246

[63] P. Zang, "Final dataset - from pass5c to pass5c+." [Online]. Available: https://qweak.jlab.org/elog/Analysis+%26+Simulation/1629

[64] ——, "BCM Renormalization (Pass5c+)." [Online]. Available: https://qweak.jlab.org/DocDB/0023/002344/010/BCM_Normalization_in_RUN1_and_RUN2_Pass5c%2B_new_mdMrn_norm.pdf

[65] D. Androic *et al.*, "First determination of the weak charge of the proton," *Physical Review Letters*, vol. 111, p. 141803, 2013. [Online]. Available: http://link.aps.org/doi/10.1103/PhysRevLett.111.141803

[66] P. Zang, "Beam Correction Summary." [Online]. Available: https://qweak.jlab.org/DocDB/0023/002376/006/Beam_Correction_Summary.pdf

[67] ——. Natural Monitor Variables 0 - Definition and Procedure. [Online]. Available: https://qweak.jlab.org/elog/Analysis+Simulation/1451

[68] ——. Tentative Quantization of Regression and Dithering Discrepancy. [Online]. Available: https://qweak.jlab.org/elog/Analysis+Simulation/1588

[69] ——. Natural Monitor Variables VI - "Beam Correction" to Beam Position Monitors. [Online]. Available: https://qweak.jlab.org/elog/Analysis+Simulation/1483

[70] J. Arrington, P. G. Blunden, and W. Melnitchouk, "Review of two-photon exchange in electron scattering," *Prog. Part. Nucl. Phys.*, vol. 66, pp. 782–833, 2011.

[71] B. P. Waidyawansa, "Beam Normal Single Spin Asymmetry Measurements from QWeak," 2016.

[72] P. King. Update for the Run1 and Run2 Transverse Asymmetry Leakage error contributions. [Online]. Available: https://qweak.jlab.org/elog/Analysis+Simulation/1663

[73] ——. Summary of blinding factor algorithm. [Online]. Available: https://qweak.jlab.org/elog/Management/24

[74] K. Bartlett and K. Mesick. Final Determination of the Effective aluminum window asymmetry(A_b1+-dA_b1) using Monte Carlo method. [Online]. Available: https://qweak.jlab.org/elog/Analysis+Simulation/1651

[75] J. Magee, "A measurement of the parity-violating asymmetry in aluminum and its contribution to a measurement of the proton's weak charge," Ph.D. dissertation, The College of William & Mary, 2016.

[76] J. Erler, A. Kurylov, and M. J. Ramsey-Musolf, "The Weak charge of the proton and new physics," *Phys. Rev.*, vol. D68, p. 016006, 2003.

[77] R. D. Young, R. D. Carlini, A. W. Thomas, and J. Roche, "Testing the standard model by precision measurement of the weak charges of quarks," *Phys. Rev. Lett.*, vol. 99, p. 122003, Sep 2007. [Online]. Available: http://link.aps.org/doi/10.1103/PhysRevLett.99.122003

[78] D. T. Spayde *et al.*, "The Strange quark contribution to the proton's magnetic moment," *Phys. Lett.*, vol. B583, pp. 79–86, 2004.

[79] T. M. Ito *et al.*, "Parity violating electron deuteron scattering and the proton's neutral weak axial vector form-factor," *Phys. Rev. Lett.*, vol. 92, p. 102003, 2004.

[80] K. A. Aniol *et al.*, "Measurement of the neutral weak form-factors of the proton," *Phys. Rev. Lett.*, vol. 82, pp. 1096–1100, 1999.

[81] ——, "Parity-violating electron scattering from $^4$He and the strange electric form factor of the nucleon," *Phys. Rev. Lett.*, vol. 96, p. 022003, Jan 2006. [Online]. Available: http://link.aps.org/doi/10.1103/PhysRevLett.96.022003

[82] ——, "Constraints on the nucleon strange form-factors at Q**2 0.1- GeV**2," *Phys. Lett.*, vol. B635, pp. 275–279, 2006.

[83] A. Acha *et al.*, "Precision Measurements of the Nucleon Strange Form Factors at Q**2 0.1-GeV**2," *Phys. Rev. Lett.*, vol. 98, p. 032301, 2007.

[84] Z. Ahmed *et al.*, "New Precision Limit on the Strange Vector Form Factors of the Proton," *Phys. Rev. Lett.*, vol. 108, p. 102001, 2012.

[85] D. S. Armstrong *et al.*, "Strange quark contributions to parity-violating asymmetries in the forward G0 electron-proton scattering experiment," *Phys. Rev. Lett.*, vol. 95, p. 092001, 2005.

[86] D. Androic *et al.*, "Strange Quark Contributions to Parity-Violating Asymmetries in the Backward Angle G0 Electron Scattering Experiment," *Phys. Rev. Lett.*, vol. 104, p. 012001, 2010.

[87] F. E. Maas *et al.*, "Measurement of strange quark contributions to the nucleon's form-factors at Q**2 = 0.230-(GeV/c)**2," *Phys. Rev. Lett.*, vol. 93, p. 022002, 2004.

[88] ——, "Evidence for strange quark contributions to the nucleon's form-factors at q**2 = 0.108 (GeV/c)**2," *Phys. Rev. Lett.*, vol. 94, p. 152001, 2005.

[89] S. Baunack *et al.*, "Measurement of Strange Quark Contributions to the Vector Form Factors of the Proton at Q**2=0.22 (GeV/c)**2," *Phys. Rev. Lett.*, vol. 102, p. 151803, 2009.

[90] C. S. Wood, S. C. Bennett, D. Cho, B. P. Masterson, J. L. Roberts, C. E. Tanner, and C. E. Wieman, "Measurement of parity nonconservation and an anapole moment in cesium," *Science*, vol. 275, pp. 1759–1763, 1997.

[91] V. A. Dzuba, J. C. Berengut, V. V. Flambaum, and B. Roberts, "Revisiting parity non-conservation in cesium," *Phys. Rev. Lett.*, vol. 109, p. 203003, 2012.

[92] M. McHugh. 877 mev total neutral dilution. [Online]. Available: https://qweak.jlab.org/elog/Ancillary/183

[93] J. F. Dowd, "Probe of electroweak interference effects in non-resonant inelastic electron-proton scattering," Ph.D. dissertation, College of William and Mary, 2019.

[94] D. Armstrong. N-Delta $Q^2$ error summary. [Online]. Available: https://dilbert.physics.wm.edu/Physics/239

[95] ——. d($R_{Q2}$) for N->Delta longitudinal. [Online]. Available: https://qweak.jlab.org/elog/Ancillary/333

[96] Nuruzzaman, "Beam normal single spin asymmetry in forward angle inelastic electron-proton scattering using the q-weak apparatus," Ph.D. dissertation, Hampton University, 2014.

[97] K. D. Bartlett, "First Measurements of the Parity-Violating and Beam-Normal Single-Spin Asymmetries in Elastic Electron-Aluminum Scattering," Ph.D. dissertation, College of William and Mary, 2018.

[98] A. V. Afanasev and N. P. Merenkov, "Collinear photon exchange in the beam normal polarization asymmetry of elastic electron-proton scattering," *Phys. Lett.*, vol. B599, p. 48, 2004.

[99] A. Lee. Summary of gas target work. [Online]. Available: https://www1.phys.vt.edu/elog/MISCELLANEOUS/559

# Appendices

# Appendix A

# Personal Contributions

The $Q_{weak}$ Experiment was performed by a large collaboration(101 collaborators). This dissertation touches on every aspect of the main measurement and describes in full one of the ancillary measurements that came out of the $Q_{weak}$ Experiment. As such, it contains the work of all the authors of $Q_{weak}$. The full list of authors can be found in the published Nature article [17] and Physical Review Letter of the commissioning results [65]. My personal contributions to the $Q_{weak}$ Experiment, both those that are included elsewhere in this dissertation and those that are not, will be described in this appendix as well as work I performed for the benefit of the next PVES experiment, MOLLER.

# A.1 Primary Measurement

The $Q_{weak}$ Experiment measured the elastic parity-violating asymmetry of the $\vec{e}+p \rightarrow e+p$ electroweak interaction at an extreme forward angle. A paper on the primary goal of the experiment, extracting the weak charge of the proton($Q_w^p$), was published in Nature in May 2018. This section will summarize my contributions to this measurement.

## A.1.1 During Running

I joined the $Q_{weak}$ experiment in August 2010. The $Q_{weak}$ apparatus had already been installed and started collecting data. As I was currently taking classes, I was only able to take a few shifts at this time as shift leader which involved being in charge of starting and stopping runs, communicating with the MCC, making sure the run plan for the shift was followed, and documenting various measurements in the electronic logbook. I also started working on the tracking data, but that will be discussed in more detail in the tracking section of this appendix.

There was a six-month down time due to upgrades to the accelerator facility. During that period of time, the luminosity monitors required some upkeep. Mark Pitt and Wade Duvall were primarily in charge of this, but John Leacock and I assisted.

When the experiment started taking data for run 2, I took 40+ eight-hour shifts, some as shift leader and some as target operator. Target operator shifts involved tracking many target variables and making sure that the target did not freeze or boil. I also took some

$Q_{weak}$ Analysis Coordinator(QwAC) shifts. These were weak long time periods where I performed offline analyses of the most recently taken data. The responsibility of the QwAC was to provide the current run coordinator a concept of how the current data appears with the aim of identifying any issues quickly.

During tracking periods, I assisted with both data-taking and manipulating the horizontal drift chamber rotator apparatus. I took as many shifts as possible during the tracking periods and used my spare time to participate in quick analyses and studies of the data as it came in.

### A.1.2 After Running

When Jefferson Lab shut down for the 12 GeV upgrades, the $Q_{weak}$ Experiment officially stopped collecting data. That meant that the $Q_{weak}$ apparatus required dismantling and removal from Hall C. Due to Mark Pitt's required attendence at Virginia Tech, Wade Duvall and I were responsible for the documentation and decabling of the components that Virginia Tech built. Specifically, the two of us removed the cabling for the horizontal drift chambers and the luminosity monitors over a few weeks.

### A.1.3 Full Data Replays

Periodically, the full data set of the primary measurement would be run through the current version of the software analyzer. This was done to take into account any upgrades or corrections applied to the analyzer over time. Over the course of these replays all gradu-

ate students, including me, participated in submitting jobs to have the Jefferson Lab server farm analyze the data.

### A.1.4 Tracking

My main focus in the $Q_{weak}$ measurement of the elastic parity-violating asymmetry and the resulting value of the weak charge of the proton was in the tracking data. As previously mentioned, I assisted during tracking periods when the data was taken, but I was responsible for multiple studies done on the horizontal drift chamber(HDC) data. This section will touch on the many ways I contributed to the tracking analysis.

My first contribution to the $Q_{weak}$ collaboration involved tracking down an issue with the triggered window in the HDCs. Originally the HDCs recorded hits when $-500$ ns $< t <$ 1500 ns, where $t = 0$ was the trigger firing. However, problems observed in the drift time distribution led to the discovery that the HDC data recording window had been shortened to $0 < t < 1500$ ns. The data recording window was corrected once this discovery was made.

I contributed to the body of software that was associated with the tracking analysis by developing multiple diagnostic scripts for the HDC performance. These diagnostic scripts created plots such as plane efficiency(when a track was made, how often was this plane used in the track), wire hit maps in each plane, and drift distance and time distributions. I later adapted some of these scripts to work as automatic scripts that could be run on the full tracking data set.

Using pointing runs, described in Section 4.2.2, I checked the reproducibility of the HDC positions between tracking periods. These pointing run studies lead to the discovery of the problem with HDC geometry(Section 4.2.2) and I used them extensively to correct the issue(Section 4.2.3).

Another study I performed using the tracking data involved extracting the gaseous hydrogen profile from two runs taken at different gas pressures. Due to the low density of the gaseous hydrogen, this required the influence of the aluminum windows to be isolated and then removed from the profiles. Once the gaseous hydrogen had been isolated, limited $Q^2$ and $\theta$ distributions could be compare with the $LH_2$ distributions. The distributions had to be limited to avoid contamination from the aluminum windows. This study is not included in this dissertation but can be found summarized in the Virginia Tech electronic logbook [99].

## A.2 Ancillary Measurement

A large part of my time and effort was devoted to my ancillary measurement, the N$\rightarrow \Delta$ transition at 877 MeV. A month before this data set was taken in April 2012, I was given the responsibility of curating it. My responsibilities started prior to data taking and will end with the analysis of this data set in this dissertation. Chapter 6 goes into detail on the 877 MeV data, analysis, and implications.

### A.2.1 Prior to Data-taking

Section 6.1.1 discusses my work done prior to the start of the 877 MeV data-taking. To summarize, I used GEANT3 to simulate the elastic and inelastic rates. These simulations were then used to determine the toroidal spectrometer setting to maximize the inelastic signal while minimizing the two pion production background process that would introduce an unknown asymmetry into the signal.

### A.2.2 During Running

While the 877 MeV data was running, I spent as much time as possible in the counting house both on shift and not. I did preliminary analyses on the data and presented them to the collaboration. I also documented the data taken, both for the main 877 analysis and any other measurements made. These other measurements included things such as tracking data, scans of the toroidal spectrometer, and data taken off peak.

### A.2.3 Analysis

I put together both the longitudinal analysis(Sections 6.2, 6.3, and 6.4) and the transverse analysis(Section 6.7). My final longitudinal asymmetry was combined with a previously measured value for the 1165 MeV data to extract a limitation on the low energy constant $d_\Delta$(Section 6.6).

## A.3 BCM calibration for the MOLLER Experiment

After the $Q_{weak}$ apparatus was disassembled and the analysis was fully underway. I was asked to run some hardware studies intended to benefit the next parity-violating electron scattering experiment, MOLLER, based on some observations of the beam current monitors(BCMs) during $Q_{weak}$.

While $Q_{weak}$ was taking data, it was observed that the width of the difference between the asymmetries viewed by two BCMs, referred to as the double difference, had a noise floor at ∼65 ppm. In other words, it never decreased far below 65 ppm no matter how high the current went. This was not an issue with the $Q_{weak}$ data, but the MOLLER Experiment requires more precision. This noise floor would need significant improvement for the MOLLER Experiment.

In order to investigate the issue and see if the MOLLER goal was feasible, I had to first recreate the double difference noise floor observed during $Q_{weak}$. This was done by using two of the $Q_{weak}$ BCMs and a RF source to mimic the input beam in a test room at Jefferson Lab. With assistance from Wade Duvall and Mark Pitt, I successfully recreated a similar noise floor(57 ppm) as seen in the $Q_{weak}$ Experiment.

After recreating the $Q_{weak}$ observations, I was able to use two of the new BCMs designed for the Møller Experiment to create a similar set-up with assistance from John Musson who built the new receivers. This allowed the expected noise floor for the Møller Experiment to be studied. The result was a noise floor of 32 ppm, an improvement over the $Q_{weak}$ value. I

also tested several different set-ups with the new BCMs to investigate the cause of the noise floor. These studies suggest that local oscillator noise might be to blame for the noise floor.